

Improving the Sensing Performance of Semiconductor Metal Oxide Gas Sensors through  
Composition and Nanostructure Design

by

Jiansong Miao

A Dissertation Presented in Partial Fulfillment  
of the Requirements for the Degree  
Doctor of Philosophy

Approved August 2020 by the  
Graduate Supervisory Committee:

Jerry Y.S. Lin, Chair  
Erica Forzani  
Jingyue Liu  
Jian Li

ARIZONA STATE UNIVERSITY

December 2020

## ABSTRACT

There are increasing demands for gas sensors in air quality and human health monitoring applications. The qualifying sensor technology must be highly sensitive towards ppb level gases of interest, such as acetylene ( $C_2H_2$ ), hydrogen sulfide ( $H_2S$ ), and volatile organic compounds. Among the commercially available sensor technologies, conductometric gas sensors with nanoparticles of oxide semiconductors as sensing materials hold significant advantages in cost, size, and cross-compatibility. However, semiconductor gas sensors must overcome some major challenges in thermal stability, sensitivity, humidity interference, and selectivity before potential widespread adoption in air quality and human health monitoring applications.

The focus of this dissertation is to tackle these issues by optimizing the composition and the morphology of the nanoparticles, and by innovating the structure of the sensing film assembled with the nanoparticles. From the nanoparticles perspective, the thermal stability of tin oxide nanoparticles with different Al dopant concentrations was studied, and the results indicate that within certain range of doping concentration, the dopants segregated at the grain surface can improve the thermal stability by stabilizing the grain boundaries.

From the sensing film perspective, a novel self-assembly approach was developed for copper oxide nanosheets and the sensor response towards  $H_2S$  gas was revealed to decrease monotonically by more than 60% as the number of layers increase from 1 to 300 (thickness: 0.03-10  $\mu m$ ). Moreover, a sensing mechanism study on the humidity influence on  $H_2S$  detection was performed to gain more understandings of the role of the hydroxyl group in the surface reaction, and humidity independent response was observed in the monolayer

film at 325 °C. With a more precise deposition tool (Langmuir-Blodgett trough), monolayer film of zinc oxide nanowires sensitized with gold catalyst was prepared, and highly sensitive and specific response to C<sub>2</sub>H<sub>2</sub> in the ppb range was observed. Furthermore, the effect of surface topography of the monolayer film on stabilizing noble metal catalyst, and the sensitization mechanism of gold were investigated.

Lastly, a semiconductor sensor array was developed to analyze the composition of gases dissolved in transformer oil to demonstrate the industrial application of this sensor technology.

## ACKNOWLEDGEMENT

First of all, I would like to express my sincere gratitude to my supervisor Prof. Jerry Lin for his support and trust. I would also like to express my appreciation to the technical staff in the core facilities, particularly Scott Ageno, Jaime Quintero, Kevin Hilgers, Kevin Nordquest, Carrie Sinclair, Timothy Karcher, Karl Weiss for the research assistance they have provided to me over the years. Next, I would like to thank my lab mates in the membrane and energy lab, especially Dr. Lie Meng, Dr. Linhui Yu, Dr. Joshua James, Dr. Oscar Ovalle-Encinia, Dr. Amr Ibrahim, Dr. Margarita Ramirez-Moreno, Dr. Zebao Rui, Dr. Stanley Ma, Dr. Ben Wu, Kishen Rafiz, Fateme Banihashemi for being such great company and for the assistance with various experiments or simulations.

Last but not least, I want to thank my wonderful wife and my caring parents for helping me to get through the difficult times I experienced during my PhD journey.

# TABLE OF CONTENTS

	Page
LIST OF TABLES.....	ix
LIST OF FIGURES .....	xii
	CHAPTER
1. INTRODUCTION .....	1
1.1 General Background.....	1
1.2 Motivation for Dissertation Research and Dissertation Structure.....	5
2. LITERATURE REVIEW .....	9
2.1 Semiconductor Gas Sensor .....	9
2.2 Key Parameters in Gas Sensing .....	14
2.3 Principles of Operation .....	16
2.3.1 Surface Chemistry.....	16
2.3.2 Charge Transfer.....	25
2.3.3 Conduction in the Sensitive Layer .....	29
2.3.4 Conduction Model and Power Law Relationship .....	31
2.3.5 Sensing Mechanism of P-type Semiconductor .....	34
2.4 Influencing Factors on the Sensing Performance.....	37
2.4.1 Sensing Film Structures .....	37

CHAPTER	Page
2.4.2 Grain Size.....	42
2.4.3 Doping.....	44
3. SELF-ASSEMBLED MONOLAYER OF METAL OXIDE NANOSHEET AND STRUCTURE AND GAS SENSING PROPERTY RELATIONSHIP .....	46
3.1 Introduction .....	46
3.2 Experimental Section .....	48
3.3 Results and Discussion.....	53
3.3.1 Structure and Surface Properties of CuO Nanosheets.....	53
3.3.2 Film Formation and Characteristics .....	56
3.3.3 Gas Sensing Performance and Modeling .....	62
3.3.4 Monolayer Film of ZnO Nanosheets as H <sub>2</sub> Sensor .....	73
4. HUMIDITY INDEPENDENT HYDROGEN SULFIDE SENSING RESPONSE ACHIEVED WITH MONOLAYER FILM OF CUO NANOSHEETS .....	76
4.1 Introduction .....	76
4.2 Material and Methods .....	80
4.2 Results and Discussion.....	81
4.2.1 Sensing Performance.....	81
4.2.2 Sensing Mechanism .....	86

CHAPTER	Page
5. NANOMETER-THICK FILMS OF ALIGNED ZNO NANOWIRES SENSITIZED WITH AU NANOPARTICLES SENSITIZED WITH AU NANOPARTICLES FOR FEW-PPB LEVEL ACETYLENE DETECTION .....	99
5.1 Introduction .....	99
5.2 Experimental .....	102
5.3 Results and Discussion.....	106
6. METAL-OXIDE NANOPARTICLES WITH A DOPANT-SEGRAGATION-INDUCED CORE-SHELL STRUCTURE: GAS SENSING PROPERTIES .....	131
6.1 Introduction .....	131
6.2 Experimental .....	133
6.2.1 Preparation of Pure and Aluminum Doped SnO <sub>2</sub> Nanoparticles .....	133
6.2.2 Characterization .....	133
6.2.3 Gas Sensor Fabrication and Sensing Measurements.....	134
6.3. Results and Discussion.....	135
6.3.1 Structure and Thermal Stability Improvement of Al-doped SnO <sub>2</sub> .....	135
6.3.2 Gas Sensing Properties and Mechanisms.....	145
7. SEMICONDUCTOR SENSOR ARRAY FOR DISSOLVED GAS ANALYSIS .....	152
7.1 Introduction and Objectives .....	152
7.2 Sensor Testing System Development.....	155

CHAPTER	Page
7.3 Development of Device Fabrication Technique .....	159
7.3.1 Response Rate Enhancement by Reducing Both Agglomeration and Sensing Layer Thickness.....	160
7.4. Sensing Materials Library Development .....	162
7.4.1 Sensing Materials Synthesis.....	162
7.4.2 Characterization Techniques for Structural, Composition, and Electrical Properties Analysis.....	167
7.4.3 Zinc (II) Oxide-based Sensing Materials .....	169
7.4.4 Tin (IV) Oxide-based Sensing Materials .....	176
7.4.5 Copper(II) Oxide-based Sensing Materials.....	179
7.5 Materials Selection for the Sensor Array .....	203
7.5.1 Sensitivity — Sum of Root Sum Square (SRSS).....	206
7.5.2 Selectivity — Sum of Euclidean Distances (SED) .....	206
7.6 Accelerated Life Testing .....	211
7.6.1 Materials and Equipment: .....	212
7.6.2 Procedure: .....	212
7.6.3 Results .....	213
7.7 Prototype Design, Construction, and Initial Tests .....	217
8. CONCLUSIONS AND FUTURE WORK.....	227



	Page
REFERENCES .....	232
APPENDIX.....	250
A. LIST OF PUBLICATIONS .....	250

## LIST OF TABLES

Table	Page
1. Composition of Polluted Air and Exhaled Breath .....	4
2. Comparison of Commercially Available Sensors Based on Different Technologies.....	5
3. Conduction Models Based on Different Sensing Film Geometries.....	30
4. Selected Works Studying 2D Metal Oxides as Gas Sensing Material, and Studies Focusing on Sensing Film Morphology Based on Metal Oxides with 0D, 1D, and 3D Nanostructures.....	49
5. Side View of (002), (110), (200), and (020) Crystal Planes of CuO and Their Calculated Surface Energy .....	58
6. Comparison of the Sensing Performance of CuO Sensors to H <sub>2</sub> S.....	69
7. Surface Concentration According to XPS Wide Scan.....	90
8. Surface Properties and Sintering Resistant Performance of Three Different ZnO Substrates .....	115
9. Key Sensing Parameters Other Than Response Measured at 325 °C Towards 25 PPM of C <sub>2</sub> H <sub>2</sub> .....	117
10. Selected Works Studying the C <sub>2</sub> H <sub>2</sub> Sensing Performance of Various MOX Gas Sensors .....	126
11. Particle Sizes of As-Synthesized and Thermally-Treated Samples with Al Content Between 0-25 Mol% and Grain Growth Rate. ....	137
12. Grain Coalescence Level as a Function of Doping Concentration.....	142

Table	Page
13. The Concentration of Dissolved Gases for Normal Operating Transformers According to IEEE Standard.....	149
14. Commercial Sensor Unit for Dissolved Gas Analysis.....	149
15. Commercial Gas Sensor Technology.....	150
16. The Specifications of the Mass Flow Controllers Used in the Gas Sensing System.	154
17. Mass Flow Controller Set Points for Achieving Concentration Between 1-1000 PPM Using a 1000 PPM Cylinder. ....	154
18. Summary of Sensor Properties Of ZnO Thick Film at 175°C. ....	167
19. Sensor Made From ZnO Nanoflower, Gas Concentration: 25 PPM, Temperature: 300°C. ....	171
20. Weight Percentages and Grain Size Information of the CuO/CeO <sub>2</sub> Composite Hollow Spheres Revealed by Rietveld Refinement.....	179
21. Crystallite Size, Cell Parameters, and BET Surface Area of Pure and Ce-Doped CuO Samples. ....	184
22. Crystallite Size, Cell Parameters, and BET Surface Area of Ce-Doped CuO Samples before and after Ball Milling.....	192
23. Percentage Recovered in 10 Min after Testing at 80°C to 50 PPM CO. ....	192
24. A List of the Sensors Selected Using Different Selection Techniques.....	205
25. Selectivity and Sensitivity Values for the Individual Selection of Sensors.....	206
26. Response Values for the Sensors Treated at 600°C for Different Amount of Times	210
27. Response Values for the Sensors Treated at 700°C for Different Amount of Times	211

Table	Page
28. Semiconductor Gas Sensors: Specifications.....	214
29. Summary of Response Values.....	215
30. Summary of Response Values.....	216
31. Summary of Response Values.....	217
32. Summary of Response Values.....	218
33. Summary of Response Values.....	219
34. Summary of Response Values.....	220
35. Summary of Response Values.....	221
36. Summary of Response Values.....	222

## LIST OF FIGURES

Figure	Page
1. Studies on N- and P-Type Semiconductor Gas Sensors .....	10
2. Schematic of Taguchi Type Sensor (A) and Electric Circuit for Measuring Sensor Resistance (B). .....	11
3. Gas Sensor Prepared by Screen-Printing on A Ceramic Substrate of Size 6 mm×8 mm. the Sensor Element Consists of a CO- And a NO <sub>x</sub> -Sensitive Layer. The Platinum Structures (Heater, Electrodes and Contact Pads) and the Two Sensitive Layers are Manufactured in Screen-Printing Technology.....	12
4. Schematic of the MGS 1100 Sensor from Motorola. Micromachined Sensor Element on the Left and Sensor Housing on the Right. The Sensitive Film was Obtained by Rheotaxial Growth and Thermal Oxidation of Tin Layer (RGTO) Deposited on the Silicon Oxide-Nitride Membrane.....	14
5. Energy Diagram of Various Oxygen Species in the Gas Phase, Adsorbed at the Surface and Bound within the Lattice of a Binary Metal Oxide <sup>16</sup> . .....	19
6. Literature Survey of Oxygen Species Detected at Different Temperatures at SnO <sub>2</sub> Surfaces with IR (Infrared Analysis), TPD (Temperature Programmed Desorption), EPR (Electron Paramagnetic Resonance). .....	20
7. The Simulated Equilibrium Coverages of the Oxygen Species. The Transition from O <sub>2</sub> <sup>-</sup> To O <sup>-</sup> Is Calculated to Be Around 700K.....	21
8. Energy Parameters of Molecules in the Gas Phase. Ionization Potential (1), Proton Affinity (2) and Electron Affinity (3). .....	24

Figure	Page
9. (A) Schematic Drawing of Surface Depletion Layer Formed by Oxygen Adsorption for an N-Type Semiconductor. (B) Schematic Diagrams of Electronic Equilibrium for Semiconductor Plates of Different Thicknesses Placed Under Various Partial Pressures of Oxygen Depth Profiles of Potential Energy (C) Typical Shapes of Crystals and Coordinate Systems Selected. ....	28
10. Calibration Lines of $\text{WO}_3$ , $\text{In}_2\text{O}_3$ and $\text{SnO}_2$ sensors at (A) High Partial Pressure of Oxygen. ....	34
11. Energy Bands Representation of the Surface Processes Associated to the Reaction with Ambient Oxygen and Reduction Gases. ....	36
12. Sputtered Film of $\text{SnO}_2$ . ....	38
13. SEM Image of $\text{SnO}_2$ Sensing Film Prepared by Screen Printing. ....	38
14. SEM Images of Sensing Layer Deposited by Microdrop Method. ....	39
15. Concentration Gradient along the Thickness of a Porous Sensing Film. ....	40
16. SEM Image of RGTO $\text{SnO}_2$ Film. ....	42
17. Gas Sensitivity of the $\text{SnO}_2$ Sensors Doped with 5 At. % Additives to: (A) 899 PPM $\text{H}_2$ , (B) 800 PPM $\text{CO}$ , and (C) 1000 PPM $\text{I-C}_4\text{H}_{10}$ . ....	43
18. Schematic of the Gas Sensor Testing System. ....	53
19. (A) XRD Pattern, (B) SEM, (C) EDS, (D) XPS Wide Scan, (E) High Resolution $\text{Cu } 2p$ , And (F) High Resolution $\text{O } 1s$ of the As-Synthesized $\text{CuO}$ Nanosheets. ....	55
20. (A) Low Magnification TEM Image of $\text{CuO}$ Nanosheets and the SAED Pattern and a Sketch of the Crystal Orientation in the Real Space as Inset; (B) Lattice Resolved HRTEM Image and the Fast-Fourier-Transform (FFT) Pattern as Inset. ....	56

Figure	Page
21. Illustration of the Monolayer Film Formation Process Using the Home-Built Coater	57
22. (A) Top Surface and (B) Cross-Section SEM Image of the CuO Nanosheet Monolayer on Glass Substrate; (C) XRD Patterns of CuO-Mono, CuO-5 $\mu$ m, and CuO-10 $\mu$ m; (D) Films Prepared with Higher than Ideal Addition Weight and Concentration, and Their SEM Images. ....	59
23. High Resolution XPS of O 1s of the Thermally Annealed CuO-Nanosheets.....	60
24. (A) SEM Top-View of CuO-5 $\mu$ m; (B) Nitrogen Adsorption Isotherm of the Multilayer Film; (C) Pore Distribution Derived from BJH Adsorption; (D) Model of a Multilayer Film with Lamellar Structure. ....	61
25. (A) Resistance Value in Air ( $R_{air}$ ) As a Function of Temperature; (B) Repeated Transient Response Test at 250 °C in 1 PPM H <sub>2</sub> S; Sensor Response (S), Response Time, and Recovery Time as a Function of (C) Temperature and (D) Concentration.....	64
26. XRD Patterns of CuO-5 $\mu$ m before and after Treated in Gas Chamber at 250 °C with Air Flow Containing 1 PPM of H <sub>2</sub> S.....	66
27. Transient Response Curve to Varied Concentration of H <sub>2</sub> S Collected at 250 °C.....	66
28. (A) Transient Response to 1 PPM of H <sub>2</sub> S at 250 °C in Wet and Dry Air; (B) Sensor Responses to 1 PPM Of H <sub>2</sub> S at 250 °C as a Function of Relative Humidity.....	67

Figure	Page
29. (A) Concentration Gradient within The Sensing Film Based on the Coupled Diffusion-Reaction Equation, with a 1D Model of Multilayer Film Sensor as Inset; (B) Linear Fit Of $1/S$ Vs. $1/C_x$ Based on the Langmuir Adsorption Assumption; (C) Simulated Curve of Sensor Signal as a Function of Film Thickness, with Experimental Data Points Obtained under 2 PPM $H_2S$ . .....	70
30. Simulated Curve of Sensor Signal as a Function of Film Thickness, With Experimental Data Points Obtained under (A) 0.2 PPM, (B) 0.4 PPM, (C) 1 PPM, (D) 5 PPM, (E) 10 PPM Of $H_2S$ . .....	72
31. Concentration Gradient within The Sensing Film Based on the Coupled Diffusion-Reaction Equation, with a 1D Model of Multilayer Film Sensor as Inset. ....	73
32. SEM Images of (A) ZnO Nanosheets with Length of 300-1000 nm and Thickness of 50 nm; (B) Top View of ZnO Monolayer Film; (C) Cross-Section View of ZnO Monolayer Film; (D) XRD Patterns of ZnO Powder, ZnO-mono (with (100) as Exposed Crystal Plane), and ZnO-5 $\mu$ m; (E) The Sensor Signals of ZnO-Mono and ZnO-5 $\mu$ m Sensors to 10 PPM $H_2$ at 250 $^{\circ}C$ . ....	75
33. SEM Images Of (A-B) CuO Nanosheet and (C) CuO Nanosheet Monolayer; (D) XRD Patterns of CuO Nanosheet Powder and Monolayer Film. ....	82
34. Transient Response Curve Measured at 325 $^{\circ}C$ , 400 PPB $H_2S$ , 0-80% RH; (B) Sensor Responses Toward Different $H_2S$ Concentrations as a Function of Relative Humidity; (C) Response and Recovery Time Toward Different $H_2S$ Concentrations as a Function of Relative Humidity. ....	83



Figure	Page
35. (A) Humidity Influences on The Response Values and The Coefficients of Variations of The Monolayer Films Toward 400 PPB H <sub>2</sub> S at Different Working Temperatures; (B) Humidity Influences on the Response and Recovery Times of the Monolayer Films Toward 400 PPB H <sub>2</sub> S at Different Working Temperatures. ....	85
36. (A). Plot of (Response-1) and Gas Concentration in Log Scale for H <sub>2</sub> S, C <sub>7</sub> H <sub>8</sub> , C <sub>2</sub> H <sub>5</sub> OH, and C <sub>3</sub> H <sub>6</sub> O Detection. The Intersections of the Linear Fit Lines and X Axis Represent the Detection Limits of the Sensor Towards the 4 Gases. (B) Long Term Test Performed at 325 °C, 50 %RH, and 1 PPM H <sub>2</sub> S. (C) Humidity Variation Test Carried Out at 325 °C, 0.4 PPM H <sub>2</sub> S, and 0-50% RH. ....	86
37. (A) Sensor Responses Towards 200 PPM Of C <sub>7</sub> H <sub>8</sub> , C <sub>2</sub> H <sub>5</sub> OH, And C <sub>3</sub> H <sub>6</sub> O in Air as a Function of Relative Humidity at 325 °C (B) Humidity Influence on the Response Values Towards 400 PPB H <sub>2</sub> S of the Multilayer CuO Nanosheet Film with Film Thicknesses of 0.5 and 10 mm Measured at 325 °C (Film Thickness Estimated by the Weight of Powders Used In Fabrication). (C) Response and Recovery Time Toward 400 PPB H <sub>2</sub> S Concentrations as a Function of Relative Humidity for CuO Multilayer Film at 325 °C. (D) Humidity Influences on The Response Values and the Coefficients of Variations of the Multilayer Films Toward 400 PPB H <sub>2</sub> S at Different Working Temperatures.....	87
38. Transient Response Curves Measured at 325°C, 400 PPB H <sub>2</sub> S, 0-80% RH for (A) CuO-0.5µm and (B) CuO-10µm. ....	89

Figure	Page
39. Resistance in Air of the Three Sensors with Different Film Thickness as a Function of Relative Humidity at 325°C.....	89
40. XPS Wide Scans of the CuO Nanosheet Films Treated in Different Conditions.....	90
41. XRD Patterns of Sample #2 and Sample #4.....	92
42. (A) Cu 2p <sub>3/2</sub> Portion of the Cu 2p Spectra of Samples Treated in Dry Condition (0% RH) Before (#1) and After Exposing to 1 PPM of H <sub>2</sub> S (#2); (B) Cu 2p <sub>3/2</sub> Portion of the Cu 2p Spectra of Samples Treated in Wet Condition (50% RH) Before (#3) and After Exposing to 1 PPM Of H <sub>2</sub> S (#4); (C) O 1s of Samples Treated in Dry Condition (0% RH) Before (#1) and After Exposing to 1 PPM of H <sub>2</sub> S (#2); (D) O 1s of Samples Treated in Dry Condition (0% RH) Before (#3) and After Exposing to 1 PPM of H <sub>2</sub> S (#4); (E) High Resolution S 2p Scan of Sample #2 and Sample #4.....	93
43. SEM Image of CuO Monolayer after Exposing to H <sub>2</sub> S in (A) Dry And (B) Wet Condition.....	96
44. Schematic of the CuO Nanosheet Sensing Layer from the Aspects of Morphology, Energy Band, and Surface Reactions Under (A) Dry and (B) Humid Conditions.....	97
45. A Schematic Showing the CuO Nanosheet Multilayer Sensing Film in Wet Air Containing H <sub>2</sub> S.....	98
46. Schematic of Gas Sensor Testing System Used in This Work.....	106
47 (A) FTIR Spectra of Pristine and Functionalized ZnO Nanowire. (B) Colloidal Solution Of ZnO Nanowire in Hexane.....	107

Figure	Page
48 (A) Scanning Electron Microscopy (SEM) Image of As-Synthesized ZnO Nanowires. (B) Surface Pressure Versus Area Isotherm of Floating ZnO Nanowires. (C) SEM Images of ZnO LB Film on Au-IDE-Coated Glass Substrate. (D) XRD Patterns of ZnO Nanowires and ZnO LB Film. (E) Transmission Electron Microscopy (TEM) Image of ZnO Nanowire and High Resolution TEM Image Showing the Lattice Fringes (Inset). (F) Illustration Of V-Grooves Topography Exhibited by ZnO LB Film. ....	109
49 (A-C) SEM of Annealed Au@ZnO-LB Samples with Initial Au Loading of 0.5 Nm (13 Wt%), 1.5 Nm (39 Wt%), and 2 Nm (52 Wt%). Particle Size Distributions of 0.5nm-2nm Au@ZnO-LB Based on SEM Images .....	110
50 (A) Texture of ZnO Sputtered Film Revealed by XRD. (B) Surface Morphology and Roughness of ZnO Sputtered Film Revealed by AFM. ....	111
51. SEM Image of Au@ZnO_SF Annealed at 400 °C for 100 H.....	112
52. (A) SEM Plane View of Au Doped on ZnO_LB Film Annealed at 400 °C for 24 H. Evolution of Au Particle Size Distribution (B) and Mean Diameter (C) with Annealing Time on ZnO LB Film. (D) SEM Plane View of Au Doped on ZnO_S Film Annealed at 400 °C For 24 H. Evolution of Au Particle Size Distribution (E) and Mean Diameter (F) with Annealing Time on ZnO_S Film. ....	113
53 XRD Patterns of Au Doped ZnO Film after Annealing at 400 °C for 24 H.....	114
54 TEM of Au Nanoparticles Supported on ZnO Nanowire after Annealing Treatment at 400 For 12 H (B) High Resolution TEM Image of Supported Gold Nanoparticle Revealing a [111] Growth Direction and High Contact Angles of 130 ° and 135 °. High Resolution XPS Spectra of Au 4f (C) and O 1s (D). ....	115

Figure	Page
55. (A) TEM of ZnO Nanoplate with (100) as Primary Crystal Facet. (B) Surface Roughness of ZnO Nanoplate. ....	117
56. (A) SEM of Au@Zno_NP Annealed at 400 °C for 24 H. (B) Particle Size Distribution. ....	117
57. Response Values Towards 25 PPM of C <sub>2</sub> H <sub>2</sub> at Different Operating Temperatures.	119
58. SEM Images of Au@ZnO_SF before (A) and after (B) the Stability Test.....	120
59. Sensor Stability Test Results Gathered from Au@ZnO_LB (A) and Au@Zno_S (B). The Sensors were Exposed to 10 PPM (25 PPM for Au@ZnO_S) of C <sub>2</sub> H <sub>2</sub> at the Optimum Operating Temperature (325 °C) and the Response Was Recorded 5 Times Per Day for 1 Week. Between Each Day's Testing, The Sensor was Soaked in Reducing Condition (10/25 PPM C <sub>2</sub> H <sub>2</sub> , 325 °C) to Accelerate the Aging Process. ....	122
60. (A) Characteristic Curve of Au@Zno_LB Obtained at The Optimal Working Condition with Linear Response Observed Between 10-5000 PPB. Inset Shows The Transient Response Curve Towards 10-1000 PPB of C <sub>2</sub> H <sub>2</sub> . (B) Response and Recovery Time Variations as a Function of Concentration. (C) Selectivity Towards C <sub>2</sub> H <sub>2</sub> Over Other Gases With And Without Au Dopant on ZnO_LB. (D) Effect of 40% Relative Humidity on The Sensitivity of Au@Zno_LB. Inset Shows the Transient Response Curve Towards 10 PPB of C <sub>2</sub> H <sub>2</sub> Obtained Under Dry and Humid Conditions.....	124
61. Schematic of Electron Conduction Mechanism of Au@Zno_LF in Air and in Reducing Gas. ....	126

Figure	Page
62. The Calibration Curves Towards Acetylene Plotted in Log-Log Scale to Reveal the Exponent Factor. ....	128
63. Schematic of the Gas Sensor Testing System.....	135
64. (A) XRD Patterns of as Synthesized Samples and (B) Thermally Treated Samples.	136
65. C/A Ratio as a Function of Doping Concentration for As-Synthesized and Thermally Treated Powders.....	137
66. (A) XPS Wide Scan for Thermally Treated Samples. (B)Surface & Bulk (Including Both Core and Shell) Concentration of Al Determined by XPS & EDS as a Function of Theoretical Concentration.....	138
67. TEM Images of Three As-Synthesized Samples with Doping Concentrations of (A) 0 Mol%, (B) 5 Mol%, and (C) 25 Mol%. ....	139
68. High-Resolution XPS Spectra at Binding Energies Corresponding to the Al 2p. ....	141
69. (A) High Level of Dopant Segregation on the Surface. (B) Nucleation of Al-Rich Particles, Surface with Low Dopant Concentration Exposed. ....	142
70. Crystallite Size of As-Synthesized Samples with 0 And 5 Mol% Doping Concentration (AS-0 & AS-5) and Thermally-Treated Samples with 0 And 5 Mol% Doping Concentration (TT-0 & TT-5) as a Function of Time at 400 °C.....	143
71. C/A Ratio of As-Synthesized Samples with 0 and 5 Mol% Doping Concentration (AS-0 & AS-5) and Thermally-Treated Samples with 0 and 5 Mol% Doping Concentration (TT-0 & TT-5) as a Function of Time at 400 °C. ....	143
72. TEM Images of (A) Pure SnO <sub>2</sub> and (B) SnO <sub>2</sub> Samples with 5 Mol% Al.....	144

Figure	Page
73. Electrical Resistance in Air at 300 °C for The Sensors Doped with Different Concentration of Al.....	146
74. Transient Response Curves for Pure and Al Doped Samples.....	147
75. Sensor Response as A Function of Al Concentration to 2-100 PPM of H <sub>2</sub> .....	148
76. (A-B) Structure and Electrical Band Models for Pure SnO <sub>2</sub> in Air and in H <sub>2</sub> ; (C-D) Structure and Electrical Band Models for SnO <sub>2</sub> with Al-Rich Shell in Air and in H <sub>2</sub> . .....	150
77. (A) Sensor Response to 100 PPM H <sub>2</sub> at 300°C, (B) Crystallite Size Derived from XRD, (C) Ratio Between Particle Size Derived from BET and Crystallite Size Derived from XRD, as Function of Al Doping Concentration.....	151
78. Photograph of the Gas Sensing System (A); Photograph of the Test Chamber (B); Photograph Illustrates a Gas Sensor Connected to 1 of the 4 Pairs of Electrical Probes by Two Micro-Clips.....	156
79. Schematic Diagram of (A) the Gas Sensor Testing System: Reference Gas (Ultra-Zero Air) Mode; and (B) Analyte Gas (Reducing Gas Mixed In Air) Mode. ....	157
80. Schematics For (A) Blade Coating and (B) Drop Coating. ....	160
81 (A) SEM Image of 1% Al-Doped SnO <sub>2</sub> Powders before Ball Milling; (B) after Ball Milling; (C) Comparison of XRD Patterns before and after Ball Milling, The XRD Peaks Become Shorter and Broader after Ball Milling, Which Suggests a Decrease of Crystallite Size. ....	160

Figure	Page
82. (A) And (B) Cross-Section and Top View of Thick Film Sensor Fabricated by Blade Coating Method; (C) and (D) Cross-Section and Top View of Thick Film Sensor Fabricated by Inkjet Printing Method. ....	161
83. (A) Response Times of 1% Al (As-Synthesized Powder, 50 Um Film), 1% Al <sub>BM</sub> (Ball-Milled Powder, 50 Um Film), and 1% Al <sub>BM_IP</sub> (Ball-Milled Powder, 10 Um Film) toward 1000 PPM H <sub>2</sub> at 300°C; (B) Sensitivity Values of Three Aforementioned Sample vs. Different H <sub>2</sub> Concentration at 300°C.....	162
84. A Current-Voltage Test Example (A) and An Electrochemical Impedance Spectroscopy Test Example (B) on ZnO Nanodisk Thick Film Sensor. ....	169
85. SEM Top View (A) and Side View (B) of the ZnO Nanodisk Sensor; Powder XRD Pattern of ZnO Nanodisk (C). ....	170
86. Transient Response Curves of the ZnO Nanodisk Sensor to 1000 Ppm H <sub>2</sub> (A)-(C); Response Vs. Temperature (D); Repeated Cycling Test (E); Response Towards 6 Dissolved Gases (F). ....	171
87. SEM Image of The Cross-Section View of ZIF-8 Coated ZnO Thick Film Sensor (A); XRD Patterns for ZnO Thick Film Sensor before and after Coating ZIF-8 (B); Transient Gas Sensor Response of ZnO Thick Film and ZIF-8 Coated ZnO Thick Film to 0.1% C <sub>2</sub> H <sub>4</sub> And H <sub>2</sub> (C). ....	174
88. SEM Images of The Urchin-Shaped ZnO.....	175
89. (A-B) SnO <sub>2</sub> Powders without PEG; (C-D) SnO <sub>2</sub> Powders Prepared with PEG; XRD Patterns of SnO <sub>2</sub> Powders with or without PEG. ....	177

Figure	Page
90. Gas Sensing Performance Test at Various Temperature. ....	179
91. A Schematic Diagram Showing the Forming Mechanism of Metal Oxide Hollow Sphere Structure. ....	180
92. SEM Images of CuO/CeO <sub>2</sub> Composite Hollow Microsphere.....	181
93. EDS Analysis on the Sphere (A) and Rod (B). The White Cross on the SEM Images Indicates the Position That EDS Analysis was Performed. ....	182
94. XRD Patterns of The CuO/CeO <sub>2</sub> Composite Hollow Spheres with Different CuO Concentration. ....	183
95 (A) The Only Cell Parameter A of CeO <sub>2</sub> Phase (Cubic Structure) as a Function of CuO Wt%; (B) The Three Cell Parameters A, B, And C of CuO Phase (Monoclinic) as a Function of CuO Wt%; (C) The Volume of Unit Cell (=A*B*C*Sin(B)) Vs. CuO Wt%. ....	185
96. The Response vs. Temperature Relationship for the Sensors Made of CuO / CeO <sub>2</sub> Composite Hollow Spheres with Different CuO Concentration.....	187
97. XRD Patterns for Pure CuO and Ce Doped CuO Samples.....	188
98. SEM Images of (A) Pure and (B) 0.5 Wt% (C) 2 Wt% and (D) 5 Wt% Ce-Doped CuO Samples. ....	189
99. The Dependence of Resistance on Temperature for Pure and Ce Doped Samples. .	190
100. Response Value vs. Temperature (A); Selectivity Value as A Function of Temperature (B). ....	191



Figure	Page
101. Dependence of the Sensitivities on the Concentration of CO (A) and H <sub>2</sub> (B) at 80 °C; Response Value to Pure CO And CO/H <sub>2</sub> Mixed Gas as a Function of CO Concentration. .....	192
102. Conduction Model For CeO <sub>2</sub> @ CuO Sensor before and after The Introducing of Reducing Gas. ....	194
103. Percentage of Resistance Value Recovered after Exposing to 50 PPM CO as a Function of Temperature.....	195
104. SEM Images of (A) CuO Before Ball Milling (B) CuO after Ball Milling.....	196
105. (A) TEM Image of CuO-Ns with SAED and HRTEM as Insets; (B) SEM Image of Ce-CuO-Ns; (C) Low Magnification and (D) High Resolution TEM Images of Ce-CuO- Ns. ....	197
106. SEM of Au-CuO (A) and Pd-CuO (B); XRD for CuO-Ns Powder and Ns Single Layer Film (C).....	198
107. CuO-Np1, Ce-CuO-Np1-HMT1: Resistance in Air vs. Temperature. ....	199
108. Ce-CuO-Np1-HMT1 @ 25°C CO. ....	200
109. Resistance in Air vs. Temperature. ....	202
110. Sensitivity vs. Temperature with 1, 10, 50 PPM of Reducing Gas from CuO (A)-(C); Sensitivity vs. Temperature with 1, 10, 50 PPM of Reducing Gas from Pd-CuO; Sensitivity vs. Temperature with 1, 10, 50 PPM of Reducing Gas from Au-CuO. ....	203
111. Schematic of a Typical Electronic Nose. ....	205
112. Normalized Response Pattern for 6 Different Analytes across All 39 Sensors.....	207

Figure	Page
113. The Resultant Dendrogram for the Normalized Response Matrix Linked by a Centroid Distance Measurement Method of Distance between Two Clusters is Defined as the Squared Euclidean Distance Between Their Means. ....	208
114. Distance Graph of the Hierarchical Clustering.....	209
115. The Respective Histograms for the Sensitivity (A) and Selectivity (B) Metrics for 100,000 Random Selection of 7 Sensors for the 6 Analytes.....	211
116. PCA Maps for 6 Dissolved Gases Obtained from (A) Max SRSS Array (B) Max SED Array (C) Random Array. ....	211
117. Transient Response Curves Towards 0.5 PPM C <sub>2</sub> H <sub>2</sub> Measured at 200 °C for the Sensors That Underwent the Accelerated Aging Treatment at 600°C for 0, 24, 48, 72, and 142 H. ....	214
118. Transient Response Curves Towards 0.5 PPM C <sub>2</sub> H <sub>2</sub> Measured at 200 °C for the Sensors That Underwent the Accelerated Aging Treatment at 700°C for 0, 24, 45, and 69 H.....	215
119. Response Average as a Function of Accelerated Aging Time. The Exponentially Fitted Curves were Used to Estimate the Failure Time. ....	216
120. Picture of Sensor Box Prototype.....	217
121.Screenshot of the Gas Sensor Control User Interface Developed by Clemson University.....	218
122. Concentration vs. Response Curves of 6 Gases.....	219
123. Concentration vs. Response Curves of 6 Gases.....	220

Figure	Page
124. Concentration vs. Response Curves of 6 Gases.....	221
125. Concentration vs. Response Curves of 6 Gases.....	222
126. Concentration vs. Response Curves of 6 Gases.....	223
127. Concentration vs. Response Curves of 6 Gases.....	224
128. Concentration vs. Response Curves of 6 Gases.....	225
129. Concentration vs. Response Curves of 6 Gases.....	226

# 1. INTRODUCTION

## 1.1 General Background

Gas sensors with a global market size valuation of USD 1.0 billion in 2019, have found applications in wide ranges of industries, including medical<sup>1</sup>, oil & gas<sup>2</sup>, automotive & transportation<sup>3</sup>, food & beverages<sup>4</sup>, mining<sup>5</sup>, and power stations<sup>6</sup>, to perform functions such as hazardous gas detection, odor recognition, and gas composition analysis. The gas types of interest includes oxygen (O<sub>2</sub>), ozone (O<sub>3</sub>), carbon monoxide (CO), carbon dioxide (CO<sub>2</sub>), ammonia (NH<sub>3</sub>), chlorine (Cl), hydrogen sulfide (H<sub>2</sub>S), nitrogen oxide (NO<sub>x</sub>), volatile organic compounds (VOC), hydrocarbons (methane, propane, butane, etc.). The technologies available for sensing these gas species are conductometric (e.g. semiconductor metal oxide gas sensor), potentiometric (e.g YSZ oxygen sensor), catalytic, electrochemical, surface acoustic wave, photoacoustic, and infrared.

The gas sensor market is projected to grow to USD 1.4 billion by 2024, at a compound annual growth rate of 6.4% from 2019 to 2024. The rapid growth is fueled by the rising environmental pollution levels and increasingly degrading indoor air quality, which have created a significant demand for gas sensors in HVAC and air quality monitoring systems. By incorporating gas sensors into the internet of things, the smart cities and building automation segment is projected to lead the gas sensors market by 2024. Another growth opportunity lies in the adoption of gas sensors in consumer electronics devices for health monitoring. By analyzing the chemical composition of human breath, early diagnosis of 7 out of the top 10 diseases that cause the most deaths worldwide have been demonstrated. Once realized, the impact on human health and well-being could be very profound.

The commercially available gas sensor can be divided into three groups based on their different operating principle:

- *Conductometric gas sensors* measure the changes in resistance of the sensing materials after being exposed to reducing or oxidizing gas molecules. Typically, semiconducting metal oxides are used as the sensing materials in these sensors because of their low cost, easy fabrication, fast response and/or recovery speed and high sensitivity to a range of gases. The most investigated semiconducting metal oxides for Conductometric gas sensors include SnO<sub>2</sub>, ZnO, WO<sub>3</sub>, In<sub>2</sub>O<sub>3</sub>, TiO<sub>2</sub>, etc. Although, Conductometric gas sensors are by far the most commercially successful types of gas sensors, they may exhibit certain disadvantages such as cross-sensitivity, high noise, and high operation temperature.
- *Electrochemical gas sensors* determine the gas concentration by oxidizing or reducing the target gas at the electrode and measuring the resulting current. The typical components of these sensors include reference electrodes (anode and cathode), electrolytes, and gas permeable membranes. Electrochemical gas sensors require very little power to operate and are widely used in confined space. They are particularly suited for the reliable and selective detection of O<sub>2</sub>. Major drawbacks of these sensors include short operating life (1-3 years) and the relatively poor capability to detect gases that are not electrochemically active.
- *Optical gas sensors* typically detect the concentration of the target gas by measuring the changes in optical properties because of the interaction between the sensing material and the analyte gas. For example, one type of optical gas sensor measures the change in surface plasmon resonance (SPR) signals which is related

to the refractive index close to the sensor surface, allowing for the measurement of bound gas molecules. Another type of optical gas sensor is the optode, which measures gas concentration by relying on the changes in optical properties such as luminescence, reflection, absorbance, light polarization, etc. A typical arrangement of an optical gas sensor consists of a laser diode and a very sensitive HgCdTe infrared (IR) detector. Optical gas sensors have high selectivity and specificity due to the unique features of the IR absorption of each individual gas. However, they are rather expensive owing to the high cost of the laser source and the IR detector, and they are also difficult to be packed in a portable device.

As shown in **Table 1**, the gas species of interest for air quality monitoring include CO<sub>2</sub>, CO, NO<sub>2</sub>, SO<sub>2</sub>, and VOCs. The concentrations range of these gases are from 10 ppb to 1000 ppm. For human breath analysis, the target gases are the more than 200 types of VOCs in the human breath, each with concentration in the range between 1-2000 ppb. Therefore, an ideal sensor technology should be able to detect gases in interest in the concentration range between 1 ppb to 1000 ppm, and exhibits features including high energy efficiency, small form factor, and low cost to be successfully incorporated into the IoT and consumer electronics.

As summarized in **Table 2**, among the commercially available technologies, semiconductor gas sensors hold clear advantages in cost and device size over electrochemical sensors, and non-dispersive infra-red sensor. Moreover, semiconductor gas sensors are most promising to provide effective solutions for the issues with analyzing complex gas mixture required by air quality and human health monitoring. Because

semiconductor gas sensors often respond to a broad range of gases, their sensor arrays generally possess good cross compatibility, which is desirable when the identification of certain gas combinations is more critical than the absolute concentration<sup>7</sup>. The major challenges for semiconductor gas sensors to be used in these new applications are power consumption, sensing at ppb range, stability, and humidity interference. Therefore, it is the goal of this research work to innovate the sensing materials and sensing film structure to address these challenges presented for semiconductor gas sensors.

**Table 1.** Composition of polluted air and exhaled breath<sup>7,8</sup>

Normal pollution level in air			Major VOCs in exhaled breath	
Name	Outdoor Conc.	Indoor Conc.	Name	Conc. (ppb)
CO <sub>2</sub>	200-400 ppm	400-1000 ppm	Isoprene	12-580
CO	2-5 ppm	20-50 ppm	Acetone	1.2-1880
NO <sub>2</sub>	20-60 ppb	20-40 ppb	Ethanol	13-1000
SO <sub>2</sub>	20-100 ppb	10-50 ppb	Methanol	160-2000
VOCs	50-200 ppb	200-2000 ppb		

**Table 2.** Comparison of commercially available sensors based on different technologies

Technology	Commercial example	Dimension (mm <sup>3</sup> )	Price (\$)	Peak power consumption (mW)	Detection limit	Cross sensitivity	Stability	Immunity to humidity interference
Chemiresistive	AMS CCS801	6	5	33	low ppm	High	Good	Low
Electrochemical	Figaro TGS5141	2000	10	0	low ppm	Low	Excellent	High
Infra-red	SGX IR12	6000	150	200	500 ppm	Low	Excellent	High

## 1.2 Motivation for Dissertation Research and Dissertation Structure

The motivation for this research work is to improve the thermal stability, sensitivity, humidity interference, and power consumption of semiconductor metal oxide gas sensor to facilitate the adoption of this sensing technology in air quality and human health monitoring applications. The strategies investigated include: (1) optimizing the composition and the morphology of the nanoparticles, and (2) innovating the structure of the sensing film assembled with the nanoparticles.

In this dissertation, the correlation between sensing film structure and the sensing device properties including sensitivity, selectivity, immunity to humidity interference, and selectivity are explained in great detail in Chapter 3-5, because the topic is less frequently explored in the field. The research work on optimizing the composition and the morphology of the nanoparticles to improve their thermal stability contains is presented in Chapter 6. In Chapter 7, a semiconductor sensor array developed for dissolved gas analysis is described to demonstrate the application of this sensor technology in power station.

The detailed accounts of each chapter of this dissertation are as follows:

Chapter 2: provides an in-depth review of the various aspects of gas sensors including an overview on gas sensor technologies and applications, semiconductor gas sensor device configuration, the operating principle of semiconductor gas-sensors, and influencing factors on device performance with a focus on deposition technique for the sensing film.

Chapter 3: describes a facile self-assembly approach to obtain monolayer film of 2D CuO nanosheets. The autonomous Self-assembly of CuO nanosheets on water surface was speculated to be governed by the anisotropy in the surface energy. To verify this theory,



all the crystal facets of the CuO nanosheet was indexed with TEM/SAED. Monolayer film and thick film made from the same materials were characterized with FIB-SEM, XRD, and BET. When comparing the H<sub>2</sub>S sensing performance between the two films, the monolayer film achieves a detection limit of 10 ppb, while for the thickest film, the detection limit was 200 ppb. The standard diffusion-reaction model was modified to fit the correlation observed between sensing film thickness and sensing response.

Chapter 4: focuses on studying the H<sub>2</sub>S detection mechanism in the presence of water vapor for the CuO nanosheet sensors. The phenomenological measurements and spectrometry information obtained by parallel quenching revealed that the H<sub>2</sub>S was oxidized into gases species which desorb quickly under dry condition. However, under wet condition, the isolated hydroxyl groups prevalent on the CuO surface promotes the formation of dielectric sulfides/sulphur phase. Under wet condition, the formation of the dielectric phase makes the electrical conduction more sensitive to changes in band bending, while the absolute difference of band bending caused by the electron injection from the reactant decreases, forming an intricate balance that leads to the observation of humidity independent response to H<sub>2</sub>S in CuO monolayer film. The influence of thickness on the H<sub>2</sub>S detection mechanism in the presence of water vapor was also considered at high temperature where diffusion-reaction effect becomes negligible under dry condition.

Chapter 5: describes yet another highly versatile technique called "Langmuir-Blodgett assembly" to fabricate monolayer film consists of aligned ZnO nanowires for C<sub>2</sub>H<sub>2</sub> sensing. The surface of the film was sensitized with Au nanoparticles by sputtering and annealing. Stabilization of high dispersion of small Au nanoparticles was obtained on the monolayer

film due to the periodic perturbation of surface energy inhibit Au particle sintering by particle migration and coalescence. Nano Au sensitize the ZnO monolayer sensing film by first enriching the surface coverage of  $C_2H_2$  at the three phase interface of Au/ZnO/air, changing the surface reaction from total oxidation on the bare ZnO surface to partial oxidation, which increases the exponent factor of the power law correlation between response and  $C_2H_2$  partial pressure. Secondly, the oxygen spill-over from nano Au leads to increase in the percent of depleted region inside the ZnO nanowire, which causes significant increase in the proportionality factor of the power law correlation.

Chapter 6: Investigates the effect of aliovalent bulk doping on the sintering of  $SnO_2$  nanograins. The evolution of Al- $SnO_2$  crystal lattice strain through a post-annealing process was monitored by analyzing the XRD patterns with Rietveld refinement. The data indicates dopant migration toward the surface of the grain due to strain and electrostatic force. The discrepancy in the doping concentration between the surface and the bulk of the  $SnO_2$  grain was verified with XPS and EDS. The resulted concentration profile of Al created a solute drag effect, which serves to stabilize the grain boundary, and in turn inhibit further grain growth. Finally, the doping concentration was fine-tuned to obtain the optimal sensing performance and thermal stability.

Chapter 7: demonstrates the application of semiconductor sensor array in analyzing the composition of gas mixtures. The chapter describes the design of high-throughput sensor testing system, development of a scalable sensor fabrication process, the establishment of a library of sensor materials meeting the requirement of the intended

application, development of sensor selection strategy for building the best array, and eventually the building and testing of a sensor array prototype.

## 2. LITERATURE REVIEW

### 2.1 Semiconductor Gas Sensor

Semiconductor gas sensors are designed for monitoring the gas composition of their surrounding environment in real time by detecting a stimulus (i.e. an analyte gas such as CO or H<sub>2</sub>) through a surface reaction, and then transducing the new steady state incurred by the surface reaction into a measurable electrical signal (i.e. conductivity change). The basic configuration of a semiconductor gas sensors can be illustrated with the multilayer structure as illustrated in **Figure 1**. A gas sensing layer made from polycrystalline oxide semiconductors is deposited on a dielectric substrate made of glass/ceramic. A pair of electrodes made from noble metals, such as Pt, Au, are buried inside the sensing layer with two tracks leading out for measuring the conductance of the sensing film. Some forms of heating elements are printed on the back of the dielectric substrate to heat up the device to 150-400 °C for operation.

Since the first commercialized semiconductor gas sensor hit the market in 1968, many studies have been carried out on developing new and better sensing materials with the help of nanotechnology to address problems such as long response time, low-sensitivity, and sensitivity to humidity and poor long-term stability, and during the process the industry and academia have amassed substantial knowledge of sensing mechanism of metal oxide. According to the internet search results from Web of Science, semiconductor metal oxide gas sensors research, to date, is strongly dominated by n-type oxide semiconductors, i.e. SnO<sub>2</sub>, ZnO, and In<sub>2</sub>O<sub>3</sub>. This is mainly because sensors made from metal oxides like Fe<sub>2</sub>O<sub>3</sub>, NiO, and Cr<sub>2</sub>O<sub>3</sub> are not chemically & thermally stable enough, even though they might

possess extremely high sensitivity for certain gas species<sup>9</sup>. In comparison to n-type sensor, p-type semiconductor including CuO, NiO, Co<sub>3</sub>O<sub>4</sub>, and Cr<sub>2</sub>O<sub>3</sub> have received relatively little attention, due to its inherent low sensitivity. Nevertheless, they should not be overlooked because of their unique catalytic capability in selective oxidation reaction.

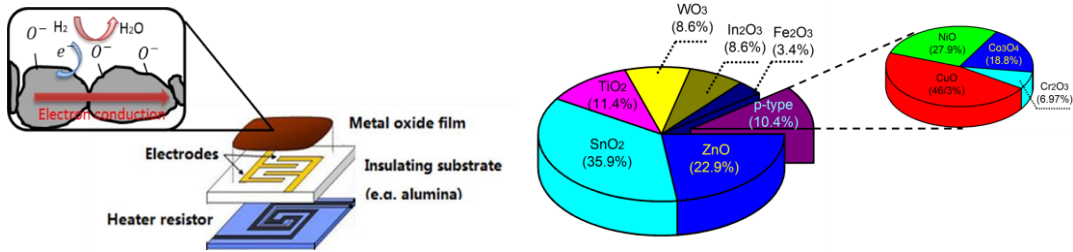
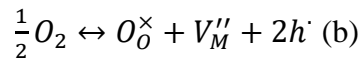
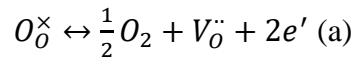


**Figure 1.** Studies on n- and p-type semiconductor gas sensors (Internet search of Web of Science on November 21, 2017)

The electrical conducting properties of oxide semiconductors originates from the non-stoichiometry in the metal oxides<sup>10</sup>. As a rule, metal oxides with oxygen deficiency are n-type, and those with metal deficiency adopt p-type behavior. The underlying reason can be illustrated based on defect reactions written using Kroger-Vink notation:



The evolution of lattice oxygen  $O_O^{\times}$  is accompanied by formation of oxygen vacancies (with effective positive charge) and electrons that determine n-type of conductivity as shown in reaction (a). In case of metal deficient phase (or oxygen excess phase), generations of acceptor metal vacancies as well as holes occur, and enables p-type of conductivity.

The schematic of the first-generation semiconductor gas sensor (i.e. the "Taguchi" sensor) is shown in **Figure 2** (a). A partially sintered thick film of gas sensing material is deposited on the surface of an alumina ceramic tube which contains an internal heater (a Ni-Cr resistor wire). The flame arrestor is made by 100 mesh SUS 316 double gauze. Activated charcoal is filled between the internal cover and the outer cover for reducing the influence of noise gases. The working temperature of the gas sensor can be controlled by adjusting the heating voltage ( $V_{\text{heating}}$ ) across a Ni-Cr resistor wire inside the ceramic tube. When the sensor is connected as shown in the basic circuit (**Figure 2** (b)), output across the load resistor ( $V_{RL}$ ) increases as the sensor's resistance ( $R_s$ ) decreases, depending on gas concentration. The key electric signal, sensor resistance ( $R_s$ ), is calculated by the following formula:  $R_s = \{(V_C / V_{RL}) - 1\} \times R_L$ .

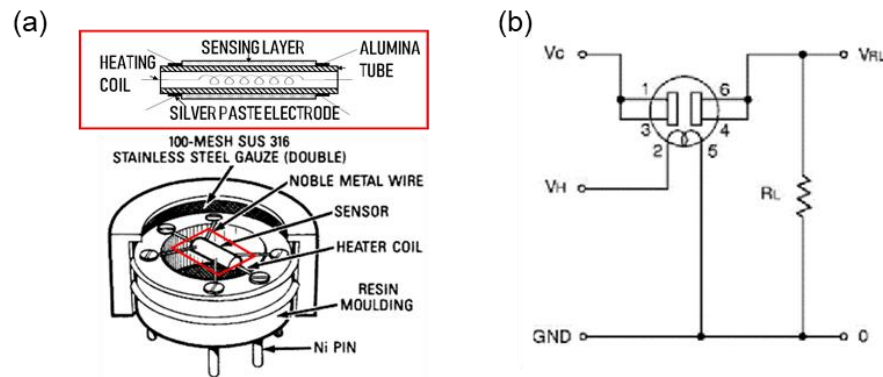


**Figure 2.** Schematic of Taguchi type sensor (a) and electric circuit for measuring sensor resistance (b).

Taguchi-type sensors are still on the market, but most of the commercially available sensors are nowadays manufactured in screen printing technique on small and thin ceramic substrates, an example is given in **Figure 3**. Screen printing technique has the advantage of a small sensor to sensor distribution within production lots attributed to batch process

fabrication. This technology is nowadays well-established and high performance of screen-printed ceramic sensors is achieved in various applications.

However, screen-printed ceramic gas sensors are, with respect to power consumption and mounting technology still in need of improvement. The power consumption of screen-printed devices is typically in the range of 200 mW to about 1 W, which is too much for battery-driven applications. The mounting of the overall hot ceramic element is difficult. One must find such designs like the one shown in **Figure 3** which ensure good thermal isolation between sensor element and housing as well as high mechanical stability.

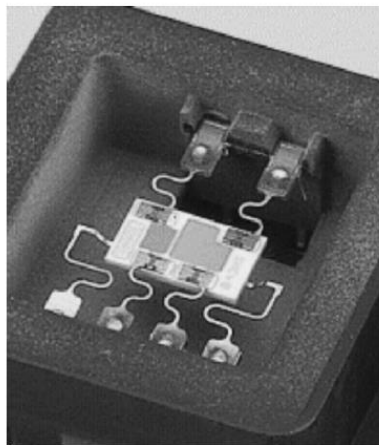


**Figure 3.** Gas sensor prepared by screen-printing on a ceramic substrate of size 6 mm×8 mm<sup>11</sup>. The sensor element consists of a CO- and a NO<sub>x</sub>-sensitive layer. The platinum structures (heater, electrodes and contact pads) and the two sensitive layers are manufactured in screen-printing technology. The sensitive layers consist of specifically doped and coated tin dioxide. Their electrical resistance is measured by interdigitated platinum electrodes located below 300 °C is achieved by a heater located on the backside of the ceramic. With help of the platinum contact pads the sensor is fixed to a sheet leadframe by parallel gap welding and mounted in the housing.

In the early 2000s, with the development of microfabrication process, the integration of gas sensitive metal oxide layers in standard microelectronic processing was achieved

and lead together with the use of micromachining steps to micromachined metal oxide gas sensors like the ones shown in Figure 4. This technology is very promising to overcome the difficulties of screen-printed ceramic sensors due to the following facts. The sensitive layer of micromachined metal oxide gas sensors is deposited onto a thin dielectric membrane of low thermal conductivity which provides good thermal isolation between substrate and the gas-sensitive heated area on the membrane. In this way the power consumption can be kept very low (typical values obtained lie in the range between 20 and 150 mW and the substrate itself stays nearly at ambient temperature. The mounting of the sensor element becomes therefore much easier than for an overall hot ceramic sensor element, and control and signal-processing electronics can be integrated on the same substrate if desired (**Figure 4**). Using standard microelectronic steps to pattern electrode structures results in a further advantage. The minimal structure sizes get much smaller, a minimal width between electrodes lying in the  $\mu\text{m}$  range can be achieved<sup>12</sup>. The gas sensitive area can in this way be tremendously reduced and the use of interdigitated electrodes with a high length-to-width ration allows even the evaluation of sensing films with very high sheet resistivity. Sensor arrays which are often needed to overcome the bad selectivity of single sensor elements can be easily implemented in this technology. Beyond that, the small thermal mass of each micromachined element allows rapid thermal programming which can be used to study the kinetics of surface processes and to achieve kinetically controlled selectivity<sup>11</sup>.



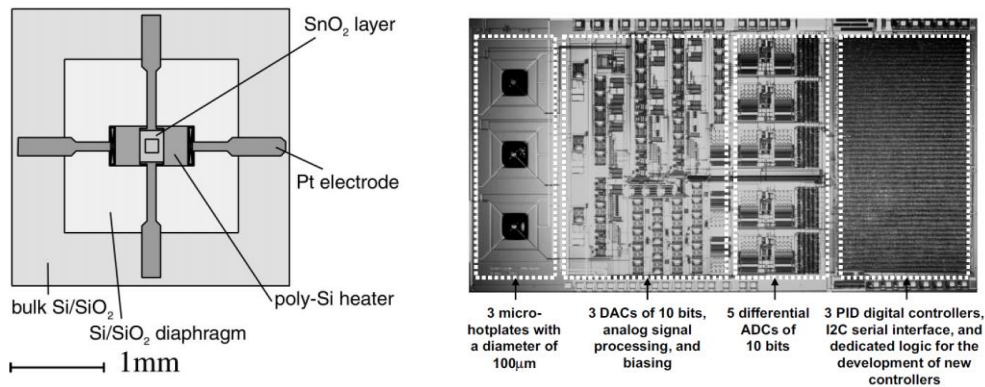


**Figure 4.** Schematic of the MGS 1100 sensor from Motorola. Micromachined sensor element on the left and sensor housing on the right. The sensitive film was obtained by rheotaxial growth and thermal oxidation of tin layer (RGTO) deposited on the silicon oxide-nitride membrane.

## 2.2 Key Parameters in Gas Sensing

The performance of a metal oxide gas sensor can be assessed by evaluating several important gas-sensing parameters<sup>13</sup>:

- i. *Range*: The range of the sensor is the maximum and minimum concentration that can be measured
- ii. *Accuracy*: The accuracy of the sensor is the maximum difference that will exist between the actual value (which must be measured by a primary or good secondary standard) and the indicated value at the output of the sensor.
- iii. *Response*: The most essential parameter of a gas sensor is its response ( $R$ ) to a target gas. If a gas sensor cannot sense a target gas, it cannot be used in practice. There are different definitions of the gas response for semiconductor-based gas sensors. The response is generally defined as the ratio of the resistance variation ( $R_a/R_g$ ) or ( $R_g/R_a$ ), where  $R_a$  and  $R_g$  represent the resistances of the gas sensor in air and in the target gas atmosphere, respectively.

- iv. *Sensitivity*: The sensitivity is a change in measured resistance ( $\Delta R$ ) with a change in analyte concentration ( $\Delta c$ ), i.e., the slope of a calibration graph:  
$$S = \Delta R / \Delta c.$$
- v. *Response and recovery time*: The response time ( $R_{resp}$ ) is defined as the time required for a gas sensor to reach 90% resistance change in the presence of the target gas, and the recovery time ( $R_{recv}$ ) is defined as the time needed for the resistance of a gas sensor to return to 90% of its original baseline value after the removal of the target gas.
- vi. *Selectivity*: It describes the ability of a sensor to differentiate a specific target gas among other interfering gases. The selectivity ( $m_{ij}$ ) of a sensor compares the sensor signal or the sensitivity to be monitored ( $S_i/m_i$ ) to the sensor signal/sensitivity of the interfering stimulus ( $S_j/m_j$ ). The selectivity of gas sensors should always be  $>1$ . A high selectivity corresponds to a higher response of the gas sensor to a target gas compared with the response to interfering gases. Typically, gas sensors are sensitive to more than one gas and exhibit cross-sensitivity.
- vii. *Detection limit*: The detection limit can be defined as the lowest concentration of gas that can be detected at a certain temperature. According to the IUPAC definition, when the signal-to-noise ratio equals 3, the signal is considered to be a true signal. The sensor noise can be calculated using the variation in the relative conductance change in the baseline using the root-mean-square deviation (RMSD). Therefore, the detection limit can be extrapolated from the linear calibration curve when the signal equals 3 times the noise.

## 2.3 Principles of Operation

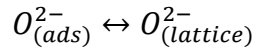
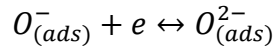
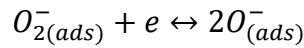
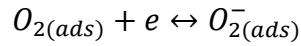
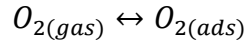
The operation of semiconducting gas sensors can be described at high-level as: the conductivity of metal oxide semiconductor materials changes according to gas concentration changes. This is caused by adsorption/desorption of oxygen and reaction between surface oxygen and gases. These reactions change the electric potential on SnO<sub>2</sub> crystal and results in the decrease of the sensor resistance under the presence of reducing gases like CO. The elementary steps of gas sensing will be transduced in electrical signals measured by appropriate electrode structures. The sensing itself can take place at different sites of the structure depending on the morphology. They will play different roles, according to the sensing layer morphology. The overall conduction in a sensor element is determined by the surface reactions, the resulting charge transfer processes with the underlying semiconducting material, and the transport mechanism within the sensing layer, which will be discussed in detail in the rest of this chapter. Because most research works focus on investigating the operating principles of n-type semiconductor sensor, the following discussions are primarily made in the premise of n-type sensing materials. There is a dedicated section later in this chapter for the p-type sensing material.

### 2.3.1 Surface Chemistry

#### 2.3.1.1 Oxygen Adsorption

Chemical interaction between the surface of a semiconductor oxide and the gas phase, which gives rise to the sensing properties, can be represented as a cyclic process. Adsorption of oxygen from pure air atmosphere is the first step in the gas and solid interaction.

The adsorption of oxygen on metal oxide surfaces is generally considered to involve the physisorption of oxygen, ionosorption of oxygen, and incorporation of doubly ionized atomic forms of adsorbed oxygen into metal oxide crystal lattice, as listed in the following equations



Here  $O_{2(gas)}$  is the oxygen molecule in the gas phase;  $O_{2(ads)}$  is the physisorbed neutral oxygen molecule;  $O_{2(ads)}^-$ ,  $O_{(ads)}^-$ , and  $O_{(ads)}^{2-}$  are the molecular ionized, atomic ionized and doubly ionized atomic forms of oxygen chemisorbed on the oxide surface, respectively; and  $O_{(lattice)}^{2-}$  is the oxygen anion occupying a lattice site in the crystal structure of the material. The neutral oxygen molecules (physisorbed oxygen and oxygen in gas phase) are generally considered to not to play any direct role in sensing, because of the lower reactivity and the lack of means to influence the electrical properties of the sensing material by delocalized charge transfer. Nevertheless, the physisorbed oxygen can perform localized charge transfer and thus leads to the build-up of surface dipoles according to the in-situ work function study conducted by Sahm et al.  $O_{(lattice)}^{2-}$  were found to participate in the partial oxidation reactions of hydrocarbons following Mars van Krevelen mechanism, which enables many transition metal oxides to find applications in selective partial oxidation catalysis<sup>14</sup>. The nucleophilic  $O_{(lattice)}^{2-}$  consumed by the dehydrogenation

reaction of adsorbed hydrocarbons is replenished by incorporation of  $O_2$ -(ads) into positions of oxygen vacancies. However, this process needs to overcome considerably higher activation energy and hence is uncommon to observe in typical semiconductor sensing scenarios.

Therefore, theoretical studies on oxygen adsorption for semiconductor gas sensor consider only the ionized oxygen species adsorbed on the surface, which are formed by undergoing a delocalized charge transfer with the semiconductor, i.e. the counter charge of the ionized adsorbate at the surface is delocalized within a depletion layer in the metal oxide and thus changes the concentration of the free charge carriers in the conduction band. Unlike conventional chemisorbed species bound to specific active sites, the ionosorbed oxygen species are regarded as free oxygen ions which are electrostatically stabilized in the vicinity of the surface. **Figure 5** shows the energies of various species of oxygen relevant to surface reactions. The energy difference between doubly-charged  $O^{2-}$  in a lattice site and in an adsorbed state is estimated to be about 2000 kJ/mole or 20 eV, and hence  $O_{(ads)}^{2-}$  is highly unstable and has to be stabilized by the Madelung potential of the lattice, i.e., on an oxygen vacancy site.<sup>15</sup> In comparison, the difference between  $O_{2(ads)}$  and  $O_{2(ads)}^-$  only amounts to 140 kJ/mol or 1.5 eV<sup>16</sup>.

The ionized oxygen species are more reactive than the nucleophilic lattice anions and have higher mobilities. They are the main oxidizing species in the oxidation of simple reducing molecules such as  $H_2$ , CO, and  $CH_4$ . They may be considered as electrophilic reactants which in reactions with hydrocarbons attack the molecules in the regions of highest electron density. In the case of olefins such electrophilic additions of  $O_{2(ads)}^-$ ,  $O_{(ads)}^-$ ,

and  $O^{2-}_{(ads)}$  could result in the formation of peroxy- or epoxy-active complexes, respectively, which under the conditions of heterogeneous catalytic oxidation are the intermediates of the degradation of the carbon skeleton and total oxidation<sup>15</sup>.

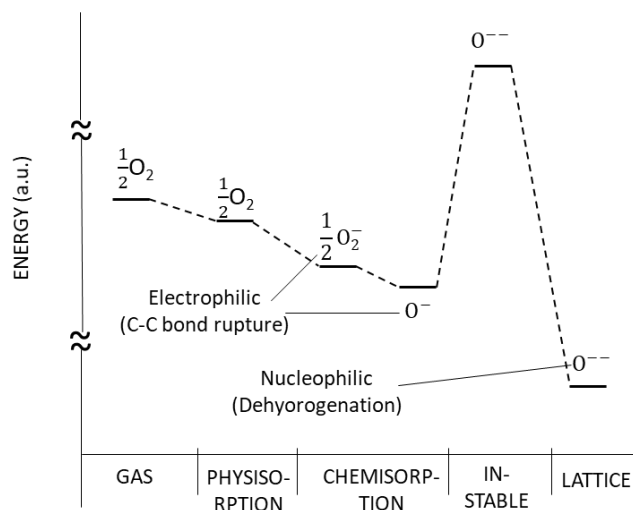


**Figure 5.** Energy diagram of various oxygen species in the gas phase, adsorbed at the surface and bound within the lattice of a binary metal oxide<sup>16</sup>.

The ionized oxygen species (both molecular and atomic species) on semiconductor metal oxide, i.e.  $SnO_2$ , have been observed by phenomenological measurements, e.g. electrical conductance and temperature programmed desorption (TPD), and spectrometry such as Electron Paramagnetic Resonance Spectroscopy<sup>17,18</sup> and FTIR at temperatures between 100 and 500 °C. As shown in **Figure 6**, at low temperatures (150-200°C) oxygen adsorbs on  $SnO_2$  non-dissociatively in its molecular form (as charged  $O_2^-$  ions). At high temperatures (between 200 and 400°C) it dissociates to atomic oxygen ( $O^-$ ). Only at temperature above 400°C can the doubly-ionized oxygen anions be observed, which is higher than the normal operating temperature range of semiconductor gas sensor.

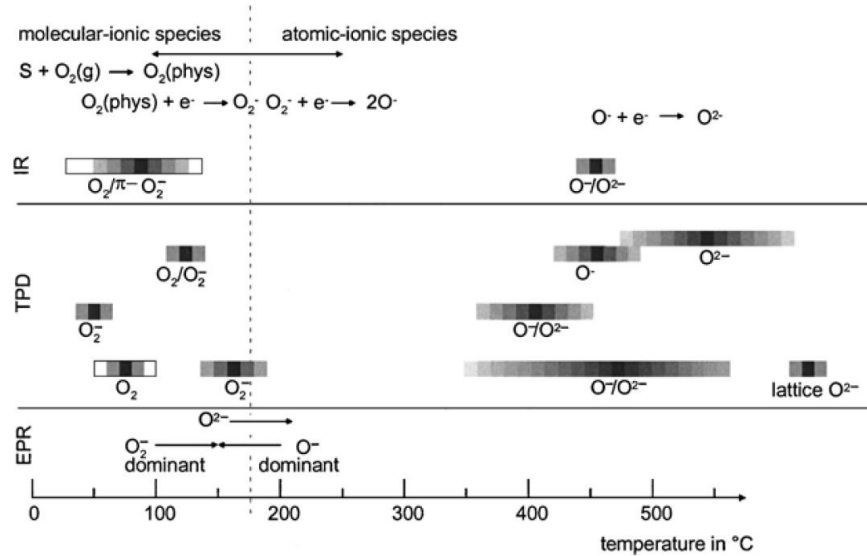


**Figure 6.** Literature survey of oxygen species detected at different temperatures at SnO<sub>2</sub> surfaces with IR (infrared analysis), TPD (temperature programmed desorption), EPR (electron paramagnetic resonance)<sup>19</sup>.

Since the reactivity of O<sup>-</sup><sub>(ads)</sub> is high and exceeds that of O<sub>2</sub><sup>-</sup><sub>(ads)</sub>, it is of interest to analyze the composition of ionized species for engineering the sensing performance. Because the processes given rise to the ionized oxygen species are all equilibrium reactions, the coverage and the ratio of ionized oxygen species are highly dependent on the temperature and on the characteristics of the adsorbent. It is challenging to get experimental results about the nature of the different oxygen surface species. Therefore, simulation of the equilibrium coverages of the oxygen species based on Monte Carlo kinetics can provide some guidance (**Figure 7**). It can be observed that the transition from O<sub>2</sub><sup>-</sup><sub>(ads)</sub> to O<sup>-</sup><sub>(ads)</sub> commence at around 300 °C from the simulation. More interestingly, the combined coverage of the two ionized species remains roughly constant through the temperature range while physisorbed O<sub>2</sub> decreases monotonically with temperature. This phenomenon indicates that the saturation coverage of oxygen ions is determined by the so-called Weitz limitation, which impose strong limitation on the concentration of charged surface species

by electronic effect. Due to Weitz limitation, the upper limit of oxygen anions coverage is around  $10^{-3}$  monolayer. The theory of the Weitz limitation will be discussed in more detail in the following chapter about charge transfer.

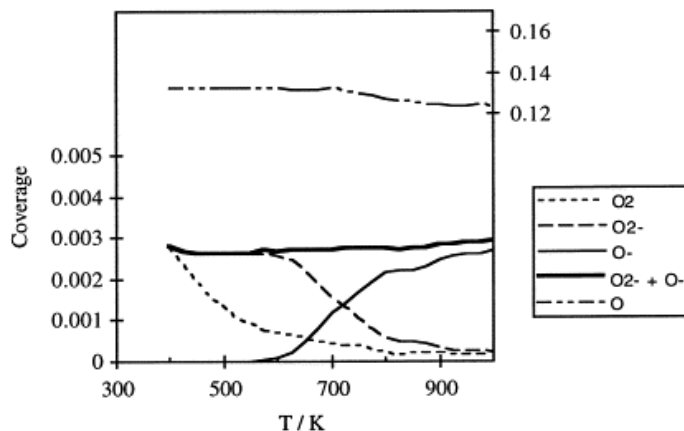


**Figure 7.** The simulated equilibrium coverages of the oxygen species. The transition from  $O_2^-$  to  $O^-$  is calculated to be around  $700K^{20}$ .

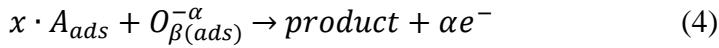
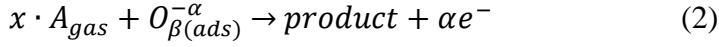
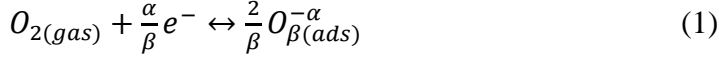
#### 2.4.1.2 Interaction of Analyte Gas with Metal Oxide Surface

The base of the gas detection is the interaction of the gaseous species at the surface of the semiconducting sensitive metal oxide layer. It is important to identify the reaction partners and the input for this is based upon spectroscopic information.

The gases detectable by semiconductor gas sensors can be classified based on their properties including the ionization potential, electron affinity and proton affinity as summarized in **Figure 8**. In this research work we primarily focus on gases in group II including  $H_2$ ,  $CO$ ,  $CH_4$ ,  $C_2H_6$ ,  $C_2H_4$ , and  $C_2H_2$ , as well as acidic gas  $H_2S$ . Group II gases exhibit the properties of weak electron donors and have rather low proton affinities. With higher proton affinity, the higher the tendency to give out electrons, compare the 6 gases, then reactivity should have this order. The commonly acknowledged reaction routine involves total oxidation in the interaction with the ionosorbed oxygen species at the surface



of the sensor material according to either an Eley–Rideal or Langmuir–Hinshelwood mechanism, which can be represented in the following quasi-chemical reactions:



The Eley–Rideal mechanism with ionized oxygen species as the adsorbed reactant and reducing gas in gas phase as the other reactant is displayed in equation 1 and 2, while for Langmuir–Hinshelwood mechanism, both reactants need to be preabsorbed before the reaction, and hence is summarized in equation 1, 3, 4. However, the reaction rate equations for both mechanisms are basically the same. Because of the very low concentration of reducing gas (usually below 0.1 vol%) encountered in the sensing procedure,  $[A_{ads}]$  should simply equals to  $K P_A$  regardless of the nature of the adsorption process. As a result, the rate equation for  $[O_{\beta(ads)}^{-\alpha}]$  at steady state can be written as:

$$\frac{d[O_{\beta(ads)}^{-\alpha}]}{dt} = k_1 P_{O_2} n_s^{2\alpha/\beta} - k_{-1} [O_{\beta(ads)}^{-\alpha}]^{2/\beta} - k_{rec} P_A^x [O_{\beta(ads)}^{-\alpha}] = 0 \quad (5)$$

Spectrometry study conducted at condition close to sensor operation have been used to verify the reaction mechanism of  $H_2$ ,  $CO$ , and  $C_3H_8$  on  $SnO_2$  surface<sup>21–23</sup>. The reactions with adsorbed oxygen anions instead of lattice oxygen were observed in most cases, and the only gases products observed were  $CO_2$  and  $H_2O$ , which indicates complete oxidation in all cases.

In comparison, interaction of gaseous H<sub>2</sub>S with oxide surfaces might involve not only oxidation reactions with ionosorbed oxygen, but also an additional donor-acceptor interaction<sup>24</sup>. This is due to that the strong reducing power of the compound ((ionization potential of H<sub>2</sub>S molecule is 10.4 eV) which facilitates direct redox reaction with metal oxide. Moreover, hydrogen sulfide is a Bronsted acid with the S-H bond capable of readily undergoing a heterolytic cleavage, especially in the formation of donor-acceptor bonds. The interaction with gaseous hydrogen sulfide on oxide surfaces leads to the changes such as formation of sulfides, partial blockage of the Lewis acid sites, and reduction of mixed-valence metal cations. For metal oxides with high sulfur affinity such as CuO and Fe<sub>2</sub>O<sub>3</sub>, sulfides may readily form in the course of heterolytic reaction of H<sub>2</sub>S molecule with the acid + base Lewis pair on the oxide surface (a chemical transformation of highly resistive p-type semiconductor CuO and n-type semiconductor Fe<sub>2</sub>O<sub>3</sub> to highly conductive sulfides Cu<sub>2</sub>S and FeS). For example, Pagnier et al. have observed formation of metal sulfides along with SO<sub>2</sub> in operando condition with Raman spectrometry on SnO<sub>2</sub>/CuO composite powders exposed to H<sub>2</sub>S in dry air<sup>25</sup>.

#### 2.4.1.3 Interference from Water Vapor

The influence of water vapor in the gas sensing with metal oxides-based gas sensors is of paramount importance in most applications. The concentration of water in the test environment (40% RH (21°C) = 10000 ppm) could be higher than the analyte gas (1-1000 ppm) by 1–4 orders of magnitude, and extremely varied depending on the weather or the condition of the human test subject. The effect of water vapor on n-type semiconductor is the increase of surface conductance and the phenomenon is often reversible, with a time constant of the order of around 1 h<sup>19</sup>. Depends on target gas, base material, fabrication

technology, doping, the presence of water vapor could have effects ranging from enhancement down to inhibition of sensing<sup>26</sup>.

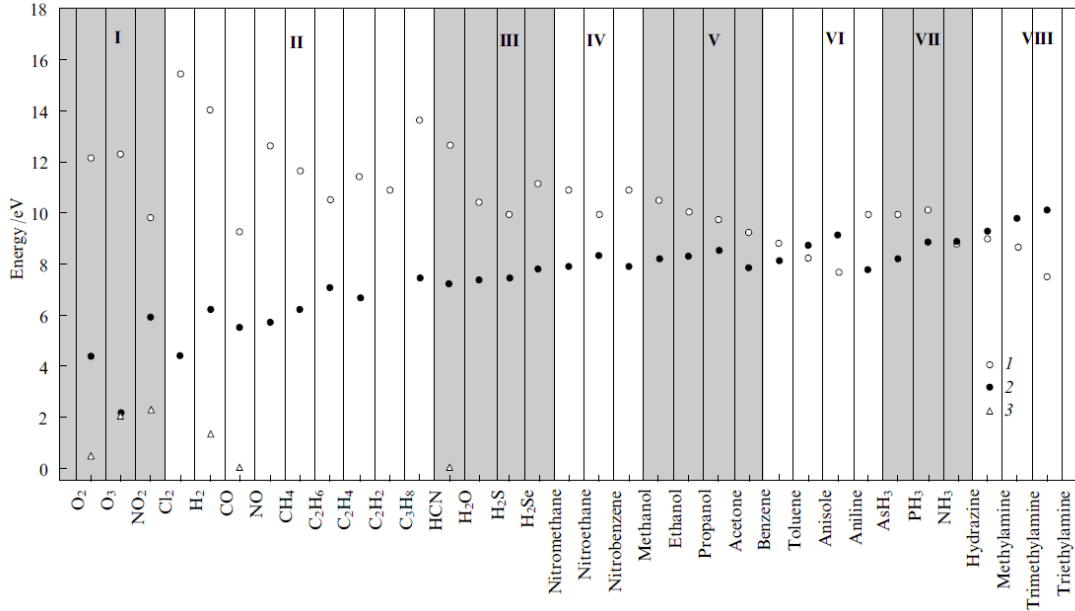
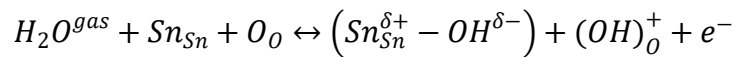
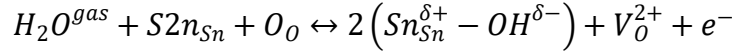


**Figure 8.** Energy parameters of molecules in the gas phase. [Ref] Ionization potential (1), proton affinity (2) and electron affinity (3).<sup>24</sup>

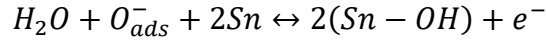
The classical theories<sup>27</sup> strived to explain the effect of water vapor on sensing performance by confining the investigation to just between the water vapor and the metal oxide surface. These mechanisms, proposed for adsorption on SnO<sub>2</sub> surface include (i) homolytic dissociation of water and reaction with lattice oxygen resulting in the formation of two types of hydroxyl groups (isolated and rooted)



(ii) homolytic dissociation of water and the formation of terminal hydroxyl groups and oxygen vacancies.



More recently, A DRIFT study reported by Koziej et al. reported spectrometric evidence of water reacting with pre-adsorbed oxygen to form terminal hydroxyl groups and release of electrons<sup>26</sup>.



Such an interaction mechanism indicates that water, under conditions of dynamic adsorption–desorption equilibrium on SnO<sub>2</sub> surface, compete with reducing gases for the pre-adsorbed oxygen species. Based on this finding, they were able to explain the dampening effect of humidity on the CO response to this water-oxygen interplay. However, in a similar study, the theory becomes invalid when the SnO<sub>2</sub> is doped with Pt and exhibited heightened response to CO under humid condition.

Due to the complex nature of the humidity interference, it is recommendable to actively develop strategies to alleviate the humidity interference along with the theoretical studies aiming to understand the process. Lately, promising advancements in curbing the humidity interference have been made including chemical modification on the sensing film surface with water adsorbent, and the adoption of the AC impedance as the source of sensing signal.

### 2.3.2 Charge Transfer

Because of the surface interactions discussed in 2.3.1, charge transfer takes place between the adsorbed species and the semiconducting sensitive material. This charge transfer can take place either with the conduction band or in a localized manner. In the first

case, the concentration of the free charge carriers will be influenced. The latter case (in contrast to the first one) will have no direct impact on the conduction, while the former determines the appearance of a depletion layer at the surface of the semiconductor material, due to the equilibrium between the trapping of electrons in the surface states (associated with the adsorbed species) and their release due to desorption and the reaction with test gases<sup>28</sup>.

To model the space charge within the semiconductor caused by the ionized oxygen species adsorbed on the surface, we first consider a simple 1-dimensional planar model as shown in **Figure 9** (a). This type of model is sufficient to model porous sensing film composed of grains with diameter much larger than the depletion width ( $w$ ) as well as compact sensing film with thickness larger than the depletion width. To simplify the calculation, it is conventionally assumed that (1) donors are completely ionized (2) the positive charge density is uniform within the entire depletion region and equals to the donor concentration ( $N_d$ ). Based on the latter assumption, the density of surface charges

$$Q_{sc} = -qN_d w = qN_t \quad (6)$$

Where  $N_t$  is the density of surface traps, which equals to  $\alpha \cdot [O_{\beta(ad_s)}^{-\alpha}]$ . Under these conditions, the electric potential,  $V$ , in the depletion region should satisfy the following Poisson equation, where  $x$  is the depth from the surface and  $\epsilon$  is the permittivity of the semiconductor

$$\frac{d^2V}{dx^2} = \frac{-qN_d}{\epsilon} \quad (7)$$

By introducing the boundary conditions that  $dV/dx$  as well as  $V$  are zero at  $x = w$ , Eq. 3 is solved to give the following depth profile of the electric potential at the surface

$$\frac{qV_s}{kT} = \frac{(w/L_D)^2}{2} = \frac{m^2}{2} \quad (8)$$

Where Debye length,  $L_D$ , is defined as  $L_D = (q^2 N_d / \epsilon k T)^{-1/2}$ , and  $m = w/L_D$ . Assuming Boltzmann distribution for the free electrons inside the depletion region, we can deduce the free electron density at the surface of the depletion region

$$n_s = N_d \exp\left(-\frac{qV_s}{kT}\right) = N_d \exp\left(-\frac{m^2}{2}\right) \quad (9)$$

For scenarios involving small grains with diameter close to the depletion width ( $w$ ) as well as compact sensing film with thickness close to the depletion width, the semiconductor physics mentioned above requires modification because firstly it is no longer appropriate to model spherical column shaped grains with 1-D planar model, and secondly the conduction electron could be depleted beyond the scheme of conventional depletion theories.

To illustrate the second point, we consider a thin plate of a semiconductor with a thickness  $2a$  (**Figure 9** (b)). In the absence of oxygen, the plate is assumed to be at the flat band state. In the presence of oxygen  $P_{O_2}$  (I) depletion takes place from both sides of the plate to attain an electronic equilibrium between the bulk and the surface states. With increasing oxygen partial pressure, the energy state of  $O^-$  decreases and then the depletion depth  $w$  also increases, finally reaching the center of the plate ( $w=a$ ) at  $P_{O_2}$  (II). With increasing  $P_{O_2}$  further to  $P_{O_2}$ (III), however, the equilibrium should be attained in a different scheme because there is no room to further extend  $w$ . That is, the profile is maintained the

same as that for  $pO_2(II)$ , but the Fermi level shifts down by an adequate value ( $pkT$ ) to satisfy the new equilibrium. In this way we recognize that there are two types of depletions. One type is a conventional one appearing in the range up to  $P_{O_2}(II)$ , which is called regional depletion here, and another one shows up in the whole volume thereafter, which is called volume depletion here.

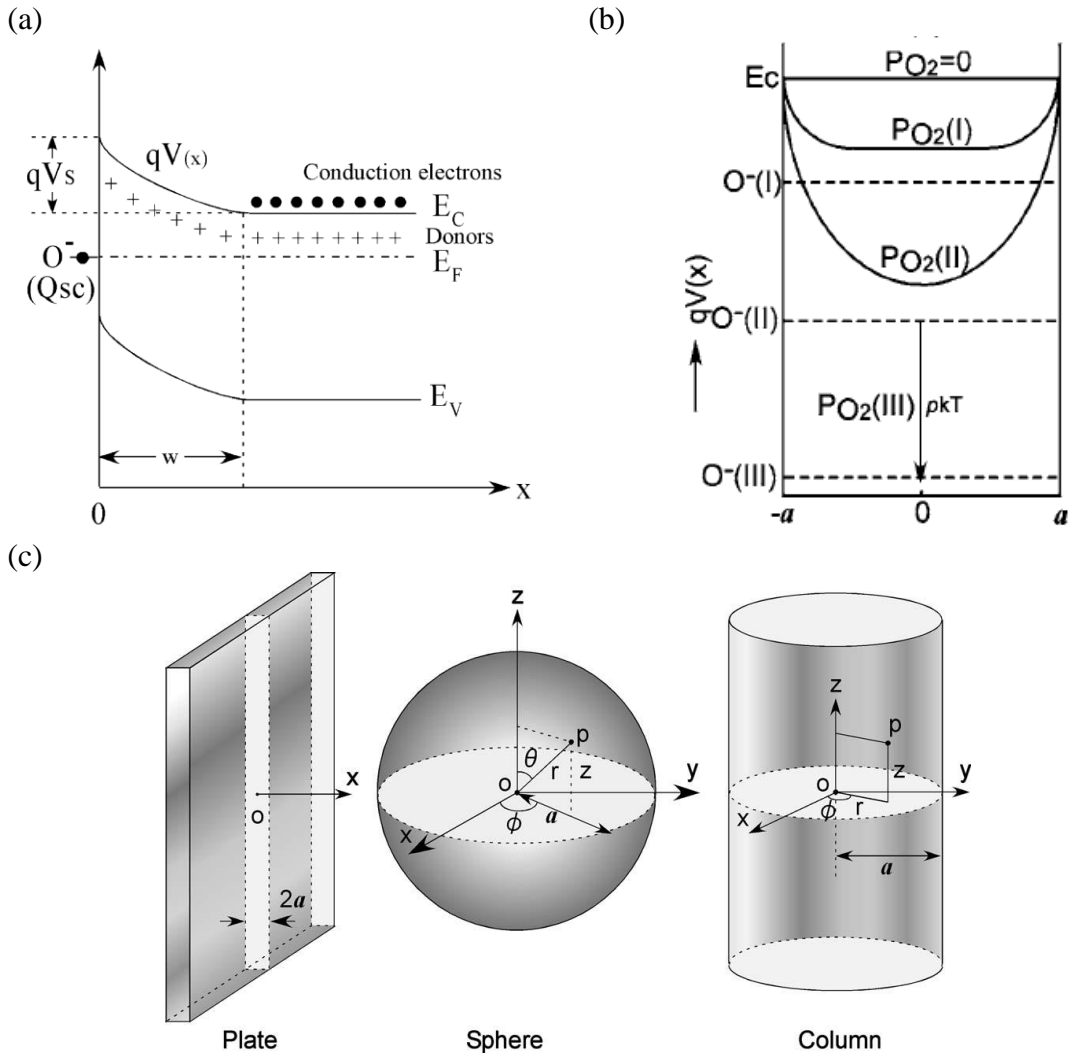


**Figure 9** (a) Schematic drawing of surface depletion layer formed by oxygen adsorption for an n-type semiconductor. (b) Schematic diagrams of electronic equilibrium for semiconductor plates of different thicknesses placed under various partial pressures of oxygen depth profiles of potential energy (c) Typical shapes of crystals and coordinate systems selected<sup>29</sup>.

For the three type of crystals displayed in **Figure 9** (c), the  $n_s$  and  $[O_{\beta(ad_s)}^{-\alpha}]$  can be written explicitly as

Plate:

$$n_s = N_d \exp\left(p - \frac{m^2}{2} \exp(p)\right) \quad (10)$$

$$[O_{\beta(ad_s)}^{-\alpha}] = -\frac{N_d e^p L_D m}{\alpha} \quad (11)$$

Sphere:

$$n_s = N_d \exp\left(p - \exp(p) \times \frac{3am^2 - 2m^3 L_D}{6a}\right) \quad (12)$$

$$[O_{\beta(ad_s)}^{-\alpha}] = -\frac{N_d e^p L_D n \{1 - [(n-m)/n]^3\}}{3\alpha} \quad (13)$$

Cylinder:

$$n_s = N_d \exp\left(p - \exp(p) \times \frac{(\alpha^2 - (a-w)^2 (1 + 2 \ln \frac{a}{a-w}))}{4L_D^2}\right) \quad (14)$$

$$[O_{\beta(ad_s)}^{-\alpha}] = -\frac{N_d e^p L_D n \{1 - [(n-m)/n]^2\}}{2\alpha} \quad (15)$$

Where  $n=a/L_D$ .  $m=n$ , for boundary and volume depletion condition.  $p>0$ , for volume depletion condition.

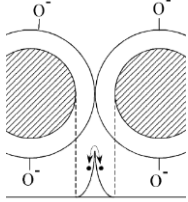
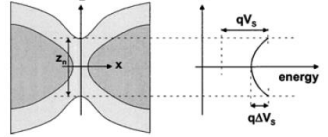
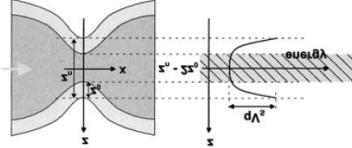
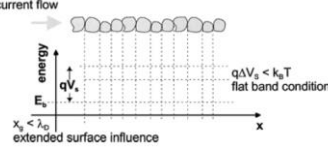
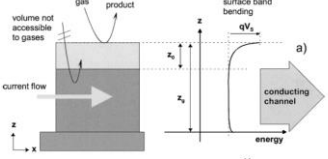
### 2.3.3 Conduction in the sensitive layer

The conduction in the sensitive layer, which translates the sensing into the measurable electrical signal. This strongly depends on the morphology of the sensitive layer. In turn, the change of the concentration of the free charge carriers is translated into a change of the overall resistance of the sensing layer. The transfer (or calibration) function depends on the



morphology of the layer.

**Table 3.** Conduction models based on different sensing film geometries

Film structure	Grain size	Neck size/depletion	Schematic	Relationship
Porous film	Large grains	No neck		$G \propto n_s^\gamma$
		Close neck		$G \propto n_s^\gamma$
		Open neck		$G \propto \ln n_s$
	Small grains	Full depletion		$G \propto n_s$
Compact film	Thick	Partial depletion		$G \propto \ln n_s$
	Thin	Full depletion		$G \propto n_s$

As shown in **Table 3**, apart from large grain with open necks and thick compact film, which has very low sensitivity to the change in electron density change at the surface, all other configuration possess a power law correlation between film conductance  $G$  and  $n_s$ . Depending on the mean free path of the electrons ( $\lambda$ ), the electrons needs to follow either diffusion (small  $\lambda$ ) or thermoelectronic emission (large  $\lambda$ ) mechanism when overcoming

the double Schottky barriers between two grains. The exponent  $\gamma$  is 1 for the thermoelectronic emission, and ranges between 0.8-1.2 for the diffusion mechanism<sup>19</sup>. For the fully depleted small grain and thin film configuration, the conductance of the film is linearly correlated to  $n_s$ .

#### 2.3.4 Conduction Model and Power Law Relationship

Based on the reaction rate equations for the surface reaction, Poisson equations, and electroneutrality equations deduced from previous sections, it is easy to deduce the correlation between the electrical resistance of the sensing film and the partial pressure of oxygen/reducing gas, which reveals a commonly and experimentally observed power law relationship as shown in **Figure 10**:

$$R = aP^n \text{ or } \log R = \log a + n \log P$$

Where P is the partial pressure of oxygen/reducing gas, n is the exponent factor, and a is the proportionality constant.

Taking CO sensing on SnO<sub>2</sub> porous film with closed-neck large grains as an example, we assume the complete oxidation by  $O_{(ads)}^-$ , and thermoelectronic emission type electron transfer through the Schottky barrier, and write down the following equations

Reactions: ( $\alpha=\beta=x=1$ )



Rate equation:

$$\frac{d[O_{(ads)}^-]}{dt} = k_1 P_{O_2} n_s^2 - k_{-1} [O_{(ads)}^-]^2 - k_{rec} P_{CO} [O_{(ads)}^-] = 0 \quad (18)$$

Correlations obtained from Poisson equation and electroneutrality:

$$n_s = N_d \exp\left(-\frac{qV_s}{kT}\right) = N_d \exp\left(-\frac{m^2}{2}\right) \quad (19)$$

$$[O_{(ads)}^-] = N_t = N_d w = N_d m L_D \quad (20)$$

Conduction equation:

$$G \propto n_s \quad (21)$$

By inserting the above equations into eq:

$$n = \frac{d \ln R}{d \ln P_{CO}} = \frac{d \ln R}{d N_t} \times \frac{d N_t}{d \ln P_{CO}} \quad (22)$$

We can obtain the exponent factor n:

$$n = -\frac{cP_A}{N_d L_D} \times \frac{j}{2(j^2+1)} \quad \text{for } \frac{N_t}{cP_{CO}} \gg 1 \quad (23)$$

$$n = -\frac{\beta x}{2\alpha} \times \left(1 - \frac{1}{2j^2+1}\right) = -\frac{1}{2} \times \left(1 - \frac{1}{2j^2+1}\right) \quad \text{for } \frac{N_t}{cP_{CO}} \ll 1, \quad (24)$$

Where  $j = N_t / N_d L_D$ ,  $c = k_{rec} / k_{-1}$ . These two equations show that the power-law exponent n is dependent on the magnitude of  $N_t / cP_A$  through  $N_t / cP_{CO}$ . When the desorption of oxygen species dominates over the consumption of  $O^-$  via oxidation with CO. As a result, the magnitude of n increases with  $P_{CO}$  from zero up to the constant value  $\frac{\beta x}{2\alpha} = \frac{1}{2}$ . When  $cP_{CO}$  is sufficiently large, the reduction of j caused by the reaction of A with O cannot be regarded as a constant at a fixed  $P_{O_2}$ , hence the power-law exponent decreases from 1/2 to 0 with any further increases in  $cP_{CO}$ . This is well consistent with experimental results<sup>30</sup>. It is well

known that high concentrations of reducing gas can cause a saturation of the gas sensor response. It should be noted that the exponent constant  $n$  is determined by the reaction order of the surface reactions ( $\alpha=1, \beta=1, x=1$ ).

As for porous film with small grains or thin compact film, we consider the gas adsorption equilibrium on a crystal inside which the electric potential can be assumed to be constant. For a spherical  $\text{SnO}_2$  grain of radius  $a$ , with same condition as the large grain case, the charge balance after the electron transfer is given by

$$\frac{4\pi}{3} a^3 N_d = \frac{4\pi}{3} a^3 [e] + 4\pi a^2 [O^-] \quad (25)$$

The left side of the equation is the total number of conduction electrons concerned, while the right side shows those electrons that either remain in the crystal first term or are combined with oxygen at the surface. Rearranging this, we obtain

$$[O^-] = \frac{a}{3} (N_d - [e]) \quad (26)$$

Insertion of this equation into Eq. 2, followed by rearrangement, gives

$$[e] = (aN_d/3) / [(K_{O_2} P_{O_2})^{\frac{1}{2}} + (a/3)] \quad (27)$$

The reduced resistance of the device using these crystals,  $R/R_0$ , is given by  $[e]_0/[e]$ , where  $[e]_0$  is the value of  $[e]$  at  $P_{O_2} = 0$ , i.e.  $[e]_0 = N_d$

$$R/R_0 = (3/a)(K_{O_2} P_{O_2})^{\frac{1}{2}} + 1 \quad (\text{sphere}) \quad (28)$$

This is an equivalent equation to Eq. 51. The difference in the intercepts has appeared because the electric potential distribution is neglected for Eq. 53. The same discussion is available for plates and columns

$$R/R_0 = (1/a)(K_{O_2}P_{O_2})^{\frac{1}{2}} + 1 \quad (\text{plate}) \quad (29)$$

$$R/R_0 = (2/a)(K_{O_2}P_{O_2})^{\frac{1}{2}} + 1 \quad (\text{column}) \quad (30)$$

It follows that the gas adsorption equilibrium on such small crystals can be treated, to a good approximation, by a conventional method where the electronic structure of crystals is disregarded. It is worth noting that the exponent constant is still unrelated to size and shape of the grain, while the proportionality constant is inversely proportional to the size of the grain. Moreover, when every parameter are identical, sphere possess higher sensor response than column and plate.

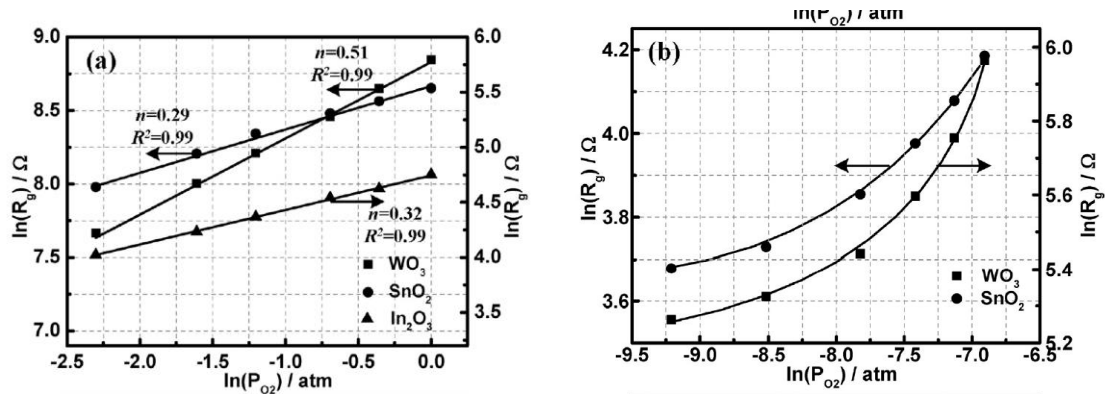
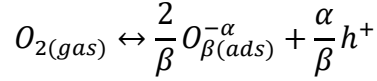


**Figure 10.** Calibration lines of  $WO_3$ ,  $In_2O_3$  and  $SnO_2$  sensors at (a) high partial pressure of oxygen<sup>31</sup>.

### 2.3.5 Sensing Mechanism of P-type Semiconductor

Because there are very few free electrons available in p-type semiconductors such as  $CuO$  and  $NiO$ , the oxygen ionsorption process requires extraction of valence electrons

from the metal oxide. In another word, the oxygens inject free holes into the valence band of the p-type semiconductor during ionosorption



This leads to the formation of a hole accumulation layer (HAL) at the surface of the n-type semiconductor (**Figure 11**). Unlike the immobilized ionized donor inside the electron depletion layer (EDL) of an n-type semiconductor, the free holes will move to the surface driven by the electrostatic force, and hence the HAL is generally much thinner than EDL. However, a finite thickness of HAL is still maintained because the density of available states in the conduction & valence band is low near the edge of the band, so without surface states, the charge cannot reside right at the surface. For smaller grain size, the conduction process through the sensing film could be approximated by the current flowing through the HAL layer. Therefore, it is reasonable to consider the conductance being linearly proportional to the average hole density in the HAL ( $\bar{p}_s$ ), which can be defined as based on Boltzmann distribution

$$\bar{p}_s = \frac{1}{x_0} \int_0^{x_0} p_b \exp\left(\frac{qV(x)}{kT}\right) dx \quad (31)$$

where  $p_b$  is the density of hole in the bulk. By solving the equation, one obtains

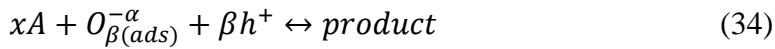
$$G \propto \bar{p}_s = p_b \exp\left(\frac{qV_s}{2kT}\right) \quad (32)$$

while for n-type semiconductor

$$G \propto \exp\left(-\frac{qV_s}{kT}\right) \quad (33)$$

Already by comparing equation 32 and 33, one can easily see that the same change of the band bending will be less efficiently differently transduced into a sensor signal by p-type semiconductor with signal only the square root of the n-type signal to be exact.

Total oxidation reaction of a reducing gas with ionized oxygen as the reaction partner can be written as:



The free holes in the HAL will be consumed by the reaction and hence leads to an increase in sensor resistance.

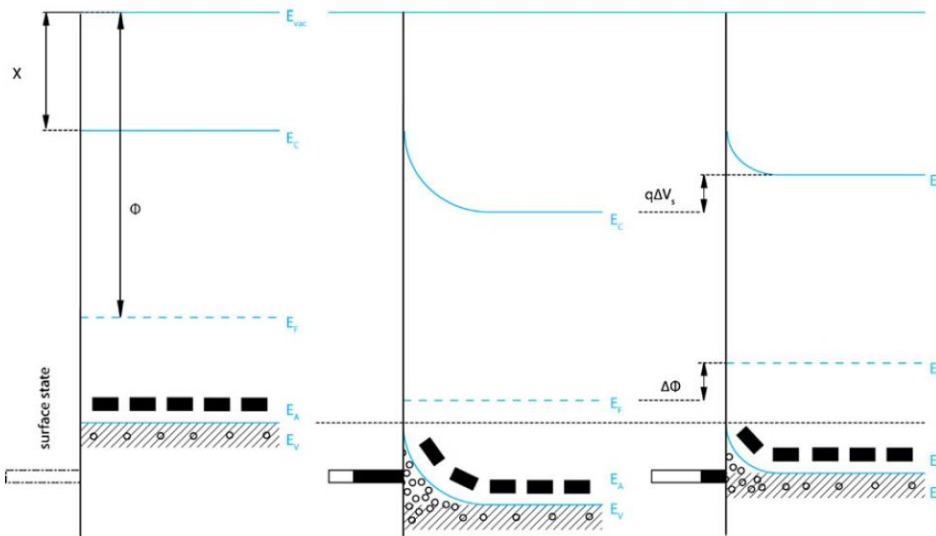


**Figure 11.** Energy bands representation of the surface processes associated to the reaction with ambient oxygen and reduction gases: left, the flat band situation prior to any surface reaction; center, the trapping of electrode due to oxygen adsorption and the formation of the holes accumulation layer; right, the decrease of the surface charge associated to the decrease of adsorbed oxygen ions following the reaction with the reduction gas.  $E_{VAC}$  is the energy level of the electron far away from the semiconductor,  $E_C$  is the energy level of the intrinsic acceptors;  $\Phi$  is the work function and  $\chi$  is the electronic affinity of the semiconductor<sup>32</sup>.

## 2.4 Influencing Factors on the Sensing Performance

### 2.4.1 Sensing Film Structures

The conduction in the sensitive layer, which translates the chemical interaction into the measurable electrical signal, is strongly depends on the morphology of the sensitive layer. Therefore, the deposition techniques used for coating the sensing film plays an important role in deciding the sensing performance since it dictates the morphology of the sensing film.

Metal oxide sensing films fabricated with high-throughput thin film deposition techniques such as PVD, CVD, and ALD have attracted limited interest from both the industry and the academia. The thin films produced in this way often exhibit compact microstructures (as shown in **Figure 12** (a)), which only permit gas-solid interaction and formation of space charges on the external surface of the film. The signal, i.e. electrical resistance change, arisen from the film surface in response to the analyte gas is overwhelmed by the constant resistance of the unaffected bulk, which is in parallel with the film surface in the equivalent circuit. As a result, only in case that the thickness of the sensing film approaches the Debye length (2-5 nm), may reasonable sensitivity be expected. However, with thickness approaching the Debye length, the interference from the interface trapped charged states on the electrical properties of the sensing film could become prominent. For compact layers they appear as a contact resistance ( $RC$ ) in series with the resistance of the sensing layer. For partly depleted layers,  $RC$  could be dominant, and the reactions taking place at the three-phase boundary, electrode-SnO<sub>2</sub>-atmosphere, control the sensing properties. As a result, sensing films with dense microstructure often exhibit low gas sensitivity.



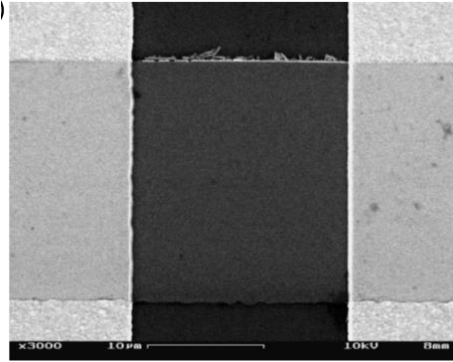


**Figure 12.** (a) sputtered film of SnO<sub>2</sub><sup>11</sup>.

Due to the limitation on the minimum feature size achievable by the screen-printing technique (around 1 mm, **Figure 13**), a microdrop process was adopted instead as the sensing film deposition technique to fabricate MEMS sensor (**Figure 14**). The technique leaves a circular lump of sensing materials with diameters between 200-600 µm and heights around 25 µm on top of the active heating area of the microheater. The active heating area is usually at the center of a suspended membrane composed of heat insulating dielectric material (e.g. SiO<sub>2</sub>, Si<sub>3</sub>N<sub>4</sub>) with thickness around 5-10 µm to reduce the heat loss to the silicon die. Although MEMS sensors with sensing film fabricated by the microdrop technique possess decent sensitivity, this thick film configuration is still far from ideal.

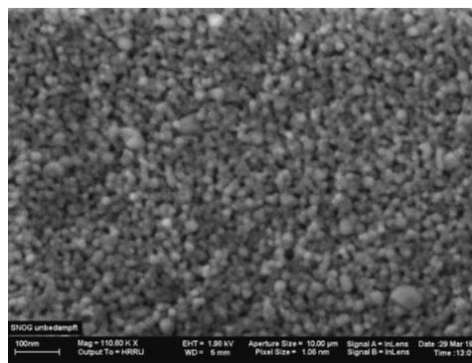


**Figure 13.** SEM image of SnO<sub>2</sub> sensing film prepared by screen printing.

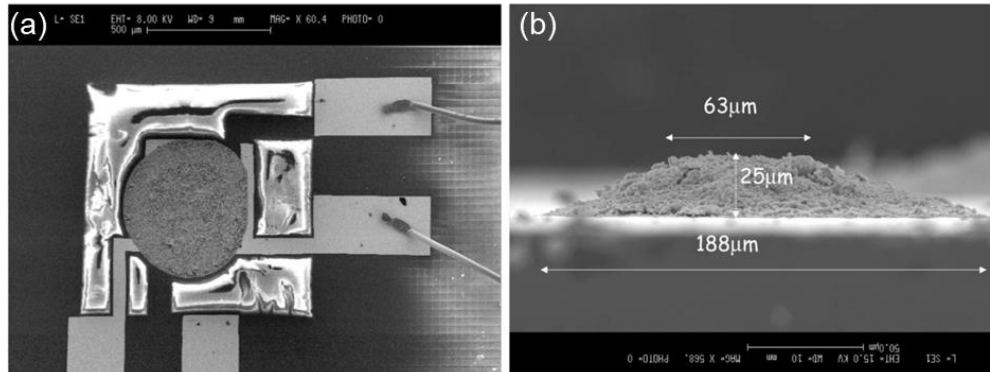


**Figure 14.** SEM images of sensing layer deposited by microdrop method (a) top view (b) side view.

Firstly, the deposition of thick sensing films comes along with the introduction of a large mass of sensing material which must be carried by a rather thin membrane. Mechanical robustness of a micromachined gas sensor requires, therefore, high mechanical strength of the membrane under the high load of a thick sensing film<sup>33</sup>.

Secondly, the sensing film introduces a large extra thermal mass which leads to an increased thermal time constant. Beyond that the larger thermal conductivity in the active region leads to a smoothing of the temperature profile over the active area and an increase in power consumption due to additional heat losses through the membrane<sup>11</sup>.

Lastly, the sensitivity of thick porous film is limited for highly reactive/slow diffusing gas species. Analyte gas diffuses through the porous structure of a sensing film, and in the meantime, some of the analyte gas is consumed by reacting with the oxygen anions (**Figure 15**). The penetration depth of the analyte gas will become very small, as the reactivity increases/diffusivity decreases, leaving only the surface region of the sensing film accessible to the gas. By circumventing this drawback with pulse-driven heating technique,

Suematsu et al. has demonstrated an improvement in detection limit by 20 times, which illustrated the significant of this effect<sup>34</sup>.

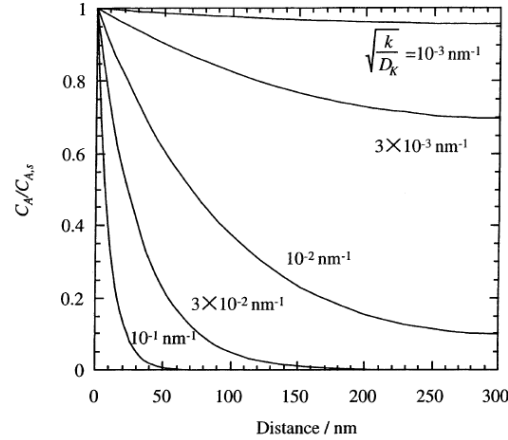


**Figure 15.** Concentration gradient along the thickness of a porous sensing film.

Therefore, a technique to fabricate thin film with porous structure and high surface area is of great significance. In the early 2000s, the SENSOR Lab in Brescia (Italy) has developed a method named Rheotaxial Growth Thermal Oxidation (RGTO) to fabricate SnO<sub>2</sub> thin film with loosely packed agglomerates of nanograins (**Figure 16**). The process involves first the preparation of a metallic thin film by sputtering from a metallic target on a substrate kept at a temperature higher than the melting point of the metal, then the thermal oxidation cycle in order to get a metal oxide layer with stable stoichiometry. The thin film possesses features beneficial to the mechanical stability, energy efficiency, and sensitivity of the MEMS sensor. However, the thermal oxidation cycle is harsh (>800 °C, for 3h, oxidizing atmosphere), and hence hard to integrate with other process steps for the CMOS circuitry due to the thermal profile. Moreover, the sensing materials that can be deposited using this technique is limited to oxides of metals having a relatively low melting point.

Tungsten oxide is one of the oxides that cannot be prepared through this method, but, at the same time, it is a widely used material for gas sensing applications, especially for its high sensitivity to oxidizing gases such as  $\text{NO}_2$  and  $\text{O}_3$ . Besides, this technique constraints itself to fabricating metal oxide nanoparticulate film, and cannot work with metal oxides with novel nanostructure, and exotic materials such as metal chalcogens, carbon nanotubes, and MOFs, which have shown good promises on revolutionizing the sensing performance.

A low temperature approach to fabricate thin porous film from a wide variety of sensing materials is therefore very desirable. Among the innovative thin film deposition strategies, Langmuir Blodgett (LB) assembly of metal oxide nanoparticles, a highly reproducible and patternable technique, is promising to yield a sensing film structure with high sensitivity. So far, assembly of various zero to two dimensional nanostructures, carbon nanotubes, and graphenes into monolayer film, which largely preserves the nanostructures' surface area and promotes fast gas diffusion, has been reported in the literature.<sup>35-38</sup> Moreover, Huo et al.<sup>30</sup> and Cheng et al.<sup>39</sup> performed studies on the LB film of  $\alpha\text{-Fe}_2\text{O}_3$  nanoparticles and  $\text{WO}_{3-x}$  nanowires, respectively, and obtained preliminary data demonstrating promising gas sensing properties.

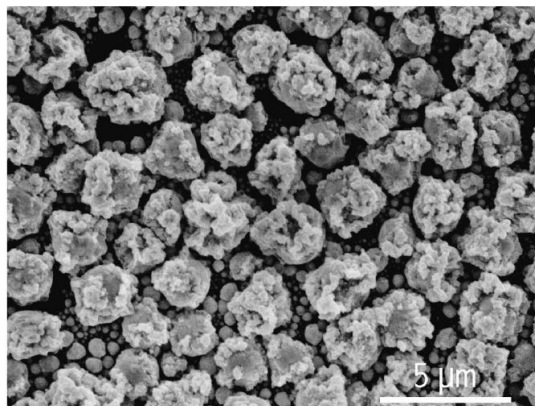


**Figure 16.** SEM image of RGTO SnO<sub>2</sub> film.

#### 2.4.2 Grain Size

The grain size effect was first observed by Xu et al.<sup>31</sup>, who noted a strong dependency of the sensitivity of SnO<sub>2</sub>-based sensors to gases such as CO, H<sub>2</sub> and i-C<sub>4</sub>H<sub>10</sub> on the crystallite size (D) (**Figure 17**). Specifically, when  $D > 20$  nm, the sensitivity of the SnO<sub>2</sub> sensors barely changed along with the crystallite size, when  $D < 20$  nm, the sensitivity rapidly increased with decreasing crystallite size, and when D is decreased to below 10 nm, the gas-sensitivity of the SnO<sub>2</sub> was significantly improved. In a related study, Xu et al. observed that the sensitivity of SnO<sub>2</sub>-based sensors steeply increased when the value of D was comparable to or less than twice the depth of the space charge layer (2LS) for SnO<sub>2</sub>. This can be explained clearly with the conduction model discussed in the previous chapter: there are very limited effect of size on the exponent factor and the proportionality constant when the grain size diameter is much larger than the Debye length  $L_D$ , while the proportionality constant becomes proportional to the inverse of the diameter when the diameter approaches  $L_D$ .

However, gas sensors made from metal oxide nanoparticles with high surface-to-bulk ratio are often susceptible to thermal degradation caused by grain growth and coalescence during service at high working temperature (200-400 °C)<sup>9,40,41</sup>. Therefore, it is crucial to develop an effective strategy to control the rate of grain growth of these nanomaterials without compromising the sensitivity. In metallurgy, a common technique to suppress grain growth is by introducing impurity atoms or phases to pin the grain boundaries, or to decrease the grain boundary energy<sup>42</sup>. Based on the same mechanism, Leite et al. doped several rare earth elements (e.g. Y, La, and Ce) into tin (IV) oxide, the most widely studied metal oxide for sensor application, to form a metastable solid solution<sup>43,44</sup>. After high temperature annealing, the aliovalent dopants segregate to the surface of the nanoparticles to minimize the elastic strain energy and electrostatic interaction energy of the system<sup>45</sup>, resulting in the formation of a dopant-segregation-induced core-shell structure with a dopant-rich shell and a dopant-less core. This structure serves to prevent further thermally-induced grain growth and coalescence by reducing the particle boundary mobility and/or the thermodynamic driving force<sup>43,44</sup>.

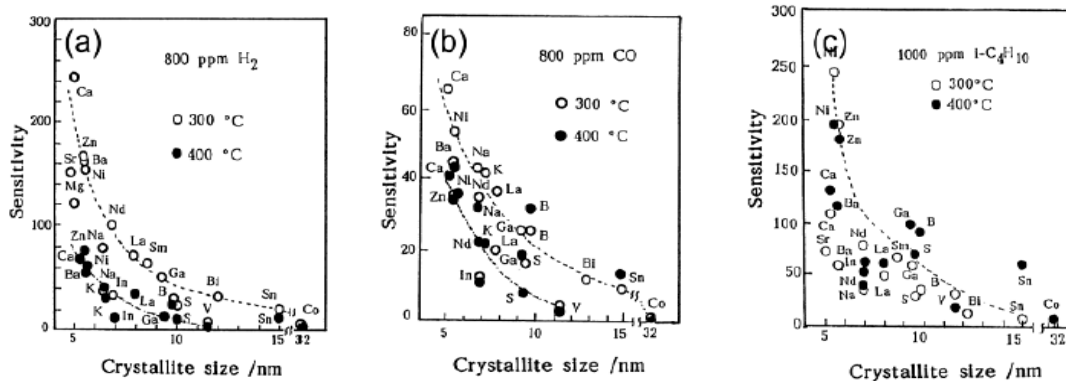


**Figure 17.** Gas sensitivity of the SnO<sub>2</sub> sensors doped with 5 at. % additives to: (a) 899 ppm H<sub>2</sub>, (b) 800 ppm CO, and (c) 1000 ppm i-C<sub>4</sub>H<sub>10</sub>.

### 2.4.3 Doping

The sensitivity and/or selectivity of metal oxide gas sensors toward certain gases can be significantly improved by dispersing a low amount of foreign metal or metal oxide additives on the oxide surface or in its volume.<sup>3</sup> For instance, various dopants have been trialed for SnO<sub>2</sub> sensor, including noble metals, transition metals, and metal oxides.<sup>20</sup> However, currently the exact mechanisms by which these additives improve the gas-sensing performance of a pure metal oxide gas sensor are still not fully understood. So far, three basic theories have been proposed to explain the gas-sensing mechanisms of doped metal oxide gas sensors:

(i) *Electronic sensitization*: the additive acts as a strong acceptor of electrons from the base semiconducting oxide material, which induces the formation of a depletion layer around the interface.<sup>3</sup> Following reaction with a reducing gas (e.g. H<sub>2</sub>), the additive is reduced, and the electrons are injected back into the host semiconductor. This type of sensitization has been noted for a number of systems, including Pd/PdO, Ag/AgO, and Cu/CuO systems.

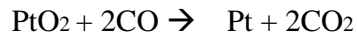
(ii) *Chemical sensitization*: arises from the high catalytic activity of the additive material. Small clusters of deposited noble metals provide preferred sites for the adsorption and desorption of the target gas and the activated fragments spill over onto the semiconducting metal oxide material. As a result, the metal oxide surface coverage of the gas is increased, and the sensitivity of the base metal oxide is enhanced. For example, in the case of Pd-doped SnO<sub>2</sub> sensor exposed to a reducing gas such as CO, the reduction of the gas molecules is first activated at the metal surface, forming the active surface species.<sup>36</sup> These surface species then react with the chemisorbed oxygen on the SnO<sub>2</sub> surface via a

spillover process. As a result of this reaction, the localized electrons are re-injected back into the bulk of the material, thus enhancing the conductivity of the material. The sensing mechanism of Pt-doped SnO<sub>2</sub> has been proposed to involve two main reactions:

The oxidation of Pt to PtO<sub>2</sub> by the chemisorbed oxygen at high temperature:



The reduction of the platinum oxide following exposure to CO:



(iii) *bulk sensitization*: The charge carrier density and grain size can be decrease simultaneously by doping aliovalent elements into the bulk of the semiconductor metal oxides. As a result, smaller grains with larger depletion width can be obtained, which serves to promote the sensitivity of the sensor.



### 3. SELF-ASSEMBLED MONOLAYER OF METAL OXIDE NANOSHEET AND STRUCTURE AND GAS SENSING PROPERTY RELATIONSHIP

#### 3.1 Introduction

Chemiresistors based on semiconducting metal oxides are one of the most frequently used solid state gas sensor with wide applications in both industrial and domestic sectors.<sup>46-</sup><sup>48</sup>The simple and compact design of chemiresistors consists of a sensing film, an insulating substrate with preprinted interdigitated electrodes, and a microheater, among which modification on the sensing materials within the sensing film has been the research focus to achieve better sensing performance. Metal oxides with two-dimensional nanostructure have recently attracted great attention as gas sensing materials due to their high surface-to-volume ratio, providing a large specific area for the adsorption of gases of interest.<sup>49-53</sup> Moreover, the majority of exposed crystal surface is attributed by one crystal plane in 2D nanostructure, and hence the reaction sites are more homogeneous, which benefits the selectivity of the sensing material.<sup>46</sup>

Some high performance 2D metal oxide sensors have been reported in the literature as summarized in **Table 4**. Most research efforts on developing 2D metal oxides sensors were devoted to tailoring the microstructure of 2D metal oxides by exposing high energy surface,<sup>54</sup> creating pores in the nanosheets,<sup>55,56</sup> and decreasing the thickness to atomic level.<sup>57,58</sup> However, there is a lack of understanding about the possible influences of deposition technique on sensing film morphology, which is a key factor for sensing performance as proven by their zero and one counterparts. For instance, monolayers of aligned tungsten oxide nanowires<sup>39</sup> (1D) and closely-packed ferric oxide nanoparticles<sup>30</sup>

(0D) were deposited by Langmuir-Blodgett trough method, and outstanding sensing performance were reported at room temperature for detecting traces of hydrogen and alcohols in air, while similar sensing performances are only observable for the thick film sensors prepared by drop casting operating at 200-300 °C.<sup>59,60</sup>

One important facet correlating sensing characteristic to film morphology involves the diffusion and surface reaction of analyte gas within the sensing film.<sup>61-68</sup> Based on the most recognized sensing mechanism, i.e., oxygen ionosorption, the detection of analyte gas (e.g., H<sub>2</sub>, CO, H<sub>2</sub>S, VOCs) with metal oxide chemiresistors is realized by the electrical conductance variation originated from the change in the coverage percentage of oxygen anions adsorbed on the surface. Analyte gas diffuses through the porous structure of a sensing film, and in the meantime, some of the analyte gas is consumed by reacting with the oxygen anions. Under steady state condition, the gas concentration inside the sensing layer would decrease with increasing diffusion depth, resulting in analyte gas dilution in the inner region of the film. The dilution effect dampens the sensor response to analyte gas, and the severity of which depends on the rates of diffusion and surface reaction, as well as the diffusion depth.

Therefore, 2D metal oxides thin films, and ideally monolayer, should be the preferred film configuration for their immunity to gas dilution effect. However, the deposition techniques applied in 2D sensor studies can only produce either thick films by applying a solvated paste on a sensor substrate<sup>54,56,57,69</sup> or thin film with undefined and inconsistent structure (e.g., those prepared by drop casting).<sup>55,57</sup> A few studies on making monolayer film of 2D metal oxides were conducted by Sasaki et al. They successfully fabricated

closely packed monolayer film of 2D Titania nanosheet by Langmuir-Blodgett trough<sup>70</sup>, and electrostatic self-assembly<sup>71</sup> methods to study the dielectric properties of the monolayer film. However, the application of monolayer films of 2D nanosheet as gas sensors has not been reported yet.

Here we report, for the first time, the fabrication of chemiresistive sensors with monolayer film of copper(II) oxide (an extensively researched sensing material for its unique catalytic properties<sup>72-74</sup>) nanosheets whereby a facile, versatile, and highly reproducible self-assembly method at air-water-interface. Rely on the same method, layer-by-layer deposition of the CuO nanosheet is also realized for preparing stacked multilayer film. By comparing the sensing characteristic of CuO monolayer and multilayer films, we illustrate the advantages of monolayer configuration, and draw critical conclusions about the dependency of sensing performance on the film morphology for 2D metal oxides.

### 3.2 Experimental Section

*Synthesis of Metal Oxide Nanosheet:* The copper (II) oxide and zinc (II) oxide nanosheets were synthesized hydrothermally based on the methods described in <sup>75,76</sup> with some modifications. The detailed procedure is described in the supporting information.

*Metal Oxide Monolayer and Multilayer Deposition:* Some commercial sensor substrates (glass preprinted with interdigitated gold electrodes, L 22.8 x W 7.6 x H 0.7 mm, bands/gaps 10  $\mu\text{m}$ , Metrohm) were first cleaned with DI water and ethanol, and then soaked in a HCl (36.5-38.0%, Fisher Chemical)-methanol ( $\geq 99.8\%$ , VWR Chemicals) solution (vol. ratio 1:1) for 20 min. Afterward, the substrates were washed again with DI water and ethanol, and dried in nitrogen flow. The as-prepared substrates were loaded on the glass

**Table 4.** Selected works studying 2D metal oxides as gas sensing material, and studies focusing on sensing film morphology based on metal oxides with 0D, 1D, and 3D nanostructures. (l: length of a nanostructure; t: thickness of a nanosheet; d: diameter of a 0D or 1D nanostructure)

Materials	Microstructure description	Target gas	Temperature (°C)	Response (fractional difference)	Deposition method	Film morphology	Ref
NiO	2D mesoporous nanosheet (l: 200 nm, t: 20 nm)	NO <sub>2</sub>	250	0.15-0.8 (2-20 ppm)	Drop-casting	Agglomerates of nanosheets	55
MoO <sub>3</sub>	2D nanosheet (l: 30 nm, t: 1.4 nm)	VOCs	300	4.6-32.4 (100 ppm)	Drop-casting	Agglomerates of nanosheets	57
ZnO	2D mesoporous nanosheet (l: 500 nm, t: 15 nm)	Formaldehyde, ammonia	250	0.6-0.95 (50-200 ppm)	Solvated paste	Thick film	56
ZnO	2D nanosheet (t: 4 nm)	Ethanol	320	0.5-300 (1-2000 ppm)	Solvated paste	Thick film	58
SnO <sub>2</sub>	2D nanosheet (l: 500 nm, t: 30 nm)	Formaldehyde	240	1.9-6 (5-100 ppm)	Solvated paste	Thick film	69
CuO	2D nanosheet with {001} exposed (l: 500 nm, t: 50 nm)	VOCs	150	1-7 (5-1000 ppm)	Solvated paste	Thick film	54
WO <sub>3-x</sub>	1D nanowire (l: 150 nm, d: 1.7 nm)	H <sub>2</sub>	25	0.5-15 (2-100 ppm)	Langmuir-Blodgett trough	Horizontally aligned monolayer	39
Au-WO <sub>3</sub>	1D nanorod (l: 500 nm, d: 50 nm)	H <sub>2</sub>	300	6.6 (50 ppm)	Solvated paste	Thick film	60
$\alpha$ -Fe <sub>2</sub> O <sub>3</sub>	0D nanoparticles (d: 6 nm)	Methanol, Ethanol, propanol	25	1-100 (10-60 ppm)	Langmuir-Blodgett trough	Closely-packed monolayer	30
$\alpha$ -Fe <sub>2</sub> O <sub>3</sub>	0D nanoparticles (d: 20 nm)	Ethanol	225	10 (100 ppm)	Solvated paste	Thick film	77

holder of a simple home-built film coater. The glass beaker (50 mL) was then filled with DI water until the substrates were fully immersed. Ethanol suspension of metal oxide

nanosheets (0.2 g/L) was then added dropwise into the beaker. The volumes of suspension required to obtain monolayer for CuO and ZnO are 2 and 1.3 mL, respectively. Once a monolayer was formed at the air-water interface, the lab jack was raised up at a rate of 5 mm/min until the glass holder was above water level to transfer the monolayer onto the substrates. After drying at room temperature for 30 min, the as-prepared monolayer sensors were annealed in a furnace at 400 °C for 6 h before sensor testing. To prepare the sensors with multilayers of metal oxide nanosheets, roughly 1 mL of more concentrated metal oxide ethanol suspension (2 g/L) were added to the beaker to form CuO multilayer at the interface. To enable continuous build-up of multilayer, a quick annealing treatment at 400 °C for 10 min was adopted after dry. The coating process was repeated multiple times to obtain 5 and 10 µm thick sensing film. The as-prepared multilayer sensors were also annealed at 400 °C for 6 h before testing.

*Synthesis of CuO nanosheets:* In a typical synthesis process, 2.5 mmol copper (II) nitrate hemi(pentahydrate) ( $\text{Cu}(\text{NO}_3)_2 \cdot 2.5\text{H}_2\text{O}$ , 98+%, Alfa Aesar), was first dissolved in 5 ml ethanol (anhydrous, Koptec). The copper nitrate solution was then added into 50 mL of 5 M sodium hydroxide (NaOH, 97+%, Acros Organics) aqueous solution dropwise while stirring. The solution was then sealed in a Teflon-lined stainless-steel autoclave (90 mL capacity). The autoclave was heated and maintained at 100 °C for 24 h. Afterwards, the autoclave was cooled down to room temperature and the precipitates were separated and washed by centrifugation. Finally, the precipitates were dried in a vacuum oven at 70 °C for 12 h.

*Synthesis of ZnO nanosheets:* In a typical experiment, 0.287 g of ZnSO<sub>4</sub> · 4H<sub>2</sub>O, 0.080 g of NaOH, and 0.083 g of NaF were successively added into a mixed solvent of 7 mL of distilled water and 3 mL of ethanol. The resulting mixture was sonicated for several minutes and transferred into a Teflon-lined stainless-steel autoclave with a capacity of about 20 mL. Then the autoclave was heated to 200 °C and held for 24 h. After the mixture was cooled to room temperature, the production was separated by centrifugation from the solution and repeatedly rinsed with distilled water.

*Characterization:* SEM images and EDX spectrum were collected on an AMARY 1910 equipped with an AMETEK EDAX detector at 15 kV. The cross-section samples of the monolayer films were prepared by focused-ion-beam (FIB) milling in a FEI Nova 200 NanoLab. The microstructure of cross-sectioned sample was observed using the scanning electron microscopy in the FIB at 5 kV. TEM, HRTEM, and SAED images were collected on a Philips CM-200-FEG at 200 kV. XRD measurements were performed on a Bruker D8 focus diffractometer using Cu K $\alpha$  radiation ( $\lambda=1.5406 \text{ \AA}$ ) with a step size of 0.02° and a scan rate of 0.6 sec/step. XPS tests were performed on a VG ESCALAB 220i-XL photoelectron spectrometer and Al K $\alpha$  radiation (15 keV) at about  $1.3 \times 10^{-9}$  mbar base pressure. The C (1s) peak is used to calibrate the peak position. Curve fitting of O (1s) spectra was done with a spin-orbit coupling of 2:1 area ratio using CasaXPS software. The same software was used for calculation of the elementary percentage from the recorded spectra. Nitrogen adsorption-desorption isotherms were recorded with a Micromeritics ASAP-2020 at -196 °C. From the adsorption curve, BJH method was applied to calculate the pore size distribution of multilayer film sample, prepared by scraping off the stacked

nanosheets from the substrates. The specific surface area of the powder sample was determined based on Brunauer–Emmett–Teller (BET) method.

*Gas sensing measurements:* A home-built sensing performance evaluation system (**Figure 18**. Schematic of the gas sensor testing system.) was used to evaluate the sensing performance. The sensors first achieved steady-state in the gas chamber at a set temperature with 200 sccm air flow for 30 min. Then the gas stream was switched between air and H<sub>2</sub>S containing air periodically to test the sensing performances at H<sub>2</sub>S concentration ranging from 200 ppb to 10 ppm. The sensing performance at different temperature was evaluated by re-establishing steady-state at a temperature range between 150 and 300 °C. Variation of humidity (0-50 %RH) in air was achieved by flowing dry air through a bubbler, the temperature of which was maintained at 25 °C by a water bath. The humidity in the gas stream coming from the outlet of the bubbler was confirmed to be 100% RH before the test by weighing the trapped water in a condenser tube connected to the bubbler. Sensor signal (S) was defined as the fractional difference between the electrical resistance in air (R<sub>air</sub>) and the electrical resistance in H<sub>2</sub>S containing air (R<sub>gas</sub>), i.e.,  $S = (R_{\text{gas}} - R_{\text{air}}) / R_{\text{air}}$ . The response time and recovery time were defined as the time required to reach 90% of the full response state in mixed gas and 90% of the fully relaxed state in the air, respectively.

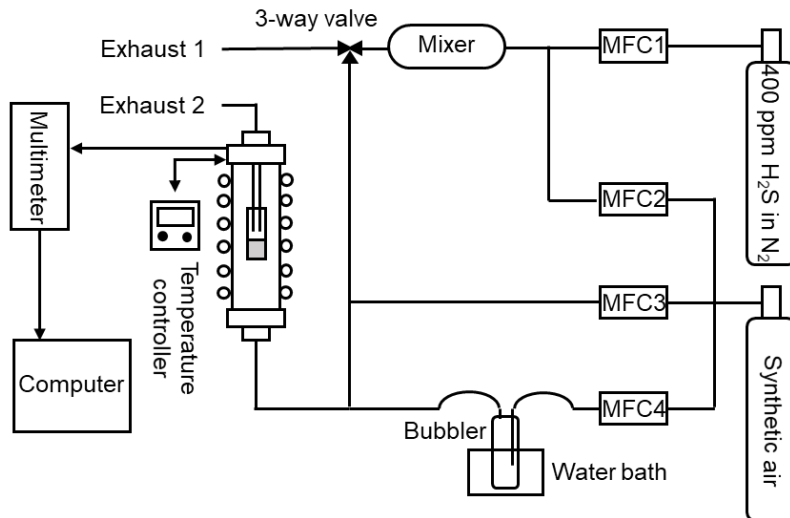


**Figure 18.** Schematic of the gas sensor testing system.

### 3.3 Results and Discussion

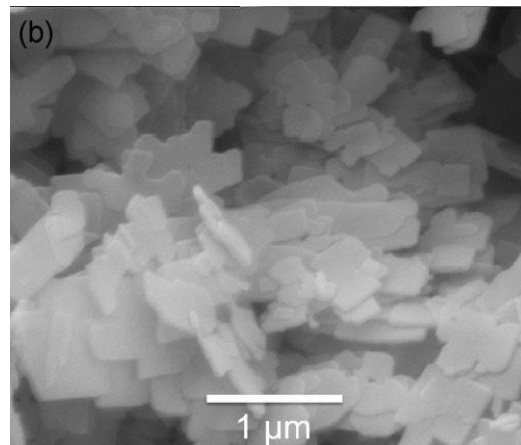
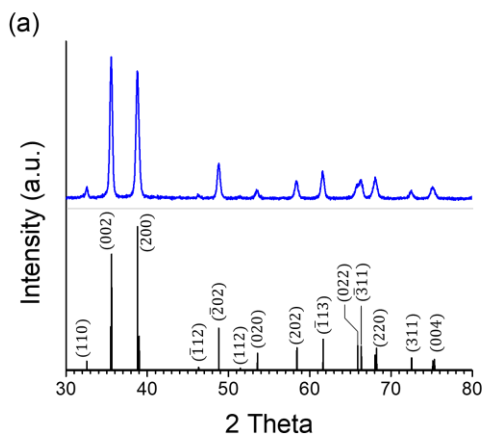
#### 3.3.1 Structure and Surface Properties of CuO Nanosheets

The crystal structure of the as-synthesized CuO powder is characterized with XRD (**Figure 19** (a)). It is found that the as-prepared sample is highly crystalline, and all the diffraction peaks can be indexed as monoclinic tenorite-type CuO (JCPDS: No. 45-0937). No peaks corresponding to impurities are observed, which indicates a complete conversion of the copper salt precursor to CuO. Moreover, the increased amplitude of the peak associated with the (002) plane with respect to the other peaks compared to the standard suggests the high percentage of (002) plane as exposed facet for the CuO nanosheets. The morphology of the as-synthesized powder is examined with SEM. As shown in **Figure 19** (b), the sample takes the shape of nanosheets with length and width ranging from 300 to 1000 nm, and the thickness is around 30 to 50 nm. The irregular shape of the nanosheets is attributed to the formation mechanism, which involves self-assembly of CuO nanorods during hydrothermal treatment.<sup>75</sup> The EDS pattern (**Figure 19** (c)) confirms that the sample



is composed of Cu and O. The C (K $\alpha$ ) and Au (M) peaks are originated from the carbon tape and the Au coating, respectively.

XPS peaks from the wide scan spectrum (**Figure 19** (d)) indicate the presence of Cu, O, and C at a ratio of 30.8:59.6:9.6. Surface contaminations like hydrocarbons and carbonyl compounds from surrounding atmosphere gives rise to the carbon peak, and possibly also responsible for the nonstoichiometry between Cu and O. Another possible reason for the excess of oxygen is that as a p-type semiconductor, excessive oxygen is necessary to induce holes for electrical conduction. The characteristic two main line peaks and the two satellite peaks shown in the high-resolution Cu 2p spectrum (**Figure 19** (e)) confirm that Cu exists in the sample as Cu (II).<sup>78</sup> The asymmetric O 1s spectrum (**Figure 19** (f)) can be deconvoluted into two components, i.e., lattice oxygen (O<sub>L</sub>) at BE=529.5 eV, and chemisorbed oxygen (O<sub>C</sub>) at BE=531.0 eV. The O<sub>C</sub> component accounting for 26.7 at% is usually attributed to chemisorbed and dissociated oxygen species and hydroxyl groups.<sup>75</sup>



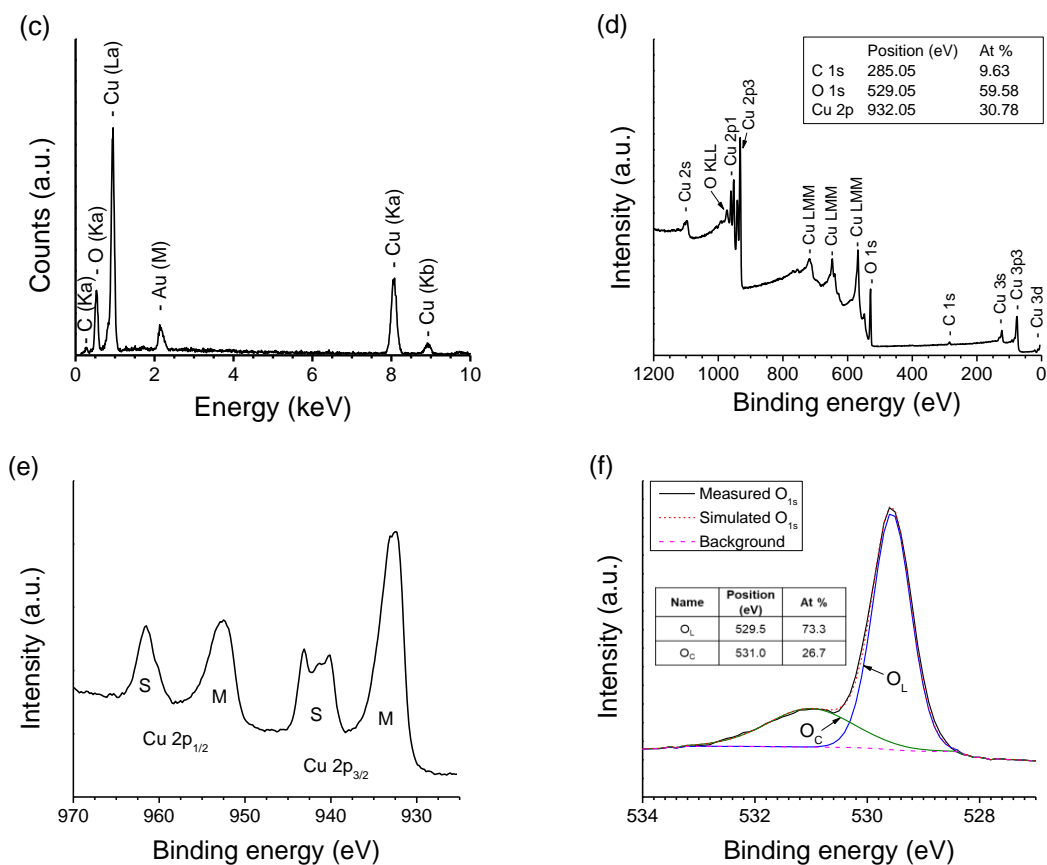


**Figure 19.** (a) XRD pattern, (b) SEM, (c) EDS, (d) XPS wide scan, (e) high resolution Cu 2p, and (f) high resolution O 1s of the as-synthesized CuO nanosheets.

TEM analysis provides more detailed crystallographic and orientational information about the CuO nanosheets. As shown in a typical low magnification TEM image (**Figure 20 (a)**), the CuO nanocrystals are thin enough to appear transparent, and the crystal boundaries are well faceted. The SAED pattern (inset in **Figure 20 (a)**) contains individual diffracting spots, suggesting that the CuO nanosheets are single-crystalline. By indexing the SAED pattern, the zone axis can be identified as [001], indicating that (002) plane is the top/bottom facets exposed for the nanosheets. Moreover, the lattice resolved HRTEM image (**Figure 20 (b)**) directly presents the (110) with 0.27 nm d-spacing, which is one of the crystal planes on zone axis [001]. Therefore, it is confirmed that (002) plane is the

primary exposed facet for the as-synthesized CuO nanosheets. Moreover, the majority of the CuO nanosheets adopt an irregular octagon shape. Measured from the low magnification TEM image (**Figure 20** (a)), the two angles formed between the length (L), the shoulder (S), and the width (W) are around  $126^\circ$  and  $144^\circ$ , for several crystals marked with red dotted lines in the image. Among the low Miller indexed planes with [001] zone axis, the two angles between (110) and (200), and (110) and (020) matches well with the measurements. Therefore, the length, width, and shoulder of the crystals can be indexed as (200), (020), and (110), respectively (inset of **Figure 20** (a)).

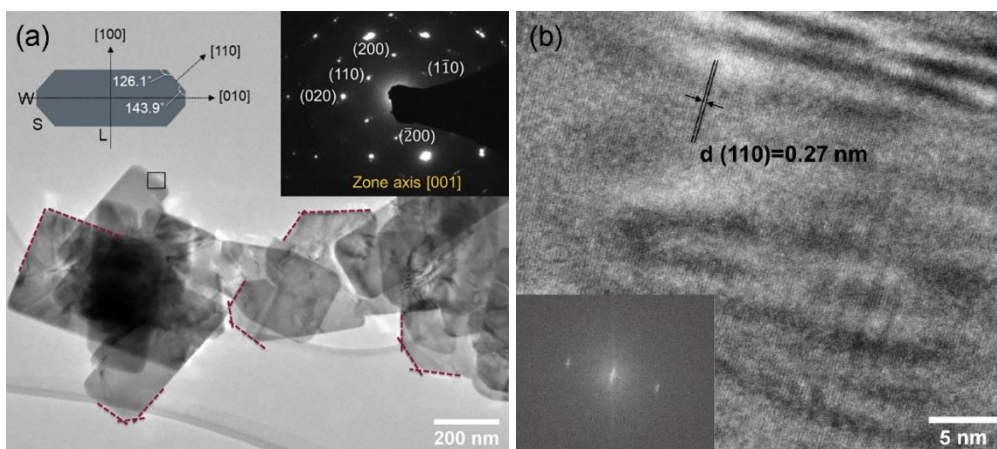
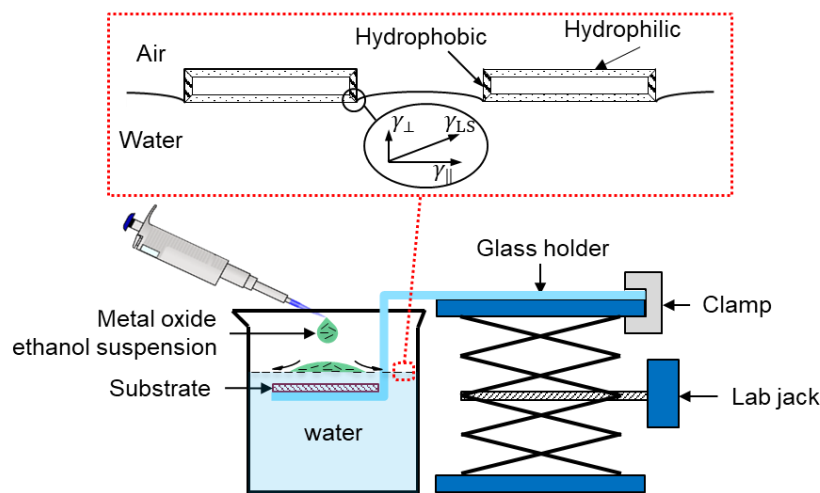


**Figure 20.** (a) Low magnification TEM image of CuO nanosheets and the SAED pattern and a sketch of the crystal orientation in the real space as inset; (b) Lattice resolved HRTEM image and the fast-Fourier-transform (FFT) pattern as inset.

### 3.3.2 Film Formation and Characteristics

The monolayer film formation process is demonstrated in **Figure 21**. When a droplet of ethanol containing CuO nanosheets reaches the water surface, it will first spread across the interface driven by surface tension gradient (Marangoni effect).<sup>79</sup> After the ethanol dissolves into the water, the CuO nanosheets are left scattering evenly at the air-water interface. To explain the floating and self-assembly behaviors of these nanosheets at the

interface, the surface properties of the nanosheets are examined. As illustrated in **Table 5**, all the exposed facets of the as-prepared CuO nanosheets are Tasker type III polar surface, among which the primary exposed facet, (002), possesses surface energy much higher than the other three facets based on DFT calculations.<sup>54,80,81</sup> Therefore, the top/bottom surface of the as-prepared CuO nanosheets should be much more hydrophilic than the edges, which renders the nanosheets amphiphilic. As a result, negative meniscus will form on the three-phase interface at the hydrophobic edges of the nanosheets. The vertical component ( $\gamma_{\perp}$ ) of the surface tension of liquid/solid interface ( $\gamma_{LS}$ ) enables the nanosheets to float at the water surface, while the lateral component ( $\gamma_{\parallel}$ ) pulls the nanosheets together, and hence self-assembly can occur at air-water interface.<sup>82,83</sup>

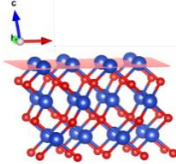
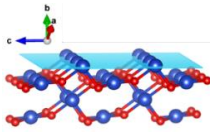
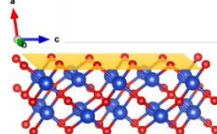
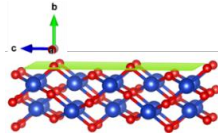


**Figure 21.** Illustration of the monolayer film formation process using the home-built coater; The red box illustrates the CuO nanosheets float on the water surface due to the formation of negative meniscus at the edges, and self-assemble due to the attraction force of same type meniscus.

The monolayer films of CuO nanosheets prepared with the self-assembly method are characterized with SEM and XRD. As shown in **Figure 22** (a), the dark parts of the SEM

image correspond to the glass substrate, which suggests that the nanosheets are loosely-packed possibly due to their irregular shape. The SEM cross-section image of the monolayer sample prepared by FIB shows a single layer of CuO nanosheet on the glass substrate (**Figure 22** (b)). The thickness of the CuO nanosheet is determined to be around 40 nm. The crystal orientation of the monolayer film was characterized with XRD. In **Figure 22** (c), only the diffraction peaks corresponding to (002) and (004) of monoclinic CuO were observed for the monolayer sample. This indicates that the nanosheets of the monolayer film all arrange in a face-up fashion.

**Table 5.** Side view of (002), (110), (200), and (020) crystal planes of CuO and their calculated surface energy.

Surface	(002)	(110)	(200)	(020)
Model				
				● Cu ● O
Surface energy (J·m <sup>-2</sup> )	4.23 <sup>52</sup>	1.00-1.37 <sup>79,84</sup>	1.68-1.83 <sup>52,79</sup>	1.35-1.62 <sup>79,84</sup>

To obtain a monolayer of CuO nanosheet by the self-assembly method, stringent control on the amount of CuO nanosheets added into the water subphase, and the concentration of the CuO ethanol suspension are necessary. The BET surface area for the as-prepared powder is around 6.6 m<sup>2</sup>/g. Considering the area of the water subphase, theoretically 0.4 mg of the as-prepared powder is required to form a monolayer as shown in **Figure 22** (a), while a film with multiple layers of CuO nanosheet was obtained when 2 times of the theoretical amount was added (**Figure 22** (d)). The concentration of the CuO

ethanol suspension is another key factor because it dictates the level of dispersion of CuO. When the concentration of the ethanol suspension is higher than ideal (0.2 g/L), irreversible flocculation of nanosheets is more likely to occur in the suspension, and hence monolayer film becomes hard to achieve. As a result, higher than theoretical amount of powders is required to form a film that can completely cover the water surface when high concentration of ethanol suspension is used (as shown in **Figure 22** (d)), and only multilayer films are obtainable in these cases.

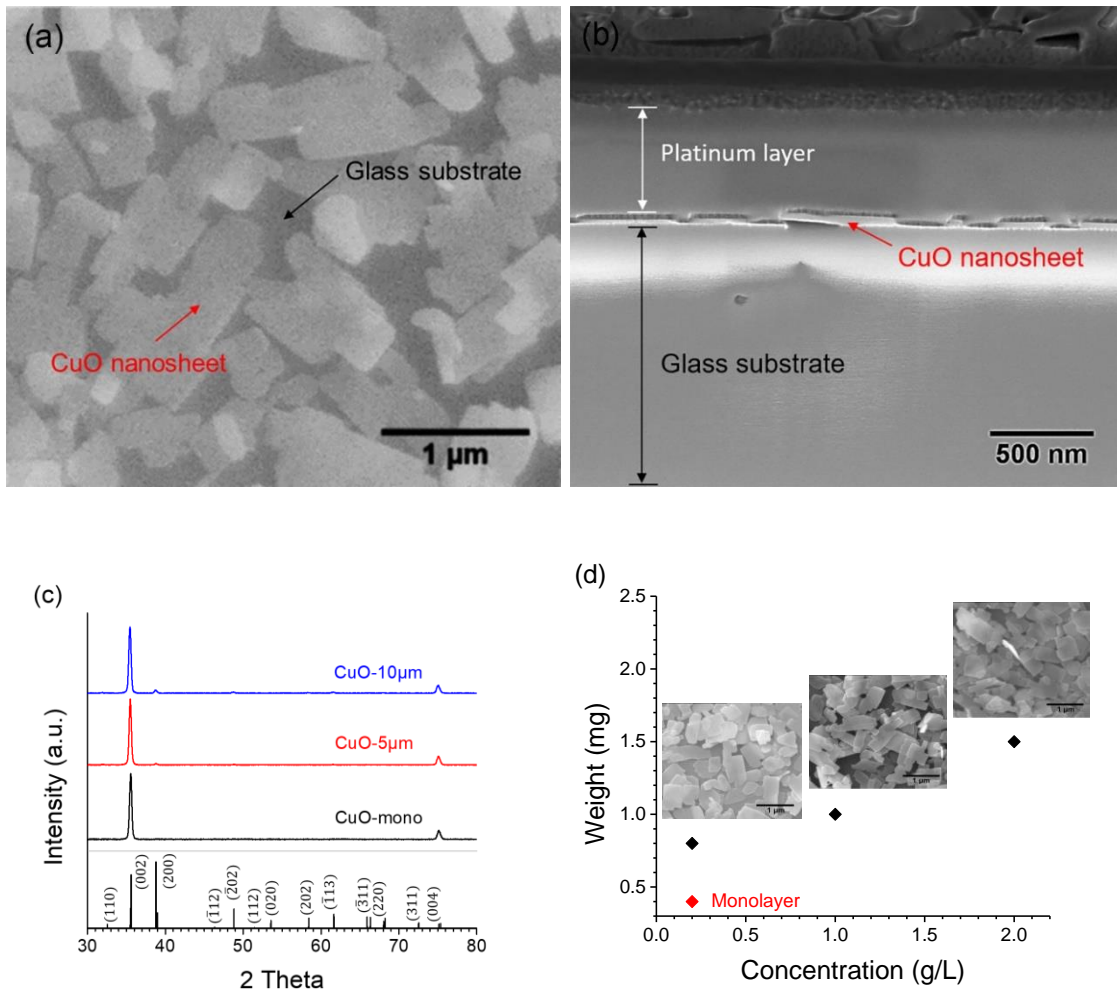


**Figure 22.** (a) Top surface and (b) cross-section SEM image of the CuO nanosheet monolayer on glass substrate; (c) XRD patterns of CuO-mono, CuO-5µm, and CuO-10µm;

(d) Films prepared with higher than ideal addition weight and concentration, and their SEM images.

In addition to monolayer film, CuO nanosheets film with thickness of 5 (CuO-5 $\mu$ m) and 10  $\mu$ m (CuO-10 $\mu$ m) were also prepared by repeating the self-assembly process multiple times. A quick annealing treatment at 400 °C was essential for preventing the detachment of previously deposited layers. The percentage of O<sub>C</sub> decreases from 26.7% to 21.1% after the annealing treatment as revealed by XPS (**Figure 23**). This could be interpreted as the desorption of hydroxyl groups after the annealing process, which leads to some changes in surface hydrophilicity that could lead to the prevention of detachment. The level of orientation of the multilayer films are not as good as that of the monolayer film as suggested by the emergence of peaks other than {001} in the XRD patterns (Figure 36c). The deterioration of orientation is due to the tilting of nanosheets when they rest on uneven surface created by the loosely packed nanosheet layer underneath.

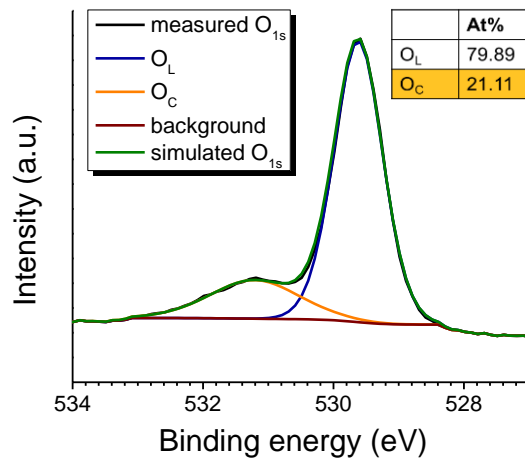


**Figure 23.** High resolution XPS of O 1s of the thermally annealed CuO-nanosheets.

The porous structure of the multilayer films is characterized with SEM and N<sub>2</sub> porosimetry. The top-down SEM image of the multilayer film (**Figure 24** (a)) reveals some

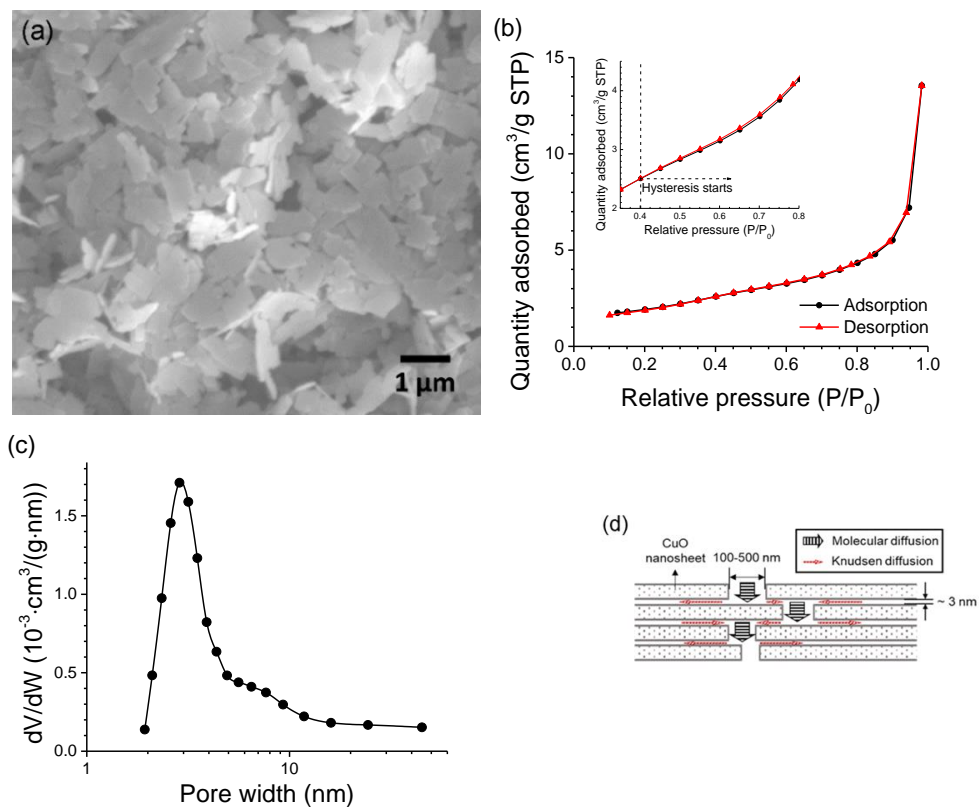


**Figure 24.** (a) SEM top-view of CuO-5 $\mu$ m; (b) Nitrogen adsorption isotherm of the multilayer film; (c) Pore distribution derived from BJH adsorption; (d) Model of a multilayer film with lamellar structure.

macro-pores with the size in the range between 100-500 nm between the nanosheets. On the other hand, the interlayer spacing of the stacked nanosheets needs to be characterized with N<sub>2</sub> porosimetry. The adsorption-desorption isotherm shown in **Figure 24** (b) resembles a typical type III isotherm, with a small hysteresis loop starts at P/P<sub>0</sub> around 0.4 (inset in **Figure 24** (b)), which originates from slit-like pores formed between aggregates of plate-like particles.<sup>85</sup> The pore distribution derived from the BJH adsorption (**Figure 24** (c)) indicates that the interlayer spacing should be around 3 nm. Therefore, the gas transport within the multilayer film should be a combination of molecular diffusion through the macro-pores and Knudsen diffusion through the interlayer spacing between the nanosheets

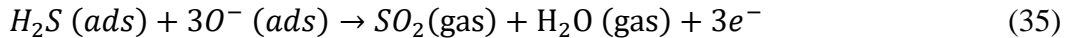


(**Figure 24** (d)), with Knudsen diffusion as the rate-limiting step for an analyte gas to diffuse vertically within the multilayer film.

### 3.3.3 Gas Sensing Performance and Modeling

The change in electrical resistance of the sensor samples in ultra-zero air ( $R_{\text{air}}$ ) was first measured as a function of temperature (**Figure 25** (a)). The variation in resistance between the CuO-mono sensors was very small (~9.5%), indicating high reproducibility of the self-assembly technique in preparing monolayer film with uniform thickness and film structure. For all the samples,  $R_{\text{air}}$  decreases exponentially at similar rate with temperature in the range between 150 and 300 °C, possibly due to the rise in the charge carrier density generated by the ionization of deep acceptors at elevated temperature. Moreover, the electrical resistance in air is inversely proportional to the thickness of the sensing film.

The sensors were first subjected to a cycling test at 250 °C under an atmosphere containing 1 ppm of H<sub>2</sub>S. As shown in **Figure 25** (b), sensor signals with good repeatability are gathered for all the sensors. The sharp increases in electrical resistance are observed for all the sensors when 1 ppm of H<sub>2</sub>S is introduced. The increase in resistance can be explained with the following surface reactions.



The H<sub>2</sub>S adsorbed on the surface of CuO nanosheets is oxidized by the ionosorbed oxygen anions. In the meantime, free electrons as one of the reaction products will be injected into the conduction band of the CuO nanosheet. As a result, some of the free holes, which are the major charge carrier in a p-type semiconductor like CuO, will be nullified by

the injected electrons, which leads to the rise in electrical resistance. When H<sub>2</sub>S containing atmosphere is replaced by air, ionosorbed oxygen will be replenished, which regenerates the nullified holes, and hence the electrical resistance will fall back to the original level. It is noted that the surface conversion of CuO to CuS shouldn't occur in this case, because conversion to CuS should lead to decrease in resistance instead<sup>25,74</sup>. To double confirm this statement, the XRD patterns of CuO film before and after test were compared (**Figure 26**) and no new peaks corresponding to CuS can be observed.

The sensing performances of CuO-mono, CuO-5 $\mu$ m, and CuO-10 $\mu$ m were then evaluated with 1 ppm of H<sub>2</sub>S in the range of temperature between 150 and 300 °C (**Figure 25** (c)). Improvements on both sensitivity and response and recovery rates are observed for the CuO nanosheet sensor with monolayer film configuration. The sensor signal (S) of CuO-mono to 1 ppm of H<sub>2</sub>S is notably higher than CuO-5 $\mu$ m and CuO-10 $\mu$ m in the whole range of testing temperature, especially at temperature  $\leq 250$  °C. To be specific, at 175 °C, CuO-mono reaches a maximum response of 378%, which is about 2 and 12 times as large as those of CuO-5 $\mu$ m and CuO-10 $\mu$ m, respectively. At temperature  $> 175$  °C, the response to 1 ppm H<sub>2</sub>S gradually decreases with temperature for CuO-mono. When temperature increases, the volume of oxygen adsorbed on the surface of CuO nanosheets decreases, while the charge carrier density increases because of the ionization of deep acceptors. The combination of these two effects leads to a thinner hole accumulation layer at the surface of CuO nanosheet, and hence the CuO-mono becomes less responsive to H<sub>2</sub>S.

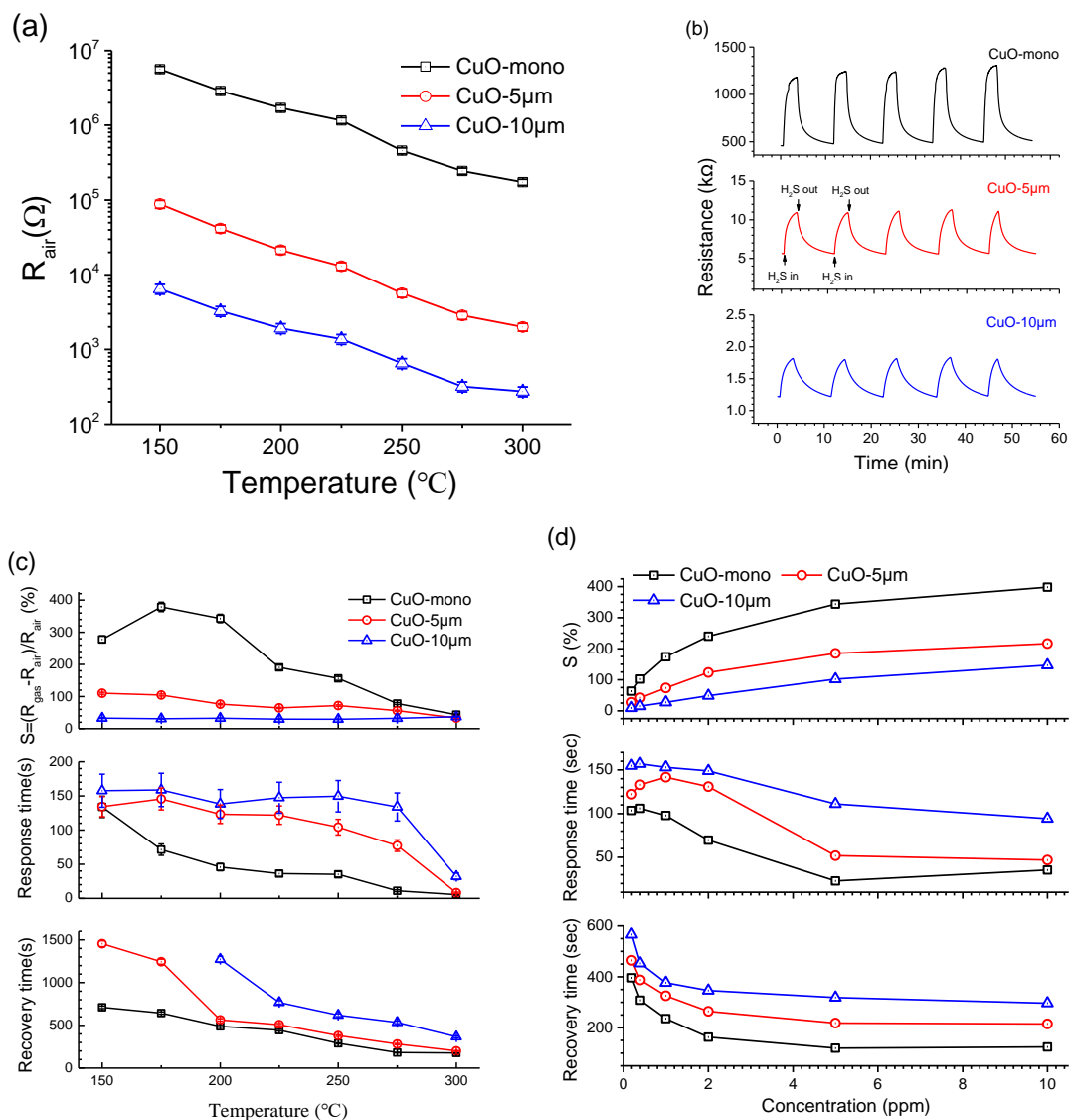


**Figure 25.** (a) Resistance value in air ( $R_{\text{air}}$ ) as a function of temperature; (b) Repeated transient response test at 250  $^{\circ}\text{C}$  in 1 ppm  $\text{H}_2\text{S}$ ; Sensor response ( $S$ ), response time, and recovery time as a function of (c) temperature and (d) concentration.

For CuO-5 $\mu\text{m}$  and CuO-10 $\mu\text{m}$ , their maximum responses seem to be at temperatures (< 150  $^{\circ}\text{C}$ ) lower than that of CuO-mono (175  $^{\circ}\text{C}$ ). This phenomenon could be attributed to the slower diffusion of  $\text{H}_2\text{S}$  in the multilayer film due to the tight interlayer spacing, which leads to severer analyte dilution within the multilayer film than the monolayer film, and

hence the sensor response of the multilayer films starts to decrease at temperature lower than that of the monolayer film. The response and recovery times of CuO-mono are much shorter than those of CuO-5 $\mu$ m and CuO-10 $\mu$ m. For identical sensing material, the common dictating factors for the transient response properties of a semiconductor gas sensor including the rates of adsorption/desorption of gases (i.e. oxygen, analyte gas, and reaction products), surface reaction, and charge transport, should remain the same. Therefore, the slow response and recovery speed of the multilayer samples should be attributed to the slow Knudsen diffusion of H<sub>2</sub>S within the mesopores of multilayer film, and the fast surface reaction that consumes H<sub>2</sub>S. As a result, the time required to achieve the steady state gas concentration profile, and in turn, to reach leveled sensor resistance will be long for the multilayer films.<sup>66,67</sup> In comparison, gas diffusion should not be a limiting factor for monolayer film because mesopores presented in the multilayer films are not present, and hence the response and recovery times of the monolayer film are shorter. The decrease in response and recovery time with increasing temperature is observed for all the sensors. This can be explained by that the steady state can be established much faster at elevated temperature because of the faster diffusion and reaction rate.

**Figure 25** (d) shows sensing performance of the CuO films at different H<sub>2</sub>S concentration and temperatures, with the raw transient response curves measured at 250 °C with the H<sub>2</sub>S concentration between 0.2-10 ppm illustrated in **Figure 27**. The response and recovery time of CuO-mono are the shortest among the sensors with different thickness, which could be attributed to the higher diffusion rate. The response and recovery time also decrease with increasing H<sub>2</sub>S concentration. A probable explanation is that the driving forces for the gas diffusion and reaction are larger at higher concentration, and hence the

time required to reach steady state is shorter. The sensor signal changes with H<sub>2</sub>S concentration in an exponential decay fashion: S increases very rapidly at first at lower concentration, and then level off to become asymptotic to a certain upper limit. The correlations between response and concentration for the multilayer samples are similar to those of CuO-mono, while the magnitude of the response is much smaller than CuO-mono in the whole concentration range.

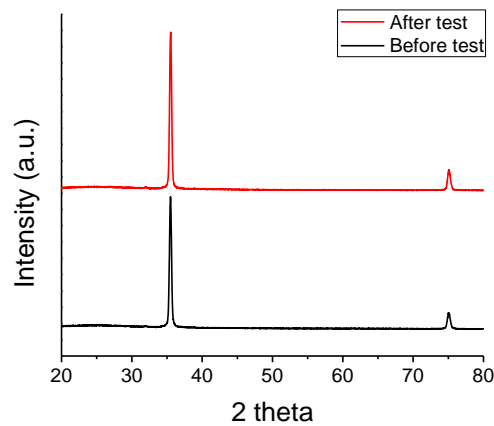


**Figure 26.** XRD patterns of CuO-5µm before and after treated in gas chamber at 250 °C with air flow containing 1 ppm of H<sub>2</sub>S.

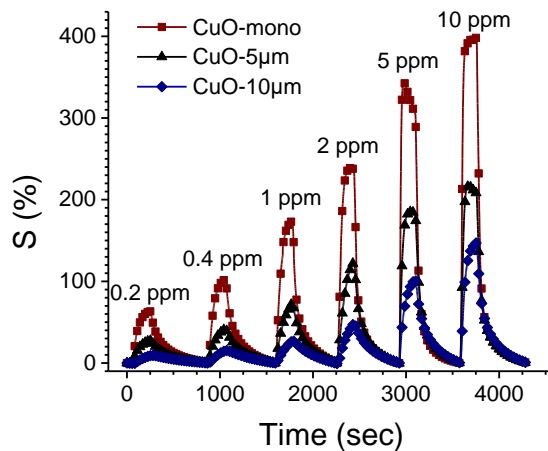
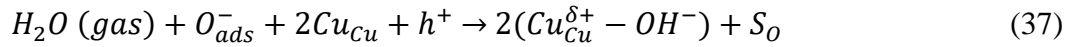


**Figure 27.** Transient response curve to varied concentration of H<sub>2</sub>S collected at 250 °C.

The humidity effect on the performance of CuO sensors was also evaluated. **Figure 28** (a) shows that the baseline resistances of the sensors with three different thicknesses all increase with humidity. This is attributed to the formation of terminal hydroxyl groups, which consumes free holes in CuO, and in turn causes the increase of baseline resistance. This surface reaction is described by the following equation.<sup>86</sup>



where  $S_o$  is a surface site for chemisorption of oxygen. Despite the changes in baseline resistance, none of the three sensors show notable change in sensor response (S) when humidity was varied between 0-50% RH as shown in **Figure 28** (b). This immunity to humidity variation is very beneficial for practical application.

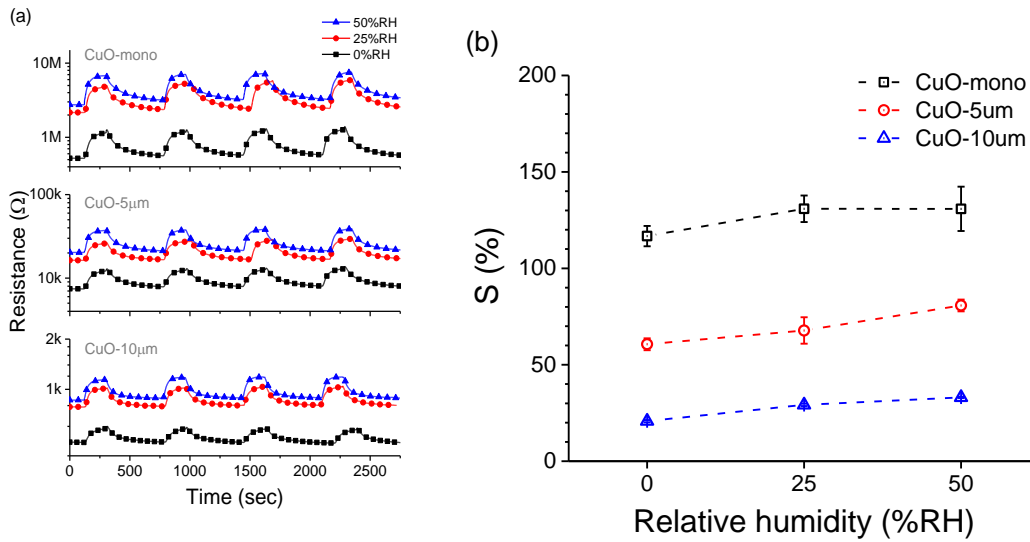


**Figure 28.** (a) Transient response to 1 ppm of H<sub>2</sub>S at 250 °C in wet and dry air; (b) Sensor responses to 1 ppm of H<sub>2</sub>S at 250 °C as a function of relative humidity.

In comparison to the CuO based H<sub>2</sub>S sensors reported in the literature (**Table 6**), the monolayer film of CuO nanosheet sensor proposed in this work shows low detection limit,

fast response and recovery speed at moderate working temperature. In addition, the small influence of humidity on the sensor signal makes the sensor more suitable for practical application. Further enhancement on sensor performance could be achieved by decreasing the thickness of CuO nanosheet, and doping with noble metals and other metal oxides. However, the excellent overall sensor performance displayed in this work can already make a strong case of the advantages of monolayer film configuration for semiconductor gas sensors.

Higher sensitivity is observed for the monolayer film across the whole range of testing temperatures and concentrations. An intuitive explanation for the sensitivity improvement can be provided by the steady-state solution of a coupled diffusion-reaction equation

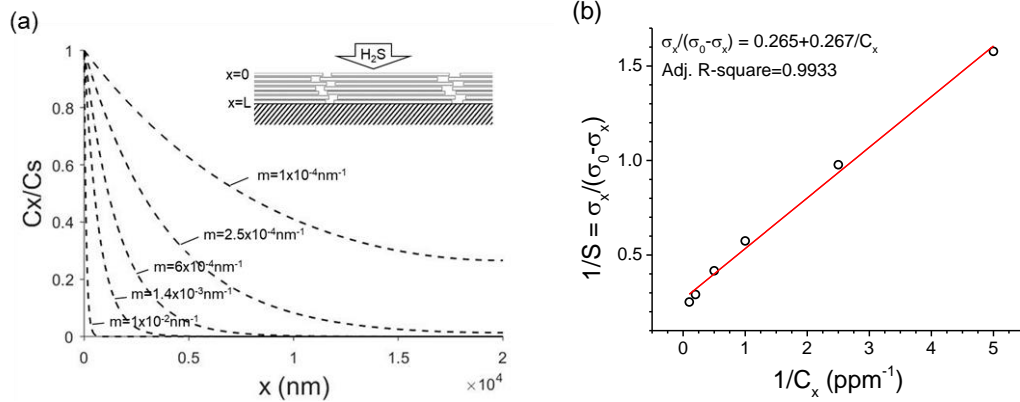
**Table 6.** Comparison of the sensing performance of CuO sensors to H<sub>2</sub>S.

Materials	Temperature (°C)	Detection limit*	Response & recovery time	Humidity effect	Ref
CuO nanosheet monolayer	250	200 ppb	20 sec / 120 sec	10% increase in S at 50 % RH	This work
Porous CuO nanosheet	240	30 ppb	5 sec / 10 sec	30% decrease in S at 50% RH	87
Suspended CuO nanowires	325	10 ppb	800 sec / 1000 sec	25% increase in S at 50% RH	88
CuO nanorod	300	20 ppm	200 sec / 600 sec		89
CuO nanowire	160	500 ppb	100 sec / $\infty$ (>5 ppm)		74
CuO nanoparticles	80	10 ppm	180 sec / 150 sec		90
Porous CuO nanosheet	25	10 ppb	300 sec / 600 sec		91
Flower-like CuO	25	100 ppb	240 sec / 1300 sec		92

\*lowest concentration tested in the literature

$$\frac{\partial C_x}{\partial t} = D_K * \frac{\partial^2 C_x}{\partial x^2} - k * C_x \quad (38)$$

where  $x$  is the distance from the top surface of the sensing film,  $C_x$  is the concentration of  $H_2S$  at depth  $x$ ,  $D_K$  Knudsen diffusion coefficient,  $k$  is the reaction rate constant, and  $t$  is time. As illustrated in **Figure 29** (a), at steady state ( $\frac{\partial C_x}{\partial t} = 0$ ), a concentration gradient will develop within the sensing film due to the consumption of analyte gas by the surface reaction. As a result, the sensor signal of a thick film will be lower than that of a monolayer film, because the analyte gas concentration at the inner part of the thick film is much smaller than that in the surrounding atmosphere. The steepness of the concentration drop is determined by  $m = \sqrt{\frac{k}{D_k}}$ , which is a term pre-determined by the analyte gas and the sensor.





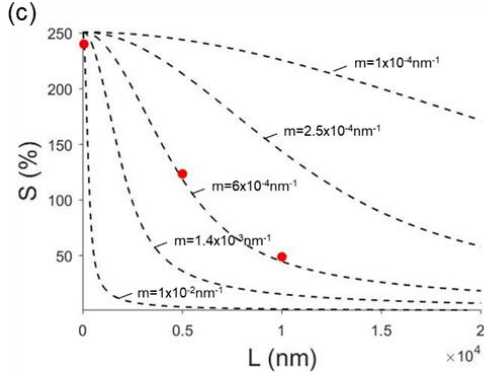


**Figure 29.** (a) Concentration gradient within the sensing film based on the coupled diffusion-reaction equation, with a 1D model of multilayer film sensor as inset; (b) Linear fit of  $1/S$  vs.  $1/C_x$  based on the Langmuir adsorption assumption; (c) Simulated curve of sensor signal as a function of film thickness, with experimental data points obtained under 2 ppm  $H_2S$ .

However, to verify this theory in sensing film prepared from 2D nanostructure, a correlation between the measurable sensor signal and the proposed concentration gradient needs to be built. Unlike the linear relationship proposed by Yamazoe et al<sup>62,67</sup>, the CuO nanosheet sensors show non-linear correlation between sensor signal and  $H_2S$  concentration. Assuming uniform  $H_2S$  concentration in the CuO monolayer film, and Langmuir adsorption as the adsorption model for  $H_2S$  on the surface of CuO nanosheets, the following correlation between the conductivity and the concentration is established

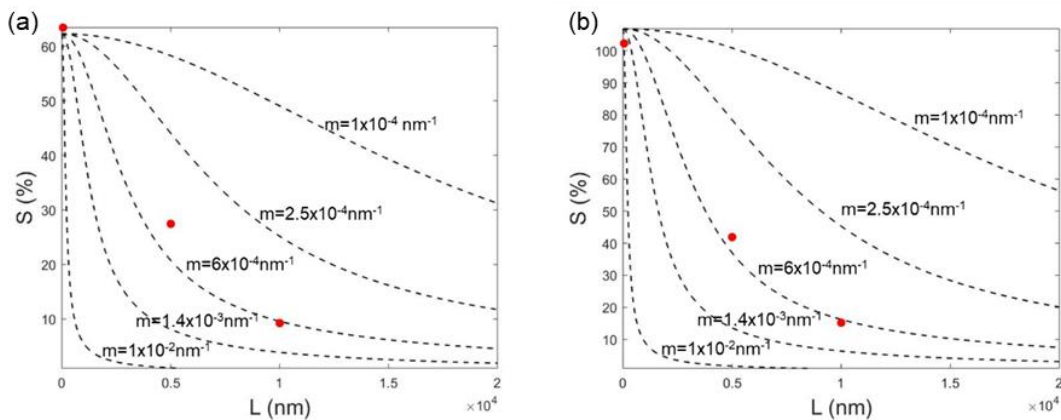
$$S = \frac{\sigma_0 - \sigma_x}{\sigma_x} = c * \theta_x = \frac{c * K_{ads} * C_x}{1 + K_{ads} * C_x} \quad (39)$$

where  $\sigma_0$  is the conductivity of the sensing film in air,  $\sigma_x$  is the conductivity of the sensing film at depth  $x$ ,  $\theta_x$  is the fractional occupancy of the adsorption sites for  $H_2S$  on the CuO surface,  $c$  is a constant defined as sensor response coefficient, and  $K_{ads}$  is the adsorption coefficient. Well-fitting between the experimental data based on eq. 5 is obtained as shown in **Figure 29** (b). And based on the fitting result, the sensor signal of multilayer films,

which have concentration gradients within, can be plotted against sensor film thickness  $L$ , by solving the following equation numerically,

$$S = \frac{\sigma_0 * L}{\int_0^L \sigma_x dx} - 1 \quad (40)$$

The simulation curves with different  $m$  value ( $m = \sqrt{\frac{k}{DK}}$ ) are plotted for the concentration range between 0.2 ppm and 10 ppm (**Figure 29** (c) and **Figure 30**). The corresponding data gathered from CuO-mono, CuO-5 $\mu$ m, and CuO-10 $\mu$ m at 250 °C were plotted on top of the curve. Good fitting was obtained when  $m = 6 \times 10^{-4} \text{ nm}^{-1}$  for all the concentrations, which confirms the validity of the reaction-coupled diffusion theory for sensing films prepared from 2D nanostructure. It is also noted that the interfacial interaction between adjacent layers should be negligible, because the analyte gas concentration differences between layers are too small to cause any notable variation in conductivity (**Figure 31**). Therefore, it is not considered in this model.



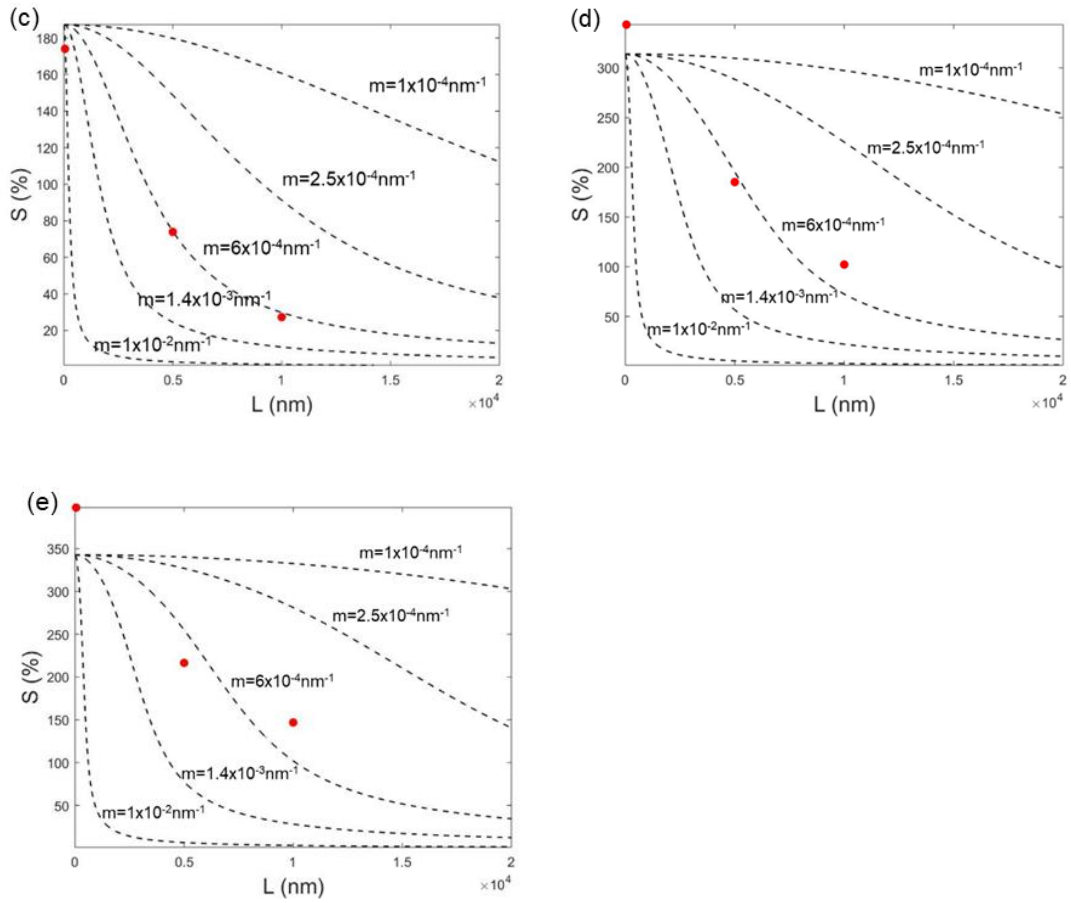


**Figure 30.** Simulated curve of sensor signal as a function of film thickness, with experimental data points obtained under (a) 0.2 ppm, (b) 0.4 ppm, (c) 1 ppm, (d) 5 ppm, (e) 10 ppm of  $H_2S$ .

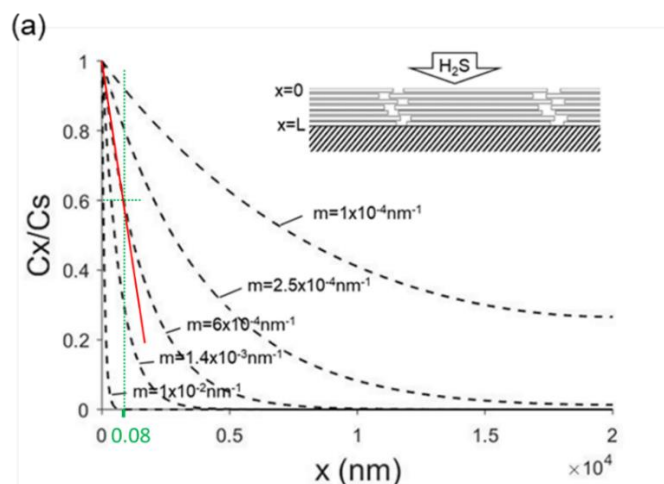


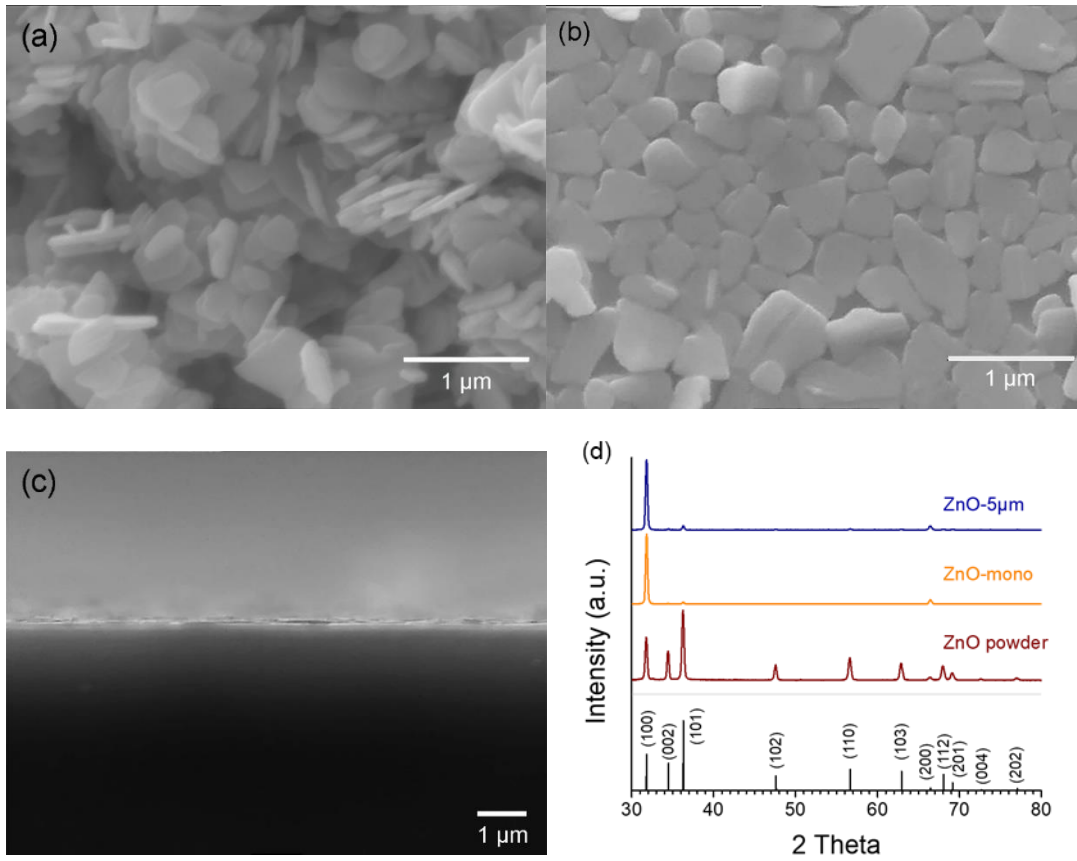
**Figure 31.** Concentration gradient within the sensing film based on the coupled diffusion-reaction equation, with a 1D model of multilayer film sensor as inset.

### 3.3.4 Monolayer Film of ZnO Nanosheets as H<sub>2</sub> Sensor

To demonstrate the versatility of the self-assembly method, ZnO nanosheets, which are 300-1000 nm in diameter and 50 nm in thickness (**Figure 32** (a)), were also synthesized and prepared into monolayer film by dispersing the ZnO-containing ethanol suspension on water surface. The ZnO monolayer film is more densely-packed than the CuO one as shown in **Figure 32** (b), possibly due to the more regular shape of the ZnO nanosheets. The quality of the monolayer film was further confirmed by the cross-section SEM and XRD (**Figure 32** (c, d)). The XRD patterns also reveal that (100), a non-polar crystal plane, is the major exposed surface for the ZnO nanosheets. This phenomenon implies that metal oxide nanosheets with either hydrophobic (i.e. ZnO) or hydrophilic (i.e. CuO) major exposed surface can all float and self-assemble at water surface.

Preliminary H<sub>2</sub> sensing data gathered from ZnO-mono and ZnO-5 $\mu$ m sensors exhibits the same dependency of sensing properties on film thickness as that of CuO H<sub>2</sub>S sensors (**Figure 31e**). To be specific, the sensor signal to 10 ppm H<sub>2</sub> of ZnO-mono is around 100%,

while less than half of that signal is achieved by ZnO-5 $\mu$ m. The response transient performance of ZnO-mono is also superior to ZnO-5 $\mu$ m. The response and recovery times for ZnO-mono are 14.6 and 12.0 sec, respectively, while for ZnO-5 $\mu$ m, the values are 31.9 and 18.2 sec, respectively.



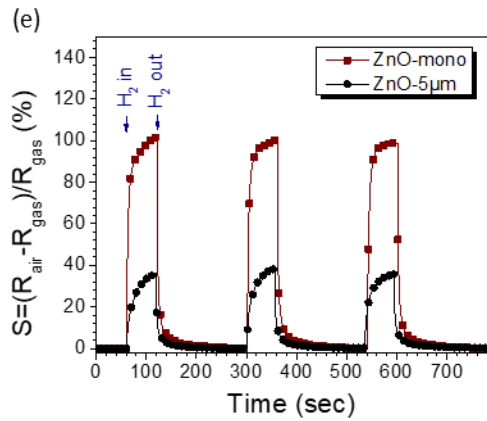


**Figure 32.** SEM images of (a) ZnO nanosheets with length of 300-1000 nm and thickness of 50 nm; (b) top view of ZnO monolayer film; (c) cross-section view of ZnO monolayer film; (d) XRD patterns of ZnO powder, ZnO-mono (with (100) as exposed crystal plane), and ZnO-5 $\mu$ m; (e) The sensor signals of ZnO-mono and ZnO-5 $\mu$ m sensors to 10 ppm H<sub>2</sub> at 250 °C.

## 4. HUMIDITY INDEPENDENT HYDROGEN SULFIDE SENSING RESPONSE ACHIEVED WITH MONOLAYER FILM OF CUO NANOSHEETS

### 4.1 Introduction

Hydrogen sulfide ( $\text{H}_2\text{S}$ ) is a colorless, flammable, poisonous gas. Although  $\text{H}_2\text{S}$  can be found in natural sources, such as hot springs, natural gas, and foods, the majority of the emission is attributed to modern industries, such as electric power plants, oil/gas drilling and refining, and paper mills<sup>1,2</sup>. The  $\text{H}_2\text{S}$  concentration in the close vicinity of these  $\text{H}_2\text{S}$  generating sites must be closely monitored for health and safety considerations. In fact, exposure to 1000-2000 parts per million (ppm) of  $\text{H}_2\text{S}$  for several seconds could lead to unconsciousness and sometimes death from respiratory failure<sup>3</sup>. Even low concentration of  $\text{H}_2\text{S}$  (5-50 ppm) could damage the respiratory, central nervous, and cardiovascular systems, if the exposure is long term and repeated<sup>4</sup>. Moreover, monitoring  $\text{H}_2\text{S}$  concentration is also of great importance to breath analysis, a noninvasive, convenient, and rapid health monitoring and disease diagnosis tool. Among the more than 250 chemicals found in human breath<sup>5</sup>,  $\text{H}_2\text{S}$  in exhaled breath ( $\leq 1$  ppm) has been widely regarded as a biomarker for halitosis<sup>6</sup>, and some recent studies have also found its correlations with asthma<sup>7,8</sup> and SIBO (small intestinal bacterial overgrowth)<sup>9</sup>.

Therefore, great demands for the sensitive and reliable detection of ppm- and sub-ppm-level airborne  $\text{H}_2\text{S}$  exist in both environmental monitoring and medical diagnosis. Conductometric gas sensors based on semiconducting metal oxides possess high sensitivities towards a wide range of reducing/oxidizing gases, and a simple device configuration, which permits facile integration of gas sensors or sensor arrays into a small

and cost-effective device. However, the reliability of conductometric gas sensors often suffers in the presence of water vapor, the concentration of which in the air (e.g. of a H<sub>2</sub>S-generating chemical plant or from a human breath) could be higher than the analyte gas by 3 to 5 orders of magnitude, and extremely varied depending on the weather or the condition of the human test subject.

The mechanism behind the humidity interference on the sensing behavior of semiconducting-metal-oxide-based conductometric gas sensors has been discussed in several studies<sup>10-12</sup>. The evidences obtained from spectrometry and work function studies suggest that a competition of reaction with the receptors of the gas sensors, i.e. pre-adsorbed oxygen anions, exists between atmospheric water vapor and analyte gases. The products of the water-oxygen anions reaction, i.e. the hydroxyl groups adsorbed on the sensor surface, are often less reactive to analyte gases than oxygen anions, and as a result, passivate the sensor surface.

Kim et al. in 2011 proposed a countermeasure strategy to combat the humidity effect by decorating the surface of SnO<sub>2</sub> (the most commonly used sensor material) with NiO nanoparticles<sup>13</sup>. Attributed to the high water affinity of NiO<sup>14</sup>, they discovered that hydroxyl groups predominantly formed on NiO, which effectively serves as an adsorbent to keep the surrounding sensing surface (i.e. SnO<sub>2</sub>) dry and reactive in humid condition. Based on this strategy, Choi et al.<sup>15</sup> and Annanouch et al.<sup>16</sup> have used CuO as surface decorating agents, which possesses water affinity similar to that of NiO, and successfully alleviated the humidity effect on SnO<sub>2</sub> and WO<sub>3</sub> based H<sub>2</sub>S sensors, respectively. However, maintaining the same level of sensitivity under highly humid environment for prolonged



period could be challenging for the strategy proposed by Kim et al. due to the potential risk of running out of adsorption sites on the surface decorating agents. Moreover, the surface decorating agents could have complicated influences on the sensing behavior of sensing material both electronically and catalytically, which could be detrimental in some cases<sup>13,17</sup>. Finally, stringent control on the size and distribution of surface decorating agents is often required to achieve humidity independency<sup>18</sup>, which poses serious challenges on fabrication.

A different strategy to prevent humidity interference in H<sub>2</sub>S sensing could be established if the as-formed surface hydroxyl groups are not as inert to the analyte gas as suggested by the previous studies<sup>10-12</sup>. In fact, hydroxides of several transition metals, including Cu<sup>19,20</sup>, Fe<sup>21,22</sup>, and Mn<sup>23</sup>, have been investigated as desulfurization catalysts for eliminating H<sub>2</sub>S in waste gas streams or natural gases. In the desulfurization process, the hydroxides are converted to metal sulfides by reacting with H<sub>2</sub>S. Therefore, the surface hydroxyl groups on the oxides of these transition metals could promote the formation of the corresponding metal sulfides on the surface of the oxides. If the sulfides possess conductivity different from those of the oxides, the reaction could lead to changes in sensing film resistance, and in turn, compensate the loss in sensor response in humid condition due to the decreasing concentration of adsorbed oxygen anions. Among the oxides of these transition metals, only CuO, a p-type semiconductor with a band gap of 1.4±0.3 eV<sup>24</sup>, has been widely investigated as a gas sensing material. The electrical properties of copper sulfides species, depending on the sulfur content, can be either metallic (i.e. CuS<sup>24</sup>) or highly resistive (i.e. Cu<sub>2-x</sub>S<sup>25</sup>). Thus, H<sub>2</sub>S sensor based on CuO can potentially maintain the same level of H<sub>2</sub>S sensitivity in humid environment, because the

reaction between hydroxyl groups and H<sub>2</sub>S could generate resistance-altering copper sulfide shell on the surface of CuO.

The H<sub>2</sub>S sensing performance data of CuO sensor in dry and wet condition has been reported by several groups<sup>26,27</sup>. Zhang et al. reported that the sensing response towards H<sub>2</sub>S of their porous CuO nanosheet sensor decreases linearly with relative humidity<sup>26</sup>, while the opposite trend was observed in Steinhauer et al. in their study based on CuO nanowire based sensing device<sup>27</sup>. The discrepancy in the findings signaled the complexity nature of the cross-sensitivity of water vapor on CuO sensor, which not only could be determined by the surface reactions, but also could depend on the structure of sensing material, and the configuration of the sensing film. Without a fundamental study based on spectrometric or work function evidence, the exact mechanism of H<sub>2</sub>S sensing in humid environment with CuO sensor is still debatable. Moreover, there has been no report on CuO sensors with H<sub>2</sub>S sensing performance independent of humidity.

In this work, we report an unprecedented humidity independent H<sub>2</sub>S sensing performance achieved with a monolayer film of CuO nanosheets fabricated by the novel self-assembly technique reported in our previous study<sup>28</sup>. In addition to the immunity to humidity effect, the sensor also shows excellent sensitivity (detection limit 3 ppb) and high selectivity to H<sub>2</sub>S, which promotes its application in real-world application such as environment monitoring or breath analysis. Moreover, we have designed extensive studies to reveal the H<sub>2</sub>S sensing mechanisms in dry and humid environment based on sensing phenomena as well as with X-ray photoelectron spectroscopy and scanning electron microscopy.

## 4.2 Material and Methods

*Sensor preparation:* The sensing material, CuO nanosheet, was prepared by a hydrothermal method. A self-assembly technique was used to deposit monolayer film of the sensing material on some commercial sensor substrates (glass preprinted with interdigitated gold electrodes, bands/gaps 10  $\mu\text{m}$ , Metrohm). The monolayer sensor (CuO-mono) thus formed was annealed at 400°C for 6h before performance evaluation. Some sensors with multilayer of CuO nanosheets as sensing film (CuO-0.5 $\mu\text{m}$  and CuO-10 $\mu\text{m}$ ) were also prepared as reference. The detailed procedures for material synthesis and sensing film deposition were described in our previous work<sup>28</sup>.

*Sensing performance evaluation:* A home-built sensing performance evaluation system described in<sup>28,29</sup> was used to evaluate the sensing performance. The sensors first achieved steady-state in the gas chamber at a set temperature with 200 sccm air flow for 30 min. Then the gas stream was switched between air and H<sub>2</sub>S containing air periodically to test the sensing performances at H<sub>2</sub>S concentration ranging from 200 ppb to 5 ppb. Variations of humidity (0-80 %RH) in air and the introduction of three VOCs (ethanol, acetone, and toluene) into the gas stream were achieved by flowing dry air through a bubbler, the temperature of which was maintained at 25 °C by a water bath. Sensor response (S) was defined as the fractional difference between the electrical resistance in air ( $R_{\text{air}}$ ) and the electrical resistance in H<sub>2</sub>S containing air ( $R_{\text{gas}}$ ), i.e.,  $S = R_{\text{gas}}/R_{\text{air}}$ . The response time and recovery time were defined as the time required to reach 90% of the full response state in mixed gas and 90% of the fully relaxed state in the air, respectively.

*Characterization:* SEM images were collected on an AMARY 1910 at 15 kV. XRD measurements were performed on a Bruker D8 focus diffractometer using Cu K $\alpha$  radiation ( $\lambda=1.5406 \text{ \AA}$ ) with a step size of  $0.02^\circ$  and a scan rate of 0.6 sec/step. XPS tests were performed on a VG ESCALAB 220i-XL photoelectron spectrometer and Al K $\alpha$  radiation (15 keV) at about  $1.3 \times 10^{-9}$  mbar base pressure. The C (1s) peak is used to calibrate the peak position. Curve fitting of O (1s) spectra was done with a spin-orbit coupling of 2:1 area ratio using CasaXPS software. The same software was used for calculation of the elementary percentage from the recorded spectra. To prepare the samples for XPS, multilayer films (thickness~0.5  $\mu\text{m}$ ) of CuO nanosheets instead of monolayer were deposited on glass slides in order to avoid interference signals from the glass substrate. The samples were first annealed at 400  $^\circ\text{C}$  for 6 h. Afterwards, the samples were treated in conditions that simulate H<sub>2</sub>S sensing in dry/humid condition.

## 4.2 Results and Discussion

### 4.2.1 Sensing Performance

The CuO nanosheets with length and width ranging from 300 to 1000 nm, and with thickness around 30 to 50 nm (**Figure 33** (a-b)) were self-assembled into monolayer film on water-gas interface, which was then transferred onto the interdigitated electrodes to fabricate the 2D CuO monolayer sensor device (**Figure 33** (c)). As revealed by X-ray diffraction (**Figure 33** (d)), the CuO nanosheet powder is pure and highly crystalline, and all the diffraction peaks can be indexed as monoclinic tenorite type CuO (JCPDS: No. 45-0937). For the monolayer film, only the diffraction peaks corresponding to (002) and (004)

of monoclinic CuO were observed, which indicates that the nanosheets of the monolayer film all arrange in a face-up fashion.

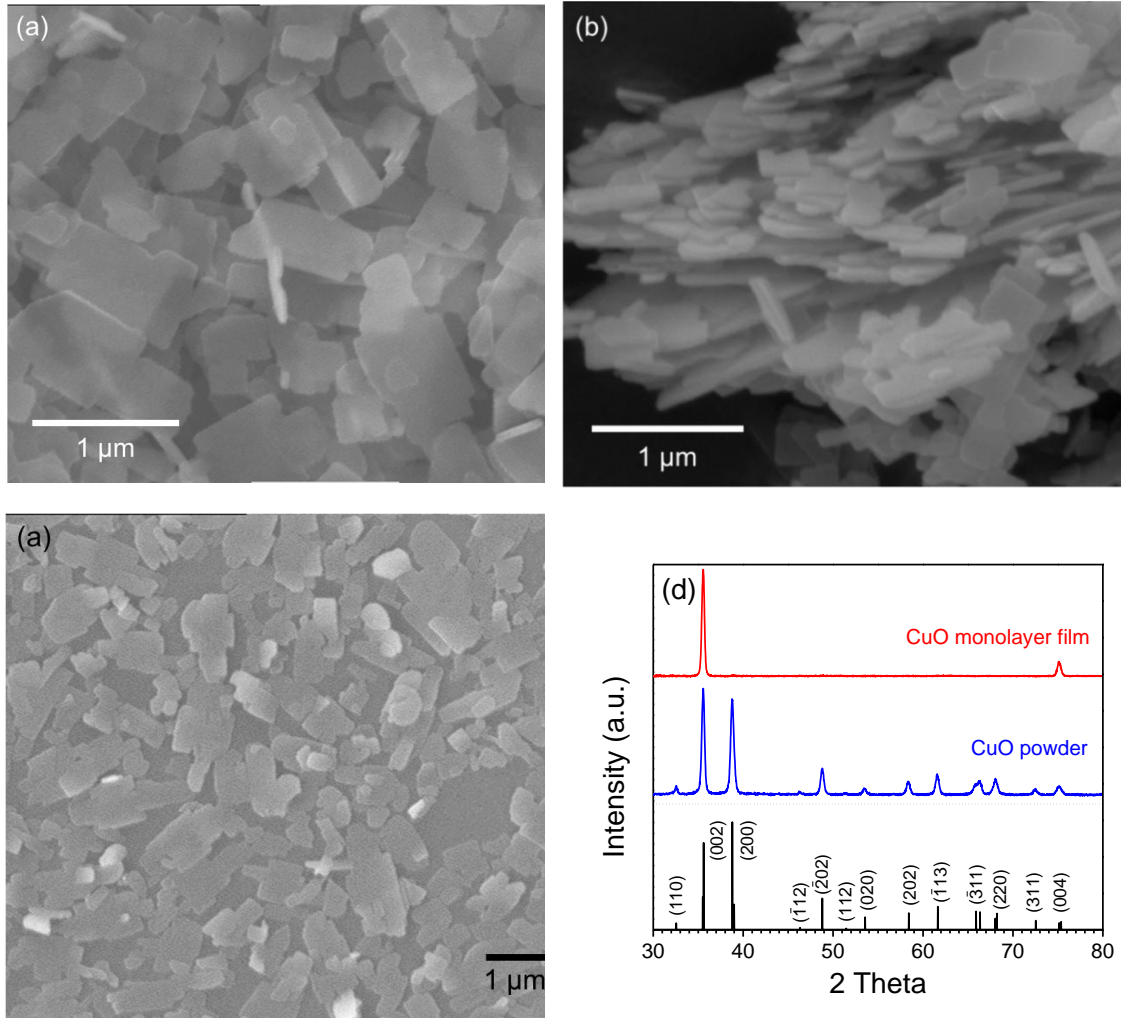


**Figure 33.** SEM images of (a-b) CuO nanosheet and (c) CuO nanosheet monolayer; (d) XRD patterns of CuO nanosheet powder and monolayer film.

The sensing performance of 2D CuO monolayer towards H<sub>2</sub>S at 0-80% relative humidity (RH) was first measured at 325°C. From the transient response curves shown in **Figure 34** (a), the electrical resistance of CuO monolayer increases notably in response to both the H<sub>2</sub>S gas and the water vapor in the gas stream. Moreover, the response value ( $R_{\text{gas}}/R_{\text{air}}$ ) towards H<sub>2</sub>S, appears to be indifferent to the change in environment humidity as

indicated by the similar peak heights (i.e.  $\log(R_{\text{gas}})-\log(R_{\text{air}})=\log(R_{\text{gas}}/R_{\text{air}})$ ) observed at different humidity in Figure 33b. The tabulated response values to 0.4-2 ppm H<sub>2</sub>S as a

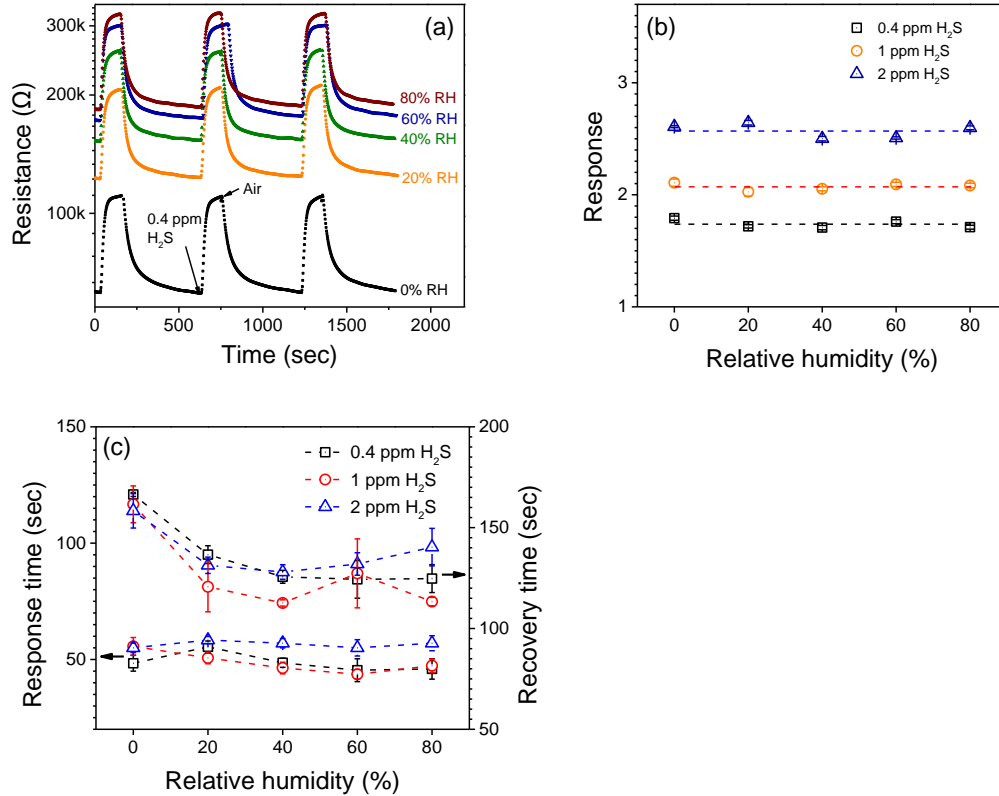


**Figure 34.** Transient response curve measured at 325°C, 400 ppb H<sub>2</sub>S, 0-80% RH; (b) Sensor responses toward different H<sub>2</sub>S concentrations as a function of relative humidity; (c) Response and recovery time toward different H<sub>2</sub>S concentrations as a function of relative humidity.

function of relative humidity were displayed in **Figure 34** (b). The interference from the water vapor in gas stream to H<sub>2</sub>S sensing appears to be negligible. The coefficient of variations (CVs) of sensor response at different humidity are only about 2.1%, 1.6%, and 2.5% towards 0.4 ppm, 1ppm, and 2 ppm H<sub>2</sub>S, respectively. The sensor's response and

recovery times toward different concentration of H<sub>2</sub>S and different relative humidity are summarized in **Figure 34** (c). The response and recovery times are indifferent to the change of H<sub>2</sub>S concentration. As for humidity level, the recovery times are noticeably shortened from ~160 sec in dry condition (0% RH) to ~125 sec in humid condition (20-80% RH), while no significant influence on response time is observed.

The humidity influence on 2D CuO monolayer was also examined at different working temperatures. As shown in **Figure 35** (a), the response values toward 400 ppb H<sub>2</sub>S under dry (0% RH), normal (40% RH) and highly humid (80% RH) conditions all drops with increasing working temperature. On the other hand, increasing the working temperature leads to enhanced immunity to humidity interference (i.e. lower CV). To be more specific, at the low working temperature of 250 °C, a notable decrease in the response value can be observed with increasing humidity, while the decrease becomes negligible at elevated working temperature (325 °C). Moreover, the response and recovery time also become shorter with increasing working temperature (**Figure 35** (b)). Therefore, 325°C is determined as the optimal working temperature in this study, because of the high immunity to humidity interference and fast kinetic observed at this temperature.

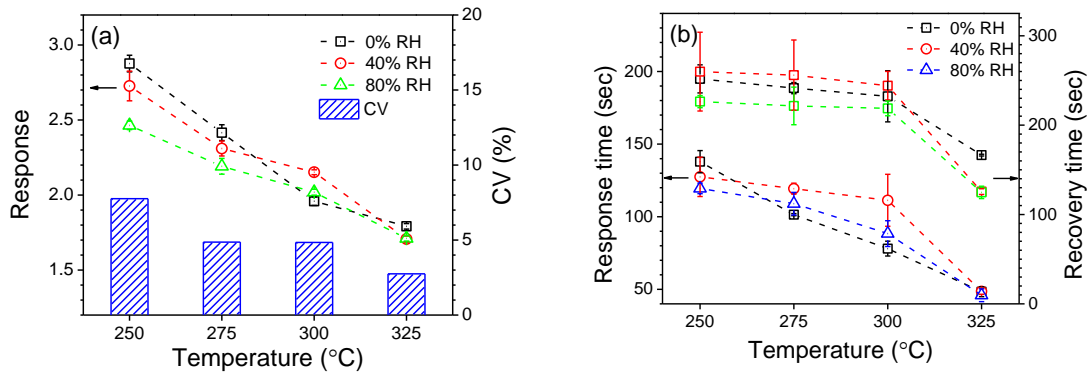


**Figure 35.** (a) Humidity influences on the response values and the coefficients of variations of the monolayer films toward 400 ppb H<sub>2</sub>S at different working temperatures; (b) humidity influences on the response and recovery times of the monolayer films toward 400 ppb H<sub>2</sub>S at different working temperatures.

To be used as H<sub>2</sub>S sensor in practical applications, the potential interferences arisen from other gases presented in the testing environments needs to be assessed. Toluene, ethanol, and acetone are three common VOCs presented in industrial environments and in human breath, and hence were selected for testing. The response values towards different concentrations of H<sub>2</sub>S and VOCs were displayed in **Figure 36** (a). When plotting both the gas concentration and response-1 ( $(R_{\text{gas}}-R_{\text{air}})/R_{\text{air}}$ ) in log scale, some linear relationships were observed for all four gases, which concur with the sensor formula derived by Hongstith et al<sup>30</sup>. The detection limits of the sensor are defined as the concentration at which signal to noise = 3, which equals to a response value of 1.1. By extrapolation, the detection limit towards H<sub>2</sub>S was around 3 ppb, while the detection limits towards the interference gases were 3-4 orders of magnitude larger than the gas of interest. which indicates the high selectivity of the 2D CuO monolayer sensor to H<sub>2</sub>S detection.

Finally, the stability of the sensor in humid environment was evaluated. The sensor's responses towards 0.4 ppm of H<sub>2</sub>S at 325 °C under 50% RH humidity were recorded 15 repetition per day, for 7 days. As shown in **Figure 36** (b), the response to 1 ppm of H<sub>2</sub>S was highly reproducible in the 15 test cycles, and no significant temporal drift was observed in 7 days of testing. The sensor's stability to humidity variations was also evaluated **Figure 36** (c). The humidity level was varied between 0 % and 50 %. The transient response curves remain the same under their respective humidity level, so do the response values.



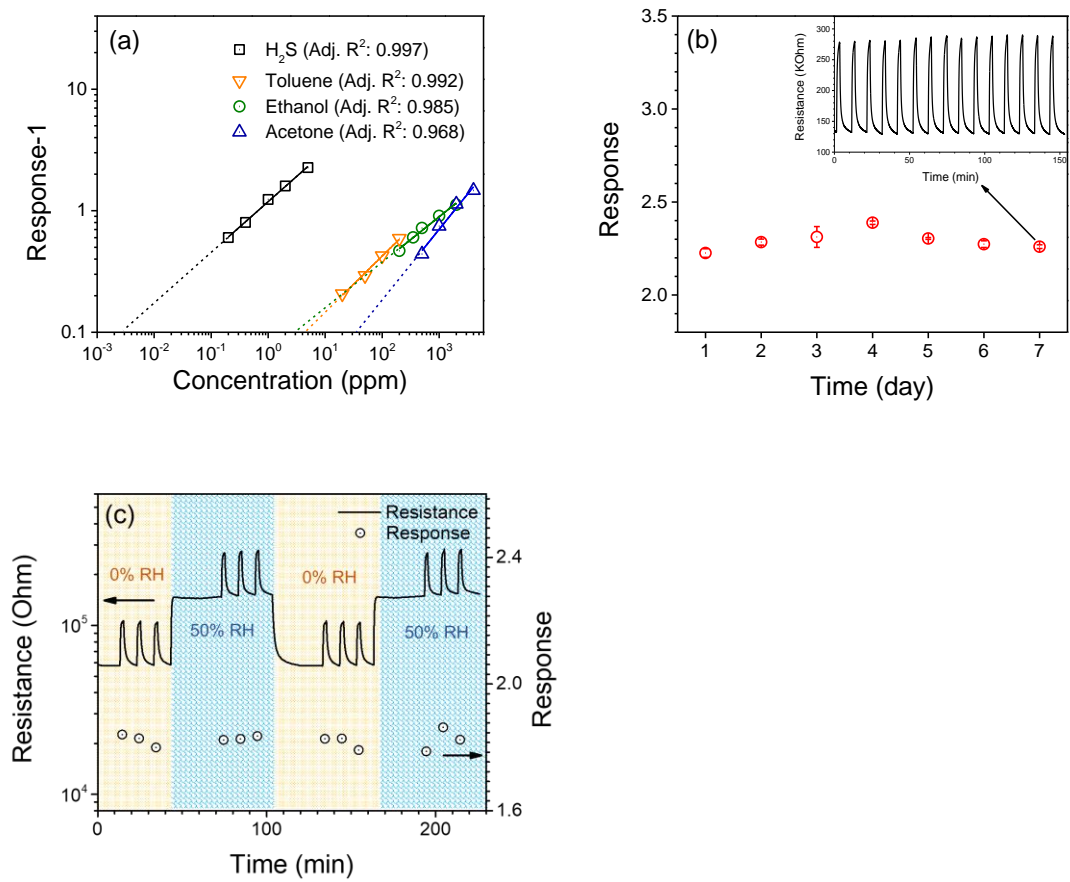


**Figure 36.** (a). Plot of (response-1) and gas concentration in log scale for H<sub>2</sub>S, C<sub>7</sub>H<sub>8</sub>, C<sub>2</sub>H<sub>5</sub>OH, and C<sub>3</sub>H<sub>6</sub>O detection. The intersections of the linear fit lines and x axis represent the detection limits of the sensor towards the 4 gases. (b) long term test performed at 325 °C, 50 %RH, and 1 ppm H<sub>2</sub>S. (c) humidity variation test carried out at 325 °C, 0.4 ppm H<sub>2</sub>S, and 0-50% RH.

#### 4.2.2 Sensing Mechanism

To understand the mechanism responsible for the humidity independent sensing behavior towards H<sub>2</sub>S, the sensing behaviors of 2D CuO monolayer sensor towards the three VOCs were also examined under different humidity. In stark contrast to the humidity independent sensing behavior towards H<sub>2</sub>S, some notable drops (~40%, **Figure 37** (a)) in response value with increasing humidity level were observed for the VOCs, conforming to the general theory on humidity interference. This contradiction suggests that the interaction

between H<sub>2</sub>S and hydroxyl groups on the surface of CuO is an outlier in the general theory of humidity interference.

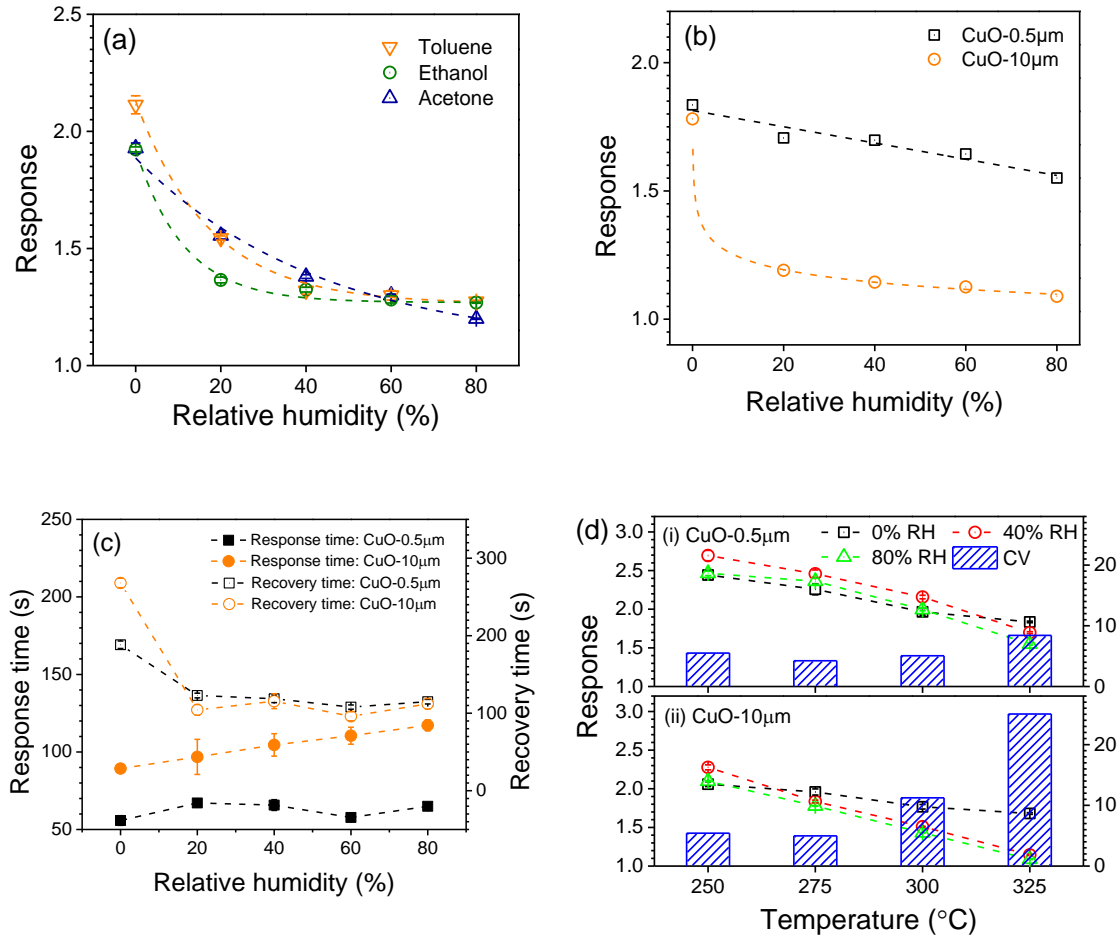


**Figure 37.** (a) Sensor responses towards 200 ppm of C<sub>7</sub>H<sub>8</sub>, C<sub>2</sub>H<sub>5</sub>OH, and C<sub>3</sub>H<sub>6</sub>O in air as a function of relative humidity at 325 °C (b) Humidity influence on the response values towards 400 ppb H<sub>2</sub>S of the multilayer CuO nanosheet film with film thicknesses of 0.5 and 10 µm measured at 325 °C (film thickness estimated by the weight of powders used in fabrication). (c) Response and recovery time toward 400 ppb H<sub>2</sub>S concentrations as a function of relative humidity for CuO multilayer film at 325 °C. (d) Humidity influences on the response values and the coefficients of variations of the multilayer films toward 400 ppb H<sub>2</sub>S at different working temperatures.

More interestingly, the sensors with multilayers of CuO nanosheets as sensing films (~10 layers for CuO-0.5µm, and ~200 layers for CuO-10µm) displayed a negative

correlation between film thickness and immunity to humidity interference at 325°C, as shown in **Figure 37** (b). From the transient response curves (**Figure 38**), the response and recovery times as a function of relative humidity can be calculated. As shown in **Figure 37** (c), the response and recovery times of CuO-0.5 $\mu\text{m}$  and their correlations with humidity are very similar to those of CuO-mono, while longer response and recovery times were observed for CuO-10 $\mu\text{m}$ . Moreover, the response time gradually increases with humidity level for CuO-10 $\mu\text{m}$  instead of remaining constant as in the cases for CuO-mono and CuO-0.5 $\mu\text{m}$ . The resistances in air ( $R_{\text{air}}$ ) all increase with humidity regardless of the sensing film thickness (**Figure 39**). The humidity influences on the two multilayer samples were also examined at different working temperatures. In stark contrast to the monolayer film, the multilayer samples displayed increased variability in response (CV) under different humidity levels with rising temperature (Figure 37d). The phenomenon is especially pronounced for CuO-10 $\mu\text{m}$ , the responses of which under humid conditions (40 and 80% RH) dropped much faster as a function of working temperature than those measured in dry condition. The change in humidity independency with sensing film thickness signified that the measured response value is affected by both the nanostructure and the surface reactions.

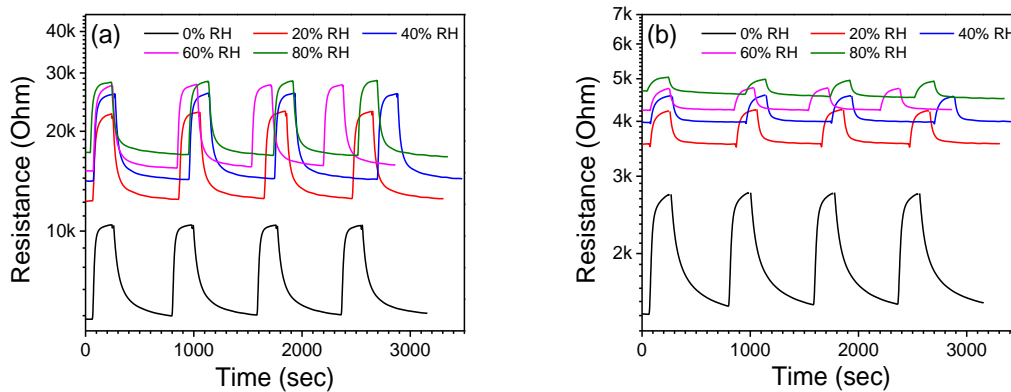


**Figure 38.** Transient response curves measured at 325°C, 400 ppb H<sub>2</sub>S, 0-80% RH for (a) CuO-0.5μm and (b) CuO-10μm.

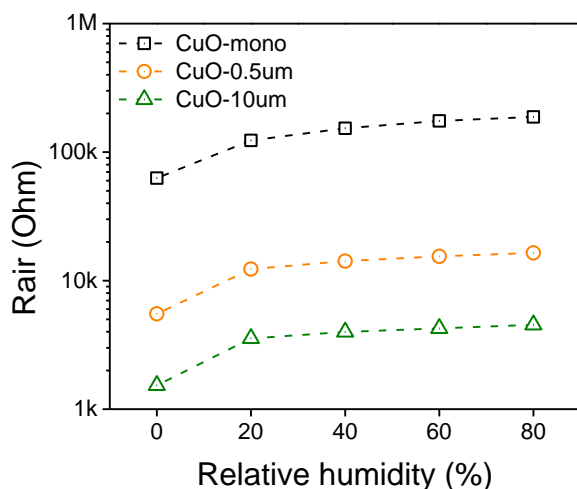


**Figure 39.** Resistance in air of the three sensors with different film thickness as a function of relative humidity at 325°C.

To shine more light on the issue, an ex-situ XPS study was designed to identify any changes in atomic composition and oxidation states on the surface of CuO nanosheet films during H<sub>2</sub>S sensing under dry and humid environment. As summarized in **Table 7**, the surface of the samples treated in dry air at 325 °C consists of only Cu and O, both before (Sample #1) and after 1 ppm of H<sub>2</sub>S was introduced into the environment (Sample #2). As for the samples treated in humid atmosphere (Sample #3 and #4), around 3.6 at % of S was identified for Sample #4, which was exposed in H<sub>2</sub>S-containing humid air.

In addition to the important information about the surface atomic composition revealed by the XPS wide scans (**Figure 40**), high resolution Cu 2p spectra of the 4 samples are of significant interest due to that Cu as a transition metal tends to show multiple oxidation states during the redox reactions with reducing gases. **Figure 42** illustrates the Cu 2p<sub>3/2</sub>

portion of the Cu 2p spectra after deconvolution. Sample #1 (Figure 56a), which was exposed in dry air, possesses two peaks at 933.5 eV and 942.4 eV that match well with the main and shake-up peaks of Cu<sup>2+</sup>, respectively.

**Table 7.** Surface concentration according to XPS wide scan

Sample #	Condition	Composition (at %)		
		Cu	O	S
1	325 °C, 0% RH, air	26.1	73.9	0
2	325 °C, 0% RH, 1 ppm H <sub>2</sub> S	23.3	76.8	0
3	325 °C, 50 % RH, air	28.4	71.6	0
4	325 °C, 50% RH, 1 ppm H <sub>2</sub> S	24.1	72.3	3.6

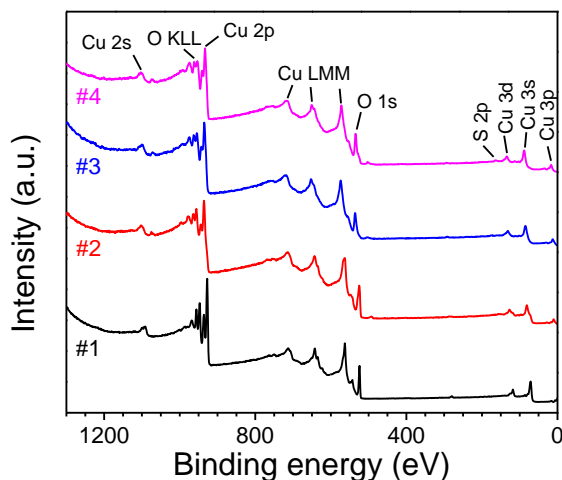
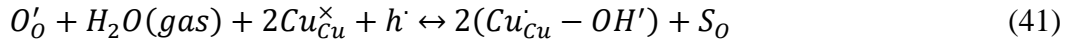


**Figure 40.** XPS wide scans of the CuO nanosheet films treated in different conditions.

The sample exposed in humid air (Sample #3, **Figure 42** (b)), however, exhibits two extra peaks located at 929.9 eV and 936.9 eV. Based on the hypothesis proposed by Hübner et al., water vapor reacts with pre-adsorbed oxygen anions, replacing them with terminal hydroxyl groups



where  $O'(ads)$  is an ionosorbed oxygen species,  $H_2O(gas)$  a water molecule,  $Cu_{Cu}^{\times}$  a Cu site on the surface,  $h'$  a free hole,  $OH$  a terminal hydroxyl group that forms a  $Cu_{Cu} - OH'$  dipole with Cu, and S a surface site for chemisorption of oxygen. Therefore, some possible designations for the peaks located at 929.9 eV and 936.9 eV are  $Cu_{Cu} - OH'$  dipole and its shake-up peak, respectively.

In the spectrum of sample #2, which simulates  $H_2S$  sensing under dry condition, one observes two peaks at 928.9 eV and 938.5 eV. Because the surface of sample #2 does not contain any S, as shown in the wide scan (**Figure 40**) and the high-resolution S 2p scan (**Figure 42e**), the two peaks at 928.9 eV and 938.5 eV cannot be attributed to  $Cu_xS$  as well as  $Cu_{Cu} - OH'$ . Instead  $Cu^+$  in  $Cu_2O$  is a more likely explanation according to literature<sup>32</sup>.

The Cu  $2p_{3/2}$  spectrum of sample #4 contains one new peak at 927.3 eV, other than the peaks of  $Cu^{2+}$ ,  $Cu_{Cu} - OH'$ , and  $Cu^+$ . Because this peak only emerged when  $H_2S$  was in the humid gas stream, and CuO surface has been known to prone to be converted to copper sulfide species when  $H_2S$  was adsorbed on its surface<sup>31</sup>, it is likely that these two peaks are generated by newly formed copper sulfide species. The  $Cu_xS$  phase, however, was undetectable with X-ray diffraction (**Figure 41**), possibly due to the extremely low concentration.

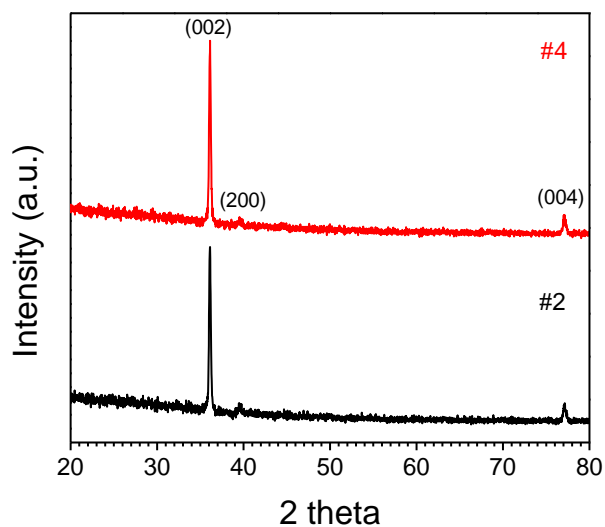


**Figure 41.** XRD patterns of sample #2 and sample #4. Only monoclinic CuO was identified in the samples.

The O 1s high resolution spectra of sample #1-4 were also deconvoluted and presented in **Figure 42** (c-d). The O 1s peak of sample #1 conforms with the spectrum of CuO reported in literature<sup>31</sup>, with a main peak located at 295.5 eV corresponding to the lattice oxygen in CuO, and a side peak at higher binding energy originated from the chemisorption of oxygen anions. The treatment in H<sub>2</sub>S-containing dry air gave rise to a new peak with a high binding energy of 531.7 eV (sample #2), which is assigned to the lattice oxygen in Cu<sub>2</sub>O. In contrast, the samples treated in wet condition (#3 and #4) exhibit a low binding energy side peak at around 527.8-528.4 eV. The shift to low binding energy is generally considered as a result of the ionic nature of the terminal hydroxyl groups bonded to the CuO surface, which leads to increased screening of the nucleus by the additional charge on the oxygen atom<sup>33</sup>. The terminal hydroxyl photopeak drops in intensity after exposing to H<sub>2</sub>S in wet condition, suggesting the hydroxyl groups have participated in the surface reaction with H<sub>2</sub>S. The photoemission peaks of chemisorbed oxygen anions are less

pronounced in sample #3 and #4, possibly because that the reactions with water and H<sub>2</sub>S have consumed most of the oxygen anions. Similar to spectrum #2, exposing to H<sub>2</sub>S in wet environment also leads to the formation of lattice oxygen bound to Cu<sup>+</sup>.

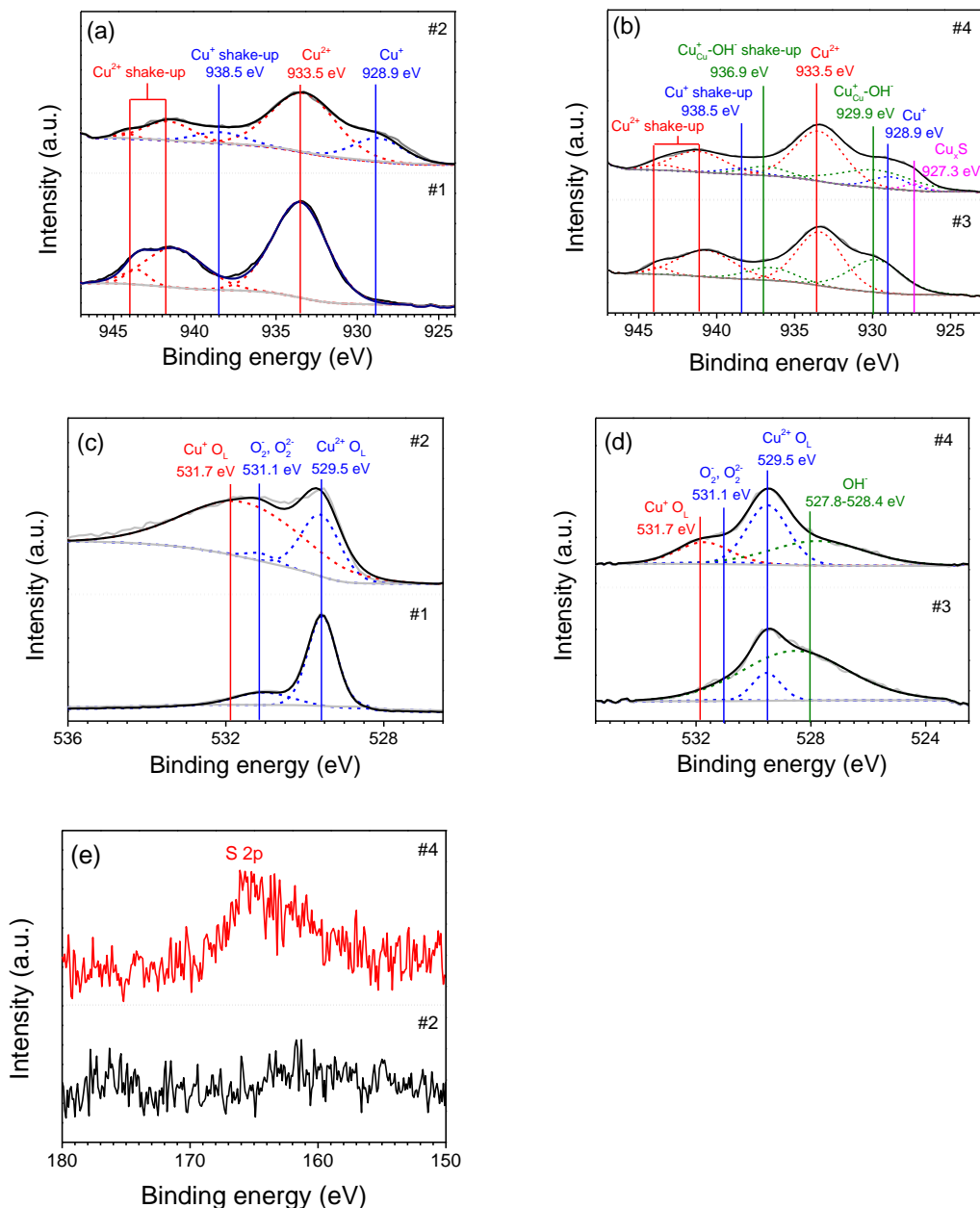
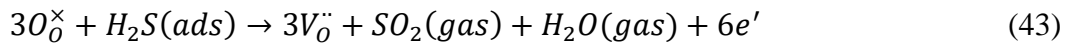
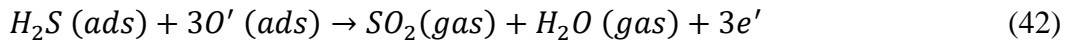


**Figure 42.** (a) Cu 2p<sub>3/2</sub> portion of the Cu 2p spectra of samples treated in dry condition (0% RH) before (#1) and after exposing to 1 ppm of H<sub>2</sub>S (#2); (b) Cu 2p<sub>3/2</sub> portion of the Cu 2p



spectra of samples treated in wet condition (50% RH) before (#3) and after exposing to 1 ppm of H<sub>2</sub>S (#4); (c) O 1s of samples treated in dry condition (0% RH) before (#1) and after exposing to 1 ppm of H<sub>2</sub>S (#2); (d) O 1s of samples treated in dry condition (0% RH) before (#3) and after exposing to 1 ppm of H<sub>2</sub>S (#4); (e) high resolution S 2p scan of sample #2 and sample #4.

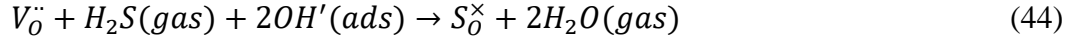
Based upon the analysis on the Cu 2p and O1s spectra, in dry condition, the 2D CuO monolayer sensor experiences the following two surface reactions when being exposed to H<sub>2</sub>S:



where  $O_O^\times$  and  $V_O^{\cdot\cdot}$  in equation 3 are an O site and an O vacancy on the surface, respectively. The generation of  $V_O^{\cdot\cdot}$  as a result of equation 3 gives rise to the formation of Cu<sup>+</sup> on the surface, which is suggested by the Cu 2p and O 1s spectra. Therefore, in dry condition, the 2D CuO monolayer sensor experiences surface reactions involving both ionosorbed oxygens (equations 2) and lattice oxygen (equation 3) that give rise to the increase in electrical resistance in response to H<sub>2</sub>S.

In humid condition, pre-adsorbed oxygen anions are partially replaced with terminal hydroxyl group (equation 1), which leads to the suppression of the sensing mechanism described in equation 2. The magnitude of this suppression effect is determined by the concentration of water molecule in the gas stream. The reaction with oxygen lattice is probably unaffected as suggested by the high-resolution Cu 2p and O 1s spectra. Therefore, if no additional surface reaction occurred, the sensor signal toward H<sub>2</sub>S would have gradually diminished with increasing humidity level as observed in the VOCs detection of this work and as reported for CO detection with CuO sensor<sup>26</sup>. However, in the case of H<sub>2</sub>S

sensing, the spectroscopic proof suggests the incorporation of S into CuO lattice facilitated by the terminal hydroxyl group on the surface:



where  $OH'(ads)$  is the terminal hydroxyl bond to Cu atom, and  $S_{O}^{\times}$  is the S in the O lattice site. The variable oxidation states of Cu promote the following redox reaction at elevated temperature<sup>34,35</sup>,



The asymmetric nature of the high-resolution S 2p peak of sample #4 (**Figure 42** (e)) also suggests the existence of multiple sulfur species on the surface of CuO in wet air containing trace amount of  $H_2S$ . As shown in **Figure 43**, the conversion of CuO to copper sulfides and possibly sulfur on the surface in wet condition was also observed with SEM. The morphology remains the same for the CuO monolayer after exposing to  $H_2S$  in dry condition (**Figure 43** (a)), while significant change in surface roughness due to the formation of some nanoparticles, presumably  $Cu_xS$  and S, on the surface (**Figure 43** (b)).

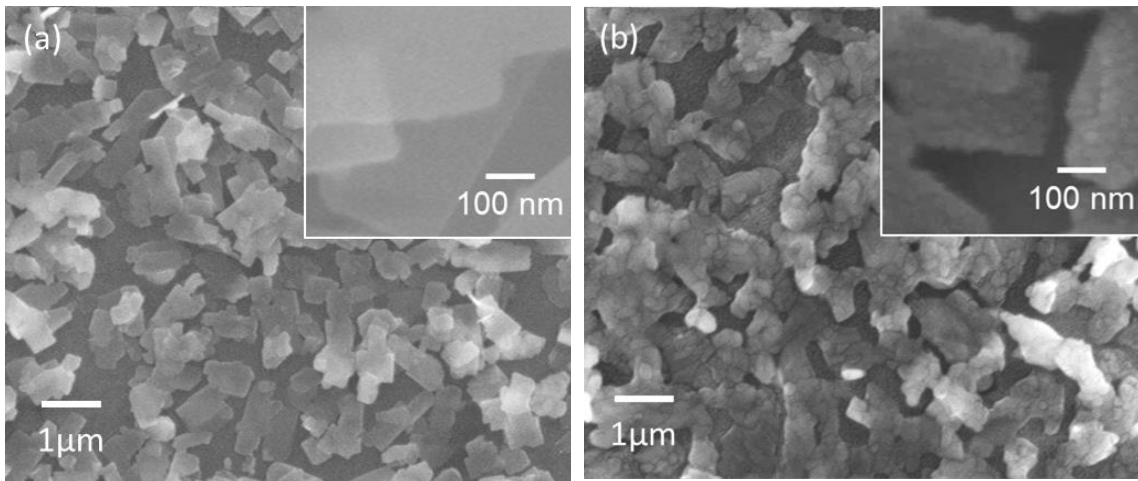


**Figure 43.** SEM image of CuO monolayer after exposing to H<sub>2</sub>S in (a) dry and (b) wet condition.

A schematic diagram of the sensing layer combining the morphological features with their corresponding energy bands representations is presented in **Figure 44**. In dry condition, the upper band bending drops considerably ( $q\Delta V_s$ ) due to the surface reactions described in equation 2 and 3, once H<sub>2</sub>S is introduced in the air. This decrease in upper band bending constitutes the change in resistance, and in turn, leads to the sensor response towards H<sub>2</sub>S in dry condition. Exposing to the same level of H<sub>2</sub>S, the drop in upper band bending ( $q\Delta V_s^*$ ) in wet condition should be smaller than in dry condition, because of the scarcity of the ionosorbed oxygen species. This should lead to a decrease in response, i.e. humidity interference. However, the formation of a resistive layer of sulfur and Cu<sub>2</sub>S on the surface in wet air containing H<sub>2</sub>S could lead to changes in the morphology of the sensing layer. Specifically, both the grain size of CuO nanosheet ( $D_G$ ) and the contact area size ( $D_C$ ) are likely to decrease due to the formation of resistive surface layer. According to the conduction model for p-type conducting semiconductor gas sensor proposed by Barsan et al.<sup>36</sup>, the resistance of a p-type sensing layer is described in the following equation:

$$R = R_B \left( \frac{L_D}{D_C} \cdot \exp\left(-\frac{qV_s}{2kT}\right) + \frac{1}{1 + \frac{L_D}{D_G} \cdot \exp\left(\frac{qV_s}{2kT}\right)} \right) \quad (46)$$

This equation indicates that the sensor response is dictated by surface effects ( $V_s$ ), bulk/material properties ( $R_B$  (bulk resistance),  $L_D$  (Debye length)), and morphology ( $D_C$  and  $D_G$ ). Therefore, it is possible to end up with the same sensor response despite the band bending change caused by the surface reactions decreases in wet condition, because the

morphological factors ( $D_C$  and  $D_G$ ) could change in favor of high response value. Moreover, the higher the humidity level, the more abundant the terminal hydroxyl group, and hence the more extensive the conversion of CuO to Cu<sub>2</sub>S and S will be, which serves to maintain the sensor response to be on the same level when humidity increases.

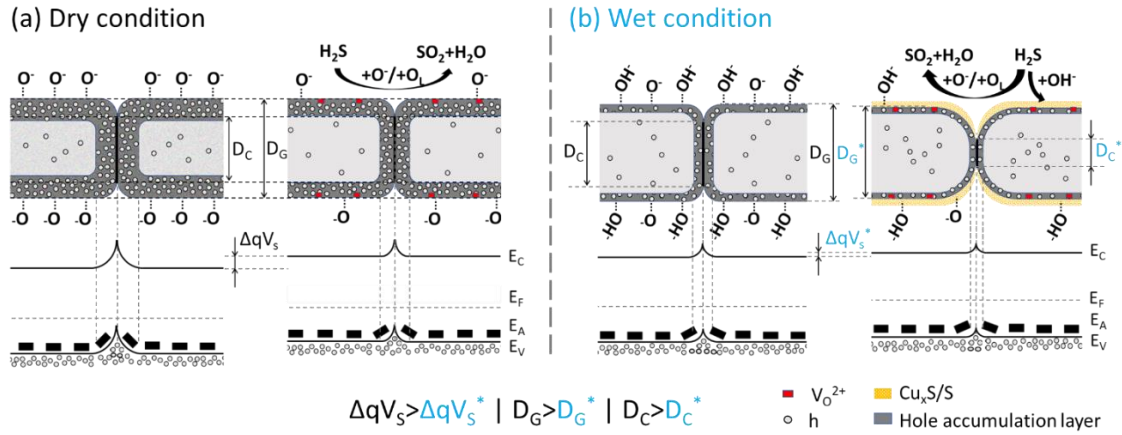


**Figure 44.** schematic of the CuO nanosheet sensing layer from the aspects of morphology, energy band, and surface reactions under (a) dry and (b) humid conditions.

Some of the aforementioned sensing behaviors can also be explained based on the formation of Cu<sub>2-x</sub>S on CuO surface in humid condition. Firstly, the decreased recovery time observed in wet condition can be explained by the low thermal stability of Cu<sub>2</sub>S. The standard Gibbs free energy of formation ( $\Delta_f G_m^\ominus$ ) for CuO, Cu<sub>2</sub>O, and Cu<sub>2</sub>S are -129.7, -146.0, and -86.2. kJ/mol, respectively<sup>37</sup>. Converting from a thermodynamically less stable phase (i.e. Cu<sub>2</sub>S) to CuO would be a much easier process than from a stable phase (Cu<sub>2</sub>O), and hence faster recovery speed was observed in humid condition.

Moreover, the influence of humidity on CuO monolayer sensor diminished with increasing temperature possibly due to that the surface reactions described in equation 4 and 5 become more drastic at elevated temperature. This theory could also explain the

rising humidity interference as a function of temperature observed in the multilayer samples. The SEM image of 2D CuO monolayer film treated in H<sub>2</sub>S-containing humid air (inset of **Figure 43** (b)) shows small protuberances (~ 10 nm) on the surface and edges of the nanosheets, which could block the gas diffusion pathway (interlayer spacing around 3 nm for stacked CuO nanosheets<sup>28</sup>) from the surface to underneath a sensor film, and from the macrocracks to the volume of sensing layer between the macrocracks (shown in **Figure 45**). As a result, for the sensing films composed of 10 and 200 layers of CuO nanosheets stacked together, the response to H<sub>2</sub>S will drop off in humid condition because the surface of the sensing film becomes dense due to the formation of resistive surface layer on the CuO nanosheets, rendering a large portion of the sensing film beneath the surface and between the macrocracks unreachable to H<sub>2</sub>S. The response drop-off becomes more pronounced as temperature increases, because the thicker resistive layer could form more rapidly at elevated temperature. Therefore, it is vital to either construct sensing film with large pores for gas diffusion or deposit monolayer film as illustrated in this work to obtain humidity independent H<sub>2</sub>S sensing performance with CuO as sensing material.

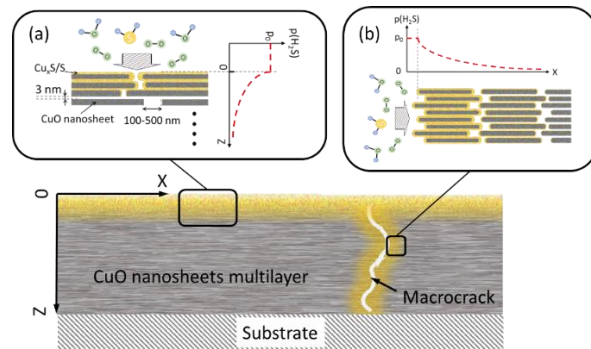


**Figure 45.** A schematic showing the CuO nanosheet multilayer sensing film in wet air containing H<sub>2</sub>S.

## 5. NANOMETER-THICK FILMS OF ALIGNED ZNO NANOWIRES SENSITIZED WITH AU NANOPARTICLES SENSITIZED WITH AU NANOPARTICLES FOR FEW-PPB LEVEL ACETYLENE DETECTION

### 5.1 Introduction

Metal oxide (MOX) gas sensors are a type of solid-state sensing device capable of transducing the binding of an analyte to a measurable signal in the form of changes in electrical resistance. To realize the incorporation of MOX sensors into wireless devices for emerging applications such as environmental and health monitoring<sup>93</sup>, the sensors must be miniature in size, extremely energy efficient (power consumption below 10 mW)<sup>94</sup>, and highly sensitive towards parts-per-billion level volatile organic compounds (VOCs). Commercial miniaturized MOX sensor (e.g. SGP30 from Sensirion<sup>®</sup>, AS-MLV-P2 from AMS<sup>®</sup>) comprises a thick porous sensing film and a micro-hotplate for heating up the device to a working temperature between 200-400 °C. Thick porous film (d: 10-100 μm) is widely regarded as the preferred sensing film structure to achieve high sensitivity,<sup>95-97</sup> yet it also contributes a considerable portion of the total heat loss from the sensing device,<sup>11</sup> preventing the sensing device from reaching the energy efficiency target.<sup>33,98,99</sup> Adopting a thin film structure with sub-micron thickness can massively reduce the heat dissipation and lead to potential breakthrough in energy efficiency. However, VOCs sensing at ppb level has rarely been reported on sensing films with thickness in the range between few tens and few hundreds of nm. Therefore, it is highly desirable to find effective ways to improve the sensitivity of thin film sensors.

The widely adopted approaches to fabricate sub-micron thin sensing films are standard high throughput deposition techniques, such as physical vapor depositions (PVDs),<sup>100,101</sup> chemical vapor depositions (CVDs),<sup>102,103</sup> and atomic layer depositions (ALDs).<sup>104,105</sup> The thin films produced in this way often exhibit compact microstructures, which only permit gas-solid interaction and formation of space charges on the external surface of the film. The signal, i.e. electrical resistance change, arisen from the film surface in response to the analyte gas is overwhelmed by the constant resistance of the unaffected bulk, which is in parallel with the film surface in the equivalent circuit. As a result, only in case that the thickness of the sensing film approaches the Debye length (2-5 nm), may reasonable sensitivity be expected.<sup>19</sup> However, with thickness approaching the Debye length, the interference from the interface trapped charged states on the electrical properties of the sensing film could become prominent.<sup>106,107</sup> Consequently, only moderate improvements on the sensitivity of compact thin film have been achieved by decreasing the film thickness.<sup>104,105</sup>

Moreover, the relatively smooth surface of compact thin films is unfavorable to the stability of precious metal catalyst decorated on the surface for sensitization purpose. As a rule, interactions of the film surface with reducing gases, such as VOCs, facilitate the migration process of noble metals on the surface.<sup>108</sup> Without significant diffusion barrier on the surface of compact thin film or strong metal support interaction, noble metal catalysts including Pt, Pd, Au, and Ag have been observed to sinter at temperature above 200 °C,<sup>109-111</sup> which leads to loss of active surface area and catalytic activity, and in turn temporal drift in sensing performance. For high mobility metals such as Au and Ag, only very low dispersion of large metal particles can be stabilized on the surface of flat metal

oxide and consequently the sensing performance improvement is limited.<sup>112,113</sup> Therefore, a catalyst stabilization method should be developed to ensure formation of noble metal clusters with a required size and density on the surface of metal oxide thin films for meaningful sensitization, and stabilization of the catalyst to avoid temporal stability loss of the sensor.

To overcome the limitations and the drawbacks of the previously developed thin film sensors and fulfil the requirement on sensitivity and energy efficiency, it is necessary to innovate the deposition technique to obtain a film microstructure good for achieving high performance, and execute a viable strategy to improve the stability of noble metal catalyst on thin film. Among the innovative thin film deposition strategies, Langmuir Blodgett (LB) assembly of metal oxide nanoparticles, a highly reproducible and patternable technique, is promising to yield a sensing film structure with high sensitivity. So far, assembly of various zero to two dimensional nanostructures into monolayer film, which largely preserves the nanostructures' surface area and promotes fast gas diffusion, has been reported in the literature.<sup>35-38</sup> Moreover, Huo et al.<sup>30</sup> and Cheng et al.<sup>39</sup> performed studies on the LB film of  $\alpha$ -Fe<sub>2</sub>O<sub>3</sub> nanoparticles and WO<sub>3-x</sub> nanowires, respectively, and obtained preliminary data demonstrating promising gas sensing properties. For metal catalyst stabilization, an effective strategy applied in heterogeneous catalyst is the introduction of physical diffusion barrier on the support surface.<sup>114-117</sup> To adopt this strategy on thin film, nanopatterns such as grooves and pits have been engraved by lithography and etch process on thin compact films and the topography structures prevent the metal nanoparticles supported on the patterned surface from sintering.<sup>118-120</sup> However, the minimum metal particle size limited



by the resolution of the patterning process is around few tens of nanometers, which is too large for achieving any sensitization effect.<sup>121,122</sup>

In this work, we utilized a Langmuir-Blodgett assembly technique to deposit 20 nm nanostructured thin film of aligned ZnO nanowire arrays with periodic v-grooves topographic structure on the substrate surface. The Langmuir-Blodgett film was then sensitized with Au nanoparticles (Au NPs) by sputtering and post-annealing. Such thin film composed of high-surface to-volume ratio 1D nanowires was expected to exhibit superior sensing performance to conventional compact film, and the unique topographic features were designed to stabilize Au NPs on the surface. The paper reports synthesis, characterization and sensing performance towards acetylene (C<sub>2</sub>H<sub>2</sub>), a key marker gas for air pollution caused by anthropogenic emission, of this Au/ZnO thin film sensor of new nanostructure.

## 5.2 Experimental

***ZnO nanowire synthesis:*** ZnO nanowires were synthesized via a solvothermal process. In a typical synthesis process, 1 mmol zinc nitrate hexahydrate (Zn(NO<sub>3</sub>)<sub>2</sub>·6H<sub>2</sub>O, 98+%, Sigma-Aldrich) was first dissolved in 10 mL ethanol (anhydrous, Koptec). The zinc nitrate solution was then added into 20 mL of 1.25 M sodium hydroxide (NaOH, 97+%, Sigma-Aldrich) ethanol solution. The as-formed white suspension was ultrasonicated for 15 min before being transferred and sealed in a Teflon-lined stainless-steel autoclave (50 mL capacity). The autoclave was heated and maintained at 100 °C for 24 h. Afterwards, the autoclave was cooled down to room temperature and the precipitates were separated and

washed by centrifugation. Finally, the precipitates were dried in a vacuum oven at 70 °C for 12 h.

***ZnO nanowire surface functionalization:*** In a glovebox, 0.05 g ZnO nanowire was first dispersed in 50 mL of 2-propanol (reagent, Sigma Aldrich). Then 0.5 mL of 20 mM 1-dodecanethiol ( $\geq 98\%$ , Sigma Aldrich) /2-propanol solution was added into the ZnO solution while stirring. The solution was kept at room temperature under constant stirring for at least 12 hours, before being removed from glovebox. The solution was centrifuged (5 krpm, 10 min) and the product was washed with 2-propanol twice to remove any excess thiol. The final pellet was dried under vacuum at room temperature overnight.

***ZnO nanowire Langmuir-Blodgett Assembly:*** 2 mg of functionalized ZnO nanowire powder was first dispersed into 3.4 mL of a mixed solvent ( $v(\text{toluene})/v(2\text{-propanol})=1.5$ ) to form a stable colloidal solution. The solution of dispersed nanowires was then spread dropwise onto the water subphase of a Langmuir-Blodgett trough (Nima Technology, model 1212D1) at a rate of 1.5 mL/hr using a syringe pump (KD scientific). After spreading all the nanowire colloid, the two barriers started to compress with a line speed of 2.5 cm/min, until the surface pressure reaches around 40 mN/m. The aligned nanowire monolayer was then transferred to a pre-submerged substrate (glass or glass with preprinted interdigitated electrode, Metrohm) by lifting the substrate at 15 mm/min. The as-formed films were calcined at 300 °C for 1 hr to remove the surfactant.

***ZnO thin film by radio frequency (RF) sputtering:*** ZnO thin films were deposited on glass and sensor substrates by RF sputtering at room temperature. Sputtering was performed using ZnO sputter target (Kurt J. Lesker, 99.9%). The base pressure before deposition was around  $1 \times 10^{-7}$  Torr. Sputtering was carried out at a pressure of 10 mTorr in

pure Ar and at a power of 100 W. The thickness of the ZnO thin film was measured with a profilometer (Dektak XT stylus profilometer) to be around 100 nm.

**ZnO nanoplates with (100) exposed:** ZnO nanoplates with predominant (100) face were synthesized following the procedure detailed in.<sup>123</sup> In a typical experiment, 0.287 g of ZnSO<sub>4</sub> 4H<sub>2</sub>O (98 %, Alfa Aesar), 0.080 g of NaOH (97+ %, Sigma-Aldrich), and 0.083 g of NaF (99.99 %, Alfa Aesar) were successively added into a mixed solvent of 7 mL of distilled water and 3 mL of ethanol. The resulting mixture was sonicated for several minutes and transferred into a Teflon-lined stainless-steel autoclave with a capacity of about 20 mL. Then the autoclave was heated to 200 °C and held for 24 h. After the mixture was cooled to room temperature, the production was separated by centrifugation from the solution and repeatedly rinsed with distilled water.

**Au NPs loading:** Au films around 0.5 nm thick were sputtered on the three types of ZnO thin films by DC sputtering at room temperature. The base pressure before deposition was around  $1 \times 10^{-7}$  Torr. Sputtering was carried out at a pressure of 5 mTorr in pure Ar and at a power of 50 W. Post heat treatments were applied on Au/ZnO film at 400 and 350 °C for different period to obtain Au NPs of different size and distribution.

**Materials characterization:** SEM images were collected on an AMARY 1910 at 15 kV. The particle size distribution of Au nanoislands were extracted using ImageJ from the SEM images. XRD measurements were performed on a Bruker D8 focus diffractometer using Cu K $\alpha$  radiation ( $\lambda=1.5406$  Å) with a step size of 0.02° and a scan rate of 0.6 sec/step. Atomic force microscopy (AFM) imaging was performed in ScanAsyst noncontact mode on a Bruker Multimode 8 system with ScanAsyst tips (Bruker). NanoScope Analysis was

used for image processing. TEM, HRTEM, and SAED images were collected on a Philips CM-200-FEG 139 at 200 kV.

***Sensing performance evaluation:*** A home-built sensing performance evaluation system described in was used to evaluate the sensing performance (**Figure 46**). The sensors first achieved steady state in the gas chamber at a set temperature with 200 sccm air flow for 30 min. Then the gas stream was switched between air and C<sub>2</sub>H<sub>2</sub> containing air periodically to test the sensing performances at C<sub>2</sub>H<sub>2</sub> concentration ranging from 10 ppb to 25 ppm. The more than 3 order of magnitude change in C<sub>2</sub>H<sub>2</sub> is obtained with a two-stage dilution system built in-house. The sensors were also tested in atmosphere containing typical interference gases, i.e. H<sub>2</sub>, CO, and CH<sub>4</sub>. Humidity in the gas stream was controlled by flowing dry air through a bubbler, the temperature of which was maintained at 25 °C by a water bath. Sensor response (S) was defined as the ratio between the electrical resistance in air (R<sub>air</sub>) and the electrical resistance in reducing gas containing air (R<sub>gas</sub>), i.e.,  $S = R_{\text{gas}}/R_{\text{air}}$ . The response time and recovery time were defined as the time required to reach 90% of the full response state in mixed gas and 90% of the fully relaxed state in the air, respectively.

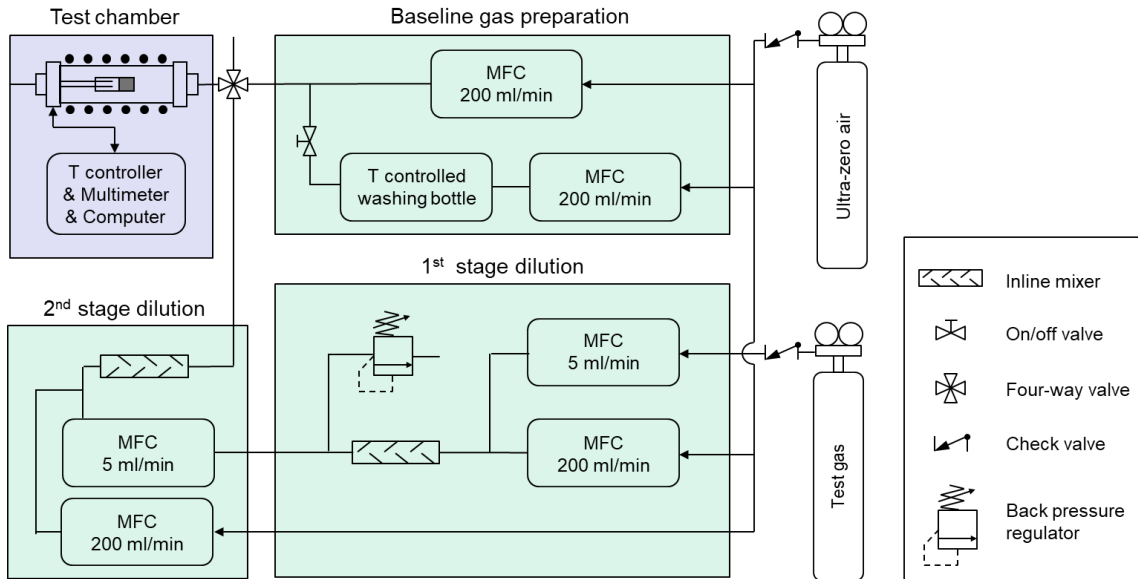


**Figure 46.** Schematic of gas sensor testing system used in this work.

### 5.3 Results and Discussion

***Fabrication of Nanostructured ZnO Langmuir-Blodgett film:*** As shown in **Figure 48 (a)**, ZnO nanowires with diameter and length around 20 nm and 1  $\mu\text{m}$ , respectively, were first synthesized as the nano-building blocks for the nanostructured ZnO Langmuir-Blodgett film (ZnO<sub>LB</sub>). For the nanowires to float at the water-air interface and assemble into film by LB technique, the surface of the nanowires was functionalized with an amphiphilic surfactant (i.e. 2-dodecanthiol) to achieve a certain level of hydrophobicity. After successful functionalization signaled by the emergence of C-H vibrational peak in the Fourier-transform infrared spectroscopy (FTIR) spectrum (**Figure 47**), the ZnO nanowires were dispersed in a mixed organic solvent (i.e. toluene/2-propanol) and a stable colloidal solution was obtained (**Figure 47**). To identify the optimal surface pressure for forming a ZnO<sub>LB</sub> film composed of a monolayer of densely packed and well aligned ZnO nanowires on the water subphase and transferring the film onto a solid substrate, the surface

pressure versus area ( $\pi$ -A) isotherm was recorded and displayed in **Figure 48 (b)**. The isotherm revealed a typical three stage evolution given rise by the change in the proximity of the floating wires. Applying excessive pressure to monolayer film in the solid phase will destabilize the monolayer, and defects, such as overlaps and folds, will form. Therefore, the optimal surface pressure was selected at 40 mN/m to achieve maximum packing density of nanowires.

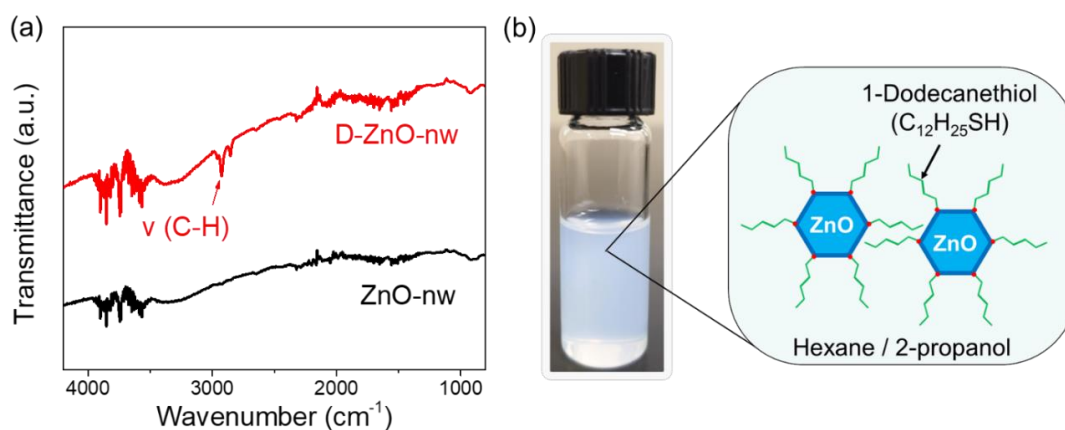


**Figure 47** (a) FTIR spectra of pristine and functionalized ZnO nanowire. (b) Colloidal solution of ZnO nanowire in hexane.

The morphology and texture of ZnO<sub>LB</sub> film deposited on glass substrate with preprinted Au interdigitated electrodes were characterized. As shown in **Figure 48 (c)**, the nanowires were densely packed and well aligned over a large area, although some defects were observed presumably due to the short nanowires formed by breakage of long nanowires during the sonication-based dispersion processes. **In Figure 48 (d)**, the x-ray diffraction (XRD) pattern of ZnO<sub>LB</sub> film indicates that the film consists of hexagonal wurtzite ZnO nanowires, which are strongly  $\langle 100 \rangle$ -oriented along the surface normal. It is speculated that ZnO nanowires reoriented and form high-order structure driven by capillary force during the drying process after the film is transferred onto a solid substrate.

To further the understanding on the microstructure of the ZnO\_LB film, the ZnO nanowires were analyzed with high-resolution transmission electron microscopy (HRTEM), and [001] is identified as the preferential growth direction based on the d-spacing of the lattice fringes (**Figure 48 (e)**). Considering the hexagonal wurtzite crystal structure, the ZnO nanowires should adopt a hexagonal prism shape with {100} as major surface planes, and the side length and the diagonal length of the hexagonal bases is 10, and 20 nm, respectively. Consequently, the surface topography of ZnO\_LB film can be represented by the illustration shown in **Figure 48 (f)**, which can be described as periodic v-shaped grooves 10 nm wide and 8.6 nm deep separated by 10 nm wide mesas.

***Au nanoparticles loading and stabilization:*** Au nanoparticle (NP) catalyst was loaded on the ZnO\_LB film by DC sputtering of Au film followed by post-annealing at 400 °C. The Au loading percentage was estimated to be around 13 wt% for 0.5 nm of Au film sputtered. As shown in **Figure 52 (a)**, Au NPs with diameters close to the mesa width ( $m = 10$  nm) were observed to form along the ZnO nanowire after 24 h of annealing treatment. Higher loadings (26 wt%/1 nm and 39 wt%/1.5 nm) were also tested, but Au NPs 4-6 times as large as the mesa were obtained after annealing (**Figure 49**), indicating that the surface topographic features of the ZnO\_LB film were ineffective to contain sintering at these high loading percentages. **Figure 52 (b)** and **(c)** show the evolution of the statistical information of Au NPs size obtained from an isothermal kinetic analysis. Within the whole range of annealing time (3-89 h), the particle size distribution remains Gaussian despite the increases in both Au NPs' mean diameter and variance. Moreover, the mean diameter initially increases quickly with annealing time, but growth rate quickly drops when the Au NPs size approaches 11 nm, a value close to the mesa width.

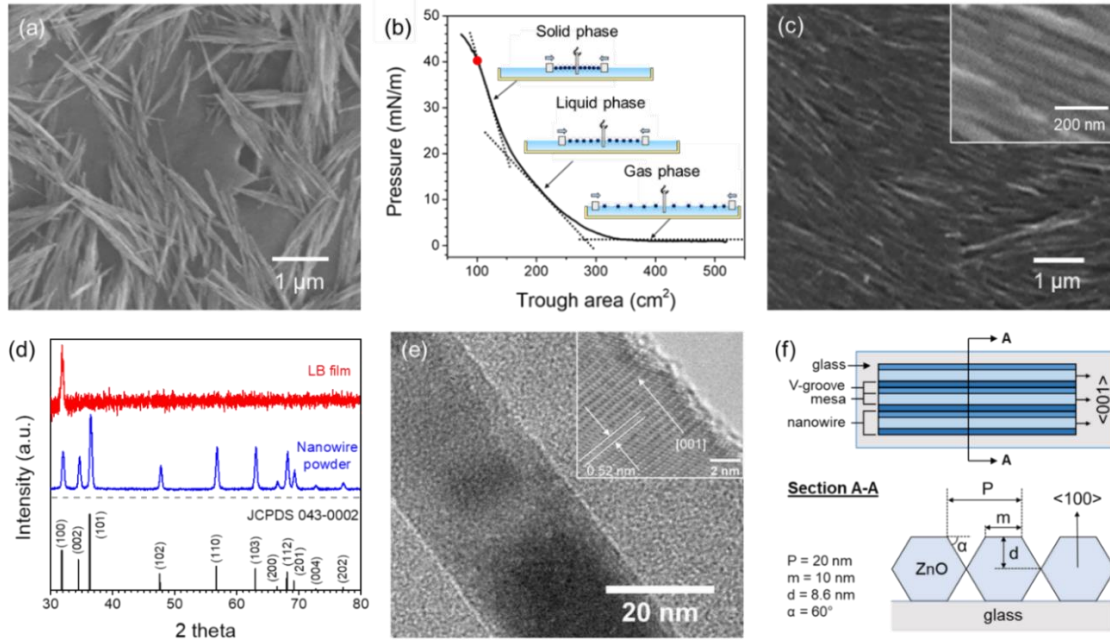


**Figure 48** (a) Scanning electron microscopy (SEM) image of as-synthesized ZnO nanowires. (b) surface pressure versus area isotherm of floating ZnO nanowires. (c) SEM images of ZnO LB film on Au-IDE-coated glass substrate. (d) XRD patterns of ZnO nanowires and ZnO LB film. (e) Transmission electron microscopy (TEM) image of ZnO nanowire and high resolution TEM image showing the lattice fringes (inset). (f) Illustration of v-grooves topography exhibited by ZnO LB film.



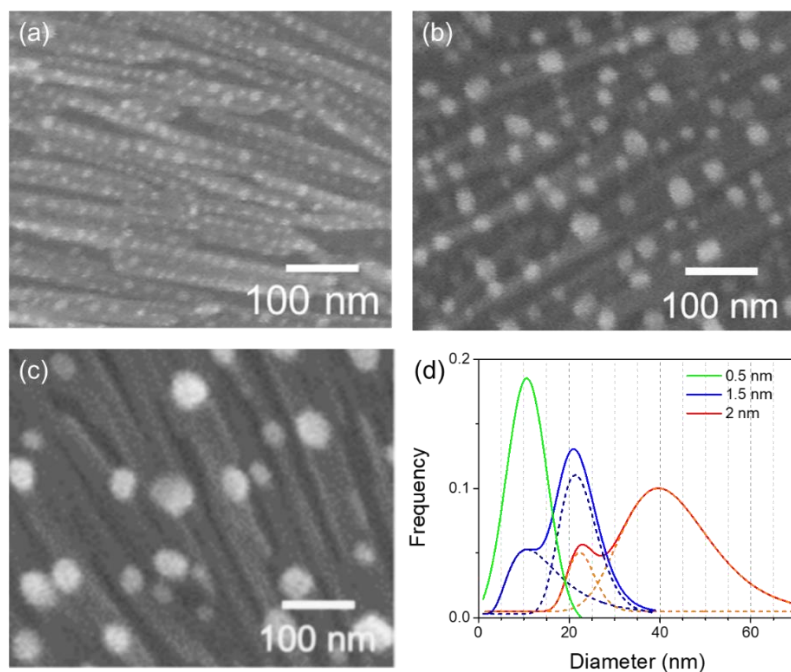


**Figure 49** (a-c) SEM of annealed Au@ZnO-LB samples with initial Au loading of 0.5 nm (13 wt%), 1.5 nm (39 wt%), and 2 nm (52 wt%). Particle size distributions of 0.5nm-2nm Au@ZnO-LF based on SEM images

To verify that the sintering of Au NPs was indeed suppressed on ZnO<sub>LB</sub> film, the sintering behavior of Au NPs on a ZnO thin film prepared by a conventional sputtering technique was investigated. The polycrystalline ZnO sputtered film (ZnO<sub>S</sub>) was 50 nm thick with lateral grain diameter of around 10 nm (**Figure 50 (a)**). Moreover, the surface comprises predominantly (002) planes and the roughness is as low as 1.01 nm (**Figure 50 (b)**). As shown in **Figure 52 (d)**, the Au NPs grew nearly twice as large and populated the ZnO<sub>S</sub> film much more sparsely than on ZnO<sub>LB</sub> film after going through the same annealing treatment. Moreover, when the annealing time was varied between 3-100 h, the particle size distribution of Au NPs reveals the evolution of a series of lognormal size distributions with long tails toward the direction of the larger sizes from an initial Gaussian-like shape obtained after 3h of annealing (**Figure 52 (e)**). This lognormal size distribution

indicates particle migration and coalescence (PMC) as the dominant sintering mechanism<sup>124</sup>. As the name PMC suggested, for supported metal catalysts to sinter and growth, smaller particles must migrate in Brownian motion fashion and when binary collision occurs, two smaller particles will fuse into one bigger particle. Generally, PMC is expected to dominate only in the initial stage of the sintering process, since the mobility of metal nanoparticles drops quickly with particle size<sup>125</sup>. However, direct observations (**Figure 51**) of coalescences of two particles as large as 20 nm were recorded for Au NPs support on ZnO\_S film at the advanced stage of sintering process (100 h at 400 °C), which suggests that PMC could be the dominant sintering mechanism for the entire sintering process. Overall, the mean diameter of Au NPs increased with annealing time by a power of around 0.3 from 9 to 26 nm (**Figure 52 (f)**), which are much larger than from 7 to 11 nm for ZnO\_LB film. Thus, a notable improvement in the sintering resistance of Au NPs on ZnO\_LB film was confirmed.

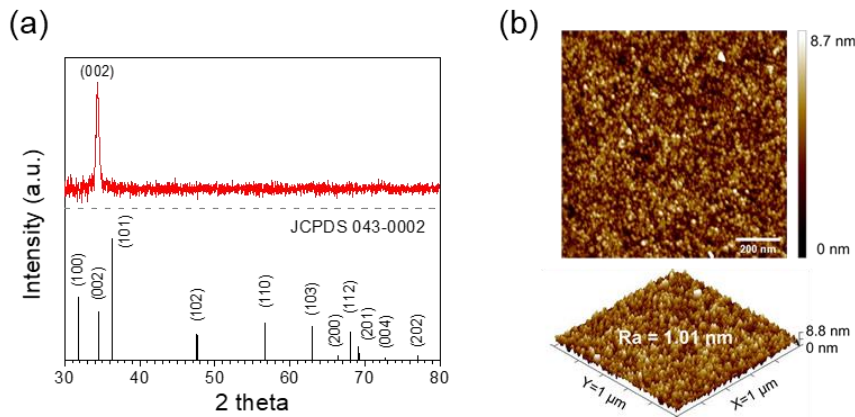


**Figure 50** (a) Texture of ZnO sputtered film revealed by XRD. (b) Surface morphology and roughness of ZnO sputtered film revealed by AFM.

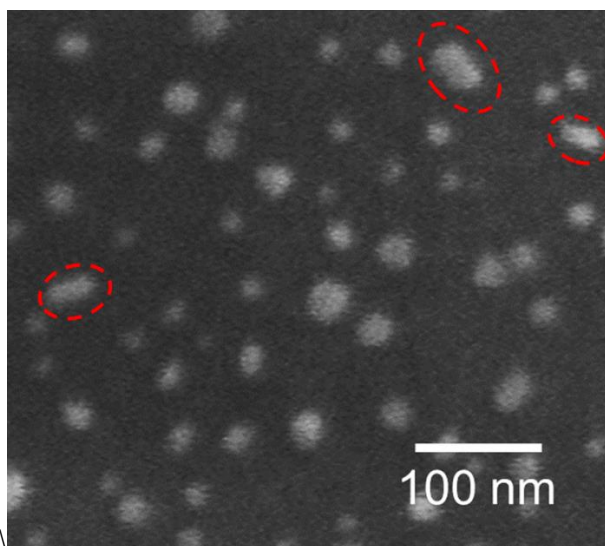


**Figure 51.** SEM image of Au@ZnO\_SF annealed at 400 °C for 100 h. Binary collisions and fusions of Au NPs as large as 20 nm are marked in red.

Particle migration and coalescence (PMC) can be inhibited by enhancing the metal support interaction (MSI), which is influenced by the atomic structure and chemical potential at the surface of the support. The strength of MSI between Au NPs and ZnO nanowires was evaluated with TEM and X-ray photoelectron spectrometry (XPS). The TEM image shows no sign of ZnO encapsulation or Au NPs sinking as reported in strong MSI (**Figure 54 (a)**). The high-resolution image (**Figure 54 (b)**) reveals poor wetting of Au on ZnO nanowire with high contact angles around 130-135 °. Moreover, a [111] growth direction was identified for the Au NPs supported on ZnO nanowires. This aligns well with the XRD pattern of Au@ZnO\_LB (**Figure 53**), where only Au (111) peak is identified. The growth direction of Au NPs supported on ZnO\_S film is also [111] as indicated in **Figure 53**. Strong MSI between Au and ZnO may also be reflected by the formation of Au<sup>3+</sup> at the interface due to high level of electron transfer<sup>126</sup>. As shown in the high resolution XPS spectra obtained from Au doped ZnO\_LB film (**Figure 54 (c-d)**), the

deconvolution of the Au 4f<sub>7/2</sub> peak yields only metallic Au at 84 eV and Au<sup>+</sup> at 85.1 eV. Au<sup>3+</sup> observed in the previous literature that reports strong MSI was absent, suggesting weaker an Au-O-Zn linkage between Au NPs and ZnO nanowires.

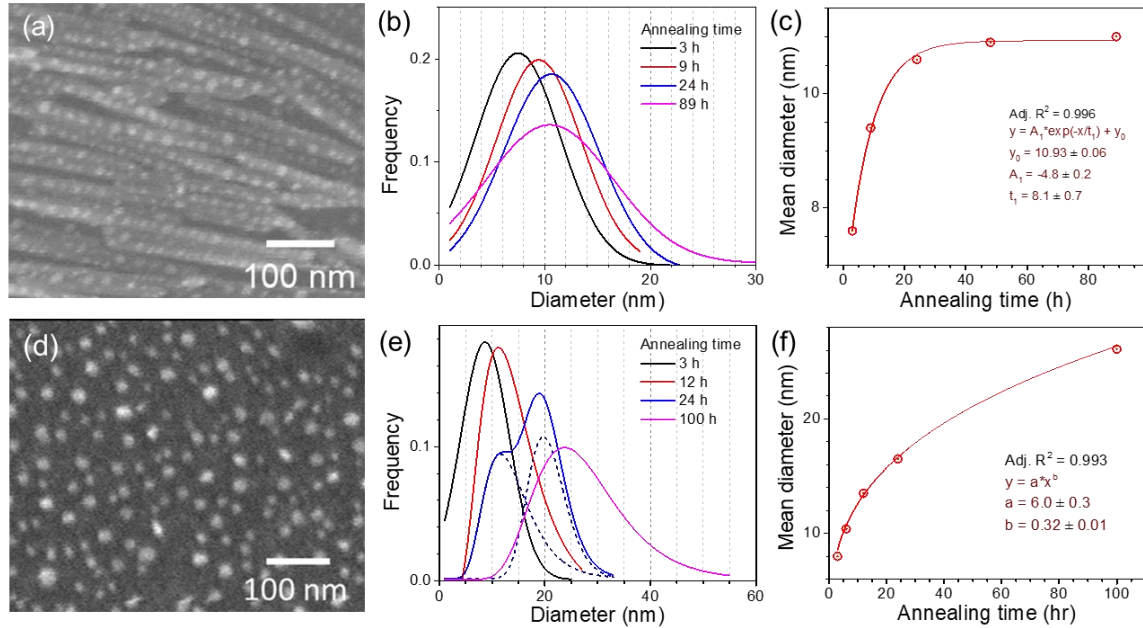


**Figure 52.** (a) SEM plane view of Au doped on ZnO\_LB film annealed at 400 °C for 24 h. Evolution of Au particle size distribution (b) and mean diameter (c) with annealing time on ZnO LB film. (d) SEM plane view of Au doped on ZnO\_S film annealed at 400 °C for 24 h. Evolution of Au particle size distribution (e) and mean diameter (f) with annealing time on ZnO\_S film.

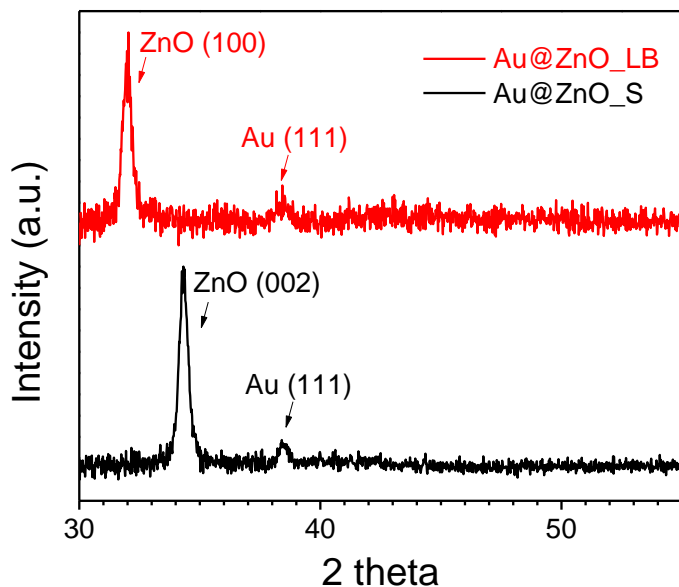


**Figure 53** XRD patterns of Au doped ZnO film after annealing at 400 °C for 24 h.

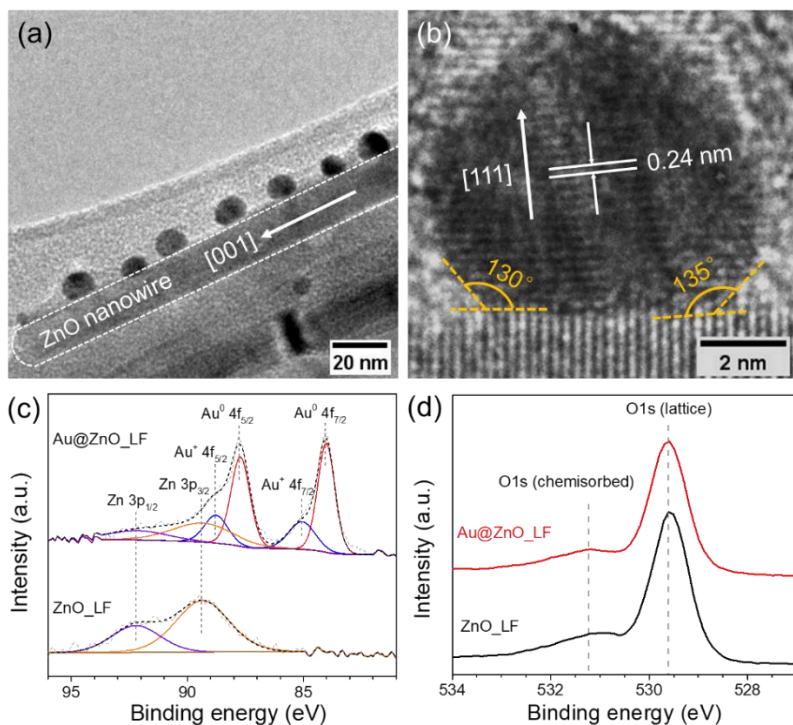


**Figure 54** TEM of Au nanoparticles supported on ZnO nanowire after annealing treatment at 400 for 12 h (b) High resolution TEM image of supported gold nanoparticle

revealing a [111] growth direction and high contact angles of 130 ° and 135 °. High resolution XPS spectra of Au 4f (c) and O 1s (d).

Another way to stop PMC is by introducing potential barriers on the path of diffusion with topographic feature (e.g. hill and valleys) on the support surface. As summarized in **Table 8**, the surface of ZnO\_S film is much smoother than ZnO\_LB film. However, their surface energies are also different, and hence the deconvolution of the two sintering resistant factors i.e. MSI and diffusion barrier is still unachievable, despite the notable difference in Au NPs size between the two supports. This issue was addressed by performing Au annealing test on ZnO nanoplates (NP) with the same surface plane as that of ZnO\_LB film but with a smooth surface ( $R_a=1.19$  nm, in  $0.2 \mu\text{m}^2$ ) (**Figure 55**). The mean diameter of Au NPs obtained with the same annealing treatment is 16.3 nm on ZnO NP (**Figure 56**), which is much closer to ZnO\_S film rather than that of ZnO\_LB film. Therefore, the topographic features on the ZnO LB film is evidently the main inhibitor of Au NPs sintering and growth on ZnO support.

**Table 8** Surface properties and sintering resistant performance of three different ZnO substrates

Sample	Ra (nm)	Surface plane	Surface energy ( $\text{J}/\text{m}^2$ ) <sup>127</sup>	Annealing condition	Mean diameter (nm)
ZnO LB film	6.5*	(100)	1.0	400 °C 24 h	10.7
ZnO_S film	1.01	(002)	2.4	400 °C 24 h	16.6
ZnO NP	1.19	(100)	1.0	400 °C 24 h	16.3

At this stage, the mechanism of sintering inhibition of Au NPs on ZnO LB film can be explained qualitatively. To be specific, the ridges at both sides of the mesa introduce

potential barriers on cross-nanowire migration of Au NPs because of the small curvature of the ridges as explained by the Gibbs Thompson equation

$$\Delta E = k \times \gamma \times \Omega \quad (47)$$

where  $\Delta E$  is the excess potential,  $k$  is the local curvature,  $\gamma$  is the surface energy of Au, and  $\Omega$  is the atomic volume of Au. Based on the mean field theory<sup>128</sup>, the slower the particle diffusion, the lower the frequency of collision. Once Au NPs reaches 10 nm in size, the collision was constraint to just along the ZnO nanowire, which means that the collision chance becomes much lower, and hence grain growth slows down to undetectable level. Attributed to improved sintering resistance, high dispersion of small Au NPs can be stabilized on the surface of ZnO\_LB film.

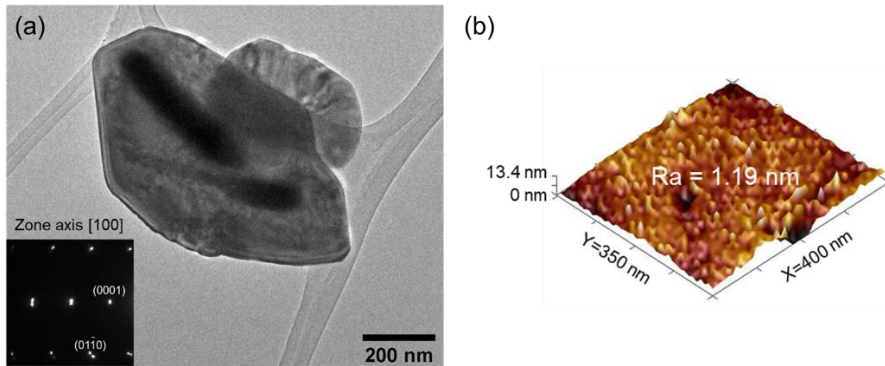


**Figure 55** (a) TEM of ZnO nanoplate with (100) as primary crystal facet. (b) Surface roughness of ZnO nanoplate.

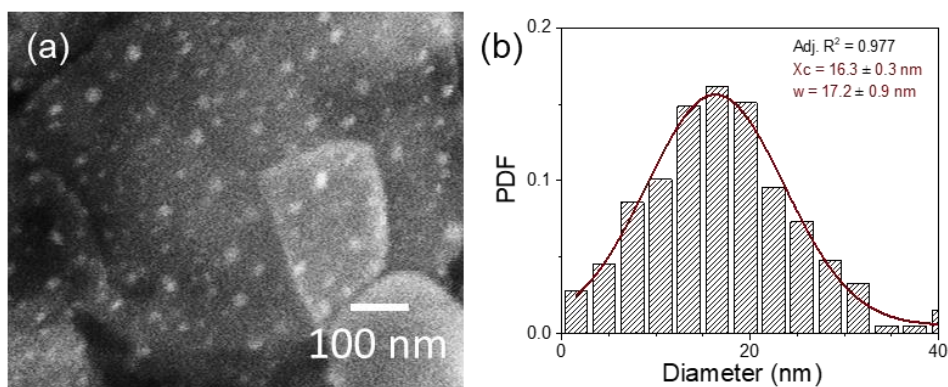


**Figure 56** (a) SEM of Au@ZnO\_NP annealed at 400 °C for 24 h. (b) Particle size distribution.

**Sensing performance:** Sensing devices prepared with ZnO\_LB film and ZnO\_S film were evaluated for acetylene (C<sub>2</sub>H<sub>2</sub>) detection. For ZnO\_LB film decorated with Au NPs (Au@ZnO\_LB), an annealing treatment at 400 °C for 40 h was employed prior to sensor testing to obtain a stable Au NPs size of around 11 nm. To obtain similar size and dispersion of Au NPs on ZnO\_S film (Au@ZnO\_S), the annealing treatment time was shortened to 12 h.

To investigate the gas sensing properties and identify the optimum sensor working condition, the dynamic response of the pristine and Au NPs-doped ZnO thin film sensors upon exposure to 25 ppm of C<sub>2</sub>H<sub>2</sub> was measured at a temperature range between 275 and 375 °C. As shown in **Figure 57**, ZnO\_LB possesses higher response value than ZnO\_S (e.g. 5.8 vs. 1.4 at 375 °C). In addition to response, the electrical resistance of ZnO\_LB in clean air is also greater than that of ZnO\_S by more than 3 orders of magnitude (**Table 9**). These phenomena could be explained by the difference in transducing mechanism: the grain boundary model applicable to ZnO\_LB is more sensitive and resistive than the surface-bulk model of ZnO\_S<sup>19</sup>. Interestingly, the Langmuir-Blodgett film structure also



possesses notably shorter response (46 vs 128 sec) and recovery time (190 vs 253 sec) than conventional thin film. A possible explanation is that microcracks, which only permit slow surface diffusion of gas species, exist within ZnO\_S, and hence prolongs the time required to achieve steady state for the ZnO\_S sensor.

With the loading of Au NPs on the surface of ZnO thin film sensors, the response values towards C<sub>2</sub>H<sub>2</sub> increased by more than 180 and 20 times for ZnO\_LB film and ZnO\_S film, respectively. Moreover, the operating temperatures for maximum response have also decreased from 375 °C to 325 °C because of Au doping. This indicates that Au NPs are effective catalyst for the surface reaction, which serves to enhance the reaction kinetic at lower temperature<sup>129</sup>. As shown in **Table 9**, Au loading also significantly affects other aspects of the gas sensing properties. With the addition of Au NPs, the resistance values in clean air increase by around 60 and 30 times for Au@ZnO\_LB and Au@ZnO\_S, respectively. The addition of Au NPs also dramatically shortens the response time by 10 and 6 times for Au@ZnO\_LB and Au@ZnO\_S, respectively, because Au as a catalyst can lower the activation energy of the C<sub>2</sub>H<sub>2</sub> oxidation reaction, and in turn, increase the reaction rate. As for the recovery process, which entails the re-adsorption of oxygen, re-trapping of free electrons, and desorption of the products of the oxidation reaction, is expedited by loading Au on ZnO\_S, but prolonged by loading Au on ZnO\_LB.

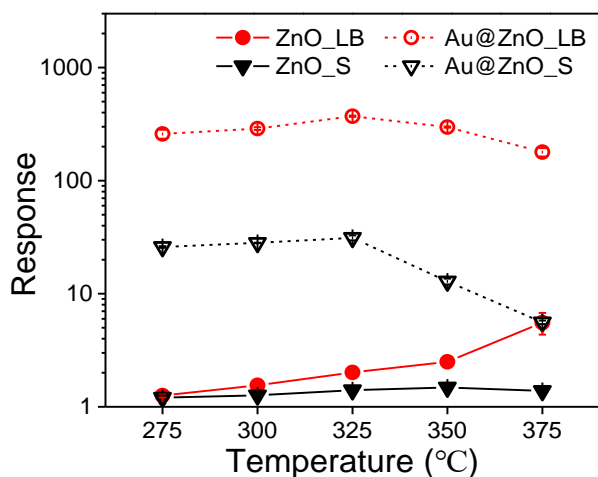


**Figure 57.** Response values towards 25 ppm of  $C_2H_2$  at different operating temperatures.

To evaluate the temporal stability of Au@ZnO\_LB and Au@ZnO\_S, the sensors were exposed to 10 ppm (25 ppm for Au@ZnO\_S) of  $C_2H_2$  at the optimum operating temperature (325 °C) and the response values were recorded 5 times per day for 1 week. Between each day's testing, the sensor was soaked in condition same as the testing condition (10/25 ppm  $C_2H_2$ , 325 °C) to accelerate the aging process.

As shown in **Figure 59 (a)**, the response value as well as resistances in standby ( $R_{air}$ ) and testing mode ( $R_{gas}$ ) remained stable during the whole stability test for Au@ZnO\_LB. On the other hand, for Au@ZnO\_S, fast deterioration of response from 26 at the beginning of the test to 1.8 in 130 hours, a value close to the response recorded with pristine ZnO\_S, was observed as shown in **Figure 59 (b)**. Along with diminishing response, the  $R_{air}$  and  $R_{gas}$  also varied significantly with time. It was revealed with SEM (**Figure 58**) that the Au NPs supported on ZnO\_S film grew from 11 nm to 17 nm during the stability test, causing the reduction in Au catalyst reactivity, and in turn, leading to severe decrease in the sensitization effectiveness. This discrepancy in operating stability signify the glaring

advantage of ZnO\_LB film over ZnO\_S film in the prevention of Au NPs sintering and growth.

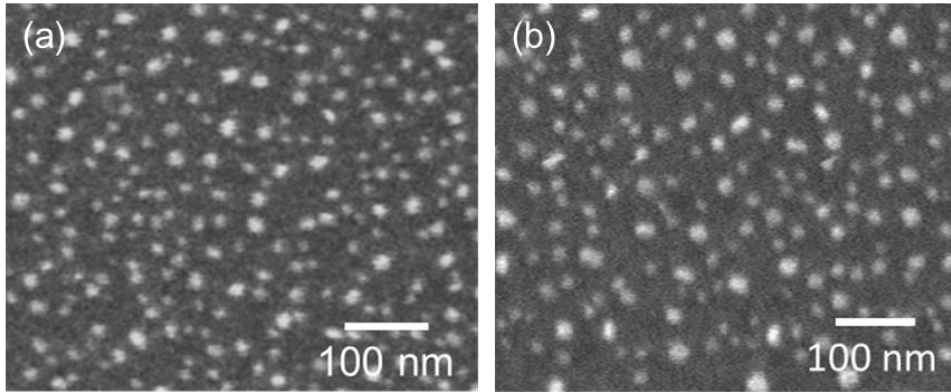


**Figure 58.** SEM images of Au@ZnO\_SF before (a) and after (b) the stability test.

Finally, the performance of Au@ZnO\_LB sensor, which displays the best sensing properties among the four sensors, was examined at its optimal operating condition as a promising C<sub>2</sub>H<sub>2</sub> sensor for air quality monitoring application. Because the concentration of C<sub>2</sub>H<sub>2</sub> in outdoor and indoor environment is in ppb-level, the sensor was exposed to 10-25,000 ppb of C<sub>2</sub>H<sub>2</sub> at 325 °C to record the characteristic curve, which is displayed in **Figure 60 (a)**. Initially, the response increases rapidly in a highly linear fashion with increasing C<sub>2</sub>H<sub>2</sub> concentration from 1.7 at 10 ppb to 178 at 5000 ppb. The sensitivity towards C<sub>2</sub>H<sub>2</sub> in ppb range was thus derived from the slope of this linear region to be around 37 ppm<sup>-1</sup>. At concentrations higher than 5000 ppb, the rate of rise gradually decreased until reaching saturation at 25,000 ppb. The dynamic response to 10-1000 ppb of C<sub>2</sub>H<sub>2</sub> is displayed in the inset of Figure 6 (a). At least three repetitions were made at each concentration, demonstrating the good reproducibility of the sensor response. The response and recovery time as a function of concentration were demonstrated in **Figure 60 (b)**. The response time drops rapidly from 77 sec at 10 ppb to 20 sec at 400 ppb, then

decreases gradually to 5 sec at 25,000 ppb. The recovery time on the other hand increases with concentration and approach a plateau value of around 200 sec at a much slower rate. In the concentration range of interest for air quality monitoring (i.e. 1-1000 ppb), the response time is around 13-20 sec, and recovery time is around 100 sec.

**Table 9.** Key sensing parameters other than response measured at 325 °C towards 25 ppm of C<sub>2</sub>H<sub>2</sub>.

Sample	R <sub>air</sub> (Ω)	Response time (sec)	Recovery time (sec)
ZnO_LB	(1.39 ± 0.02) x 10 <sup>7</sup>	46 ± 1	190 ± 30
ZnO_S	(6.4 ± 0.3) x 10 <sup>3</sup>	128 ± 1	253 ± 6
Au@ZnO_LB	(8.4 ± 0.1) x 10 <sup>8</sup>	5.1 ± 0.4	320 ± 10
Au@ZnO_S	(2.08 ± 0.08) x 10 <sup>5</sup>	19.6 ± 0.7	31.6 ± 0.3

**Figure 60 (c)** shows the response of the Au@ZnO\_LB sensor to common interference gases from the testing environment including carbon monoxide (CO), Hydrogen (H<sub>2</sub>), methane (CH<sub>4</sub>), ethane (C<sub>2</sub>H<sub>6</sub>), and ethylene (C<sub>2</sub>H<sub>4</sub>). A much higher selectivity to C<sub>2</sub>H<sub>2</sub> can be observed in comparison to the pristine ZnO\_LB<sup>130</sup>. The effect of humidity on C<sub>2</sub>H<sub>2</sub> sensing properties was also analyzed. As illustrated in **Figure 60 (d)**, a significant drop in sensitivity from 37 in dry condition to 2.3 ppm<sup>-1</sup> was observed under 40% RH. The dynamic resistance change towards 10 ppb of C<sub>2</sub>H<sub>2</sub> under dry and wet condition was illustrated in the inset of **Figure 60 (d)**. A still discernable signal of 1.07 towards this low concentration of analyte gas was obtained under humid condition. The dramatic drop in R<sub>air</sub> under humid condition conforms with the oxygen-water vapor interplay theory<sup>26</sup>. Moreover, with increasing humidity, the response and recovery time also shortened from 70 to 35 sec and 100 to 25 sec, respectively.

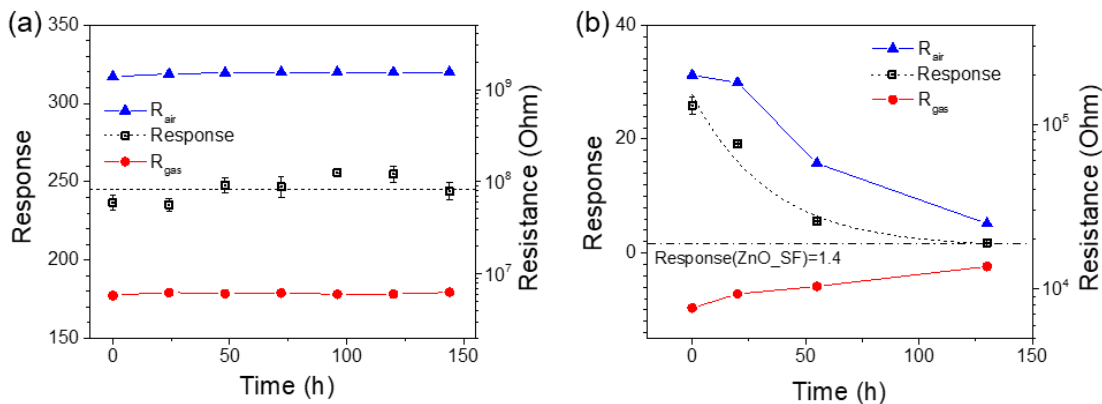


**Figure 59.** sensor stability test results gathered from Au@ZnO\_LB (a) and Au@ZnO\_S (b). the sensors were exposed to 10 ppm (25 ppm for Au@ZnO\_S) of C<sub>2</sub>H<sub>2</sub> at the optimum operating temperature (325 °C) and the response was recorded 5 times per day for 1 week. Between each day's testing, the sensor was soaked in reducing condition (10/25 ppm C<sub>2</sub>H<sub>2</sub>, 325 °C) to accelerate the aging process.

It is necessary to further the investigation on the mechanisms of surface reaction and electrical conduction to explain the extraordinary improvement on the sensitivity towards C<sub>2</sub>H<sub>2</sub> achieved by loading Au NPs. It is commonly observed experimentally that the sensor response is well correlated with the partial pressure of target gas of interest, P<sub>A</sub>, by the following equation:

$$Response = a * P_A^n$$

Where the proportionality constant *a* increases with decreasing D/x<sub>0</sub> ratio (D: diameter of the grain; x<sub>0</sub>: depletion layer width)<sup>29,131</sup> and the exponent factor *n* is mainly dictated by the type of ionized oxygen species (molecular or atomic) and the reaction order of P<sub>A</sub> in the surface reactions<sup>31,132</sup>.

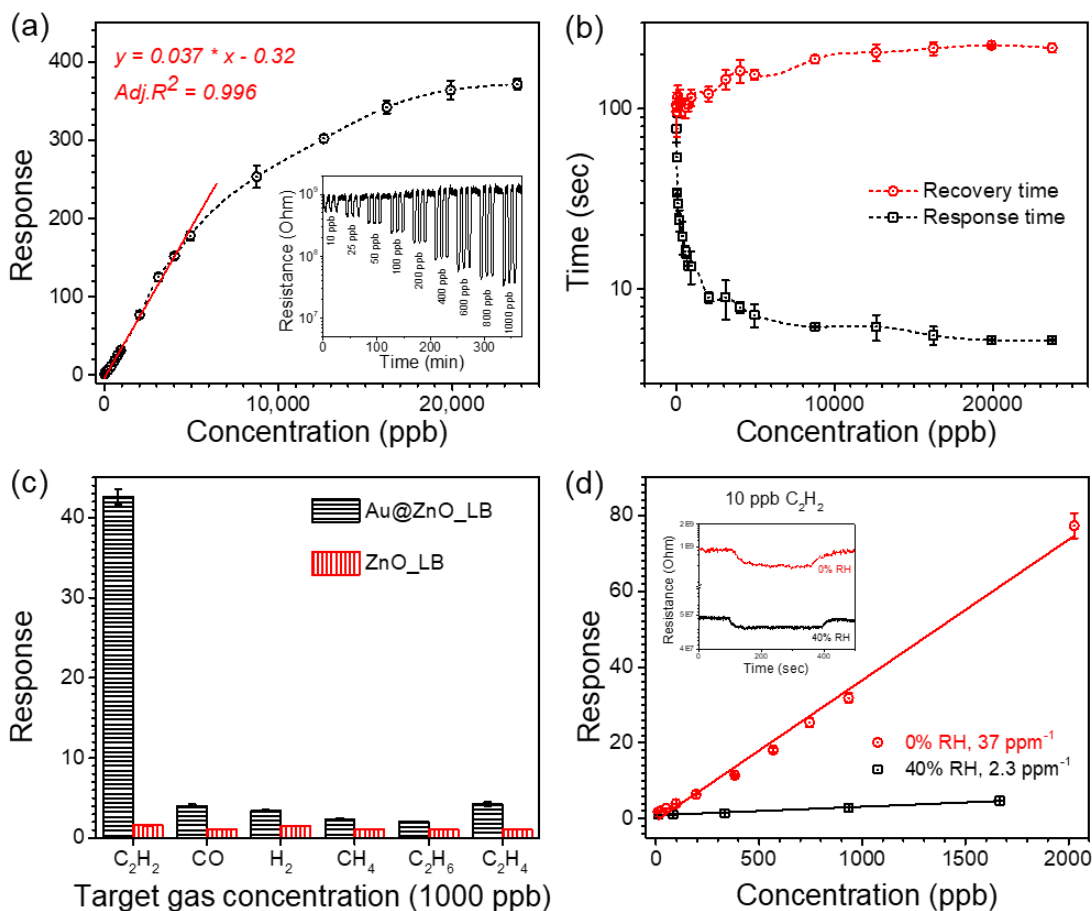


**Figure 60.** (a) Characteristic curve of Au@ZnO\_LB obtained at the optimal working condition with linear response observed between 10-5000 ppb. Inset shows the transient response curve towards 10-1000 ppb of C<sub>2</sub>H<sub>2</sub>. (b) Response and recovery time variations as a function of concentration. (c) selectivity towards C<sub>2</sub>H<sub>2</sub> over other gases with and without Au dopant on ZnO\_LB. (d) effect of 40% relative humidity on the sensitivity of Au@ZnO\_LB. Inset shows the transient response curve towards 10 ppb of C<sub>2</sub>H<sub>2</sub> obtained under dry and humid conditions.

Firstly, loading the Au NPs on ZnO films led to notable increase in the baseline resistance of ZnO thin film (i.e. 60 and 30 times for ZnO\_LB and ZnO\_S, respectively). Because the Au NPs are isolated and only present at the top surface of the sensing film, the increase in the baseline resistance should be attributed to the decrease of conductivity in

the ZnO thin films underneath, which provide the main path for electron conduction. As illustrated in **Figure 61** (a) the transportation of electron within the ZnO\_LB film could be severely throttled due to the formation of deeper electron depletion layer (EDL) underneath the ZnO/Au contact. The expansion of EDL (decrease of  $D/x_0$ ) could arise from either the formation of Schottky junction between Au and ZnO, or by the oxygen spill-over effect of Au NPs<sup>133</sup>. When the sensor is exposed to reducing gas (e.g.  $C_2H_2$ ), the reducing gas molecules react with oxygen anions and release the electrons back to the conduction band, causing reduced charge depletion depth and thereby opens the conduction channel within the nanowire as shown in **Figure 61** (b). Electrons under bias may then flow freely through the conduction channel, and the sensor becomes much more conductive. As a result, a small gas concentration can then work like a switch closing or opening the conducting channel of ZnO nanowires, leading to tremendous sensor response.

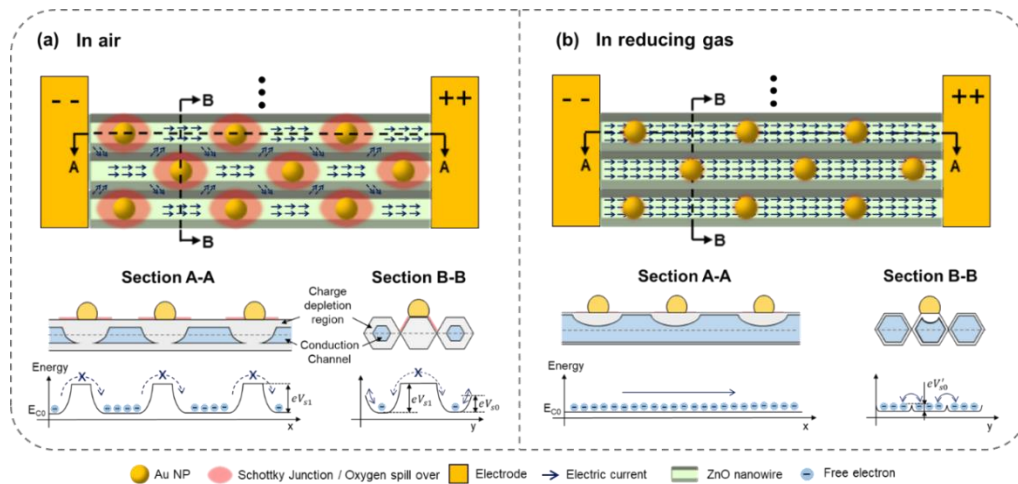
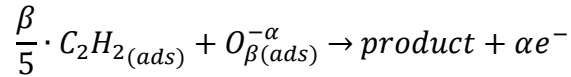
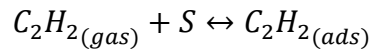
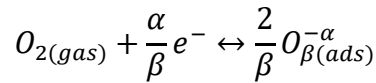


**Figure 61.** Schematic of electron conduction mechanism of Au@ZnO\_LF in air and in reducing gas. In air, electron may only flow in short distance along the nanowires within the conduction channel, before being forced to diverge from the high potential barrier  $eV_{s0}$  in the fully depleted region to adjacent nanowires by overcoming a lower potential barrier  $eV_{s0}$ . While in reducing atmosphere, the consumption of oxygen species leads to

reduced charge depletion depth. Electrons under bias may then flow freely through the conduction channel, and the sensor becomes much more conductive.

Secondly, the exponent factor  $n$  is sensitive to the change in the reaction order of the surface reaction, which is strongly affected by the degree of coverage achieved by a reactant for a surface-catalyzed reaction<sup>134</sup>. Considering the most frequently proposed reaction scheme for reducing gas detection with semiconducting metal oxides, involving the total oxidation of reducing gas by one predominant type of ionosorbed oxygen species via a Langmuir-Hinshelwood mechanism<sup>132</sup>, the following quasi-chemical reactions are proposed for  $C_2H_2$ :



By considering the rate equation and space charge layer formation<sup>132</sup>, the theoretical value of exponent factor  $n$  for sensing  $C_2H_2$  gas can be easily deduced to be 0.4 when the predominant ionized oxygen species are  $O_2^-$ , and 0.1 when the predominant oxygen anions are  $O^-$ . **Figure 62** shows that for the pristine ZnO\_LB sample, the exponent factor matches the theoretical value for total oxidation with  $O_2^-$ , while the Au doped sample has an exponent factor of 1, which is much higher than the theoretical values under the premise of total oxidation. This indicates that the Au NPs might have altered the reaction order by changing the relative concentration of  $C_2H_2$  to ionized oxygen on the ZnO surface by  $C_2H_2$



spillover effect. The higher ratio of  $C_2H_2$  to ionized oxygen should be more favorable to partial oxidation reaction, and hence the response becomes more sensitive to the concentration change of  $C_2H_2$ .

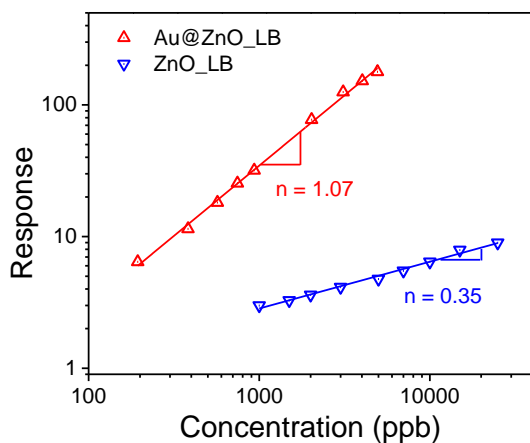


**Figure 62.** The calibration curves towards acetylene plotted in log-log scale to reveal the exponent factor.

The excellent selectivity of Au@ZnO\_LB towards  $C_2H_2$  can be explained by its strong and selective chemisorption on Au NPs at high temperature.  $C_2H_2$  has been observed to adsorb strongly on the surface of noble metals, due to its high capacity as an electron donor<sup>135</sup>. This characteristic is verified by experiments conducted by Azizi et al. where inhibition of CO oxidation was observed in the presence of  $C_2H_2$ <sup>134</sup>. A fundamental study of acetylene oxidation on the (1 1 1) platinum surface revealed that the adsorption of acetylene occurs through a strong  $\pi$ - $\sigma$  bonding between the gas and platinum surface<sup>136</sup>, which is absent in gas species like  $H_2$ ,  $CH_4$ , and  $C_2H_6$ . As for the selectivity over  $C=C$ s, it has been postulated by DFT calculations<sup>137</sup> and verified experimentally<sup>138</sup> that only  $C\equiv C$ s

are adsorbed and activated in the periphery of Au nanoparticles, whereas C=Cs are not bonded, despite both possess unsaturated  $\pi$  bonds.

By benchmarking Au@ZnO\_LB sensor against state-of-the-art semiconductor-type acetylene sensors reported in the last decade (**Table 10**), it is apparent that Au@ZnO\_LB sensor developed in this work possesses unmatched sensitivity, more than 10 times higher than the best record reported in the literature. Attributed to this unprecedented sensitivity, detection limit of 3 ppb (the concentration at which signal-to-noise ratio equals to 3) becomes achievable, whereas previously detection below 30 ppb was impossible. Other than sensitivity, the sensor developed in this work also possesses high selectivity and fast response and recovery time in comparison to literature.

**Table 10.** Selected works studying the C<sub>2</sub>H<sub>2</sub> sensing performance of various MOX gas sensors

Materials	Microstructure	Sensitivity (ppm <sup>-1</sup> )	LOD (ppb)	Selectivity			t <sub>res</sub> /t <sub>rec</sub> (sec)	Ref
				C <sub>2</sub> H <sub>2</sub> /CO	C <sub>2</sub> H <sub>2</sub> /H <sub>2</sub>	C <sub>2</sub> H <sub>2</sub> /CH <sub>4</sub>		
Au-ZnO	aligned nanowires	37	3	11	12	18	14/115 (1 ppm)	this work
Au-ZnO	nanoring thick film	0.22	30	9	-	14	4/3 (100 ppm)	139
Pt-Al <sub>2</sub> O <sub>3</sub> /ZnO	vertical nanowire array	0.033	1000	-	-	6	300/500 (20 ppm)	140
ZnO	particulate porous film	1.5	120	-	-	-	10/30 (20 ppm)	141
ZnO	mesoporous nanosheet thick film	0.41	60	38	15	38	10/10 (10 ppm)	142
Au-ZnO	3D porous microspheres thick film	3.1	40	30	60	60	1/20 (20 ppm)	143
Ag-ZnO-RGO	3D porous microspheres thick film	0.34	220	-	-	-	43/100 (100 ppm)	144

ZnO-RGO	particulate porous film	0.19	4800	14	3	-	100/24 (100 ppm)	145
Ag-ZnO	vertical nanowire array	0.16	30	8	6	-	8/43 (1000 ppm)	146
Ni-ZnO	random oriented-nanowire thick film	0.0065	5900	-	-	-	5/10 (2000 ppm)	2
Au-ZnO/In <sub>2</sub> O <sub>3</sub>	random oriented-nanowire thick film	0.020	550	2.5	-	7	9/20 (100 ppm)	147
Co-ZnO	3D porous microspheres thick film	0.20	330	-	3	2	35/51 (400 ppm)	6
ZnO	3D porous flower likes thick film	0.099	170	1.6	1.4	1.3	-	148
Pt-SnO <sub>2</sub>	3D porous flower likes thick film	0.26	30	-	-	1.7	-	149
SmFeO <sub>3</sub>	particulate porous film	0.021	2200	8	-	-	10/60 (80 ppm)	150
RGO-SnO <sub>2</sub>	particulate porous film	0.45	120	6	3	1.5	54/23 (1ppm)	151
Sm <sub>2</sub> O <sub>3</sub> -SnO <sub>2</sub>	particulate porous film	1.1	220	8	5	-	10/13 (500 ppm)	152

---

## 6. METAL-OXIDE NANOPARTICLES WITH A DOPANT-SEGREGATION-INDUCED CORE-SHELL STRUCTURE: GAS SENSING PROPERTIES

### 6.1 Introduction

Metal-oxide-based chemiresistors are a type of solid-state gas sensors with wide applications in both industrial and domestic sectors<sup>153–155</sup>. When a metal-oxide-based chemiresistor is exposed to reducing/oxidizing gas species, redox reactions occur between the reducing/oxidizing gas species and the surface oxygen of a metal oxide (either chemisorbed or in the crystal lattice), and lead to a change in the electrical resistance on the surface as the output signal of the chemiresistor. Because the surface reaction is the main contributor to the electrical signal, a successful strategy to improve the sensitivity is to increase the surface area to bulk volume ratio by decreasing the size of metal oxide to the nanometric level<sup>156–158</sup>.

However, gas sensors made from metal oxide nanoparticles with high surface-to-bulk ratio are often susceptible to thermal degradation caused by grain growth and coalescence during service at high working temperature (200–400 °C)<sup>9,40,41</sup>. Therefore, it is crucial to develop an effective strategy to control the rate of grain growth of these nanomaterials without compromising the sensitivity. In metallurgy, a common technique to suppress grain growth is by introducing impurity atoms or phases to pin the grain boundaries, or to decrease the grain boundary energy<sup>42</sup>. Based on the same mechanism, Leite et al. doped several rare earth elements (e.g. Y, La, and Ce) into tin (IV) oxide, the most widely studied metal oxide for sensor application, to form a metastable solid solution<sup>43,44</sup>. After high temperature annealing, the aliovalent dopants segregate to the surface of the nanoparticles

to minimize the elastic strain energy and electrostatic interaction energy of the system <sup>45</sup>, resulting in the formation of a dopant-segregation-induced core-shell structure with a dopant-rich shell and a dopant-less core. This structure serves to prevent further thermally-induced grain growth and coalescence by reducing the particle boundary mobility and/or the thermodynamic driving force <sup>43,44</sup>. Aluminum is a promising dopant for SnO<sub>2</sub> sensors that can promote the sensitivity and possibly enhance thermal stability. Several research groups <sup>159,160,161</sup> have reported the promoting effect of doping Al on the sensitivity of SnO<sub>2</sub> sensors, and they found Al dopant serves to increase oxygen chemisorption, decrease particle size, and increase charge depletion depth. However, information about the influence of this core-shell structure and dopant concentration on gas sensing performance is lacking.

In this work, we report for the first time the formation of dopant-segregation-induced core-shell structure on Al-doped SnO<sub>2</sub> nanoparticles, and study the effect of forming this structure on the H<sub>2</sub> sensitivity. To uncover any composition-structure-properties (Al-conc., core-shell structure, H<sub>2</sub> sensitivity) relationship within this system requires a synthesis method that allows the formation of Al<sub>2</sub>O<sub>3</sub>-SnO<sub>2</sub> metastable solid solution with wide range of Al-concentration. For this reason, a polymeric precursor method was chosen in this work to synthesize Al-doped SnO<sub>2</sub> nanoparticles because it enables formation of metastable solid solution even at doping concentration as high as 50 mol% <sup>162</sup>. The present paper reports characterization results of the surface and the bulk of such formed powders, and the influence of the core-shell structure and doping concentration on gas sensing sensitivity in terms of morphology and surface chemistry of the Al doped SnO<sub>2</sub> film.

## 6.2 Experimental

### 6.2.1 Preparation of Pure and Aluminum Doped SnO<sub>2</sub> Nanoparticles

Citric acid, SnCl<sub>2</sub>·2H<sub>2</sub>O and ethylene glycol (all from Alfa Aesar, USA). Al(NO<sub>3</sub>)<sub>3</sub>·9H<sub>2</sub>O (from Fisher Scientific, (USA), all of reagent grade, were used without further purification. Tin citrate aqueous solution was first made from SnCl<sub>2</sub>·2H<sub>2</sub>O and citric acid with a citric acid/metal molar ratio of 3:1. Following the same ratio, aluminum citrate aqueous solution was prepared from Al(NO<sub>3</sub>)<sub>3</sub>·9H<sub>2</sub>O and citric acid. For aluminum doped samples, proper amount of aluminum citrate aqueous solution was added into tin citrate aqueous solution, and the Al concentration of each sample was calculated based on the Al/Sn molar ratio. Ethylene glycol was added to the final solution at a mass ratio of 2:3 in relation to the citric acid to promote polymerization. An xerogel was formed after heating the solution on a hot plate at 150 °C for 5 h, and further calcined at 350 °C for 5 h. It was then ball milled for 12 h at a frequency of 15 Hz. The obtained powder was calcined in a furnace at 600 °C for 4 h to obtain Al<sub>2</sub>O<sub>3</sub>-SnO<sub>2</sub> metastable solid solutions (as-synthesized). To facilitate the formation of Al-rich surface layer, the Al<sub>2</sub>O<sub>3</sub>-SnO<sub>2</sub> solid solution powders underwent a post-thermal-treatment at 1100 °C for 4 h (thermally-treated).

### 6.2.2 Characterization

X-ray diffraction (XRD) patterns were recorded on a Bruker D8 focus diffractometer using Cu K $\alpha$  radiation ( $\lambda=1.5406 \text{ \AA}$ ) and Rietveld refinement was performed for grain size and cell parameters analysis using the BGMN program<sup>163,164</sup> and the graphical interface Profex<sup>165</sup>. X-ray photoelectron spectra were obtained using a VG ESCALAB 220i-XL photoelectron spectrometer and Al-K $\alpha$  radiation (15 KeV) at about  $1.3 \times 10^{-9}$  mbar base pressure. C(1s), Al (2p), O(1s) and Sn(3d5/2) core level high-resolution spectra and wide

scan spectra were. C(1s) peak is used to calibrate peak position. Curve fitting of O(1s) spectra was done with a spin-orbit coupling of 2:1 area ratio using CasaXPS software. The same software was used for calculation of the elementary percentage from the recorded spectra. Field emission scanning electron microscopy (AMRAY 1910,) and energy dispersive x-ray spectrometry (EDS) were used for morphological and semi-quantitative atomic compositional studies. For the EDS tests, they were performed under the following testing condition: accelerating voltage 15 kV, take-off angle 46.40°, and spot size of the electron beam around 50 nm. Specific surface area determinations were performed using the Brunauer–Emmett–Teller (BET) method with a nitrogen adsorption porosimeter (model ASAP 2020, Micromeritics). Long term stability test was performed on as-synthesized samples and thermally treated samples with 0 and 5 mol% of dopants at 400°C in air. The changes in crystallite size and cell parameters were monitored with XRD.

### 6.2.3 Gas Sensor Fabrication and Sensing Measurements

Thick sensing layers (~10 μm) were deposited by dropping thermally treated powder aqueous suspension dispersed by ultrasonication on alumina substrates with preprinted gold interdigitated electrodes (bands/gaps 200 μm, DROPSSENS). After deposition, the sensors were first dried at 40 °C and 60 RH mol% for 1 h, and then annealed at 500 °C for 5 h. Gas sensing characteristic was measured with a home-built gas sensor testing system (as shown in **Figure 63**) consisting of a test chamber made of quartz tube, a temperature control system (including a ceramic heater, a thermocouple, and a temperature controller), a data acquisition system (a Keithley multimeter-2700 connected to a PC), and mass flow controllers. The sensors were tested at 300 °C for H<sub>2</sub>/air mixture with a concentration

between 2 ppm to 50 ppm. Sensitivity was defined as the ratio ( $S = R_a/R_g$ ) of the resistance of the sensor in target gases ( $R_g$ ) and that in dry air ( $R_a$ ).

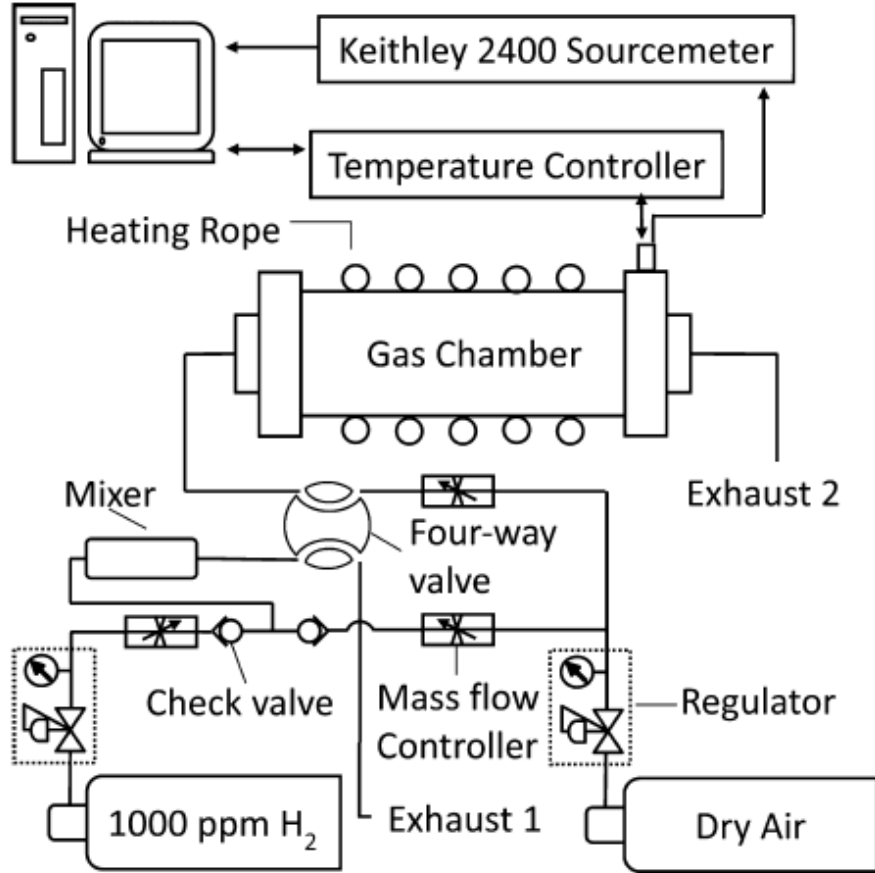


**Figure 63.** Schematic of the gas sensor testing system.

### 6.3. Results and Discussion

#### 6.3.1 Structure and Thermal Stability Improvement of Al-doped SnO<sub>2</sub>

##### 6.3.1.1 Formation of Dopant-segregation-induced Core-shell Structure

**Figure 64** shows XRD patterns of the as-synthesized and thermally-treated Al-doped SnO<sub>2</sub> powders. Only XRD peaks corresponding to SnO<sub>2</sub> with rutile structure are observed for as-synthesized and thermally-treated samples, except for the thermally-treated sample



with a doping concentration of 25 mol%, which is polyphasic because of the appearance of  $\alpha$ -alumina peaks. Therefore, solid solutions of  $\text{Al}_2\text{O}_3$  and  $\text{SnO}_2$  are formed for both as-synthesized and thermally-treated samples in the doping range between 0-10 mol%.

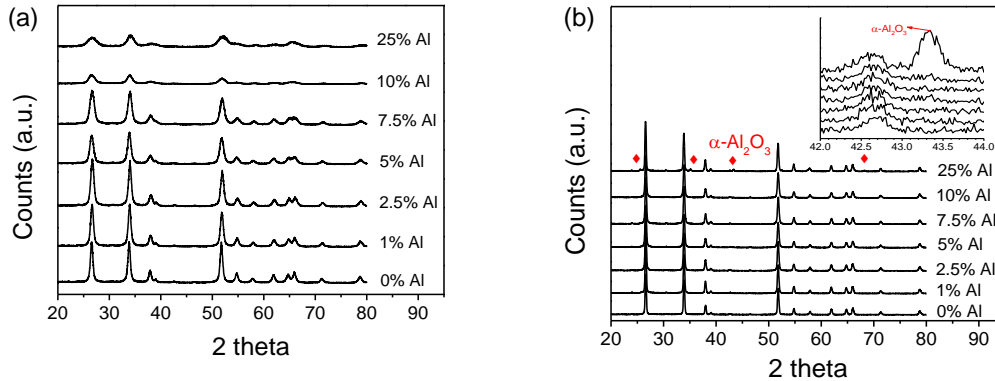


**Figure 64.** (a) XRD patterns of as synthesized samples and (b) thermally treated samples.

Detailed crystallographical information revealed by Rietveld refinement is shown in **Figure 65**. For the as-synthesized samples, the cell parameter ratio  $c/a$  of the rutile  $\text{SnO}_2$  phase decreases linearly with doping concentration, suggesting an anisotropic compression of the unit cell along the  $c$  axis. This compression becomes stronger as the doping concentration is increased. This indicates that smaller  $\text{Al}^{3+}$  ions ( $0.51 \text{ \AA}$ ) have been incorporated into  $\text{SnO}_2$  lattice by substituting the larger  $\text{Sn}^{4+}$  ions ( $0.71 \text{ \AA}$ ), and metastable solid solutions are formed even at doping concentration as high as 25 mol%<sup>162</sup>. On the other hand, the  $c/a$  ratio remains constant over the entire range of doping concentration after the thermal treatment at  $1100 \text{ }^\circ\text{C}$  for 4 h, suggesting that the solid solution formation is probably restricted to the surface of particles, and hence undetectable by XRD. Therefore, driven by strain energy and electrostatic interaction energy<sup>45</sup>,  $\text{Al}^{3+}$  ions have migrated from the inner lattice sites towards the surface of the particles, and form the Al-rich shell during

the post-heat-treatment. In comparison, dopant segregation process cannot be initiated for as-synthesized sample, because the synthesis temperature (600 °C) is too low to overcome the activation energy required. For the thermally-treated sample with a doping concentration of 25 mol%, a core-shell structure formed by dopant segregation is probably still very thermodynamically unstable. As a result, a complete phase separation might have occurred, which left the whole doping element resides in particles of own oxide, and left the SnO<sub>2</sub> phase dopant-free (c/a ratio same as pure SnO<sub>2</sub>).

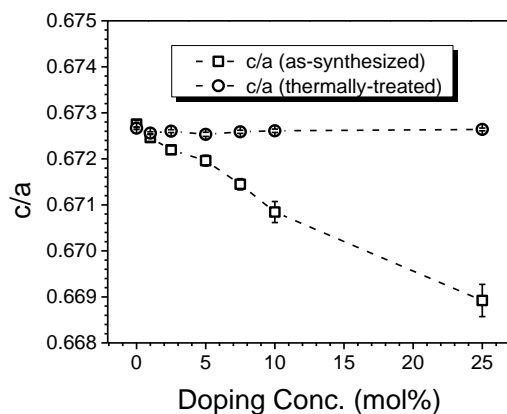


**Figure 65.** c/a ratio as a function of doping concentration for as-synthesized and thermally treated powders.

To further confirm the formation of dopant segregation induced core-shell structure, XPS wide scans of thermally-treated samples with doping concentration range from 0-10 mol% was performed (25 mol% Al-doped sample is not included because of its polyphasic nature revealed by XRD). As shown in **Figure 65** (a), the presences of Sn, Al and O are confirmed. The presence of carbon peak is due to surface contamination or adsorbed carbonaceous species. As shown in **Figure 65** (b), the quantitative analysis of XPS results show that the Al concentration at the surface is 2 to 10 times larger than the doping

concentration used when preparing the samples. To confirm the bulk composition (including both core and shell) of the samples, energy-dispersive X-ray spectroscopy (EDS), a characterization technique with a depth resolution of the order of microns, was used to analyze the samples, and the results are also given in **Figure 66** (b). As shown, the EDS measured bulk compositions for all the samples are essentially the same as the theoretical doping concentrations, which is expected because of the large sample size (hundreds of nanoparticles) probed by EDS. Combining the evidences of XPS quantifying high concentration of Al on the sample surface, XRD showing no secondary phase formation and constant  $c/a$  ratio for samples with Al doping content  $\leq 10$  mol%, and EDS of consistent Al concentration in the bulk, confirm the formation of dopant-segregation-induced core-shell structure for the Al-doped SnO<sub>2</sub> samples after the thermal treatment<sup>43</sup>.

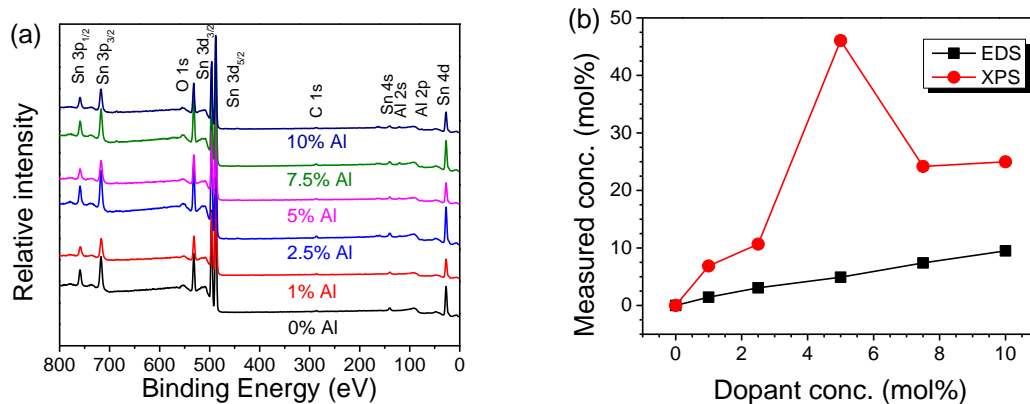


**Figure 66.** (a) XPS wide scan for thermally treated samples. (b) Surface & bulk (including both core and shell) concentration of Al determined by XPS & EDS as a function of theoretical concentration.

### 6.3.1.2 Particle Size of Pure and SnO<sub>2</sub> Samples with Core-shell Structure

Low-magnification bright-field (BF) transmission electron microscopy (TEM) images of three as-synthesized samples with doping concentrations of 0, 5 and 25 mol%,

respectively are shown in **Figure 67**. In the as-synthesized state, the particles are uniform and well crystallized, which is confirmed by the clear lattice fringes shown in the insets of **Figure 67**. The mean particle sizes for the three samples based on the TEM images are around 20, 15, and 5 nm, respectively, which are very close to the crystallite size estimated using the Rietveld Refinement method based on the XRD result. Therefore, particle size changes of pure and doped SnO<sub>2</sub> samples were evaluated based on the XRD results. As shown in **Table 11**, after the thermal treatment at 1100°C for 4h, grain growth is observed for samples with or without Al-rich shell. However, the solute-drag effect occurred in the core-shell structure slows down the grain growth rate from  $3.87 \times 10^{-2} \text{ nm}/^\circ\text{C}\cdot\text{h}$  for pure SnO<sub>2</sub> particles to  $1.52 \times 10^{-2} \text{ nm}/^\circ\text{C}\cdot\text{h}$  for 5 mol% Al-SnO<sub>2</sub> particles. As a result, particles covered with Al-rich shell are smaller than bare SnO<sub>2</sub> samples.

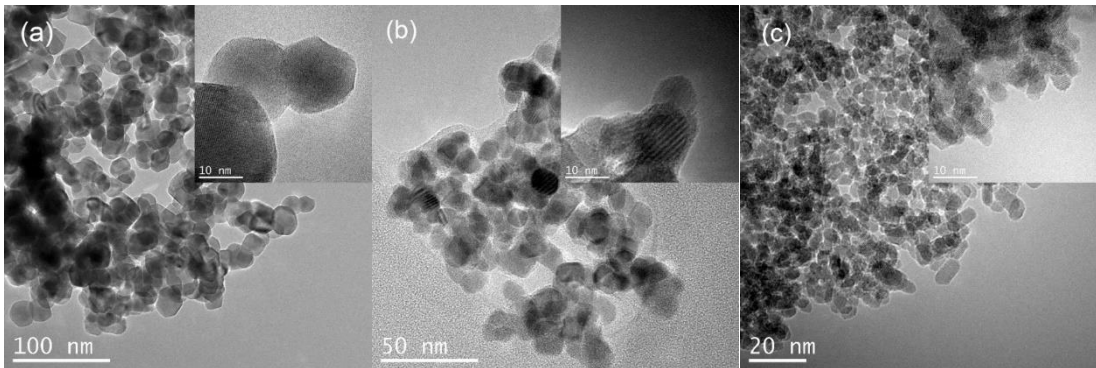


**Figure 67.** TEM images of three as-synthesized samples with doping concentrations of (a) 0 mol%, (b) 5 mol%, and (c) 25 mol%.

In terms of the influence of doping concentration on the core-shell structure, the grain growth rate initially decreases from  $3.54 \times 10^{-2} \text{ nm}/^\circ\text{C}\cdot\text{h}$  at 1 mol% to a minimum value of  $1.52 \times 10^{-2} \text{ nm}/^\circ\text{C}\cdot\text{h}$  at 5 mol%. This suggests that the efficacy of the Al-rich shell in inhibiting grain growth increases with doping concentration until an optimum value is reached at 5 mol%. According to the classical model for solute drag effect proposed by

Lücke and Detert in <sup>166</sup>, the solute drag force exerted on the surface of individual particles can be written as

$$P_i = nC^0 f$$

where n is the number of dopants per unit area on the surface, f is the force exerted on the surface by a single dopant, and C<sup>0</sup> is the concentration of dopants near the surface. Because the surface concentration of Al increases with doping concentration in the range between 1 and 5 as revealed with the XPS results, the enhancement in the grain growth inhibiting ability of the Al-rich shell achieved in this dopant concentration range can be explained based on the resulted increase in solute drag force.

**Table 11.** particle sizes of as-synthesized and thermally-treated samples with Al content between 0-25 mol% and grain growth rate.

Doping Conc. (mol%)	D <sub>as-synthesized</sub> (nm)	D <sub>thermally-treated</sub> (nm)	Grain Growth Rate (10 <sup>-2</sup> nm/°Ch)
0.0	19.1	96.4	3.87
1.0	17.4	88.1	3.54
2.5	15.3	65.7	2.52
5.0	12.1	42.5	1.52
7.5	10.9	56.8	2.30
10.0	7.2	53.4	2.31
25.0	4.1	99.4	4.77

For the samples with doping concentration exceeding 5 mol%, the grain growth rate rises again from 1.52x10<sup>-2</sup> nm/°Ch at 5 mol% to 2.31\*10<sup>-2</sup> nm/°C.h at 10 mol%. In this concentration range, the Al-rich shell is likely to be over-saturated. This over-saturation is often relaxed by the nucleation of amorphous dopant rich particles on the surface, which are less effective in terms of controlling grain growth <sup>167</sup>. The high-resolution XPS spectra of the Al 2p peak of the thermally-treated samples (Figure 22) shows no obvious shift in

binding energy, which suggests that Al remains as dopant in SnO<sub>2</sub> instead of forming a second phase at doping concentration higher than 5 mol%<sup>168</sup>. Moreover, as depicted in **Figure 68**, the decrease in Al surface concentration observed in XPS can be explained by the nucleation of dopant rich particles, which serves to lower the Al concentration in the shell<sup>168</sup>. When the dopant distribution is homogeneous across the sample surface (**Figure 69 (a)**), XPS, a technique probes only the top few atomic layers of a sample, will reveal notable Al enrichment on the sample surface because of dopant segregation. For the samples with 7.5 and 10 mol% Al, nucleation of Al-rich particles will expose surface with lower doping concentration (**Figure 69 (b)**). As a result, fewer photoelectrons corresponding to Al will be generated per unit of area.

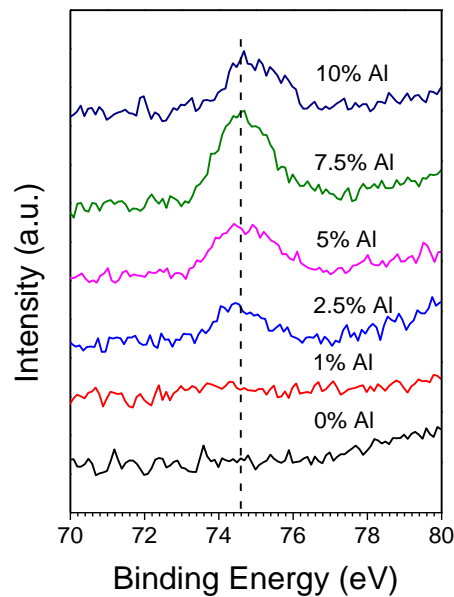


**Figure 68.** High-resolution XPS spectra at binding energies corresponding to the Al 2p.

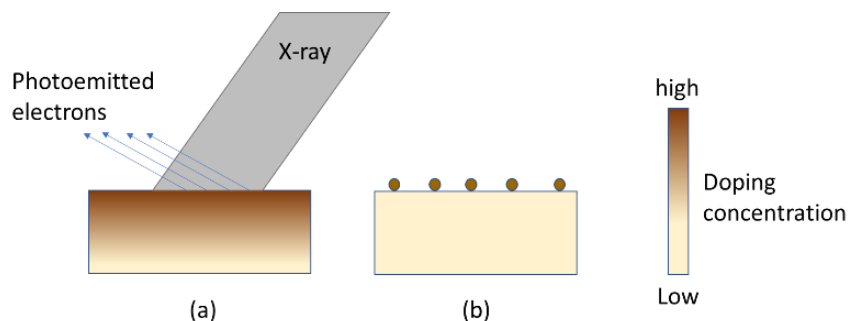


**Figure 69.** (a) high level of dopant segregation on the surface, therefore, the dopant concentration measured by XPS is much higher than theoretical doping concentration; (b) nucleation of Al-rich particles, surface with low dopant concentration exposed.

To illustrate the effectiveness of the core-shell structure on controlling thermal degradation during sensor use, Al-doped SnO<sub>2</sub> powders with core-shell structure underwent thermal treatment at 400 °C in air for 15 days, and the crystallite size remained constant (**Figure 70**). In comparison, after the long-term stability test, the crystallite sizes of as-synthesized SnO<sub>2</sub> with 0 and 5 mol% dopants increase by 70 % and 35 %, respectively. This suggests that the as-synthesized samples have low thermal stability, possibly due to their low crystallinity and defect-rich surface, both of which serve to promote atomic diffusion on the surface<sup>169,170</sup>. On the other hand, the stability of the thermally-treated samples is much improved due to higher crystallinity. Besides, the formation of core-shell structure also serves to stabilize the structure by reducing the particle boundary mobility and the thermodynamic driving force<sup>43,44</sup>. Interestingly, although notable grain growth has been observed for the as-synthesized samples, the *c/a* ratio remains constant throughout the whole testing period (**Figure 71**). This suggests that dopant segregation process doesn't occur under normal working condition for gas sensing, and hence the core-shell structure may persist once formed.

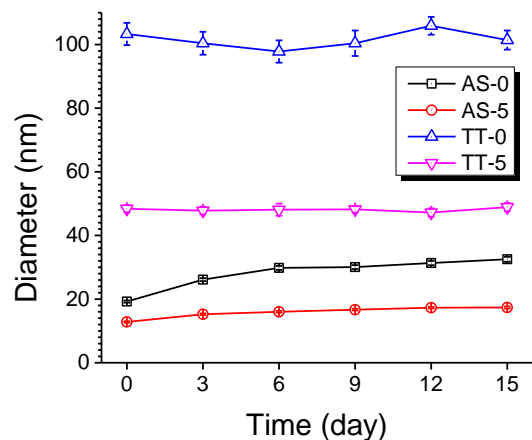


**Figure 70.** Crystallite size of as-synthesized samples with 0 and 5 mol% doping concentration (AS-0 & AS-5) and thermally-treated samples with 0 and 5 mol% doping concentration (TT-0 & TT-5) as a function of time at 400 °C.

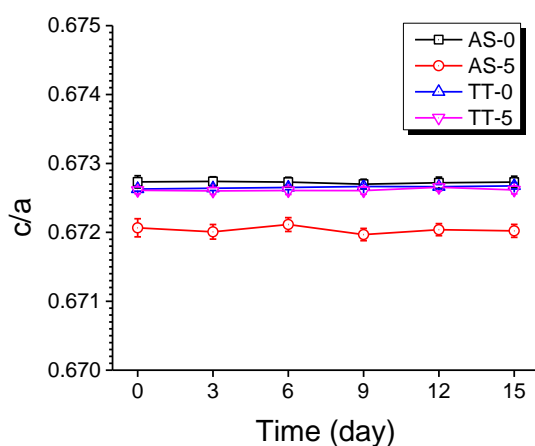


**Figure 71.** c/a ratio of as-synthesized samples with 0 and 5 mol% doping concentration (AS-0 & AS-5) and thermally-treated samples with 0 and 5 mol% doping concentration (TT-0 & TT-5) as a function of time at 400 °C.

### 3.3.1.3 Coalescence Degree of Bare and SnO<sub>2</sub> Samples with Core-shell Structure

To evaluate the difference in the level of coalescence of the pure SnO<sub>2</sub> and the Al-rich shell covered SnO<sub>2</sub> samples, surface area measurements were performed based on the Brunauer-Emmett-Teller (BET) method for the thermally-treated samples. As shown in



**Table 12**, the samples with core-shell structure have higher surface area value than the bare SnO<sub>2</sub> sample. Assuming the particles are spherical in shape for all samples, an effective particle size value ( $D_{\text{BET}}$ ) can be deduced from the surface area value, and the ratio between  $D_{\text{BET}}$  and  $D_{\text{XRD}}$  should be a valid indicator for the degree of agglomeration<sup>43</sup>. The pure SnO<sub>2</sub> sample is in a more advanced stage of coalescence than SnO<sub>2</sub> sample with core-shell structure, because the ratio for pure SnO<sub>2</sub> is the smallest among all the samples. This observation is further confirmed with TEM. As shown in the insets of **Figure 72** (a), broad well-defined necks formed between pure SnO<sub>2</sub> particles can be observed, while no obvious neck formation is observed for Al-doped SnO<sub>2</sub> with core-shell structure (**Figure 72** (b)).

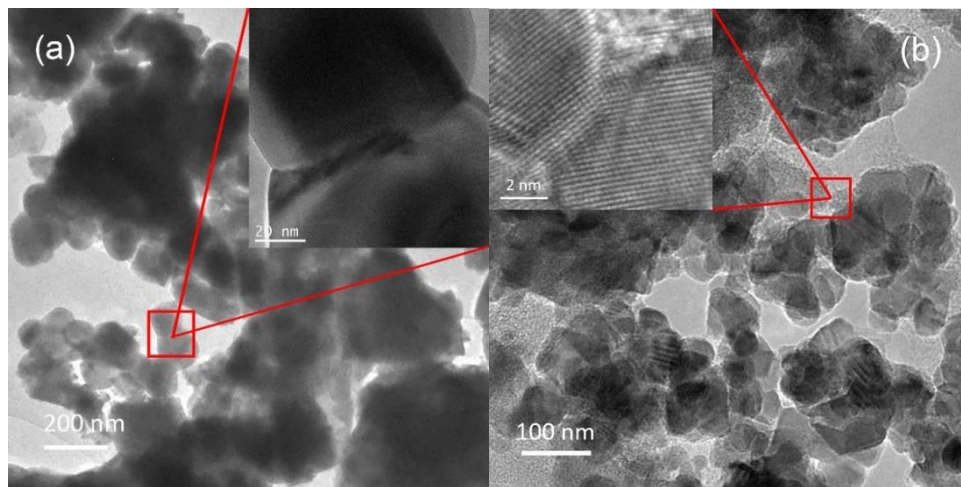


**Figure 72.** TEM images of (a) pure SnO<sub>2</sub> and (b) SnO<sub>2</sub> samples with 5 mol% Al.

In terms of the dependence of coalescence level on doping concentration, a trend similar to that of particle size can be observed. Within the dopant rich shell, the dislocation mobility is impaired due to the same solute drag effect, and hence the neck formation process is also retarded. With increasing doping concentration, the solute drag effect initially becomes more pronounced because of the increase in dopant concentration within the dopant rich shell. When doping concentration exceeds 5 mol%, the solute drag effect

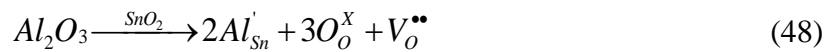
is weakened due to the nucleation of dopant rich particles. As a result, the coalescence level of the samples with core-shell structure becomes higher at doping concentration larger than 5 mol%.

**Table 12.** Grain coalescence level as a function of doping concentration

Doping Conc. [mol%]	BET Surface Area [m <sup>2</sup> /g]	Particle Size (D <sub>BET</sub> ) [nm]	Particle Size (D <sub>XRD</sub> ) [nm]	D <sub>BET</sub> /D <sub>XRD</sub>
0.0	1.27	671.4	96.4	7.1
1.0	2.12	401.4	88.1	4.5
2.5	4.24	200.5	65.7	3.0
5.0	12.49	68.1	42.5	1.6
7.5	8.82	96.3	56.8	1.7
10.0	7.73	110.0	53.4	2.0

### 6.3.2 Gas Sensing Properties and Mechanisms

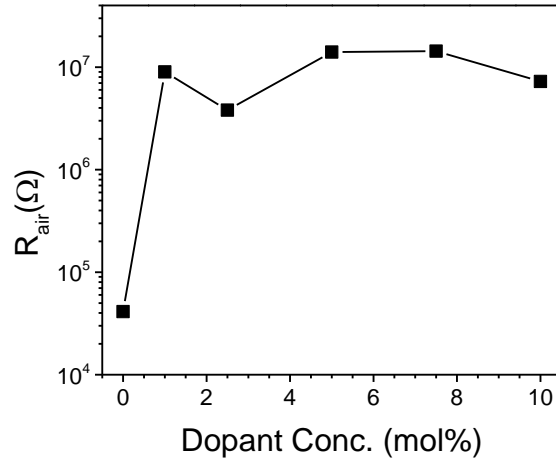
Pure SnO<sub>2</sub> and SnO<sub>2</sub> powders with dopant-segregation-induced core/shell structure (1-10 mol% Al conc.) were used to fabricate thick film sensors. The electrical resistance values of all the sensors were first measured in air at 300°C. As shown in **Figure 73**, the resistance of the samples with core-shell structure is more than 2 orders of magnitude larger than that of pure SnO<sub>2</sub>. The substitution of Sn<sup>4+</sup> with Al<sup>3+</sup> can be expressed in the following Kröger-Vink notation as:



For n-type SnO<sub>2</sub>, the formation of the oxygen vacancy drives the following reaction towards right:

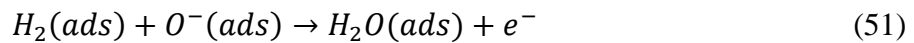
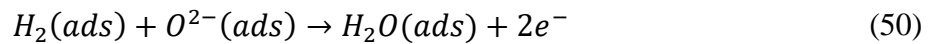


which reduces free-electrons in the conduction band. Therefore, the sharp increase in electrical resistance should be attributed to the formation of this highly resistive shell.



**Figure 73.** Electrical resistance in air at 300 °C for the sensors doped with different concentration of Al.

The sensor response to H<sub>2</sub> in the form of resistance change is displayed in **Figure 74**. The results show a decrease in resistance when the sensor is exposed to a reducing gas, typical for n-type metal oxide semi-conductor sensor. Al-doped samples with core-shell-structure also exhibit n-type sensing behavior, even with the concentration of acceptor dopant (Al<sup>3+</sup>) as high as 47 mol% on the surface. The reduction in resistance when exposure to a reducing gas is due to increase in the electronic concentration described by the following defecation reaction:



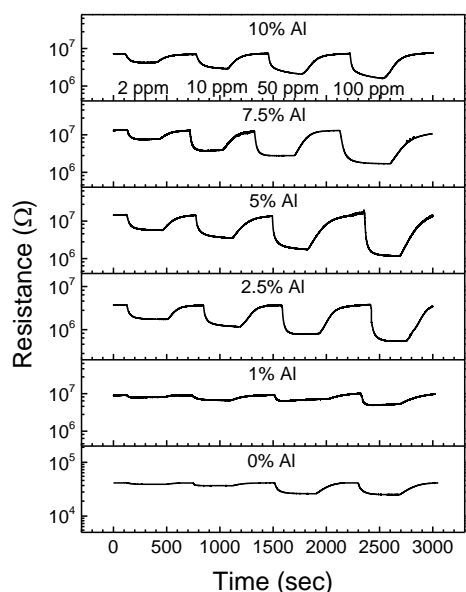


**Figure 74.** Transient response curves for pure and Al doped samples.

The sensor responses ( $R_{\text{air}}/R_{\text{gas}}$ ) of pure  $\text{SnO}_2$  and  $\text{SnO}_2$  with Al-rich shell to  $\text{H}_2$  are demonstrated in **Figure 75**. The sensor response of the sensor made from pure  $\text{SnO}_2$  is extremely low, i.e. 1.7 in response to 100 ppm  $\text{H}_2$ . In contrast, significant improvement in sensitivity has been achieved for  $\text{SnO}_2$  samples with Al-rich shell. To be specific, the sample with 5 mol% Al dopant shows a response value of 12.6 at 100 ppm  $\text{H}_2$ , which is more than ten times larger than that of bare samples. Among the samples with core-shell structure, an optimal doping concentration of 5 mol% is observed for achieving the highest sensitivity.

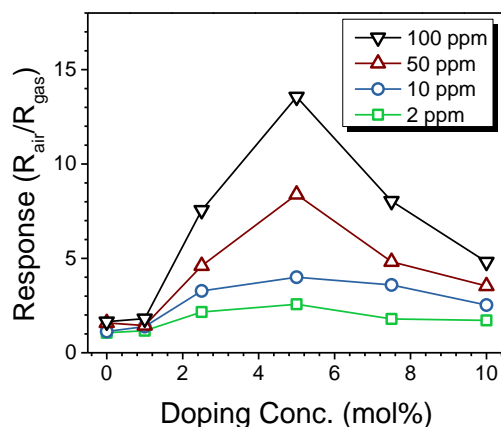


**Figure 75.** Sensor response as a function of Al concentration to 2-100 ppm of H<sub>2</sub>.

Based on the structural analysis presented in the previous section, the sensing layer of the pure SnO<sub>2</sub> sample consists of aggregates of partially sintered crystallites, as depicted in **Figure 76** (a). The high  $D_{\text{BET}}/D_{\text{XRD}}$  ratio (7.1) suggests that coalescence of crystallites should be ubiquitous, and the necks formed should be wide. Moreover, the average diameter of the crystallites ( $D=96.4\text{nm}$ ) should be considerably larger than the thickness of depletion layer ( $L\approx\text{few nanometers}$ ). Considering these two factors, electron transfer within the conductive core of the aggregates as well as the intercrystallite electron transfer through grain necks should be insensitive to any interaction between SnO<sub>2</sub> surface and the gas phase. Therefore, the major contributor to gas sensitivity should be the double Schottky barriers at the grain boundaries (GB) connecting the aggregates. To be specific, the height of double Schottky barriers,  $qV_{\text{B}}$ , where  $q$  is the electron charge, and  $V_{\text{B}}$  is the grain boundary potential, depends on the ionosorbed oxygen concentration on the surface<sup>132</sup>. When H<sub>2</sub> is introduced into the gas phase, the concentration of ionosorbed oxygen is reduced based on Equ 3 and 4. This leads to lower double Schottky barrier, and in turn, higher conductivity, as shown in **Figure 76** (b). However, because of the extensive

coalescence between crystallites, the quantity of GB is limited, and hence the sensitivity to H<sub>2</sub> is limited.

For the samples with core-shell structure, decreases in both  $D_{\text{BET}}/D_{\text{XRD}}$  ratio and crystallite size are observed, and the changes in the conduction model is illustrated in **Figure 76** (c). Smaller  $D_{\text{BET}}/D_{\text{XRD}}$  ratio suggests that the aggregates consist of fewer crystallites for the samples with core-shell structure. In other word, more double Schottky barrier formed at GB will exist on the intercrystallite charge transport pathways to affect conductivity. Moreover, because the ratio between L (thickness of depletion layer) and D (crystallite size) is also increased due to the decrease in D, some constricted conduction channels could also form inside grain necks because of the extension of insulating electron depletion layer into the neck. Accordingly, when H<sub>2</sub> is introduced to the gas phase, the constricted conduction channels will expand and lead to sizable increase in conductivity (**Figure 76** (d)), because the electrons released by the surface reactions between H<sub>2</sub> and ionosorbed oxygen leads to the retreat of electron depletion layer. Therefore, the

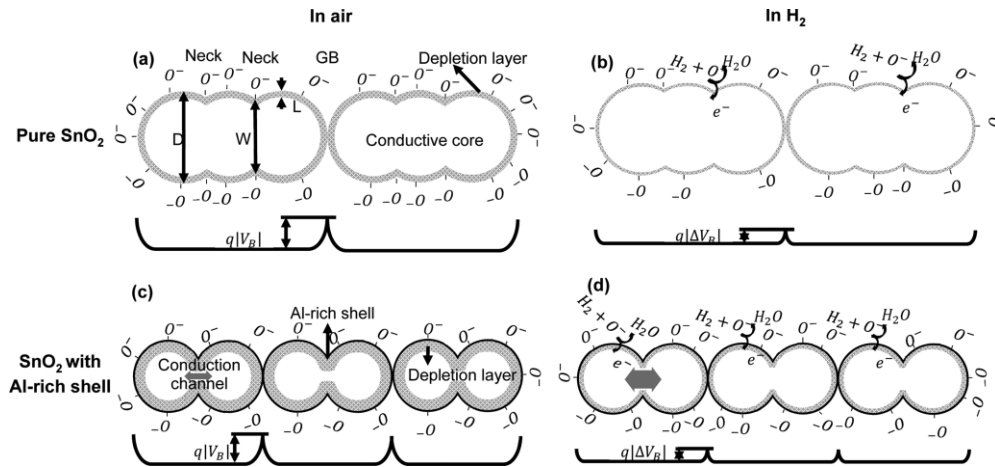


**Figure 76.** (a-b) Structure and electrical band models for pure SnO<sub>2</sub> in air and in H<sub>2</sub>; (c-d) Structure and electrical band models for SnO<sub>2</sub> with Al-rich shell in air and in H<sub>2</sub>.

the considerable gas sensitivity improvement observed in the samples with core-shell structure should be attributed to the abundant Schottky barriers at grain boundaries and the constricted conduction channels formed inside grain necks.

Based on the model proposed above, the dependence of H<sub>2</sub> sensitivity on Al doping concentration for the SnO<sub>2</sub> samples with core-shell structure can be explained from the perspective of crystallite size and  $D_{\text{BET}}/D_{\text{XRD}}$  ratio. As illustrated in **Figure 77**, initially with increasing doping concentration, both factors become smaller because solute drag effect becomes more pronounced, and as a result, the sensitivity gradually improves with doping concentration until reaching a maximum at 5 mol%. Further doping instead leads to weakening of solute drag effect, and crystallite size and  $D_{\text{BET}}/D_{\text{XRD}}$  ratio rise with doping concentration, which makes the sensitivity decrease.

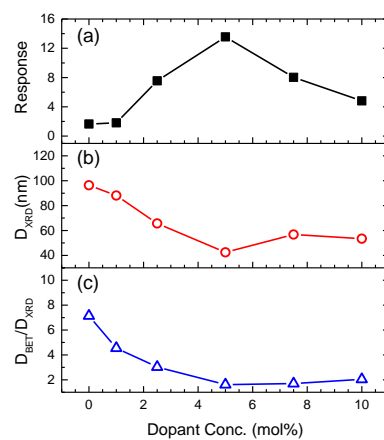


**Figure 77.** (a) Sensor response to 100 ppm H<sub>2</sub> at 300°C, (b) crystallite size derived from XRD, (c) ratio between particle size derived from BET and crystallite size derived from XRD, as function of Al doping concentration.



## 7. SEMICONDUCTOR SENSOR ARRAY FOR DISSOLVED GAS ANALYSIS

### 7.1 Introduction and Objectives

Transformers are ubiquitous in modern interconnected power systems. In a large public power utility, the number of transformers in the subtransmission and transmission network can be from a few hundred to over one thousand. Power transformers are generally very reliable, with a 20-35 year design life. However, the in-service failure of a transformer is potentially dangerous to utility personnel through explosions and fire, potentially damaging to the environment through oil leakage, is costly to repair or replace (replacing cost could be millions of dollars)<sup>171</sup>. To prevent these failures and to maintain transformers in good operating condition is a very important issue for utilities.

Dissolved gas analysis (DGA), a method involves sampling of the transformer oil to measure the concentration of the dissolved gases, has emerged as one of the most effective diagnostic methods for preventive and predictive maintenance of transformer<sup>172</sup>. When the insulating material of transformer deteriorates, it releases various gas species into the transformer oil, so the concentration of gas dissolved in transformer oil can indicate the condition of the equipment. **Table 13** indicates the upper threshold limit of concentration for the dissolved gases in the transformer oil. According to the key gas method described in IEEE standard, the relative ratios between these three gases can serve to discern all four types of electrical fault behavior with good confidence. Moreover, by monitoring the generation rate of these gases, the severity of the fault can also be measured.

The commercially available gas sensors for constructing an online monitoring system are either based on Infrared adsorption spectroscopy or based on Photoacoustic

Spectroscopy<sup>173</sup>(**Table 14**). Both of the techniques can accurately detect the concentrations of most dissolved gas species, but these diagnostic tools are very expensive (around \$50,000 per unit). Considering the large number of transformers used in the power industry, replacing the off-line test with online monitoring system built with optical sensors in large scale is unrealistic.

**Table 13.** The concentration of dissolved gases for normal operating transformers according to IEEE standard<sup>2</sup>

Gas	H <sub>2</sub>	CH <sub>4</sub>	C <sub>2</sub> H <sub>2</sub>	C <sub>2</sub> H <sub>4</sub>	C <sub>2</sub> H <sub>6</sub>	CO	TDG
Concentration (ppm)	100	120	35	50	65	350	720

Conductometric gas sensors are designed for monitoring the gas composition of their surrounding environment in real time by transforming chemical signal (i.e. gas concentration) into a measurable electrical signal (i.e. conductivity change). As shown in **Table 15**, this type of gas sensors are very cost effective (around \$10 per unit) and have wide applications in the automobile industry, energy exploitation industries, petrochemical manufacturing industries, and domestic/industry environmental control<sup>4</sup> to monitor flammable and hazardous gases such as H<sub>2</sub>, CO, NO<sub>2</sub>, and VOCs<sup>5</sup>.

The project aimed to develop sensing materials for analyzing the gas mixture dissolved in transformer oil encompasses H<sub>2</sub>, CO, CH<sub>4</sub>, C<sub>2</sub>H<sub>6</sub>, C<sub>2</sub>H<sub>4</sub>, and C<sub>2</sub>H<sub>2</sub>. For every sensing material, the detection limit towards all the gases of interest must be below 1 ppm; the response time must be shorter than 1 min; and the service life must be longer than 3 years. Moreover, a strategy to select optimal sensing material combination for building a high-performance sensor array for the dissolved gas analysis needs to be designed and executed.

**Table 14** Commercial sensor unit for dissolved gas analysis

	Product and Company names	Require carrier gas	Specification (detectable gas no, detection range,)	Cost (\$/unit)	Accuracy	Ref.
Photoacoustic	TOTUS DGA, Camlin Power©	No	6 gases, 0.5-10000 ppm	50,000	±5%	[1]
Non-dispersive Infrared	SmartDGA, LumaSense technologies©	No	6 gases, 50-10000 ppm	30,000	±5%	[2]
Gas chromatograph	Multi Gas Serveron, Qualitrol©	Yes	6 gases, 10-10000 ppm	15,000-20,000	±5%	[3]

**Table 15** Commercial gas sensor technology

Technology	Commercial example	Dimension (mm <sup>3</sup> )	Price (\$)
Semiconductor type MEMS	Bosch BME680	5	7
Electrochemical	Figaro TGS5141	2000	10
Non-dispersive infra-red	SGX IR12	6000	150

The following chapters are arranged in a way to reflect the research and development process for developing the sensor array meeting the project requirements, which involves:

- Design and build sensor testing system
- Develop device fabrication process which is easy to scale up and promotes sensor response speed
- Develop sensing materials library:

- A main focus on obtaining high sensitivity and varied response pattern to the dissolve gases by temperature control, applying physical/chemical filter, and introducing chemical modifiers
- A secondary focus on improving the temporal stability of the sensor material
- Select optimal subset of sensor materials from the materials library to form the sensor array
- Accelerated life testing on the selected sensor materials to estimate the service life
- Sensor array prototype building and testing

## 7.2 Sensor Testing System Development

The function of this gas sensor testing system is to gather and analyze the change in electrical resistance of semiconductor gas sensors while being exposed to six gas species (carbon monoxide, hydrogen, methane, ethane, ethene, ethylene) to evaluate the sensitivity, response time, and selectivity of these gas sensors.

Gas sensing characteristic was measured with a custom-made gas sensor testing system (as shown in **Figure 78** (a)) containing four sectors:

Sector 1: a test chamber made of a quartz tube and two custom-made vacuum fittings (S16-1TF200IN6, Swagelok), holding four pairs of silver probes made in-house (**Figure 78** (c)).

Sector 2: temperature control system including a rope heater (FGR-060, Omega) (**Figure 78** (b)), a thermocouple (TJ36-CAIN-116G-6, OMEGA), a variable transformer

(0-130V, 3 Amp, Electronix express), and a temperature controller (CN16PT-305, OMEGA).

Sector 3: a gas delivering system consisting of four mass flow controllers (MKS GM50A) and one mass flow controller power supply/readout unit (MKS 247D) (specification summarized in **Table 16**).

Sector 4: a data acquisition system (a Keithley multimeter-2700 connected to a PC).

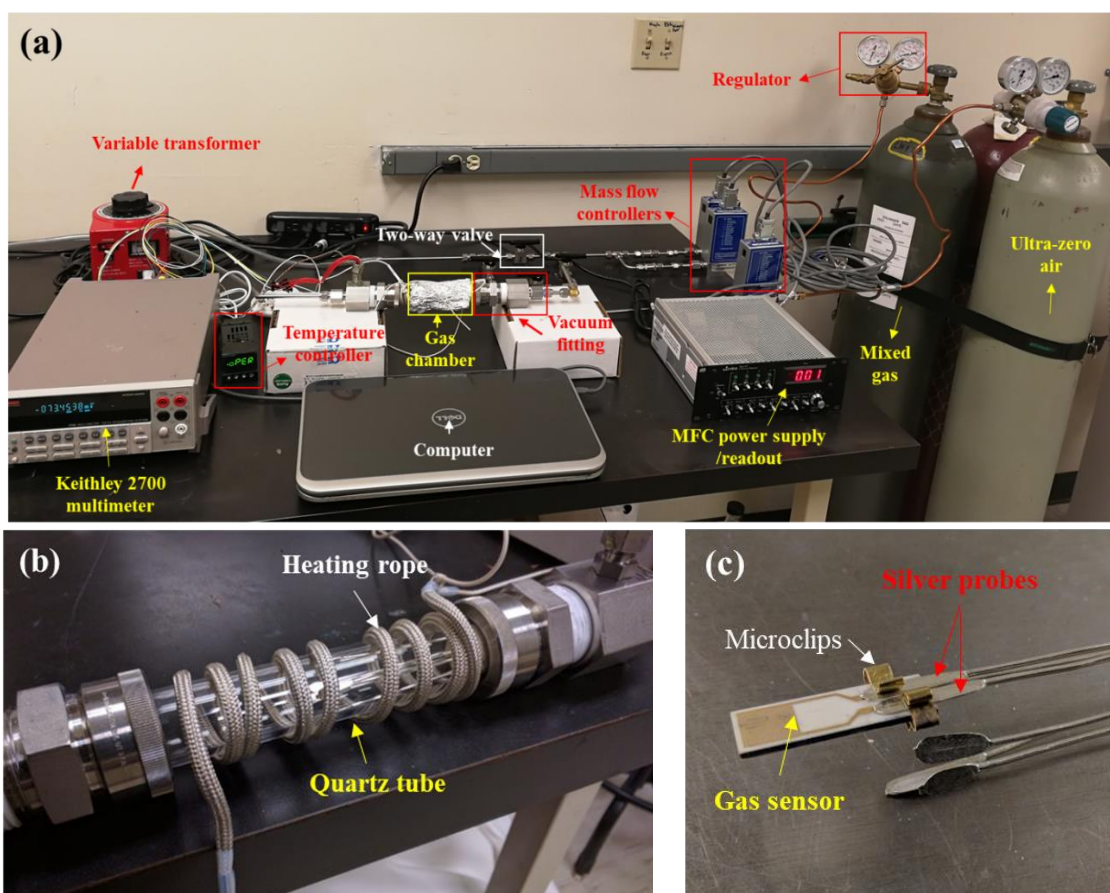


**Figure 78.** photograph of the gas sensing system (a); photograph of the test chamber (b); photograph illustrates a gas sensor connected to 1 of the 4 pairs of electrical probes by two micro-clips.

The test chamber heated by the heating rope had wide working temperature range between RT to 350 °C, and support simultaneous testing of four sensors. The size of the

test chamber is minimized ( $\sim 40 \text{ cm}^3$ ) to eliminate the dispersion effect. The delivery of mixed gas with varied concentration and the switching between mixed gas and air were achieved with four mass flow controllers (the specifications are listed in **Table 16**) and a four-way valve (4 two way valves). MFC1 and MFC4 were both connected to ultra-zero air, while the flow rate of 1000 ppm mixed gas was regulated by either MFC2 or MFC3. Mixed gases with a concentration between 1-1000 ppm were prepared by setting the MFCs to the setpoints listed in **Table 17**. The switching between the air gas stream to the mixed gas stream was achieved by turning the 4-way valve as shown in **Figure 79**.

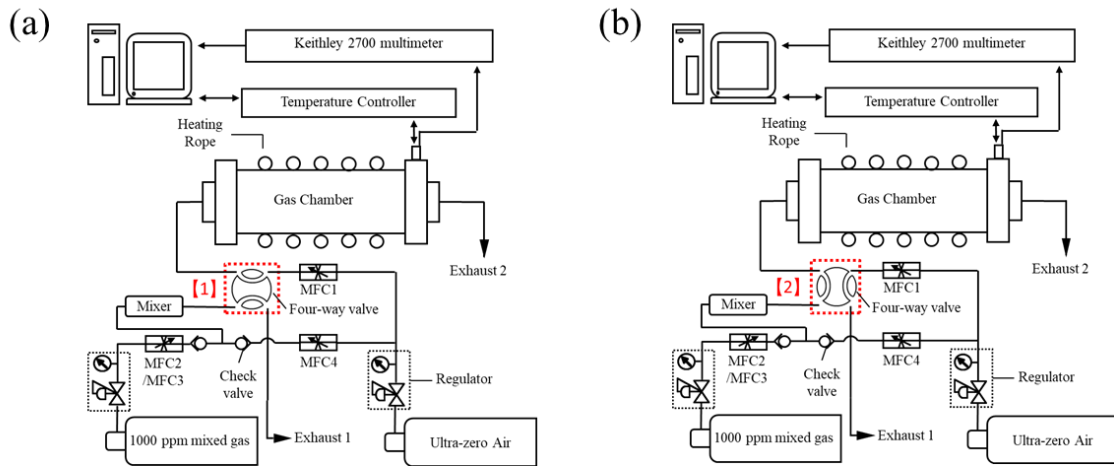


**Figure 79.** schematic diagram of (a) the gas sensor testing system: reference gas (ultra-zero air) mode; and (b) analyte gas (reducing gas mixed in air) mode.

To conduct gas sensor testing, the sensors were first stabilized in the gas chamber at set working temperatures with 200 sccm air flow for 30 min, with the aim of achieving thermal equilibrium. Then the two gas streams were switched periodically to test the sensing performances at different gas species and at different gas concentrations. The sensing performance at different temperature was evaluated by re-establishing thermal equilibrium at a different temperature. Sensor response ( $S$ ) for n-type sensors ( $\text{SnO}_2$  and

ZnO-based) was defined as the ratio,  $R_a/R_g$  (or  $C_g/C_a$ ), where  $R_a$  ( $C_a$ ) and  $R_g$  ( $C_g$ ) are the resistances of the sensor in dry air and in mixed gases, respectively. For p-type sensors (i.e. CuO-based), sensor response was defined as the ratio,  $R_g/R_a$  (or  $C_a/C_g$ ), to keep the value larger than 1. The ratio between the sensor response for different gases was defined as the selectivity. The response rate and recovery rate were defined as the time required to reach 90% of the fully excited state in mixed gas and 90% of the fully relaxed state in the air, respectively.

**Table 16.** the specifications of the mass flow controllers used in the gas sensing system.

Description	Min flow rate (sccm)	Max flow rate (sccm)	Cylinder(s) connected
Mass flow controller 1 (MFC1)	1	200	Ultra-zero air
Mass flow controller 2 (MFC2)	0.1	5	1000 ppm CO, H <sub>2</sub> , CH <sub>4</sub> , C <sub>2</sub> H <sub>6</sub> , C <sub>2</sub> H <sub>4</sub> , C <sub>2</sub> H <sub>2</sub> in air
Mass flow controller 3 (MFC3)	1	200	Ultra-zero air
Mass flow controller 4 (MFC4)	1	200	1000 ppm CO, H <sub>2</sub> , CH <sub>4</sub> , C <sub>2</sub> H <sub>6</sub> , C <sub>2</sub> H <sub>4</sub> , C <sub>2</sub> H <sub>2</sub> in air

**Table 17.** Mass flow controller set points for achieving concentration between 1-1000 ppm using a 1000 ppm cylinder.

Concentration (ppm)	MFC1 (sccm)	MFC2 (sccm)	MFC3 (sccm)	MFC4 (sccm)
1	200	0.2		199.8
3	200	0.6		199.4
5	200	1		199
10	200	2		198
30	200		6	194
50	200		10	190
100	200		20	180
300	200		60	140
500	200		100	100
1000	200		200	0

### 7.3 Development of Device Fabrication Technique

Planer-type sensor configuration was used in this work. The support with preprinted interdigitated electrodes were procured from commercial source, hence the focus of development was on sensing layer deposition. Two strategies were investigated:

*Blade coating method:* thick sensing films (thickness > 10  $\mu\text{m}$ ) were deposited on alumina substrates with preprinted gold interdigitated electrodes (bands/gaps 200  $\mu\text{m}$ , DROPSENS). Terpeneol/Ethyl cellulose (95/5 wt%) was prepared as an organic vehicle. 100  $\mu\text{L}$  of the organic vehicle was added to 0.5 g of powder to prepare a paste with suitable rheology properties. A proper amount of paste was first transferred on the alumina substrate, and then a continuous film with preset thickness was formed by dragging a blade coater across the substrate. The thick film sensors were then dried at 70  $^{\circ}\text{C}$  for 12 h followed by calcination at 400  $^{\circ}\text{C}$  for 6 h to remove the organic vehicle.

*Drop coating method:* Sensing films with medium thickness ( $\sim 10 \mu\text{m}$ ) were deposited by drop coating method. Typically, 50  $\mu\text{l}$  of aqueous suspensions of powders (0.1g/ml) dispersed by ultrasonication was dropped on alumina substrates with preprinted gold interdigitated electrodes (bands/gaps 200  $\mu\text{m}$ , DROPSENS). The substrates were first treated in HCl/methanol (1:1) solution to improve hydrophilicity for better spreading of the droplets. After deposition, the sensors were first dried at 40  $^{\circ}\text{C}$  and 60 RH mol% for 1 h and then annealed at 500  $^{\circ}\text{C}$  for 5 h.

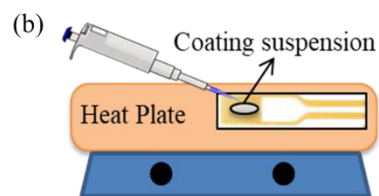
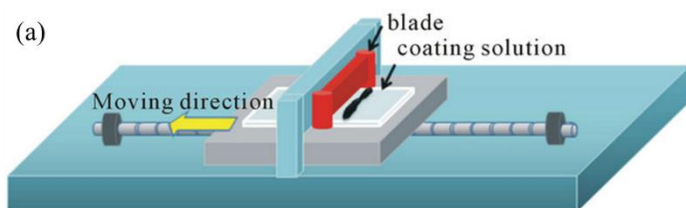




**Figure 80.** Schematics for (a) blade coating and (b) drop coating.

### 7.3.1 Response rate enhancement by reducing both agglomeration and sensing layer thickness

The results described in section 5.3.1.1 and 5.3.1.2 were obtained from thin film sensors prepared with ball-milled powders with a low level of agglomeration by drop coating method. The sensors show excellent sensitivity to H<sub>2</sub> and fast response & recover speed. The current section presents sensor response & recover rate data obtained from heavily agglomerated powders and thick film sensors, to boasts the effectiveness of the ball-milling process and drop coating method on response rate enhancement. As shown in **Figure 81** (a), gas diffusion inside those large nonporous agglomerates will be much slower than through inter-agglomerates pores. Therefore, by breaking down the solid agglomerates, gas diffusion would become easier and lead to a faster response. Post ball milling treatment was performed on the 1%-Al powders and thick film sensors were made by blade coating. The SEM image (**Figure 81** (b)) shows that the agglomerates were completely broke apart by the ball milling process. After the ball milling process, crystallite size also decreases from 37 nm to 21.7 nm according to XRD results (**Figure 81** (c)).

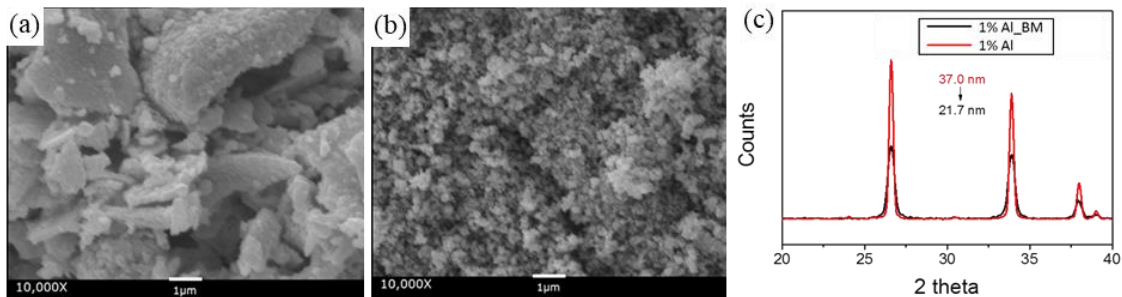


**Figure 81** (a) SEM image of 1% Al-doped SnO<sub>2</sub> powders before ball milling; (b) after ball milling; (c) comparison of XRD patterns before and after ball milling, the XRD peaks become shorter and broader after ball milling, which suggests a decrease of crystallite size.

Making thick film sensor thinner also shorten response time because of shorter diffusion length for gas species. As shown in Figure **Figure 82** (a) and (c), the film thickness values achieved by blade coating method and inkjet printing method are 50  $\mu\text{m}$  and 10  $\mu\text{m}$ , respectively. The SEM top-view images (**Figure 82** (b) and (d)) show that both techniques can produce the porous film with no agglomeration.

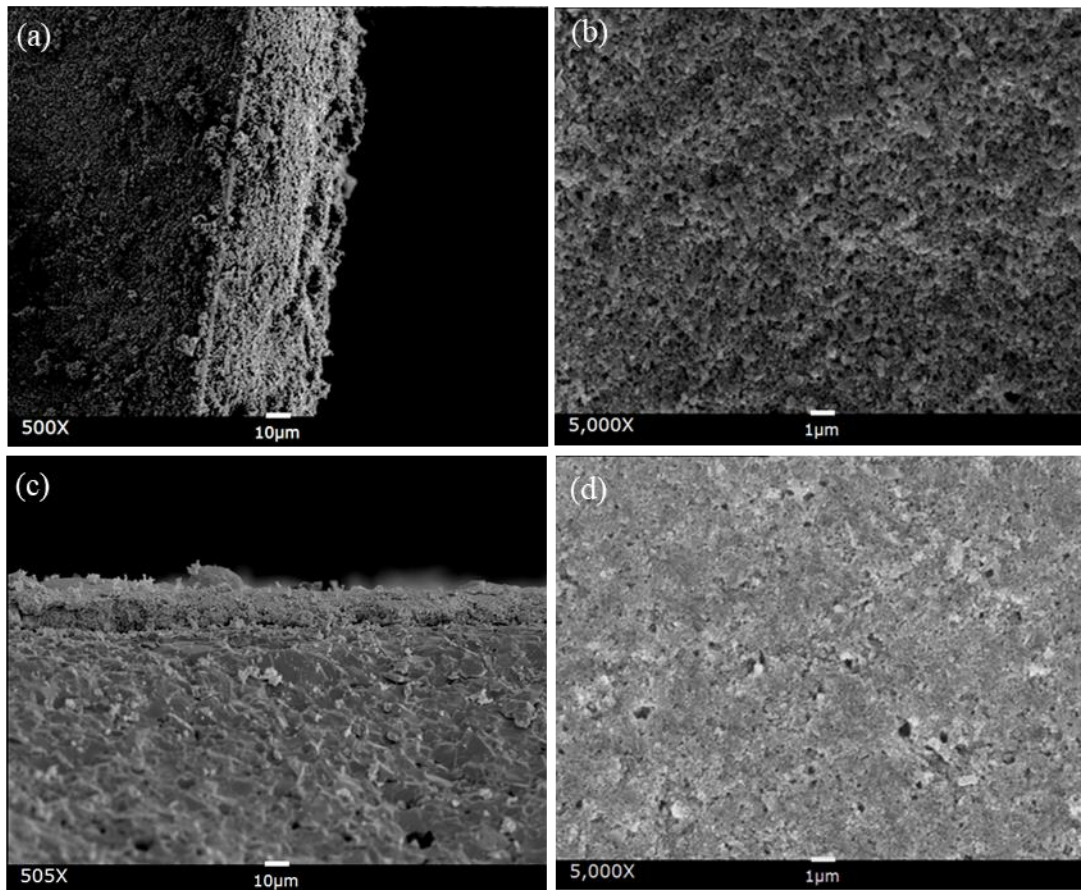


**Figure 82.** (a) and (b) cross-section and top view of thick film sensor fabricated by blade coating method; (c) and (d) cross-section and top view of thick film sensor fabricated by inkjet printing method.

The gas sensing result (**Figure 83** (a)) shows that by doing ball milling, the response time to 1000 ppm  $\text{H}_2$  at 300  $^\circ\text{C}$  can be shortened from 307 s (1% Al) to 130 s (1% Al<sub>BM</sub>).

Sample fabricated by drop coating method shows further improvement in response rate (43 s, 1% Al<sub>BM\_IP</sub>). Therefore, a combined strategy of first powder de-agglomeration by post ball milling treatment and then film deposition by drop coating yields sensor with the fastest response. In addition to response time, the sensitivity values of different sensors at different H<sub>2</sub> concentrations are also compared (**Figure 83** (b)). The very similar response values suggest that post ball milling treatment and inkjet printing deposition process haven't influenced the sensitivity, since for 1% Al<sub>BM\_IP</sub> sample, the detection limit is smaller than 1 ppm as well.

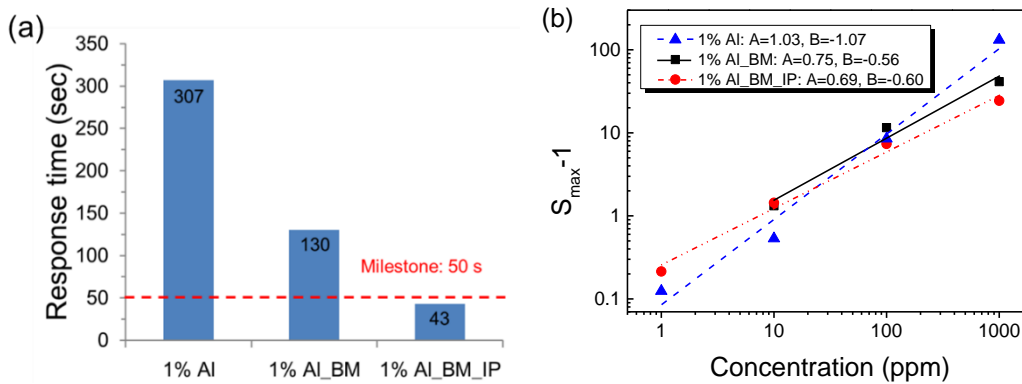


**Figure 83.** (a) response times of 1% Al (as-synthesized powder, 50  $\mu$ m film), 1% Al<sub>BM</sub> (ball-milled powder, 50  $\mu$ m film), and 1% Al<sub>BM\_IP</sub> (ball-milled powder, 10  $\mu$ m film) toward 1000 ppm H<sub>2</sub> at 300°C; (b) sensitivity values of three aforementioned sample vs. different H<sub>2</sub> concentration at 300°C.

## 7.4. Sensing Materials Library Development

### 7.4.1 Sensing Materials Synthesis

#### 7.4.1.1 Zinc (II) Oxide Based

*Zinc oxide nanoparticles:* 0.7184 g ZnCl<sub>2</sub> anhydrous and 0.3304 g citric acid were first dissolved in 36 ml of DI water, and then 6.6 ml of 2 M NaOH aqueous solution was added dropwise. After magnetic stirring for 10 min, 36 ml of DI was poured into the white

suspension. The suspension underwent hydrothermal treatment in an autoclave (capacity 90 ml) at 200 °C for 20 h. The product of the hydrothermal reaction was washed with DI water and ethanol, and the white powders were collected after washing/centrifugation and drying at 80°C for 20 h.

*Zeolitic imidazolate framework-8/ Zinc oxide nanodisk composite:* a Thick film of ZnO nanodisk was first placed in a 0.5 M Hmim methanol solution at 25 °C for 2.5 h for activation. Secondly, the activated film was transferred to another synthesis solution with a molar composition of 0.65 HCOONa: 1.0 ZnCl<sub>2</sub>: 1.5 Hmim: 450 MeOH at 100°C for 5 h for ZIF-8 film growth. After the solvothermal reaction, the as-synthesized bilayer film was taken out, naturally cooled to room temperature and thoroughly washed with methanol and dried at 25 °C for 24 h.

*Urchin-shaped ZnO microcrystals:* 0.9297 g Zn(NO<sub>3</sub>)<sub>2</sub>·6H<sub>2</sub>O was first dissolved in 40 ml of DI water, after which 10 ml of 3 M NaOH aqueous solution was added dropwise and the white suspension was stirred for 30 min before being transferred into an autoclave (capacity 90 ml). After hydrothermal treatment at 180 °C for 5 h, the product of the hydrothermal reaction was washed with DI water and ethanol, and the white powders were collected after washing/centrifugation and drying at 80°C for 20 h.

#### 7.4.1.2 Tin (IV) Oxide Based

*Pristine and Al-doped SnO<sub>2</sub> nanoparticles via polymeric precursor method:* Tin citrate aqueous solution was first made from SnCl<sub>2</sub>·2H<sub>2</sub>O and citric acid with a citric acid/metal molar ratio of 3:1. Following the same ratio, the aluminum citrate aqueous solution was prepared from Al(NO<sub>3</sub>)<sub>3</sub>·9H<sub>2</sub>O and citric acid. For aluminum doped samples, the proper amount of aluminum citrate aqueous solution was added into tin citrate aqueous solution, and the Al concentration of each sample was calculated based on the Al/Sn molar ratio.

Ethylene glycol was added to the final solution at a mass ratio of 2:3 in relation to the citric acid to promote polymerization. A xerogel was formed after heating the solution on a hot plate at 150 °C for 5 h, and further calcined at 350 °C for 5 h. It was then ball milled for 12 h at a frequency of 15 Hz. The obtained powder was calcined in a furnace at 600 °C for 4 h to obtain Al<sub>2</sub>O<sub>3</sub>-SnO<sub>2</sub> metastable solid solutions (as-synthesized). To facilitate the formation of Al-rich surface layer, the Al<sub>2</sub>O<sub>3</sub>-SnO<sub>2</sub> solid solution powders underwent a post-thermal-treatment at 1100 °C for 4 h (thermally-treated).

*Pristine and noble-metals / metal-oxides doped SnO<sub>2</sub> nanoparticles via sol-gel and impregnation method:* 14.04 g SnCl<sub>4</sub>·5H<sub>2</sub>O was first dissolved in 400 ml of DI water. Ammonia aqueous solution (pH = 12.5) was added dropwise into the solution with constant stirring until pH value reached 6. Wet gel was obtained by centrifugation at 10000 rpm for 5 min. To eliminate any residue chlorine ions in the wet gel, a solution composed of diethylamine and nitric acid (pH=6) was used to wash the wet gel 3 times. Afterward, the same solution was used to redisperse the wet gel, and 10 ml of polyethylene glycol-400 was also added as a dispersant. The suspension was aged with stirring for 24 h. The product was then separated via vacuum filtration and dried at 80 °C overnight. Finally, pristine SnO<sub>2</sub> nanoparticles were obtained by calcination at 600 °C for 6 h.

For doping SnO<sub>2</sub> nanoparticles, several drops of 0.01 M metal salts aqueous solution (including AuCl<sub>3</sub>, PdCl<sub>2</sub>, AgNO<sub>3</sub>, Cu(NO<sub>3</sub>)<sub>2</sub>, NiCl<sub>2</sub>, Co(NO<sub>3</sub>)<sub>2</sub>) were added to the SnO<sub>2</sub> nanoparticles forming some viscous pastes. The pastes were ground with mortar and pestle until they dried off, and the dried mixtures were calcined at 600 °C for 4 h to convert the

metal salts into a single element or oxide states. The doping concentrations were controlled at around 0.5 wt%.

#### 7.4.1.3 Copper(II) Oxide Based

*CuO/CeO<sub>2</sub> composite hollow microsphere*: 5.406 g D-glucose was dissolved in 50 ml of DI water. 0.002 mol of metal salt precursors (Ce(NO<sub>3</sub>)<sub>2</sub> · 6H<sub>2</sub>O and Cu(NO<sub>3</sub>)<sub>2</sub> · 2.5H<sub>2</sub>O) were dissolved in 10 ml of DI water. The two solutions were mixed with a magnetic stirrer for 15 min. After hydrothermal treatment at 180 °C for 24 h, the product of the hydrothermal reaction was washed with DI water and ethanol, and the black char was collected after washing/centrifugation and drying at 80°C for 20 h. The final products with CuO wt% ranging between 0-100 were obtained by removing the polymer template at 500 °C for 3 h.

*CeO<sub>2</sub> doped CuO nanoparticles*: CuO nanoparticles were synthesized by the same method for synthesizing *CuO/CeO<sub>2</sub> composite hollow microsphere*. For doping CeO<sub>2</sub>, several drops of 0.01 M Ce(NO<sub>3</sub>)<sub>3</sub> aqueous solution was added to the CuO nanoparticles forming some viscous pastes. The pastes were ground with mortar and pestle until they dried off, and the dried mixtures were calcined at 500 °C for 3h to convert the metal salts into oxide states. The doping concentration values were 0.5, 2, and 5 wt%.

*Pristine and CeO<sub>2</sub>/Pd/Au-doped CuO nanosheets*: CuO nanosheets were synthesized by hydrothermal method. 1.163 g of Cu(NO<sub>3</sub>)<sub>2</sub> · 2.5H<sub>2</sub>O was first dissolved in 10 ml ethanol. The prepared solution was added dropwise into 100 ml of 5 M NaOH aqueous solution with vigorous stirring. After continuous stirring for 30 min, the suspension was divided equally into two parts and transferred to two 90 ml autoclaves. After hydrothermal

treatment at 100 °C for 24h, the product was washed with a large quantity of warm DI water and ethanol to remove any residue sodium ions, and the black powders were collected after washing/vacuum filtration and drying at 80°C for 24 h.

For doping CeO<sub>2</sub>, 0.05 g CuO nanosheets were dispersed in 40 ml of ethanol/water mixture solution (volume ratio 1:1) by ultrasonication for 30 min. Afterward, the suspension was transferred into a round bottom three-way flask. 0.0217g (or 0.0434g for higher doping concentration) Ce(NO<sub>3</sub>)<sub>3</sub> · 6H<sub>2</sub>O and 2.5 ml of hexamethylenetetramine aqueous solution (0.02 g/L) were added into the suspension with constant stirring. The temperature was increased to 70 °C and the refluxing process was carried out for 2 h. The product was washed with DI water and ethanol to remove any impurity, and the black powders were collected after washing/vacuum filtration and drying at 60°C for 24 h.

Deposition-precipitation method was used for doping Pd and Au at the surface of CuO nanosheets. For 5 wt% Pd doped CuO nanosheet, 0.025 M PdCl<sub>2</sub> aqueous solution was first prepared by adding 0.0887g PdCl<sub>2</sub> and 0.0584g NaCl in 20 ml DI water. 0.1 g CuO nanosheets were dispersed in 60 ml water/methanol (1:1) by vigorously stirring. 1.8794 ml of the PdCl<sub>2</sub> aqueous solution was added in the CuO suspension, and 0.5 M Na<sub>2</sub>CO<sub>3</sub> aqueous solution was added to adjust the pH value to around 8.5. After stirring for 10 min, the black powders were collected after washing/centrifugation (10000 rpm 10 min) and drying at 70°C overnight. For Au doped CuO nanosheet, similar procedure was followed expect the container used need to be covered by Al-foil because of the light sensitivity of AuCl<sub>3</sub>.

## 7.4.2 Characterization Techniques for Structural, Composition, and Electrical Properties Analysis

X-ray diffraction (XRD) patterns were recorded on a Bruker D8 focus diffractometer using Cu K $\alpha$  radiation ( $\lambda=1.5406 \text{ \AA}$ ) and Rietveld refinement was performed for grain size and cell parameters analysis using the BGMN program <sup>163,164</sup> and the graphical interface Profex <sup>165</sup>.

X-ray photoelectron spectra (XPS) were obtained using a VG ESCALAB 220i-XL photoelectron spectrometer and Al-K $\alpha$  radiation (15 KeV) at about  $1.3 \times 10^{-9}$  mbar base pressure. C(1s), Al (2p), O(1s) and Sn(3d5/2) core level high-resolution spectra and wide scan spectra were. C(1s) peak is used to calibrate peak position. Curve fitting of O(1s) spectra was done with a spin-orbit coupling of 2:1 area ratio using CasaXPS software. The same software was used for calculation of the elementary percentage from the recorded spectra.

Field emission scanning electron microscopy (AMRAY 1910,) and energy dispersive x-ray spectrometry (EDS) were used for morphological and semi-quantitative atomic compositional studies. For the EDS tests, they were performed under the following testing condition: accelerating voltage 15 kV, take-off angle  $46.40^\circ$ , and spot size of the electron beam around 50 nm.

Brunauer-Emmett-Teller (BET) and Barret-Joyner-Halenda (BJH) analyses were used to determine the surface area and pore size distribution with a nitrogen adsorption porosimeter (model ASAP 2020, Micromeritics). The BET surface area was calculated using experimental points at a relative pressure of  $P/P_0 = 0.05-0.25$ . The pore size



distribution was derived from the adsorption branch using Barret-Joyner-Halenda (BJH) method.

Transmission electron microscopy images were collected on a 200 kV Philips CM-200. The samples were dispersed in ethanol via sonication for 10 min and then added dropwise to a carbon-coated copper grid. Multiple spots were examined to ensure sample uniformity.

Current-voltage (I-V) test was used to determine the nature of electrical contact of the planer-type gas sensor device. Via a two-terminal method, A single voltage sweep started by sweeping up from zero bias voltage to 500 millivolts, down to a negative voltage of 500 millivolts, then back to zero. An example of an I-V sweep on ZnO nanodisk thick film sensor is shown in **Figure 84** (a). The linear fit plotted along with the data shows that the I-V curve in this range of bias voltages, which indicates Ohmic behavior,

Electrochemical impedance spectroscopy (EIS) was used to determine the identification of different elements of a complex device, such as a thick film gas sensor. A PARSTAT 2263 Princeton potentiostat was used for the EIS measurements. The measurements were performed in a frequency range of 2 MHz to 0.1 Hz with an AC amplitude of 10 mV (**Figure 84** (b)). The Nyquist plot of complex impedance measurements on ZnO nanodisk thick film sensor is shown in Figure 106b. At a temperature below 75 °C, the curves were composed of two semicircles, which suggested two capacitors with different time constants presented in the equivalent circuit. The semicircle at low-frequency end could relate to the contribution of the surface depletion layer (mainly shallow interface states at grain boundaries) because interface states at grain

boundaries cannot follow the high-frequency ac signal. The high-frequency results from the contribution of crystalline grains. When the temperature rose up, the low-frequency semicircle became smaller and eventually disappeared at 75 °C. This could be explained by the increasing number of free electrons at a high temperature. When there are more free electrons presented in the bulk, the thickness of the depletion layer decreases, and hence the low-frequency semicircle becomes indistinguishable.

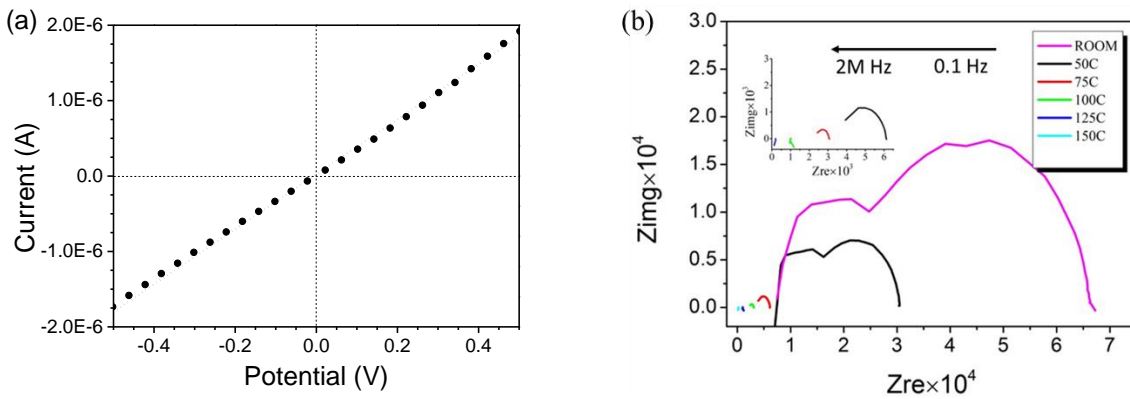


**Figure 84.** a current-voltage test example (a) and an electrochemical impedance spectroscopy test example (b) on ZnO nanodisk thick film sensor.

### 7.4.3 Zinc (II) Oxide-based Sensing Materials

#### 7.4.3.1 Zinc Oxide Nanoparticles

Zinc oxide nanoparticles prepared by the hydrothermal method are between 200 nm and 1 μm in diameter. The thick sensing film (~50 μm in thickness) was homogeneously deposited on an alumina substrate with preprinted electrodes by blade coating method. The SEM images (**Figure 85(a-b)**) are the top and side views of the as-prepared sensor. The film is highly porous and possesses no apparent grain neck formation. XRD pattern on the nanoparticles confirms the formation of wurtzite ZnO (**Figure 85 (c)**). The crystallite size ( $r$ ) is calculated based on Scherrer's equation:

$$r = \frac{K\lambda}{\beta \cos \theta}$$

Where K is a dimensionless shape factor, with a value close to unity,  $\lambda$  is the X-ray wavelength,  $\beta$  is the line broadening at half the maximum intensity (FWHM), and  $\theta$  is the Bragg angle. The result of this calculation shows that the crystallite size is around 90 nm which is smaller than the particle size, and hence the ZnO nanoparticles are polycrystalline.

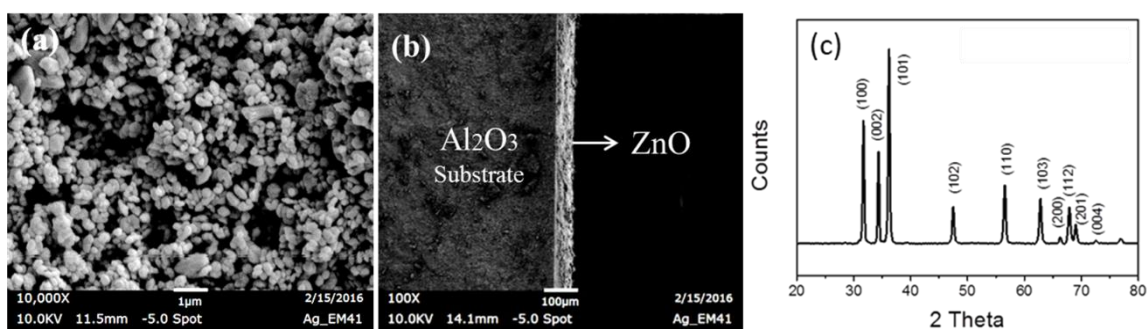


**Figure 85.** SEM top view (a) and side view (b) of the ZnO nanodisk sensor; powder XRD pattern of ZnO nanodisk (c).

The sensor's response ( $C_g/C_a$ ) towards 1000 ppm H<sub>2</sub> increases with working temperature from 150 to 200 °C as shown in **Figure 86**. In addition, the sensor's response and recovery rate also increase with working temperature. The reproducibility of the sensor response is demonstrated in Figure 108. In the 5 h testing period, the response curves look similar, despite some drifting in the baseline is observed. The sensor response towards all six reducing gases dissolved in oil was also tested at 175 °C. The results are summarized in **Table 18**. Overall, the response values are quite low (1.04-1.19), and the response rate and recovery rate are slow (2.6 – 20 min). The low sensing performance is attributed to the

low working temperature selected for testing, the large particle size, and the large film thickness of the ZnO nanoparticle sensor.

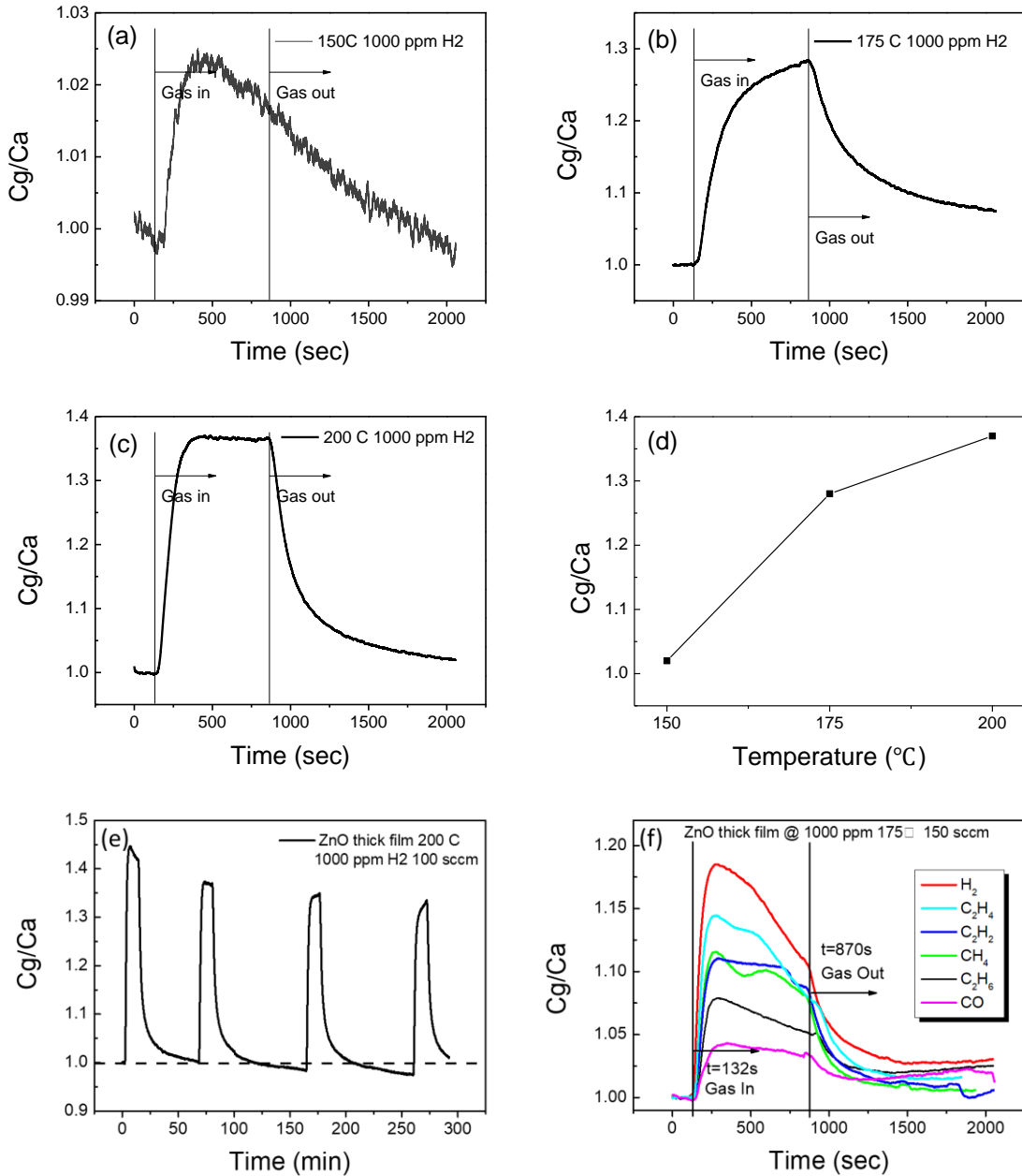


**Figure 86.** transient response curves of the ZnO nanodisk sensor to 1000 ppm H<sub>2</sub> (a)-(c); Response vs. temperature (d); Repeated cycling test (e); Response towards 6 dissolved gases (f).

#### 7.4.3.2 Zeolitic Imidazolate Framework-8/ Zinc Oxide Nanoparticles Composite

The sensors made from pristine zinc oxide nanoparticles are cross-sensitive to all six dissolved gases. The cross-sensitivity renders them unsuitable for the construction of sensor array. Placing a filter layer over the sensing materials is an effective way to improve sensor selectivity. Filters made from common porous materials including activated carbon and zeolite can reduce interference from unwanted gas species by either adsorption or molecular sieving. However, because of the weak bonding strength between the sensing layer and filter layer, the filter layer needs to be very thick ( $>100\ \mu\text{m}$ ) to be effective. As a result, a huge trade-off must be made between selectivity and sensitivity/response speed when applying filter made from the common porous material.

**Table 18.** Summary of sensor properties of ZnO thick film at 175°C.

	Sensitivity ( $R_a/R_g$ )	Response time (min)	Recovery time (min)
H <sub>2</sub>	1.19	2.7	11.2
CO	1.04	3.8	>20
CH <sub>4</sub>	1.12	2.6	17.7
C <sub>2</sub> H <sub>6</sub>	1.08	2.6	8.8
C <sub>2</sub> H <sub>4</sub>	1.14	6.1	10.8
C <sub>2</sub> H <sub>2</sub>	1.11	3.0	>20

Zeolitic imidazolate framework-8 (ZIF-8), a type of new microporous material called metal-organic frameworks (MOFs), has been reported to have H<sub>2</sub>/C<sub>2</sub>H<sub>4</sub> separation factor greater than 103 in the form of a defect-free membrane. By a facile sacrificial secondary growth process, a ZIF-8 layer can be grown on ZnO film by consuming part of the ZnO as

a reactant. Very thin ZIF-8 layer with good filtering performance can be achieved because of the strong bonding between ZIF-8 and ZnO.

Therefore, we selected ZnO as the semiconducting metal oxide film and ZIF-8 for the MOF membrane to explore this novel concept of selectivity enhancement. ZnO nanoparticles of about 300 nm were synthesized by hydrothermal method. A thick porous film of ZnO (thickness: 50  $\mu\text{m}$ ) was then coated on an alumina substrate with preprinted gold electrodes using a blade coater. An annealing process at a high temperature was performed and a dense ZnO thick film sensor was made. A continuous ZIF-8 membrane of about 15  $\mu\text{m}$  thick was then coated on ZnO film by a secondary growth method. A ZIF-8/ZnO composite device was made and the SEM cross-section image and XRD results are given in Figure **Figure 87** (a-b).

Studies on the gas transport of  $\text{H}_2$  and  $\text{C}_2\text{H}_4$  were performed respectively using bare ZnO film sensor device and ZIF-8/ZnO composite device. The air was chosen as the reference gas, and the testing temperature was 175°C. The device was in equilibrium with air and then a gas mixture of air containing 1000 ppm  $\text{H}_2$  or  $\text{C}_2\text{H}_4$  was introduced into the gas chamber at a flow rate of 100 sccm. The transient sensor response value of ZnO sensing film (the ratio of resistance before and after introducing  $\text{H}_2$  or  $\text{C}_2\text{H}_4$ ) on the bare ZnO sensor and that on the ZIF-8/ZnO sensors were measured and the results are given in Figure 109c.

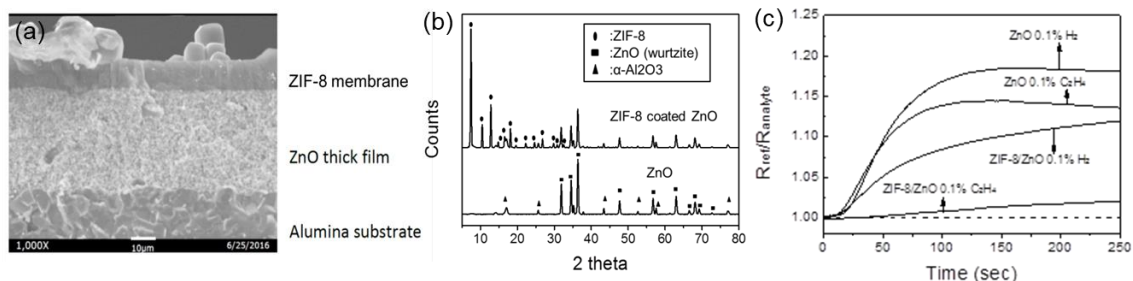


**Figure 87.** SEM image of the cross-section view of ZIF-8 coated ZnO thick film sensor (a); XRD patterns for ZnO thick film sensor before and after coating ZIF-8 (b); Transient gas sensor response of ZnO thick film and ZIF-8 coated ZnO thick film to 0.1% C<sub>2</sub>H<sub>4</sub> and H<sub>2</sub> (c).

A preliminary test on ZIF-8 coated ZnO thick film sensor shows that the ZIF-8 coating has an influence on the selectivity between H<sub>2</sub> and C<sub>2</sub>H<sub>4</sub>. (**Figure 87** (c)) The response of ZIF-8 coated ZnO thick film to H<sub>2</sub> is close to that of bare ZnO thick film (15% vs 18%), while the response to C<sub>2</sub>H<sub>4</sub> is marginally smaller than bare thick film (3.5% vs 14%). Therefore, a nearly 4.5X increase in selectivity has been achieved by the addition of ZIF-8 filter layer. The transient responses curves for ZIF-8/ZnO composite, corresponding to the transient concentration curves at the interface between ZIF-8 membrane and ZnO film, are slower than those for the bare ZnO film. These differences are clearly due to the different mass transport resistance for H<sub>2</sub> and C<sub>2</sub>H<sub>4</sub> in the ZIF-8 membrane.

Although promising selectivity enhancement has been observed, the ZIF-8 layer was not thermally stable at 175 °C. Further study, starting from developing a ZnO-based sensor with the near room temperature working condition is required.

#### 7.4.3.3 Urchin-shaped Zinc Oxide Microcrystals

By performing hydrothermal synthesis at high temperature (180 °C), urchin-shaped zinc oxide microcrystals were obtained by the self-assembly of ZnO nanorods. As shown

in **Figure 88**, the microcrystals are between 2-5  $\mu\text{m}$  in diameter and the building block ZnO nanorods are around 200 nm in diameter. XRD pattern on the microcrystals confirms the formation of wurtzite ZnO. By performing Rietveld refinement, the crystallite size is calculated to be around 70 nm, which is much smaller than the size of ZnO nanorods.

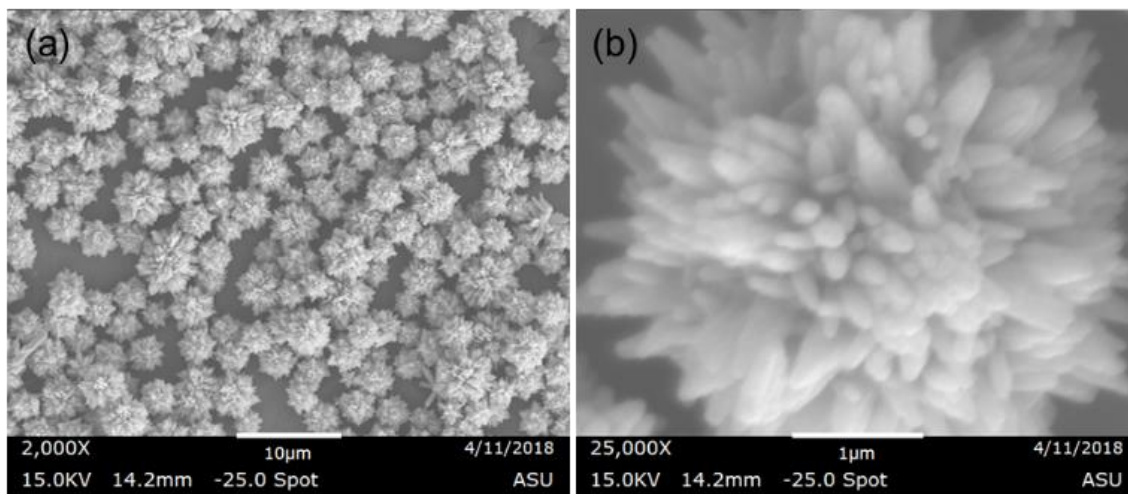


**Figure 88.** SEM images of the urchin-shaped ZnO.

Thin film ( $\sim 5 \mu\text{m}$  thick) of urchin-shaped ZnO was deposited on an alumina substrate with preprinted electrodes by drop coating method. The sensing performance of the as-formed sensor was evaluated at  $300 \text{ }^\circ\text{C}$ . The gas concentration was set to be 25 ppm. The results summarized in **Table 19** indicates a notable selectivity to  $\text{C}_2\text{H}_2$  among all the dissolved gases. In the atmosphere containing 25 ppm of  $\text{C}_2\text{H}_2$ , the response rate is also much faster when comparing to other gases.

#### 7.4.4 Tin (IV) Oxide-based Sensing Materials

Pristine  $\text{SnO}_2$  nanoparticles were first synthesized following literature. Basically, ammonium hydroxide aqueous solution was added dropwise in  $\text{SnCl}_4$  aqueous solution while continuous stirring. The pH was controlled at 6.5 to allow the formation of  $\text{Sn}(\text{OH})_4$

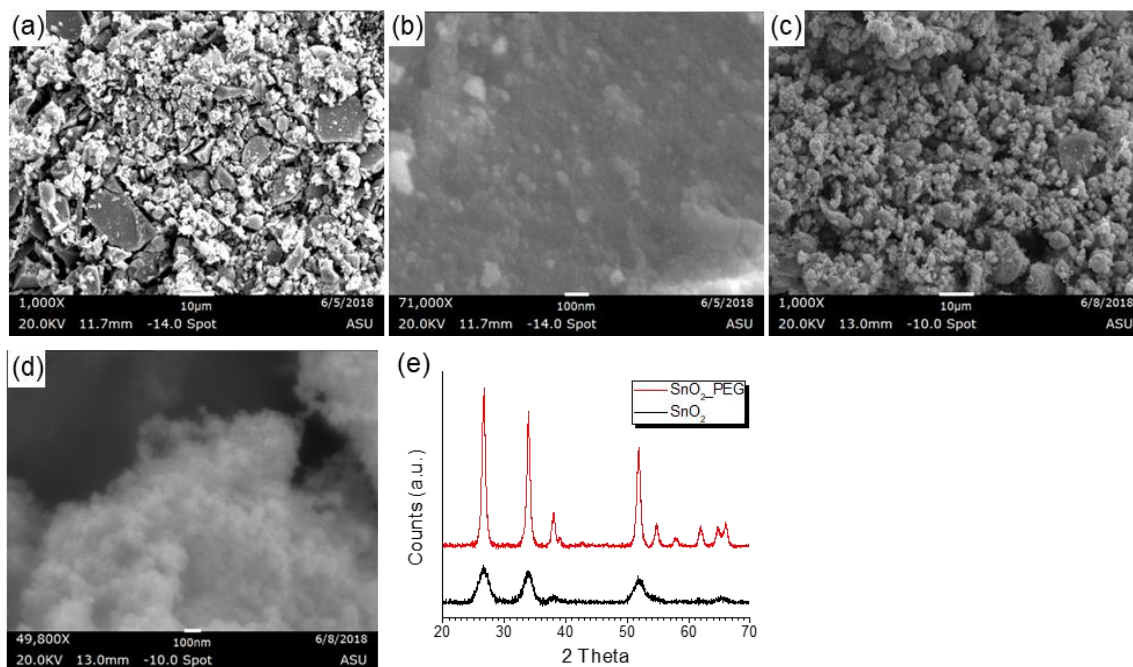


sol. The sol was converted into a gel by centrifugation, and the gel was washed with DEA/HNO<sub>3</sub>/water (pH=6.5) solution for 3 times to remove residue Cl<sup>-</sup>. The cleaned gel was then re-dispersed in DEA/HNO<sub>3</sub>/water (pH=6.5) and allowed to age overnight. After that, the gel was again separated by vacuum filtration, and then dried at 60 °C for 12 h. Finally, the dried gel was calcined at 600 °C for 6 h. The SnO<sub>2</sub> powders formed based on this method was heavily agglomerated, as shown in **Figure 89** (a-b), and the crystallinity was very low as shown in **Figure 89** (e).

**Table 19** Sensor made from ZnO nanoflower, gas concentration: 25 ppm, temperature: 300°C.

	$R_a/R_g$	Response time (sec)	Recovery time (sec)
H <sub>2</sub>	1.8	103.8	189
CO	1.4	101.0	149.8
CH <sub>4</sub>	3.3	70.8	165.3
C <sub>2</sub> H <sub>6</sub>	2.4	25.4	85.2
C <sub>2</sub> H <sub>4</sub>	2.7	488.3	597.9
C <sub>2</sub> H <sub>2</sub>	36.6	10.2	202.2

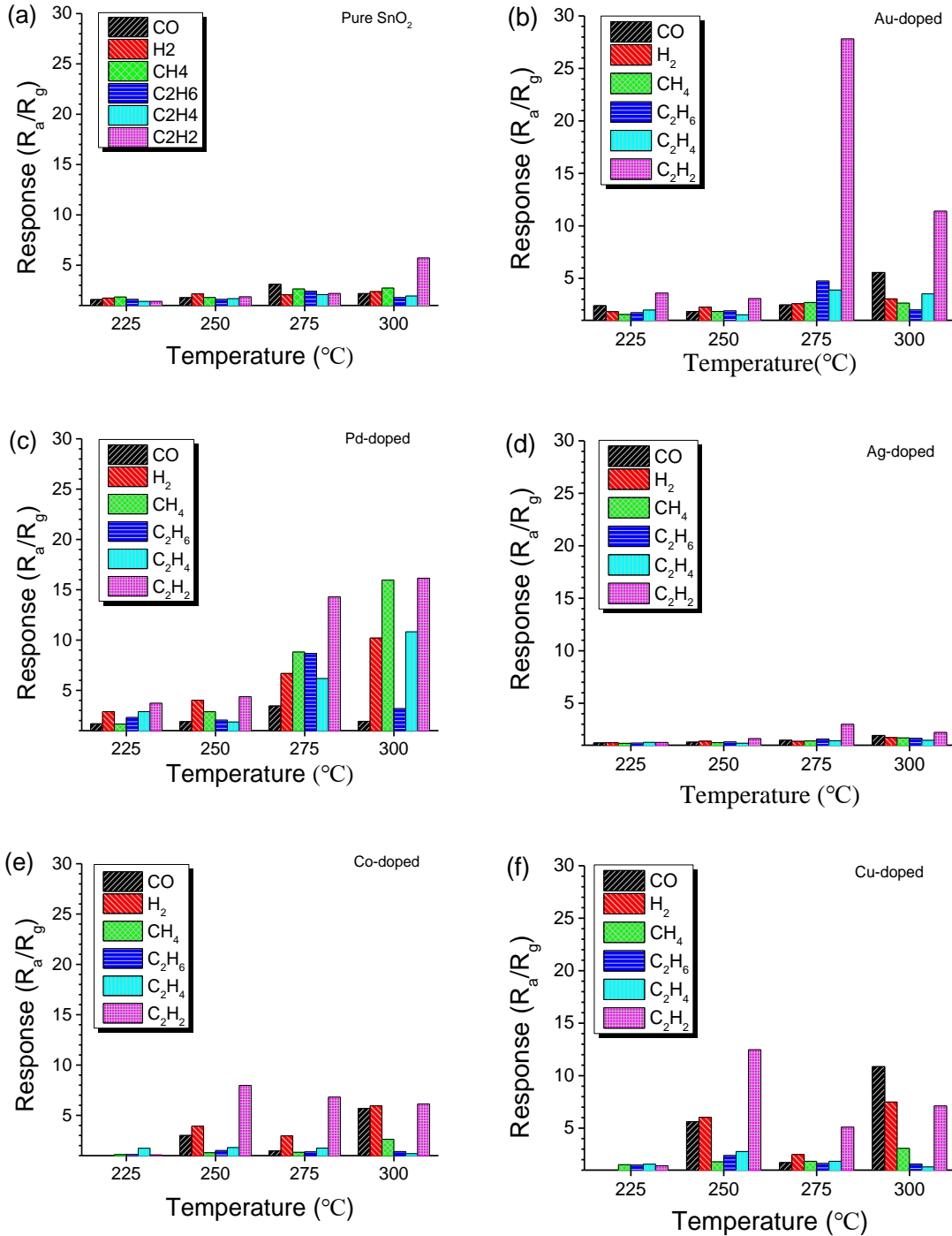
Therefore, we modified the synthesis method by adding PEG-400 as a surfactant in the aging to prevent aggregation of primary particles during the following drying step. The strategy is proven very effective. As shown in **Figure 89** (c-d), the particles are more loosely-packed and pores can be seen between particles. The crystallinity also improved due to the addition of PEG-400.



**Figure 89.** (a-b) SnO<sub>2</sub> powders without PEG; (c-d) SnO<sub>2</sub> powders prepared with PEG; XRD patterns of SnO<sub>2</sub> powders with or without PEG.

The loosely-packed SnO<sub>2</sub> nanoparticles were used as base material, and six dopants including Au, Pd, Ag, Co, Cu, and Ni were added for surface modification by a wet-impregnation method. The doping concentration is controlled to be around 1-2.5 wt%, and the sensing performances were characterized at various working temperature by introducing 6 type of reducing gases (5 ppm) successively. The results are shown in **Figure 90**. The addition of 1 wt% of Au leads to notable increases in the sensitivities to C<sub>2</sub>H<sub>2</sub> (max 29 at 275 °C) and CO (max 6 at 300 °C). The addition of 1 wt% Pd leads to sensitivity increase to all gas species except for CO. To be specific, H<sub>2</sub> reaches max value of 10 at 300 °C; CH<sub>4</sub> reaches max value of 16 at 300 °C; C<sub>2</sub>H<sub>6</sub> reaches max value of 8 at 275 °C; C<sub>2</sub>H<sub>4</sub> reaches max value of 11 at 300 °C; C<sub>2</sub>H<sub>2</sub> reaches max value of 16 at 300 °C. The addition of 1 wt% Ag, unlike the other two noble metal additives, doesn't lead to a

sensitivity increase. The addition of 2.5 wt% base metal oxide (p-type) leads to similar types of sensitivity enhancement in CO, H<sub>2</sub>, and C<sub>2</sub>H<sub>2</sub>. This suggests that the p-type metal oxide dopants electronically sensitize the pristine SnO<sub>2</sub> gas sensor.



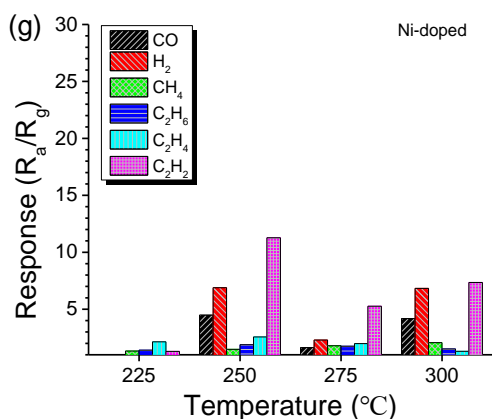


**Figure 90.** gas sensing performance test at various temperature.

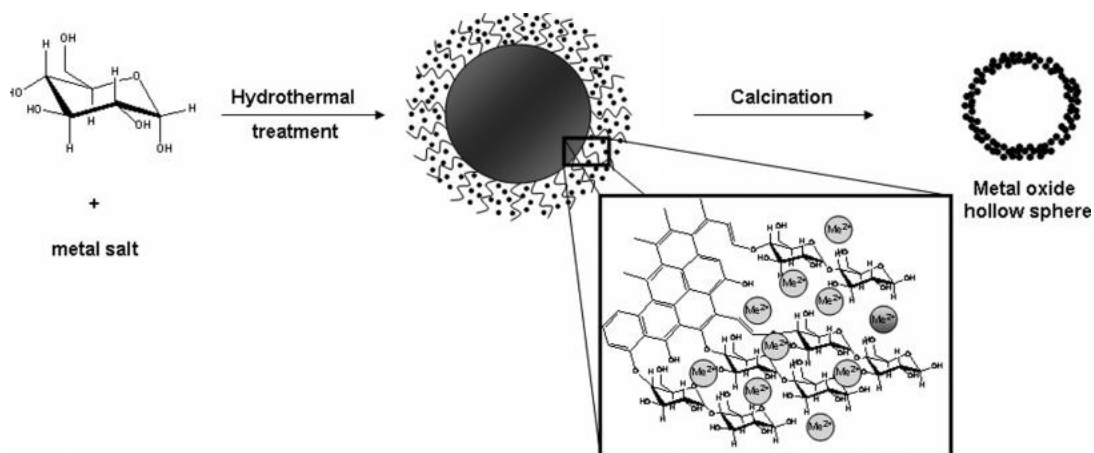
#### 7.4.5 Copper(II) Oxide-based Sensing Materials

##### 7.4.5.1 CuO/CeO<sub>2</sub> Composite Hollow Microsphere

CuO/CeO<sub>2</sub> is an extensively studied CO preferential oxidation (CO-PROX) catalyst [9], which can selectively remove CO in H<sub>2</sub> stream by oxidation at a temperature around 150°C. The key to achieving selectivity is the interfacial sites between CuO clusters and CeO<sub>2</sub> substrate (or CeO<sub>2</sub> clusters and CuO substrate). These interfacial sites allow the formation of intermediate product (i.e. Cu<sup>+</sup>-carbonyl) that serves to selectively decrease the activation energy and accelerate the reaction speed of the CO oxidation reaction at room temperature, while the oxidation of H<sub>2</sub> occurs at higher temperature (>100 °C) at reduced copper sites formed on top of the CuO particles.

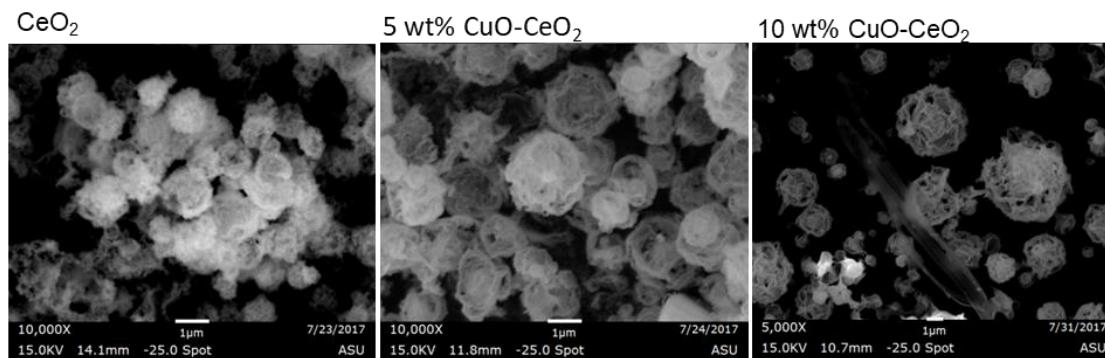
Both CuO (p-type semiconductor) and CeO<sub>2</sub> (n-type semiconductor) have been investigated as gas sensor material (e.g. reducing gas, oxygen). However, the gas sensing properties of CuO/CeO<sub>2</sub> composite material has not been studied before. Because the gas sensing of semiconductors relies on the electron density change generated by the oxidation reactions of reducing gases (e.g. CO, H<sub>2</sub>), the same catalytic reaction that the CO-PROX

catalyst based on, CuO/CeO<sub>2</sub> composite as gas sensor material should show the same level of selectivity towards CO as it has as CO-PROX catalyst.



**Figure 91.** a schematic diagram showing the forming mechanism of metal oxide hollow sphere structure.

Hollow structure due to its high surface-to-bulk ratio and its resistance to agglomeration is a very advantageous configuration for gas sensing application. CuO/CeO<sub>2</sub> composite hollow spheres with CuO weight percentages ranging from 0 to 95 were synthesized by a sucrose-mediated hydrothermal method (illustrated in **Figure 91**). The hydrothermal treatment leads to the formation of carbon spheres, on which metal ions (i.e. Ce<sup>4+</sup>, Cu<sup>2+</sup>) will segregate. The carbon cores are then burnt away during the following calcination step, leaving a porous shell composed of metal oxide nanocrystals.



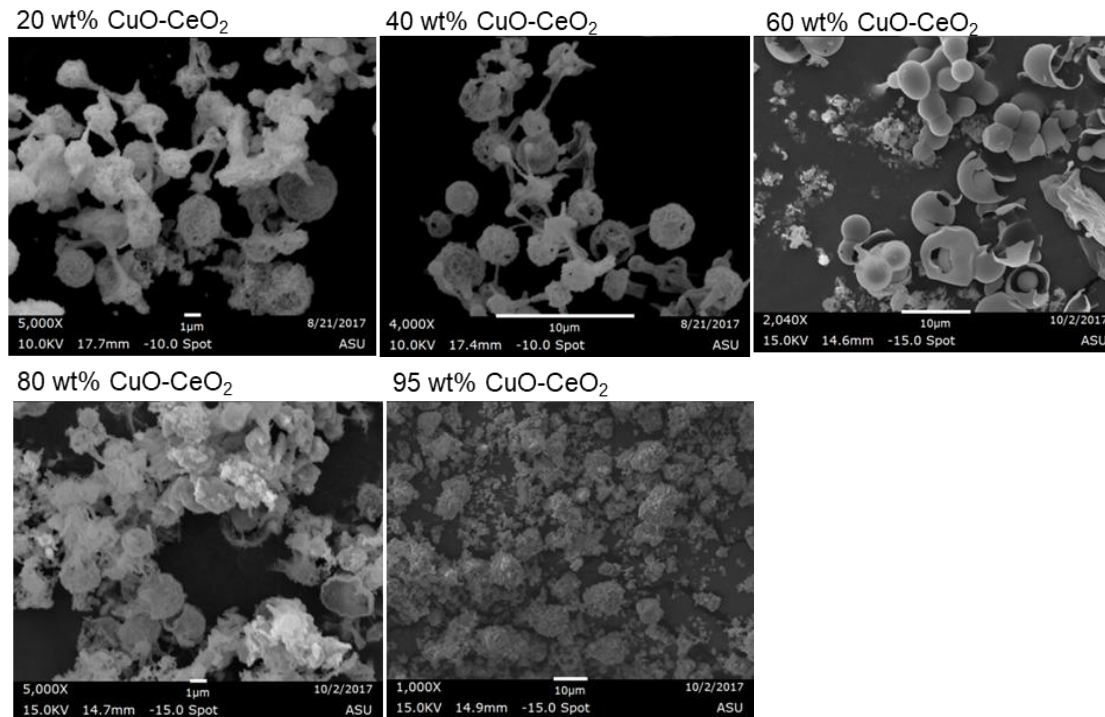


**Figure 92.** SEM images of CuO/CeO<sub>2</sub> composite hollow microspheres.

The morphological characteristics of CuO/CeO<sub>2</sub> composite hollow spheres were studied by SEM. For the present experimental parameters, the pure CeO<sub>2</sub> hollow spheres exhibit diameters of around 1.18 μm. The SEM micrographs (**Figure 92**) further reveal that the shell is formed out of aggregated metal oxide nanoparticles, and the sub-micron sized gaps on the shell are clear evidence for the hollow nature of these spheres. The addition of copper salt in the precursor solution leads to an increase in particle size from 1 to around 2 μm. In addition to particles size, morphology also changes with the addition of copper oxide. Aside from the usual hollow spheres, many rods connecting the spheres are observed for samples with 5-80 wt% CuO concentration. The atomic composition of a rod observed in 5 wt% CuO-CeO<sub>2</sub> was characterized by EDS (**Figure 92**), and the composition of the rod is close to that of the spheres, which suggests that despite the morphological

complexity, the levels of mixing between the two metal oxides are consistent throughout the spheres and the rods, and hence the gas sensing properties shouldn't be affected by the morphological change. The 60 wt% CuO sample is one exception: aside from hollow spheres with smooth thin shell, no rods can be observed. Hollow sphere structure no longer exists in 95 wt% CuO sample. Instead, the sample appears to be just agglomerates of nanoparticles.

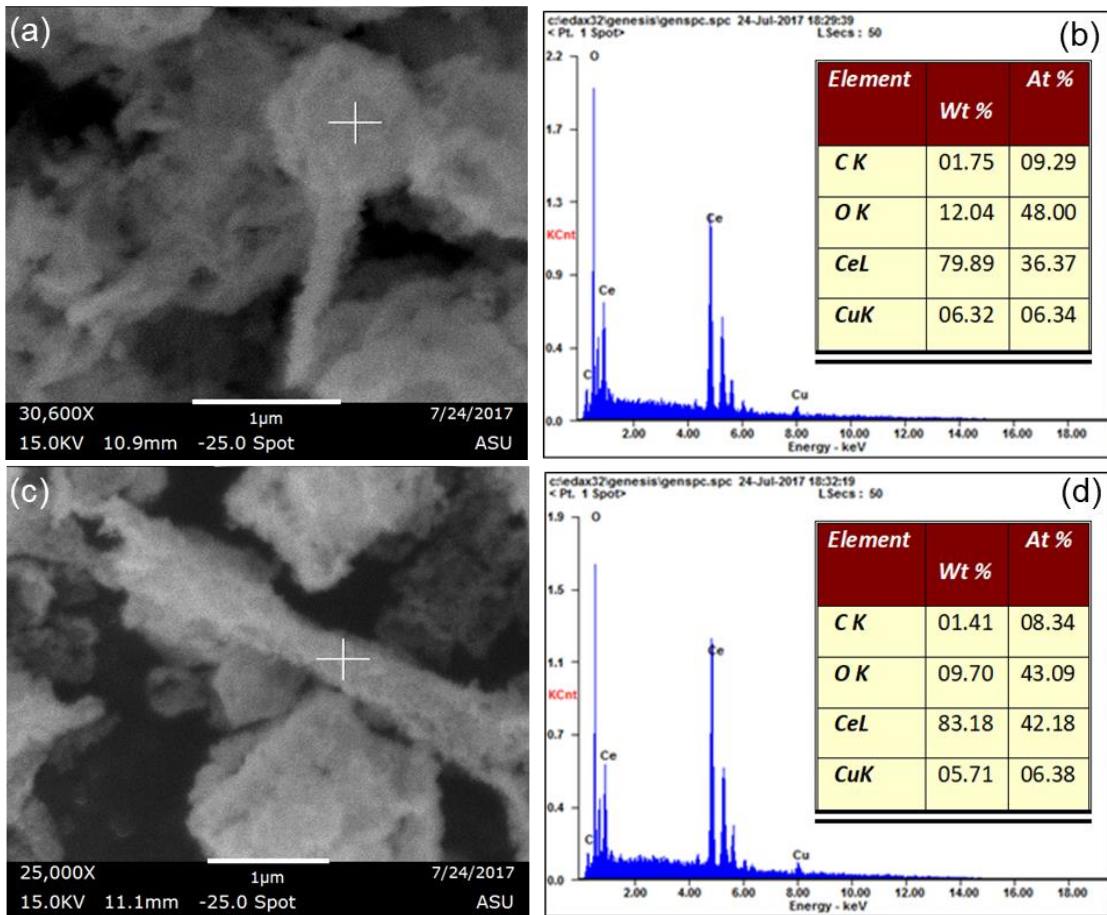


**Figure 93.** EDS analysis on the sphere (a) and rod (b). The white cross on the SEM images indicates the position that EDS analysis was performed.

The crystallographic information about the CuO/CeO<sub>2</sub> composites was investigated by XRD. Peaks corresponding to CuO (monoclinic structure) and CeO<sub>2</sub> (fluorite structure)

have been identified (**Figure 94**). Rietveld refinement on these XRD patterns has also been performed. The weight percentage of  $\text{CeO}_2$  and  $\text{CuO}$  have been confirmed to be close to theoretical values (**Table 20**). The grain size of  $\text{CeO}_2$  and  $\text{CuO}$  are around 15 and 60 nm, respectively, which confirms the fact that the hollow spheres are formed out of aggregated metal oxide nanoparticles. The cell parameters of  $\text{CeO}_2$  and  $\text{CuO}$  were also revealed by Rietveld refinement (**Figure 95**): for  $\text{CeO}_2$ , a remains constant until a significant decrease is observed at 95% wt%  $\text{CuO}$ , which suggests doping of  $\text{Cu}$  into  $\text{CeO}_2$ ; for  $\text{CuO}$ , the three cell parameters start to change at  $\text{CuO}$  wt% below 10%, and the cell volume increase sharply below 10%, which suggests doping of  $\text{Ce}$  into  $\text{CuO}$ .

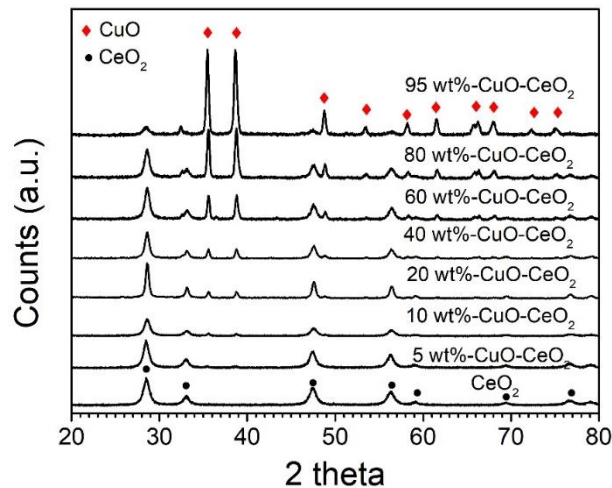


**Figure 94.** XRD patterns of the  $\text{CuO}/\text{CeO}_2$  composite hollow spheres with different  $\text{CuO}$  concentration.

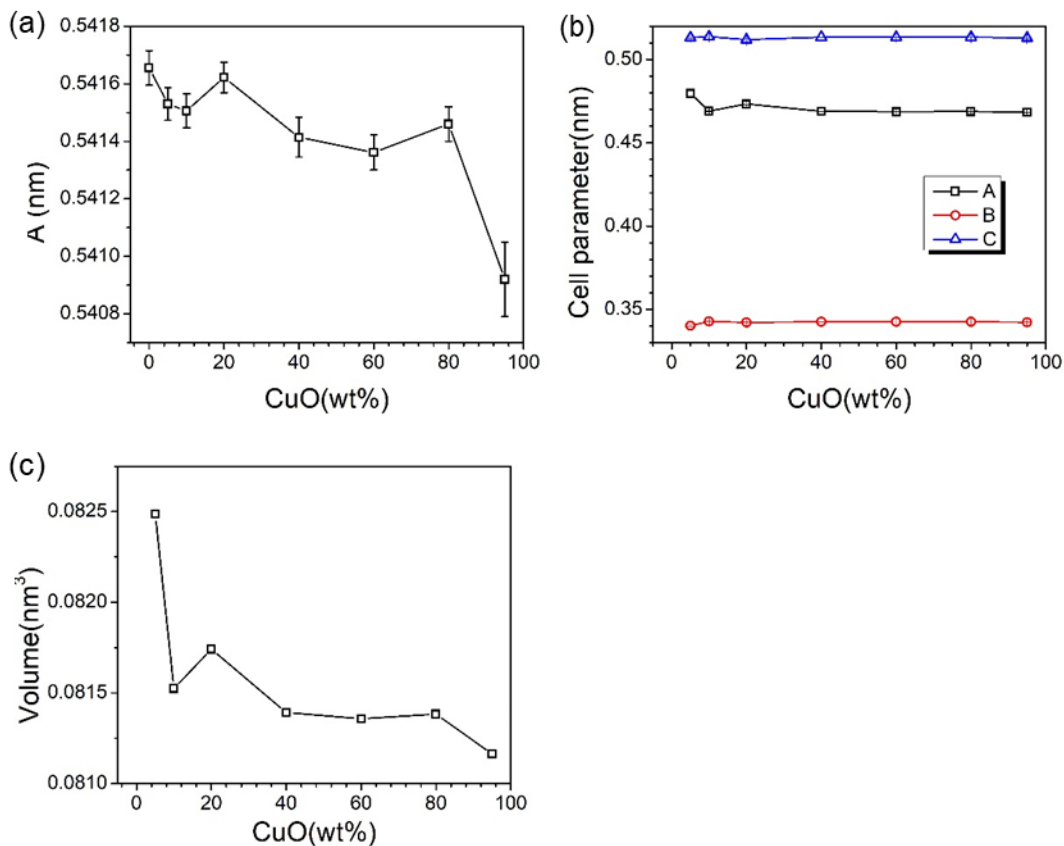
The  $\text{CuO}/\text{CeO}_2$  composite hollow spheres were made into gas sensors and their sensor response as a function of temperature toward 1000 ppm of  $\text{H}_2$  and  $\text{CO}$  were recorded (**Figure 95**). An n-type response (resistance decrease when reducing gases are introduced) is observed for the pure  $\text{CeO}_2$  hollow sphere. The highest response values for  $\text{H}_2$  and  $\text{CO}$



are observed at 300°C, and throughout the whole temperature range, the response towards CO is always smaller than that of H<sub>2</sub>. With the addition of CuO even at a concentration as low as 5 wt%, the sensor response behavior becomes p-type, which means that CuO is the key factor deciding the resistance value of the whole composite sensor. With the increase in CuO concentration until 40 wt%, the ultimate operation temperature, at which the response value reaches a maximum, decreases from 300 to 150 °C. However, the sensors are still more sensitive to H<sub>2</sub> than CO. For the sensor made of 60 and 95 wt% CuO, higher sensor response toward CO is achieved at a temperature range between 150 to 250 °C. However, the highest selectivity (CO response/H<sub>2</sub> response) achieved is only 1.24 for 60 wt% CuO-CeO<sub>2</sub> sensor at 150 °C.

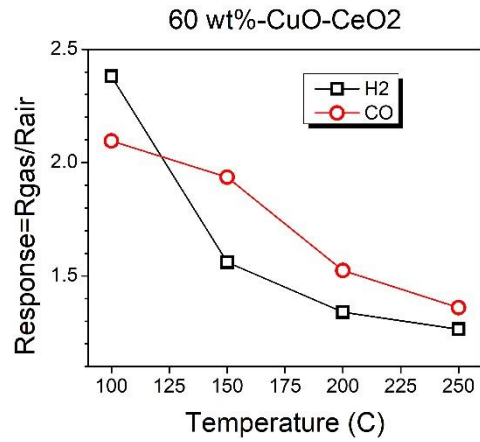
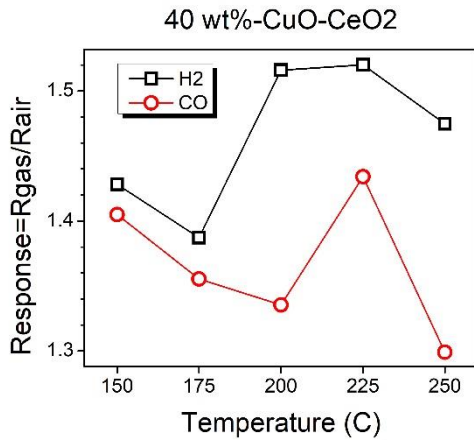
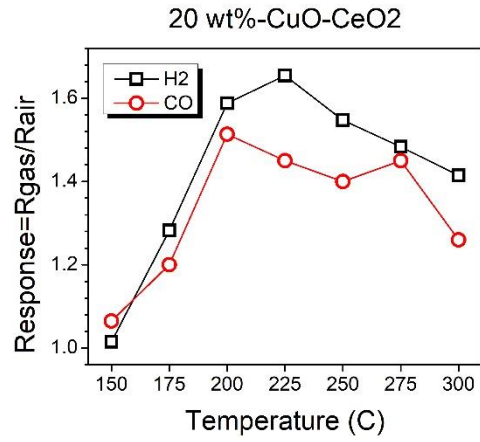
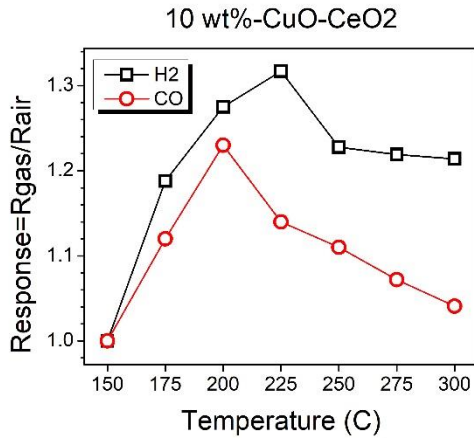
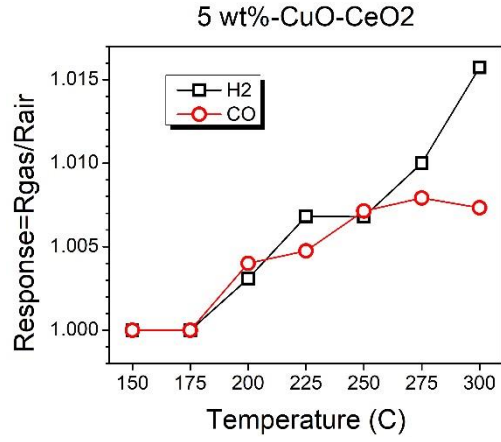
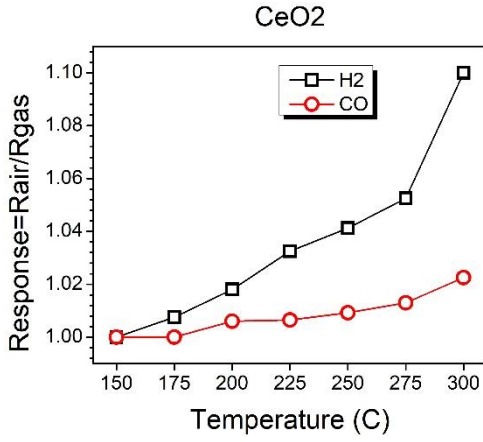
**Table 20.** Weight percentages and grain size information of the CuO/CeO<sub>2</sub> composite hollow spheres revealed by Rietveld refinement.

Samples	CeO <sub>2</sub> wt%	CuO wt%	CeO <sub>2</sub> grain size (nm)	CuO grain size (nm)
CeO <sub>2</sub>	1	0	10.42	N/A
5 wt%-CuO-CeO <sub>2</sub>	0.914	0.086	13.83	44.40
10 wt%-CuO-CeO <sub>2</sub>	0.863	0.137	11.626	57.1
20 wt%-CuO-CeO <sub>2</sub>	0.873	0.127	27.52	54.7
40 wt%-CuO-CeO <sub>2</sub>	0.621	0.379	16.33	73.00
60 wt%-CuO-CeO <sub>2</sub>	0.477	0.523	13.91	69
80 wt%-CuO-CeO <sub>2</sub>	0.264	0.737	14.64	83.30
95 wt%-CuO-CeO <sub>2</sub>	0.0610	0.9390	10.77	53.8



**Figure 95** (a) the only cell parameter A of CeO<sub>2</sub> phase (cubic structure) as a function of CuO wt%; (b) the three cell parameters A, B, and C of CuO phase (monoclinic) as a function of CuO wt%; (c) the volume of unit cell ( $=A*B*C*\sin(\beta)$ ) vs. CuO wt%.

In conclusion, no selectivity can be observed for these samples. The low selectivity toward CO can be attributed to the less active interface formed between CuO and CeO<sub>2</sub>. The formation of large, well-crystalline grains for both phases (15nm for CeO<sub>2</sub>, and 60 nm for CuO) as revealed by the Rietveld refinement results preclude a strong interaction between the two phases at their interfaces. Besides, the interfacial area/surface area ratio is also very small due to the large grains.



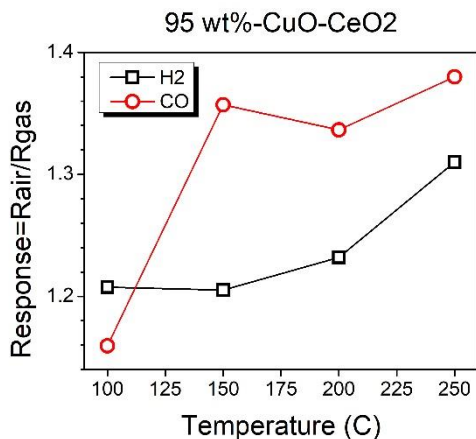


**Figure 96.** the response vs. temperature relationship for the sensors made of CuO / CeO<sub>2</sub> composite hollow spheres with different CuO concentration.

#### 7.4.5.2 CeO<sub>2</sub> Doped CuO Nanoparticles

CeO<sub>2</sub> was doped into CuO nanoparticles by the wet-impregnation method. The crystal structures of the as-synthesized CuO powders with Ce loading up to 5wt% were analyzed with XRD. As shown in **Figure 97**, pure CuO powder exhibits monoclinic crystal structure. A broad peak at 28.6° corresponds to the (111) peak of CeO<sub>2</sub> with fluorite structure is observed for the CuO samples with 2 and 5 wt% Ce loading. However, the same peak is not observed in 0.5-Ce-CuO sample, either because the CeO<sub>2</sub> concentration is likely below the detection limit of XRD, or because of the formation of a CeO<sub>2</sub> monolayer. Detailed crystallographical information revealed by Rietveld refinement is listed in **Table 21**. The addition of CeO<sub>2</sub> by impregnation does not lead to an obvious change in the mean crystallite size of CuO, which is around 50 nm for pure and Ce-loaded samples. A slight increase in the mean crystallite size of CeO<sub>2</sub> from 4.3 to 5.7 nm is observed when loading content is increased from 2 to 5 wt%, which indicates the growth of CeO<sub>2</sub> cluster size with heavier loading. The incorporation of Ce in CuO lattice is unlikely because the cell parameters of the Ce-loaded samples are very similar to those of the pure CuO sample.

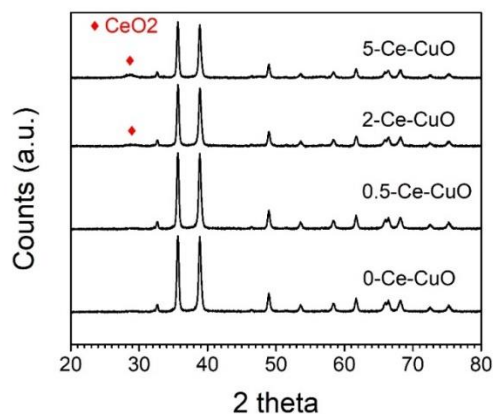


**Figure 97.** XRD patterns for pure CuO and Ce doped CuO samples.

The BET surface area of the as-synthesized CuO sample is around 1 m<sup>2</sup>/g, which is much smaller than the theoretical value for loosely-packed CuO crystals with a diameter around 50 nm. This indicates that the CuO powder synthesized in this work is severely agglomerated. This statement is confirmed by the SEM analysis. The secondary electron images (**Figure 98**) show the samples mainly consist of agglomerates as large as several microns.

**Table 21.** Crystallite size, cell parameters, and BET surface area of pure and Ce-doped CuO samples.

Ce-content (wt%)	CuO crystallite size (nm)	CeO <sub>2</sub> crystallite size (nm)	a (Å)	b (Å)	c (Å)	BET surface area (m <sup>2</sup> /g)
0	51.5±3.0	—	4.6871±0.0005	3.4277±0.0004	5.1345±0.0004	0.9769 ± 0.0194
0.5	50.4±2.9	—	4.6871±0.0005	3.4273±0.0004	5.1343±0.0004	—
2	48.3±3.1	4.28±0.37	4.6872±0.0006	3.4283±0.0005	5.1353±0.0005	—
5	53.7±3.9	5.68±0.26	4.6863±0.0006	3.4276±0.0005	5.1343±0.0005	—

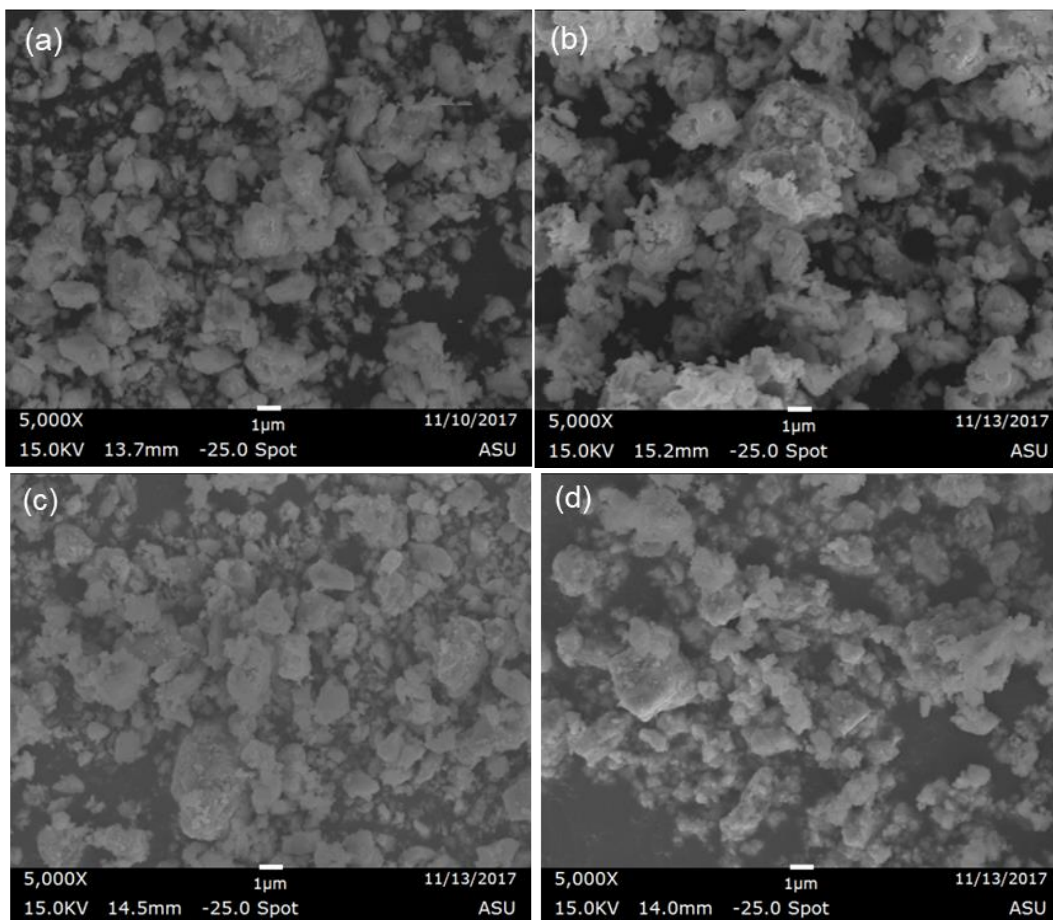


**Figure 98.** SEM images of (a) pure and (b) 0.5 wt% (c) 2 wt% and (d) 5 wt% Ce-doped CuO samples.

Thick film sensors were fabricated with CuO powders with Ce loading up to 5 wt%. The sensors' electrical resistance value in air decreases with increasing temperature, which confirms the intrinsic semiconducting nature of the sensing materials (**Figure 99**). To be specific, the quasi-free holes within CuO, which is a p-type semiconductor, are activated due to temperature increase, and as a result, the electrical conductivity increases. It should be noted the observed correlation between the resistance value and doping content does not follow the typical trend shown in other n-p type metal oxide composites (Resistivity increases with  $C_{\text{dopant}}$  until reaches a minimum). This is attributed to the geometric

variations of the sensing layers among the sensors prepared by the drop-coating method, and hence the absolute resistance values are not representative to resistivity.

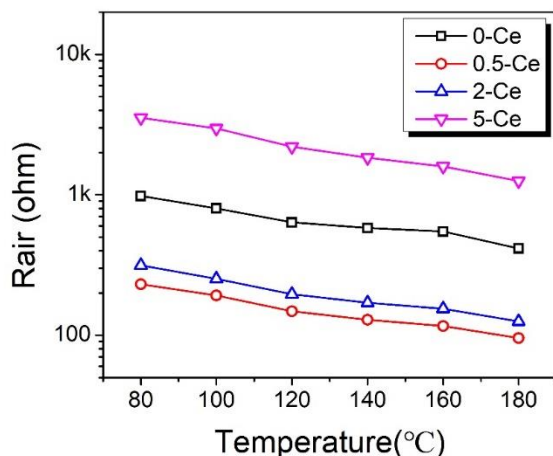


**Figure 99.** the dependence of resistance on temperature for pure and Ce doped samples.

**Figure 100** (a) shows the sensitivities to CO (50 ppm) and H<sub>2</sub> (50 ppm) of the sensors fabricated from CuO powders with Ce loading up to 5 wt%. The sensor fabricated from pure CuO powder shows very minimum p-type response toward both CO and H<sub>2</sub> at the entire temperature, which is expected considering the extremely low surface area of the sample. In comparison, even at Ce loading as low as 0.5 wt%, a significant enhancement in sensitivities to both CO and H<sub>2</sub> is observed. Adding an even higher dosage of CeO<sub>2</sub> further improves CO sensitivity, while the improvement in H<sub>2</sub> sensitivity is negligible. It is apparent that the presence of CeO<sub>2</sub> leads to a shift of the temperatures for the maximum sensitivities towards lower temperature, especially for CO. The selectivity values for CO calculated based on the single gas measurement on pure and Ce-loaded CuO samples as a function of testing temperature is shown in **Figure 100** (b). The pure CuO sample displays no selectivity for CO at the whole temperature range. For Ce-loaded samples, the

selectivity improves with decreasing temperature and increasing doping concentration. The highest selectivity value recorded is 3.55 for CuO with 5 wt% Ce loading at 80 °C.

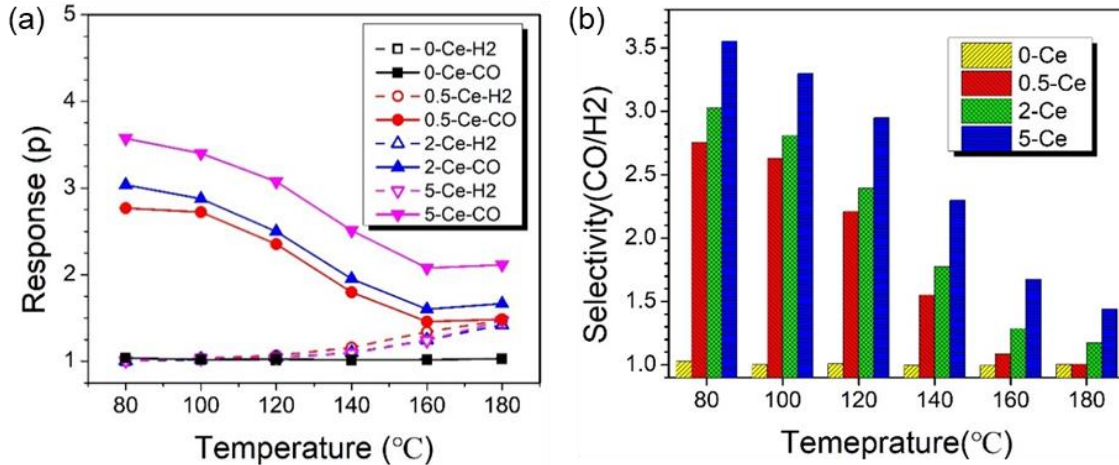


**Figure 100.** Response value vs. temperature (a); Selectivity value as a function of temperature (b).

**Figure 101** (a) shows the dependence of the sensitivities on the concentration of CO and H<sub>2</sub> at 80 °C. The sensor response achieved for 50 ppm CO with 5-Ce sample (3.55) is much higher than the response value for 950 ppm H<sub>2</sub> (1.05), even though the concentration of H<sub>2</sub> is 19 times higher. This serves as a strong evidence for the realization of high CO selectivity sensor against H<sub>2</sub>. However, in a more realistic setting with both CO and H<sub>2</sub> in the analyte gas stream, the situation could be complicated by some potential interfering effects stemming from the interaction between CO and H<sub>2</sub> or the products of their oxidation reaction. H<sub>2</sub>O, which is the product of H<sub>2</sub> oxidation, has a promoting effect on CO oxidation. Besides, H<sub>2</sub> could also compete with CO for adsorption/reaction sites. This competition could be non-negligible when the concentration ratio between H<sub>2</sub> and CO is high. Therefore, sensor testing is also performed for the CO/H<sub>2</sub> mixture gas stream. Four CO/H<sub>2</sub> mixtures were prepared with a total reducing gas concentration of 1000 ppm and an H<sub>2</sub>/CO ratio



ranging from 1 to 19. The results shown in **Figure 101** (c) demonstrates that the sensitivities to CO mixed with H<sub>2</sub> are very close to that of pure CO with the same concentration. Therefore, Ce/CuO has demonstrated true CO selectivity against H<sub>2</sub> with negligible interference signal from H<sub>2</sub> even in H<sub>2</sub>-rich H<sub>2</sub>/CO mixture.

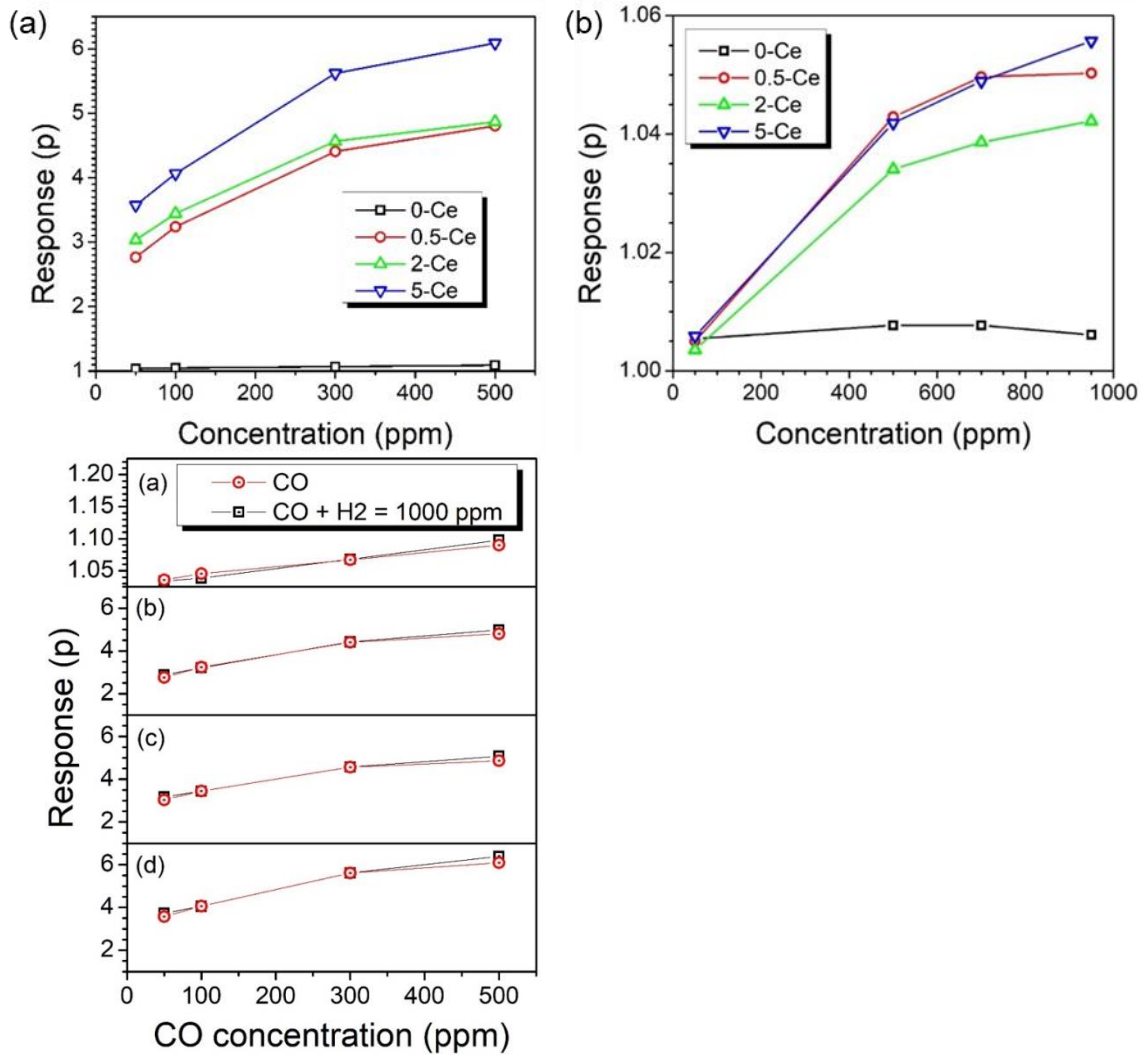
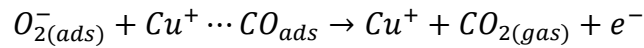
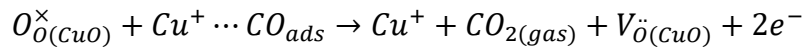


**Figure 101.** dependence of the sensitivities on the concentration of CO (a) and H<sub>2</sub> (b) at 80 °C; response value to pure CO and CO/H<sub>2</sub> mixed gas as a function of CO concentration.

Based on the results of sensor testing and previous research works on CeO<sub>2</sub>/CuO CO-PROX catalyst, the sensing mechanism is proposed. As shown in **Figure 102**, the

geometric interpretation for electrical conduction in the CuO with Ce loading samples can be summarized as CuO matrix on which CeO<sub>2</sub> clusters (~5nm) strongly bond. Because CuO is a p-type semiconductor, the adsorption of oxygen creates a hole-rich low-resistance shell, which should dictate the overall resistance. Although the p-n junction formed at the CuO-CeO<sub>2</sub> interface should be depleted of charge carriers, the depleted region in CuO side is probably too small to cause significant band bending in the conductive shell because of the much higher charge carrier density in comparison to CeO<sub>2</sub>. When CO is introduced into the atmosphere, it will be strongly adsorbed on the highly catalytic Cu<sup>+</sup> sites form at the CuO-CeO<sub>2</sub> interface, and then oxidized by either lattice oxygen or adsorbed oxygen species as demonstrated in the following two equations:



Electrons are formed and neutralized by the free holes in CuO. As a result, a large depletion region is formed. This leads to the formation of potential energy barriers on the conduction path, and hence an additional resistance term  $R_{vs}$  should be introduced:

$$R_{vs} = R_0 e^{\frac{qV_s}{kT}}$$

where  $R_0$  is the initial resistance before band bending,  $q$  is the charge of an electron,  $V_s$  is the potential energy barrier height,  $k$  is Boltzmann's constant, and  $T$  is the temperature of the sensing material.  $R_{vs}$  plays the key role in the chemical sensitization of CuO. Therefore, the proportional relationship between CO sensitivity and Ce wt% can be explained as such that more CuO-CeO<sub>2</sub> interface will cause larger  $R_{vs}$  value and hence

higher sensor response.  $H_2$  because of its lack of reactive species at this temperature range, will react with neither  $Cu^+$  nor  $Cu^{2+}$ . Therefore, within the temperature range of effective CO-PROX reaction, only CO will be oxidized by the catalyst in a  $CO/H_2$  mixture regardless of the partial pressure of  $H_2$ .

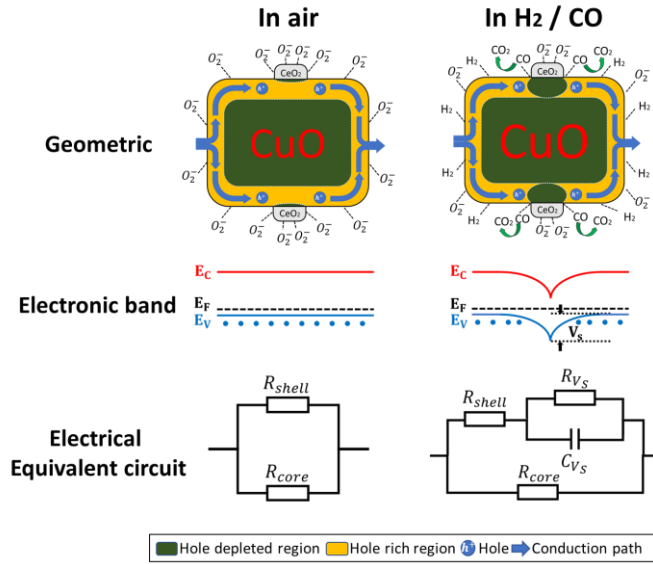


**Figure 102.** Conduction model for  $CeO_2 @ CuO$  sensor before and after the introducing of reducing gas.

Because of the severe agglomeration of  $CuO$  particles, the diffusion rate within the agglomerates is extremely slow, which leads to long recovery time ( $> 30$  min). In **Figure 103**, the recovery rate represented by the percentage recovered after 10 min ( $((R_{max} - R_{10\ min}) / (R_{max} - R_{air}))$ ) as a function of testing temperature for the Ce-loaded  $CuO$  samples is presented. The percentage recovered decreases with temperature, which means that recovery rate is slower at a lower temperature. The recovery rate also improves with Ce-wt%.  $CeO_2$  is known for its high oxygen storage capacity, and high ionic conductivity. Therefore, a higher concentration of  $CeO_2$  helps to facilitates the re-oxidation

process. Preventing the formation of compact CuO agglomerates could solve the long recovery time problem.

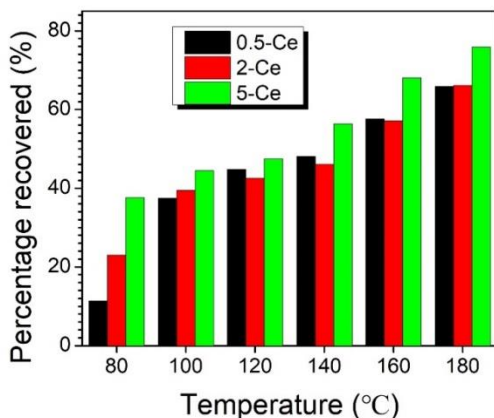


**Figure 103.** Percentage of resistance value recovered after exposing to 50 ppm CO as a function of temperature.

The CuO powder was ball-milled for 24 h at a frequency of 13 Hz. The severity of agglomeration appears to decrease after ball milling process as confirmed by SEM (**Figure 104**). The crystallite size of CuO decreases from 53.7 nm to 32 nm after the ball milling process as revealed by XRD (**Table 22**), while the surface area increases from 1 to 4 m<sup>2</sup>/g. The recovery rates of the sensors fabricated from ball-milled CuO samples are characterized based on the recovered percentages 10 mins after the sensor testing at 80°C to 50 ppm CO. After ball milling, the recovery percentage increases from 37.6% to 52.5% for 5 wt%-Ce-CuO sensors. Further enhancement in recovery rate (52.5% -> 64.7%) can be achieved by increasing the doping concentration to 10 wt% (**Table 23**).

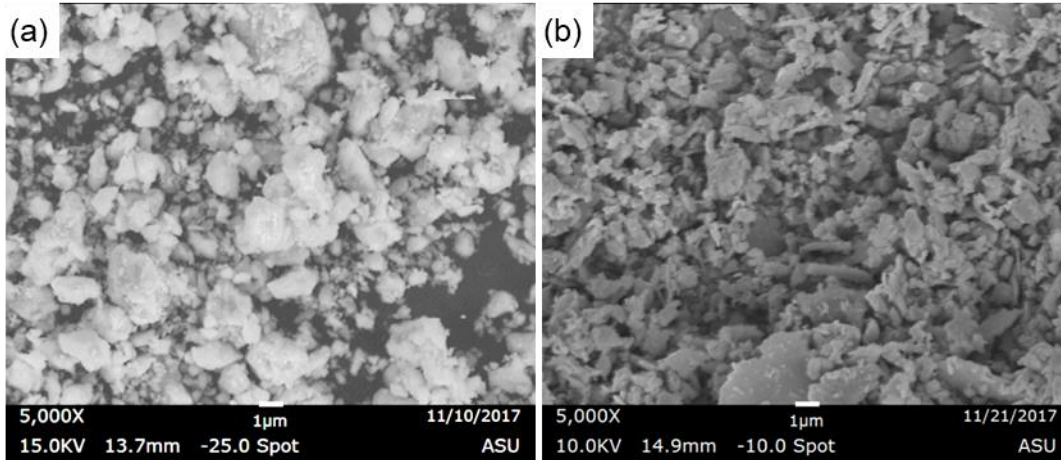


**Figure 104.** SEM images of (a) CuO before ball milling (b) CuO after ball milling.

**Table 22** Crystallite size, cell parameters, and BET surface area of Ce-doped CuO samples before and after ball milling.

	Ce-content (wt%)	CuO crystallite size (nm)	CeO <sub>2</sub> crystallite size (nm)	a (Å)	b (Å)	c (Å)	BET surface area (m <sup>2</sup> /g)
No BM	5	53.7±3.9	5.68±0.26	4.6863±0.0006	3.4276±0.0005	5.1343±0.0005	0.9769±0.0194
BM	5	32.0±1.8	5.05±0.45	4.6807±0.0009	3.4235±0.0009	5.1309±0.0009	4.2389±0.0464
	10	35.3±2.0	5.02±0.25	4.6796±0.0001	3.4228±0.0001	5.1300±0.0001	64

**Table 23.** Percentage recovered in 10 min after testing at 80°C to 50 ppm CO.

	No BM			BM	
Ce content (wt%)	0.5	2	5	5	10
% recovered in 10 min	11.3	23.0	37.6	52.5	64.7

#### 7.4.5.3 Pristine and CeO<sub>2</sub>/Pd/Au-doped CuO nanosheets

Pristine CuO nanosheets (CuO-ns) are obtained by a hydrothermal method. Na<sup>+</sup> ion is reported to be the capping agent used to synthesize 2 D structure because it refrains the growth of high energy plane. The surface modification of CuO-ns with CeO<sub>2</sub> nanocubes

was realized via an HMT method (CuO-np in water/ethanol binary solution,  $\text{Ce}(\text{NO})_3$ , atomic ratio Cu: Ce = 12.6: 1, Hexamethylenetetramine (HMT) aqueous solution,  $70^\circ\text{C}$ , refluxing), Ce-CuO-ns was obtained. The atomic composition of Ce-CuO-ns was analyzed using EDS, and the atomic ratio of Cu/Ce is 16.5. **Figure 105** (b-d) the SEM image and TEM image of Ce-CuO-ns. Here we see the CuO-ns has covered with  $\text{CeO}_2$  nanocubes with length around 10 nm. The  $\text{CeO}_2$  nanocubes show clear lattice fringes in the HR-TEM image, indicating good crystallinity.

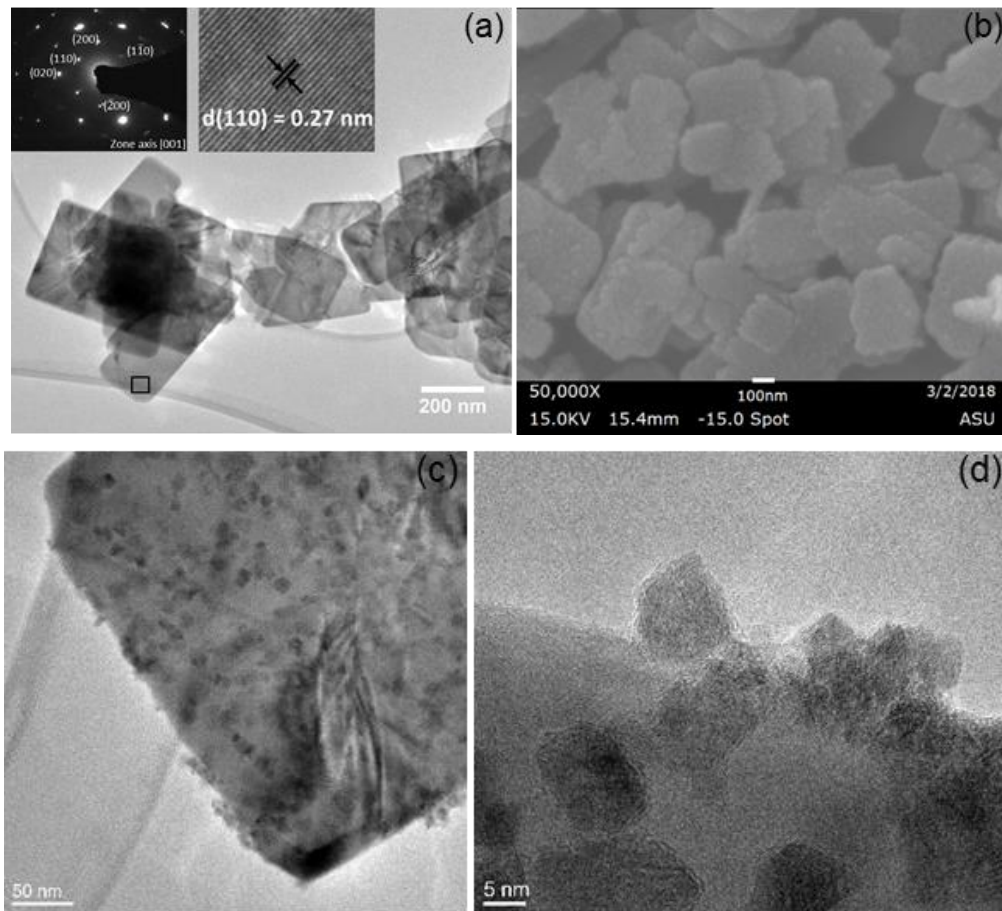


**Figure 105.** (a) TEM image of CuO-ns with SAED and HRTEM as insets; (b) SEM image of Ce-CuO-ns; (c) low magnification and (d) high resolution TEM images of Ce-CuO-ns.

Au and Pd were deposited on CuO-np by a deposition-precipitation method. The SEM images of Au-CuO-ns and Pd-CuO-ns were shown in **Figure 106** (a-b), respectively. The weight percentages of Au and Pd were around 5 according to EDS.

As shown in **Figure 106** (c), the XRD pattern from the CuO-ns powder is identical to that of pure CuO, indicating the formation of single-phase CuO with a monoclinic structure. The XRD patterns from monolayer CuO-ns and doped CuO-ns films on glass show mainly two peaks corresponding to (002) and (004) crystal plane of monoclinic CuO. This suggests the monolayer film possess strong crystal orientation at [002] direction and further confirms that the exposed crystal plane of CuO-ns is (002). Because of the low sample quantity, no peaks corresponding to the dopants can be observed for Au/Pd/Ce-CuO-ns on glass samples.

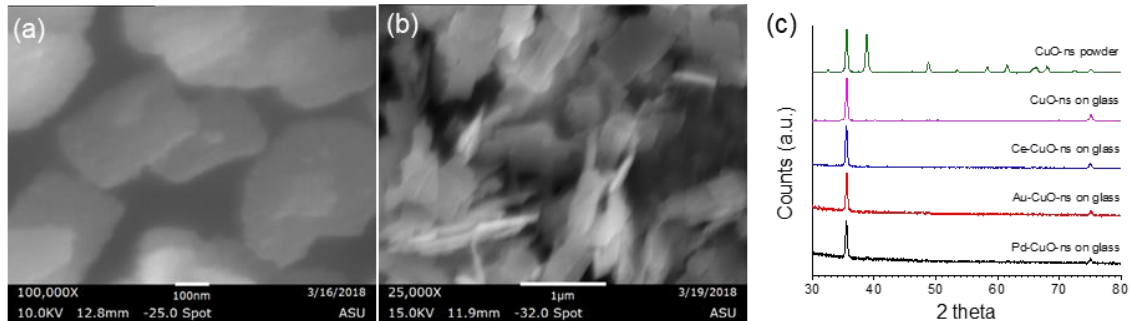


**Figure 106.** SEM of Au-CuO (a) and Pd-CuO (b); XRD for CuO-ns powder and ns single layer film (c).

Because of the low conductivity of the Ce-CuO-ns monolayer film, glass substrates with dense interdigitated electrodes (distance between electrode  $\sim 10 \mu\text{m}$ ) were used to fabricate three Ce-CuO-ns monolayer film sensors. Three CuO-ns monolayer film sensors were prepared using the same type of substrates as a reference. The resistance vs

temperature curve was shown in **Figure 106**. The error bar was quite small which suggests the excellent reproducibility of the deposition technique. The resistance of Ce-CuO-n<sub>s</sub> sensor is 1000 times higher than CuO-n<sub>s</sub>. Figure 130 demonstrates the response vs temperature curves for CO, H<sub>2</sub>, and CH<sub>4</sub> (100 ppm). The response value is defined as  $(R_g - R_a)/R_a$ . The addition of CeO<sub>2</sub> leads to a notable increase in sensitivity for CO and H<sub>2</sub>, both of which witness a nearly 4 times increase at 250 °C. demonstrates the reproducibility of the sensing process towards CO at 300 °C for CuO-n<sub>s</sub> and Ce-CuO-n<sub>s</sub> sensors. A response vs. CO concentration test was performed on a Ce-CuO-n<sub>s</sub> sensor at 250 °C (shown in **Figure 108**). The test illustrates that Ce-CuO-n<sub>s</sub> sensor can detect 10-400 ppm CO in the air.

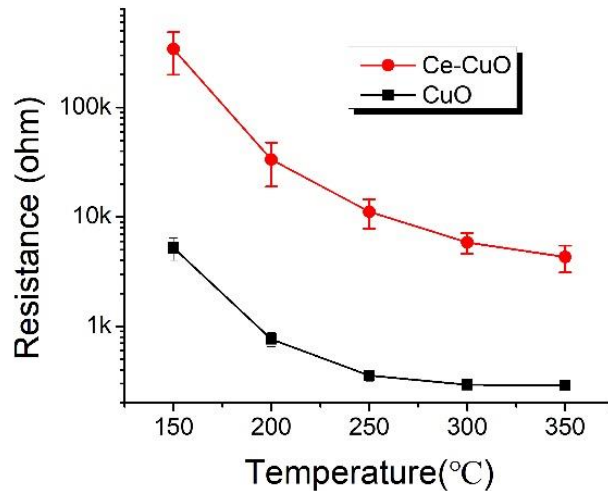


**Figure 107.** CuO-n<sub>p1</sub>, Ce-CuO-n<sub>p1</sub>-HMT1: Resistance in air vs. Temperature.



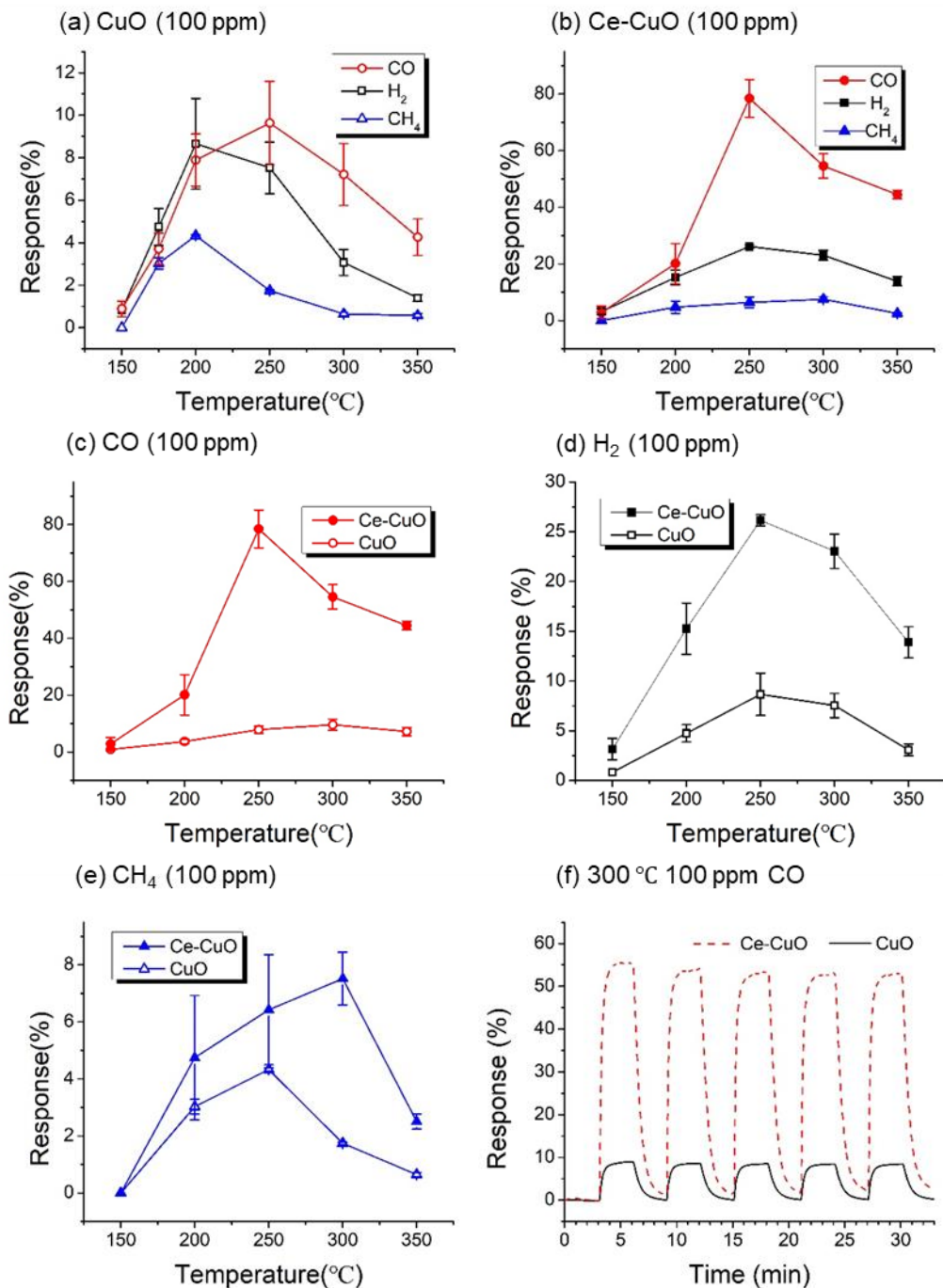


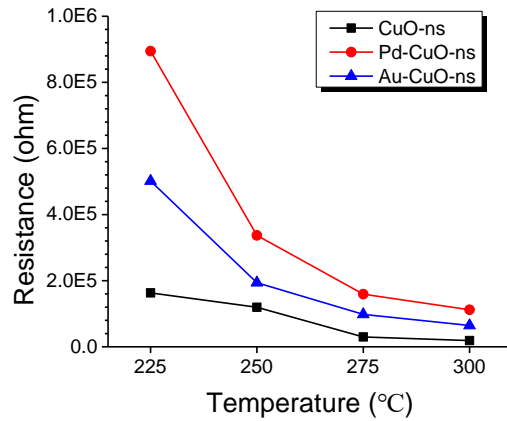
**Figure 108.** Ce-CuO-np1-HMT1 @ 25°C CO.

For Au and Pd-CuO-n, some ceramic substrates with sparse interdigitated electrodes (distance between electrode ~ 200 μm) were used to fabricate sensors. A CuO-n monolayer film sensors were prepared using the same type of substrates as a reference.

The resistance vs temperature curve was shown in **Figure 109**. The resistances of doped CuO-np sensors are larger than the pristine CuO-np sensors. The sensing properties were investigated at a temperature range between 225-300°C, to six gases (CO, H<sub>2</sub>, CH<sub>4</sub>, C<sub>2</sub>H<sub>6</sub>, C<sub>2</sub>H<sub>4</sub>, C<sub>2</sub>H<sub>2</sub>), with three different concentration (1 ppm, 10 ppm, 50 ppm). **Figure 110** shows the response varied with temperature for 1 ppm (a) 10 ppm (b) and 50 ppm (c) of 6 gases. When examine the change of response with temperature, it is clear that the trends are similar for 1 ppm and 10 ppm: (1) response to C<sub>2</sub>H<sub>2</sub> is the highest except at low-temperature end and the absolute value fluctuate at certain value with temperature (2) response to CO increases with decreasing temperature (3) response to C<sub>2</sub>H<sub>4</sub> increases with increasing temperature (4) response to H<sub>2</sub> increases with temperature, and becomes highest at 225°C (5) C<sub>2</sub>H<sub>6</sub> and CH<sub>4</sub> has minimal response (close to 1) at 275 and 300°C, and both increases with decreasing temperature, except for a really high response for CH<sub>4</sub> observed at 250°C. At 50 ppm, the response to C<sub>2</sub>H<sub>2</sub> is much higher than other gases and the response value increases with decreasing temperature.

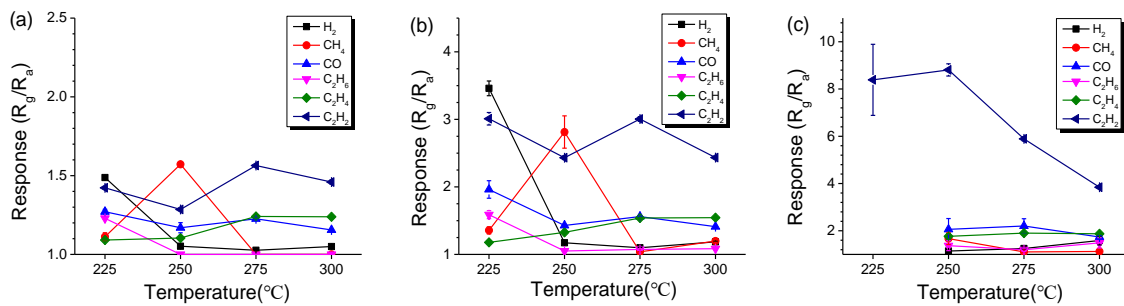
The response vs. concentration at different temperature can also be compared based on **Figure 110**. It can be seen that 275°C should be the optimal operating temperature for CuO-np-monolayer sensor to function as a C<sub>2</sub>H<sub>2</sub> sensor because at this temperature, the selectivity is very high and the sensor response towards C<sub>2</sub>H<sub>2</sub> remains the highest at the whole concentration range. Another phenomenon needs to point out is that CuO-np-monolayer sensor has a lower response to 50 ppm CH<sub>4</sub> than to 10 ppm CH<sub>4</sub> as shown in **Figure 110**. One possible explanation is that the desorption of CH<sub>4</sub> or its oxidation products

are a slow process which makes the sensor surface less reactive to CH<sub>4</sub> when it was introduced into the test chamber for the second and third times.



**Figure 109.** Resistance in air vs. temperature.

Pd and Au were deposited on CuO-np by the deposition-precipitation method, and a monolayer of these sensing materials was deposited on the ceramic substrate with preprinted gold electrodes. The sensing performance was evaluated as CuO-np. There is no significant modification in sensing behavior after doping CuO-np with a noble metal as shown in Figure 132.



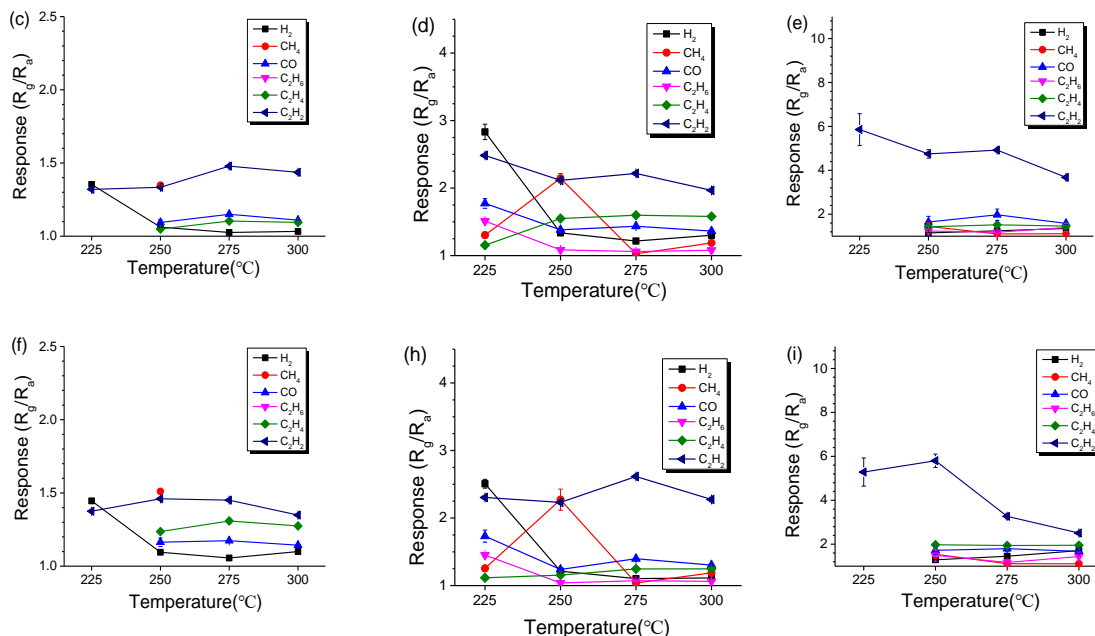


**Figure 110.** Sensitivity vs. temperature with 1, 10, 50 ppm of reducing gas from CuO (a)-(c); Sensitivity vs. temperature with 1, 10, 50 ppm of reducing gas from Pd-CuO; Sensitivity vs. temperature with 1, 10, 50 ppm of reducing gas from Au-CuO.

### 7.5 Materials Selection for the Sensor Array

A sensor array is comprised of multiple metal oxide chemiresistors with partial selectivity. When a sensor array is paired with an appropriate pattern-recognition system, a so-called "electronic nose", capable of recognizing individual components or mixtures of gases/vapors, is built.

**Figure 111** shows the generic architecture of an electronic nose. A gas mixture ( $j$ ) is presented to the sensor array, which converts the chemical input into electrical signals ( $V_{ij}$ ). The individual sensors  $i$  within the electronic nose produce a time-dependent electrical signal  $V_{ij}(t)$  in response to an odor  $j$ . The transient information in the sensor signal (e.g. rise and decay time) often depends upon multiple external and internal factors (e.g. flow & temperature profile, reaction kinetics, diffusion within active material), so instead of transient data, steady-state models are more commonly used to process gas mixtures sensor

signals. For example, relative ( $x_{ij} = (V_{ij}^{max}/V_{ij}^{min})$ ) and fractional difference ( $x_{ij} = (V_{ij}^{max} - V_{ij}^{min})/V_{ij}^{min}$ ) models are most frequently applied because they help compensate for the temperature sensitivity of the sensor. Moreover, the fractional difference model linearizes the mechanism that generates a concentration dependence in metal oxide chemiresistors. Logarithmic analysis ( $x_{ij} = \log(V_{ij}^{max} - V_{ij}^{min})$ ) can be used to linearize a highly nonlinear concentration dependency.

The response from an array made up of n sensors is a vector  $X_j$ , which can be written as  $X_j = \{x_{1j}, x_{2j}, x_{3j} \dots, x_{nj}\}$ . The data needs to be conditioned by performing normalization on the signals from each sensor ( $x'_{ij} = x_{ij}/(x_{ij}^{maxj} - x_{ij}^{minj})$ ) or from the whole array ( $x'_{ij} = x_{ij}/\sum_i x_{ij}^2$ ).

The conditioned response vectors generated by the sensor array are then analyzed using a pattern-recognition (PARC) engine. In most cases, there are two stages used in the pattern-recognition process. First, the output of the sensor array is trained by the PARC method using mathematical rules that relate the output from a known gas mixture to a set of descriptors (k classes) held in a knowledge base. This process is known as supervised learning. Then the response from an unknown gas mixture is tested against the knowledge base and the predicted class membership is given.

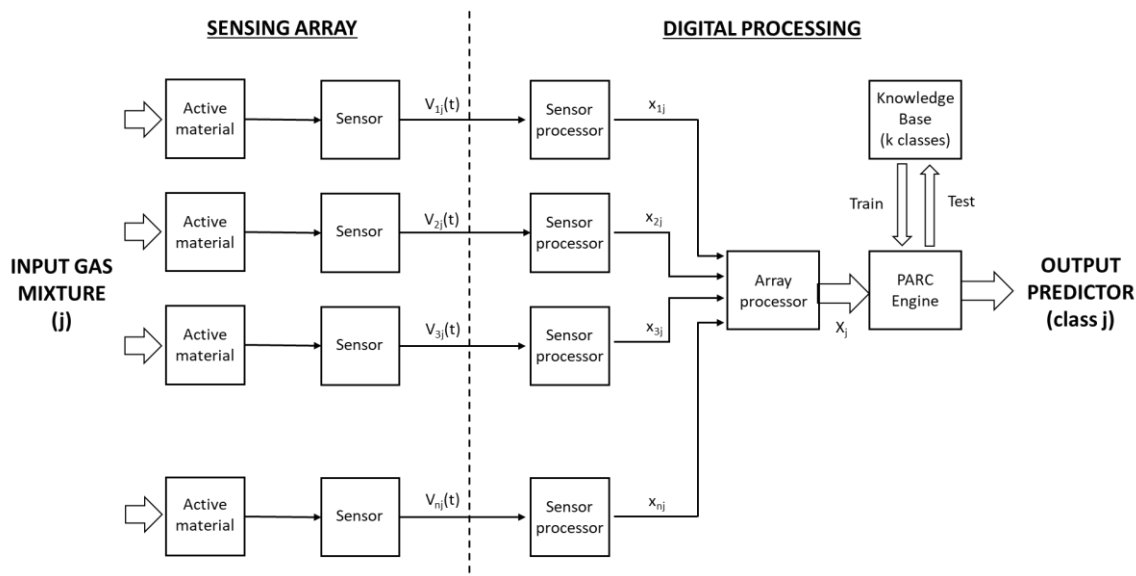


**Figure 111.** schematic of a typical electronic nose.

Several steps are taken in selecting an optimized set of 7 sensors. A hierarchical cluster analysis HCA. is performed on the normalized sensor library data to determine the similarity of sensors based on their measured intensity responses. The data for each analyte is normalized by dividing the individual sensor elements response by the sum of all the absolute modulus. Responses of all sensor elements to that analyte. The resulting dendrogram groups together sensors which give similar responses across all analytes. From each group, the sensor with the highest sensitivity value is retained. An overall sensitivity and selectivity value is then calculated for the optimized array. These values are used as a means to quantify the performance of this array with other such arrays, since selecting sensors on the basis of a visual examination of a dendrogram is insufficient in itself. The metrics for these selections is then compared with their respective population distributions for selectivity and sensitivity values calculated for 7 sensors selected at random. This allows us to evaluate the performance of our optimized array with the theoretical optimum.

### 7.5.1 Sensitivity — Sum of Root Sum Square (SRSS)

A measure of the overall sensitivity of any one-sensor element can be calculated as shown below

$$RSS = \left( \sum_{c=1}^n X_c^2 \right)^{1/2}$$

where X is the normalized response for analyte c on a c given sensor element. The sensitivity for an array of sensors is then calculated by summing the RSS values for the selected sensors, such that:

$$SRSS = \sum_{i=1}^m \left( \sum_{c=1}^n X_c^2 \right)^{1/2}$$

where m is the number of elements in the array. Note that sensitivity is calculated on the normalized response matrix (39 sensors by 6 analytes) such that each calibrant has an equal weighting in the overall calculation. The response matrix X is normalized by dividing the individual intensities by the sum of absolute intensities across all analytes for each sensor.

### 7.5.2 Selectivity — Sum of Euclidean Distances (SED)

Discrimination is simply a measure of how different the two or more response vectors are from one another. We can quantify this by calculating the Euclidean distance (ED) between pairs of analyte responses. Since we wish to maximise the discrimination between all the pairs of analytes, the overall selectivity measure is calculated by summing across all combinations. Therefore, for 6 calibrants, there are a total of 15 paired combinations of analytes, where the number of possible combinations for N analytes is given by

$\sum_{i=1}^N(N_i - 1)$ . Moreover, the SED between is1 I pairs of analyte responses is calculated as follows:

$$SED = \sum_{k=1}^{N-1} \left( \sum_{i=k+1}^N d_{ki} \right)$$

where  $d_{kl} = \sqrt{\sum_{j=1}^m (x_{kj} - x_{lj})^2}$

where m is the number of elements in the array, x is the j normalized response for sensor j towards a particular analyte k and l, and d is the ED between pairs of k l analytes k and l, while N is the total number of analytes in the response matrix (X).

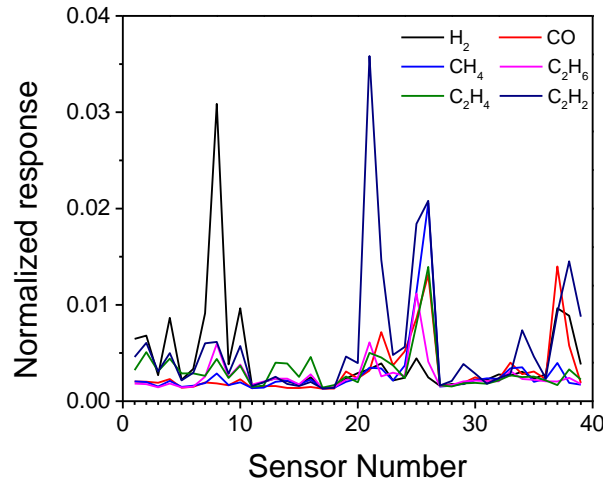


**Figure 112.** Normalized response pattern for 6 different analytes across all 39 sensors

The response matrix data contains the intensity change ( $\Delta R/R$ ) induced by the adsorption of the analyte onto the surface of the metal oxide sensors. The resistance changes for the response matrix, normalized across all sensors, are shown in **Figure 112**. A different colored line represents each analyte, and for purposes of abbreviation the



sensors are numbered 1 to 39 and are referred to accordingly. From a visual perspective, these responses look to be highly correlated. This clearly highlights the need to select an alternative subset of sensors whose responses are much less correlated and whose sensitivities are much higher.

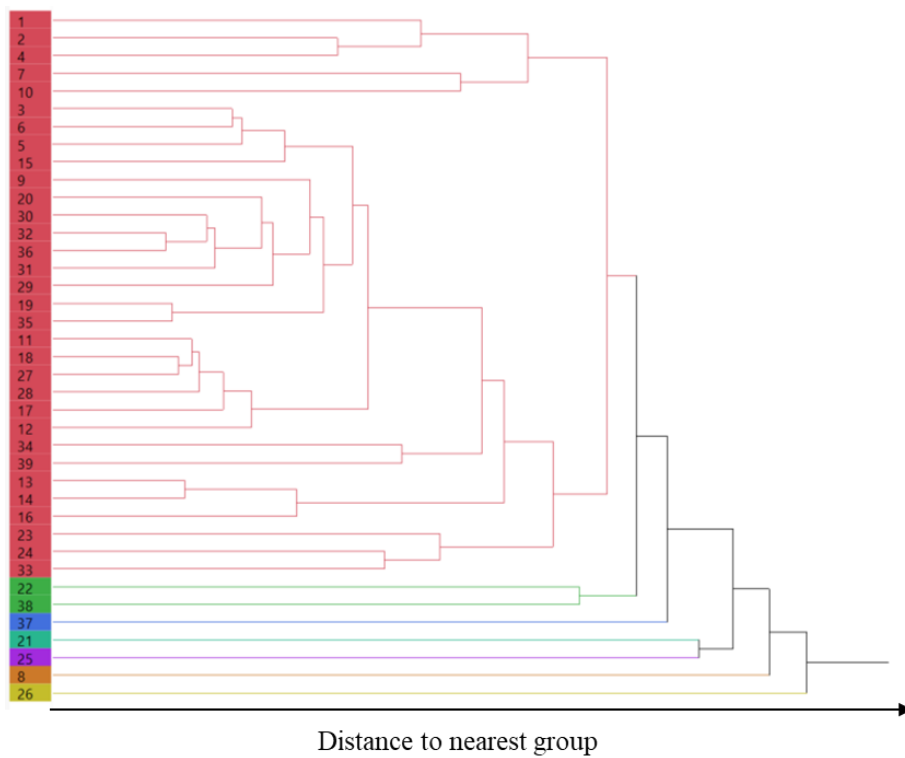


**Figure 113.** The resultant dendrogram for the normalized response matrix linked by a centroid distance measurement method of distance between two clusters is defined as the squared Euclidean distance between their means.

The results of the HCA on the normalized response matrix are displayed in **Figure 113**. In the resulting dendrogram, sensors are linked by a method of centroid, such that the distance between two clusters is defined as the squared Euclidean distance between their means. The ED between individual groups of sensors is shown on the horizontal axis. As this distance value increases, the individual points are grouped together into a few distinct

clusters, each containing more points. A grouping of 7 clusters was selected from distance graph (**Figure 114**) where the distance starts to level off.

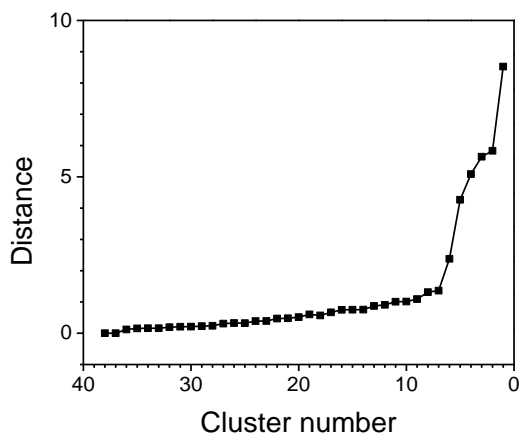


**Figure 114.** Distance graph of the hierarchical clustering

From each cluster, a sensor was chosen which showed the best sensitivity (SRSS) or selectivity (SED) towards the analytes. In addition, an array of 7 sensors was also randomly selected from the candidate pool to serve as reference. The configurations for each of these theoretical arrays are listed in **Table 24** below.

The relative performance of each of these arrays was assessed using the sensitivity and selectivity metrics. The results for this are presented in **Table 25**. The two arrays selected based on maximum SRSS and SED values both demonstrate much higher sensitivity and selectivity values than those of the randomly selected array. Moreover, the Max SED array achieves both the highest SSRS and SED values.

These numbers can be put into context by the distribution of the theoretical metric values, calculated for 100,000 random selections of 7 sensor elements. The SED and SRSS values for the Max SED array both situated in the upper tail of the distribution (**Figure**

114), while for the Max SRSS array only the sensitivity value reaches the upper tail. For the randomly selected array, both values located at the middle of the histograms.

**Table 24.** A list of the sensors selected using different selection techniques

Sensor selection		
Max SRSS	Max SED	Random
8	7	1
10	8	2
21	21	13
25	25	17
26	26	18
37	37	28
38	38	29

**Table 25.** Selectivity and sensitivity values for the individual selection of sensors

	SSRS	SED
Max SRSS	0.21	0.18
Max SED	0.21	0.40
Random	0.11	0.06

To evaluate the performance of the arrays on recognizing different gas species, three different concentrations (10, 100, 1000 ppm) of the analytes were analyzed, and the resultant sensory intensity response data were analyzed using principal component analysis. The first two principal components captured between 70-80% of the total variance in the data. The corresponding map is displayed in **Figure 116**. From a visual perspective it is evidently clear that the different analytes are better discriminated by the two optimized set

of sensors than they are by the randomly selected sensors. However, the hydrocarbons are still closely clustered in one of the quadrants, suggesting opportunities to further improving the discrimination of the hydrocarbons.

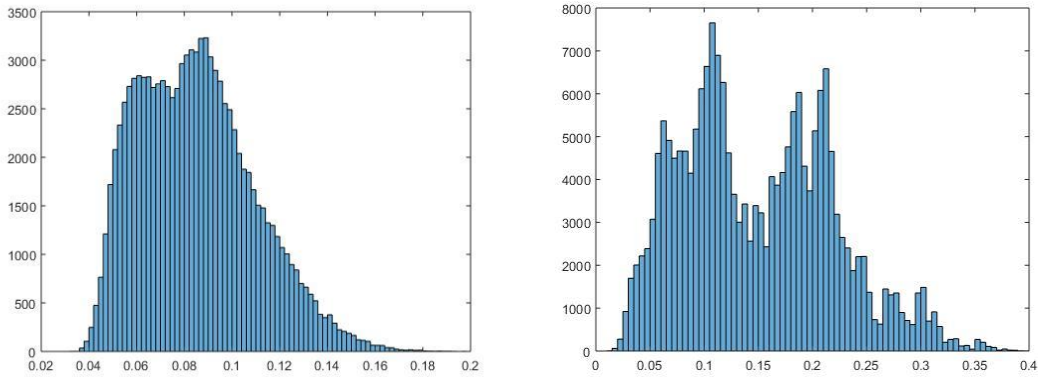


**Figure 115.** the respective histograms for the sensitivity (a) and selectivity (b) metrics for 100,000 random selection of 7 sensors for the 6 analytes.

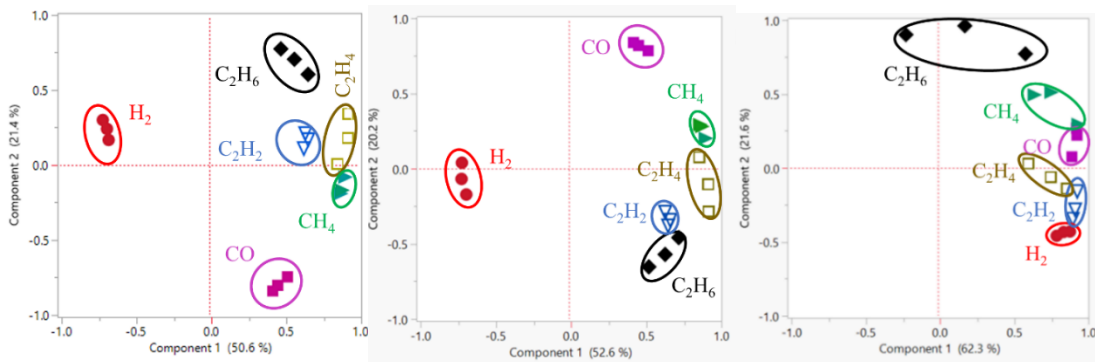


**Figure 116.** PCA maps for 6 dissolved gases obtained from (a) Max SRSS array (b) Max SED array (c) Random array.

### 7.6 Accelerated Life Testing

An accelerated life testing experiment was designed to estimate the service life of the metal oxide gas sensing materials used in the sensor box.

Gold-doped tin oxide was selected as the material of interest, because the metal/metal oxide is the most frequently adopted composition in this project, and the passivation of metal dopant is the dictating factor responsible for the temporal degradation of gas sensing performance.

Thermal stress was applied to obtain accelerated time to failure data, which is defined as the length of time required for the response to drop to 50% of original level. Based on Arrhenius model, activation energy of the aging process can be deduced, and in turn, the service life of the sensing material at normal operating condition can be estimated.

In this supporting document, the detailed procedure of the accelerated life testing was first described. In section 2, the results of the accelerated life testing were presented, and based on the calculation, the service life of the sensing material is estimated to be more than 13 years.

#### 7.6.1 Materials and Equipment:

Eleven sensor chips made from Au-SnO<sub>2</sub>, a tube furnace connected to gas cylinder containing 1000 ppm of C<sub>2</sub>H<sub>6</sub>, a gas sensor testing system

#### 7.6.2 Procedure:

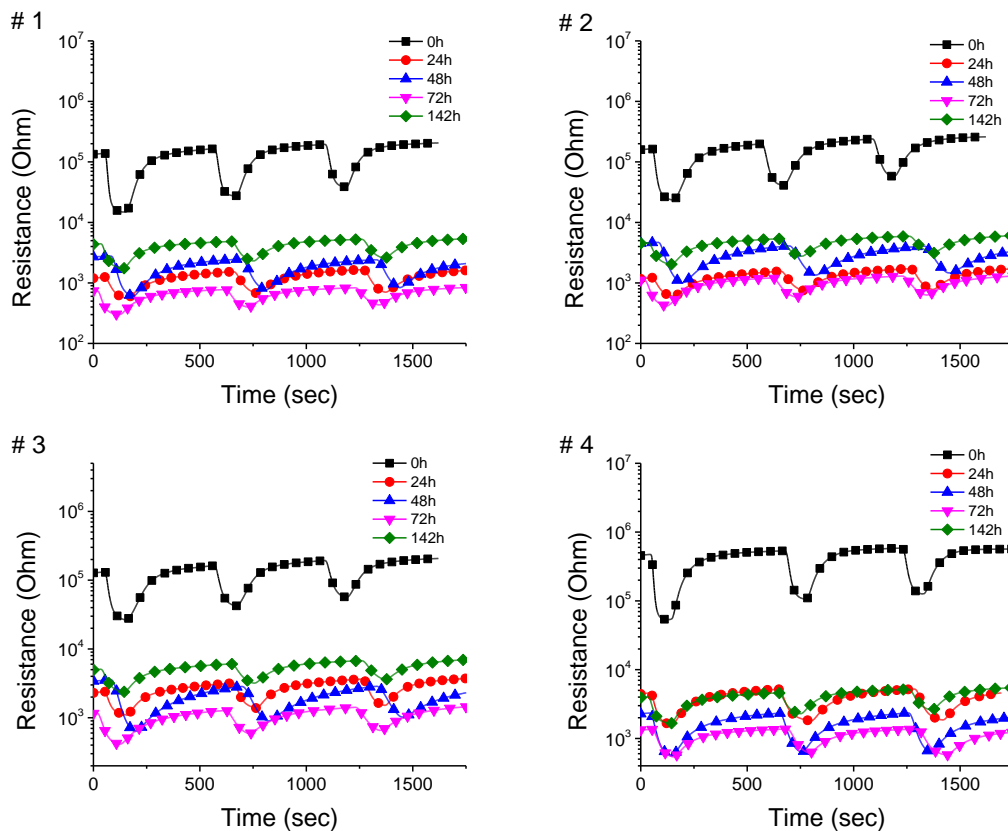
- i. The responses of all 11 fresh sensor chips toward 0.5 ppm C<sub>2</sub>H<sub>2</sub> were recorded at normal operational temperature (200°C) with the gas sensor testing system.
- ii. 6 of the fresh sensors underwent accelerated aging treatment at 600°C in the tube furnace. The atmosphere of the tube furnace contains 1000 ppm of C<sub>2</sub>H<sub>2</sub>, to simulate the real sensing environment, which contains roughly 1000 ppm of hydrocarbons. The sensors were removed periodically from the tube furnace to

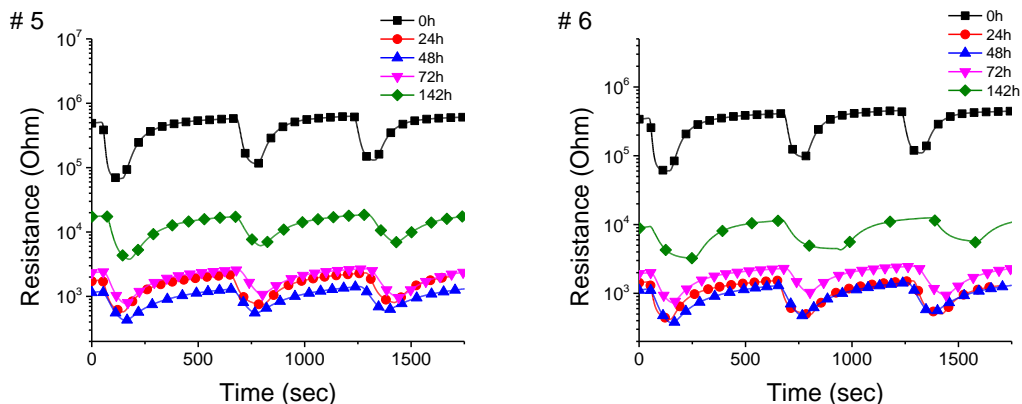
record the responses toward 0.5 ppm C<sub>2</sub>H<sub>2</sub> at normal operational temperature as a function of aging time.

- iii. The rest of the fresh sensors underwent the same accelerated aging treatment except the temperature of the tube furnace was risen to 700°C.

### 7.6.3 Results

The transient response curves of the samples that underwent accelerated aging treatment at 600°C and 700°C were demonstrated in **Figure 116** and **Figure 117**, respectively. The calculated response values for the samples with different aging time were summarized in **Table 26** for 600°C treatment and in **Table 27** for 700°C.

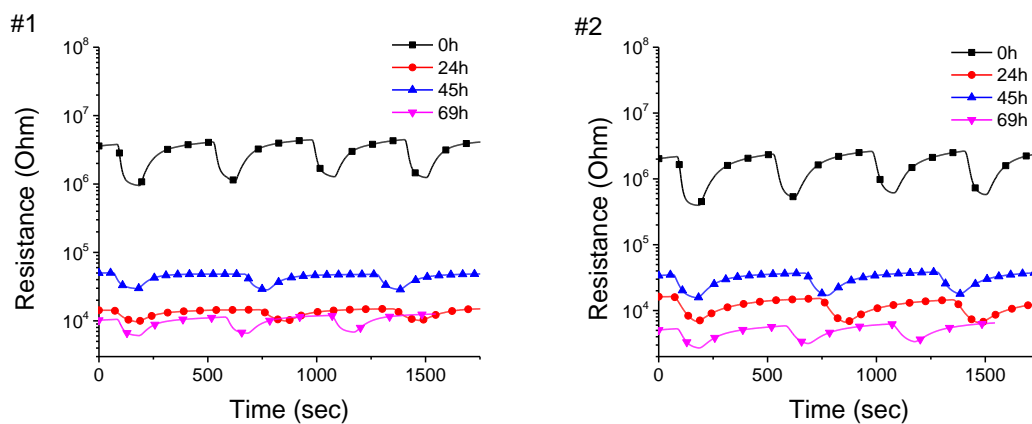




**Figure 117.** Transient response curves towards 0.5 ppm C<sub>2</sub>H<sub>2</sub> measured at 200 °C for the sensors that underwent the accelerated aging treatment at 600°C for 0, 24, 48, 72, and 142 h.

**Table 26.** Response values for the sensors treated at 600°C for different amount of times

Aging time (h)	Response (R <sub>air</sub> /R <sub>gas</sub> )						Average
	#1	#2	#3	#4	#5	#6	
0	5.3 ± 0.6	4.3 ± 0.4	3.5 ± 0.3	4.6 ± 0.4	4.8 ± 0.2	4. ± 0.10	4 ± 2
24	2.9 ± 0.3	2.8 ± 0.2	2.9 ± 0.3	3.9 ± 0.3	2.5 ± 0.3	2.9 ± 0.2	3 ± 1
48	2.29 ± 0.06	2.11 ± 0.08	2.31 ± 0.09	2.85 ± 0.06	2.98 ± 0.13	3.2 ± 0.3	2.6 ± 1.0
72	1.94 ± 0.02	2.09 ± 0.06	2.20 ± 0.07	2.26 ± 0.11	2.6 ± 0.3	2.4 ± 0.2	2.2 ± 0.9
142	2.06 ± 0.04	1.90 ± 0.04	1.87 ± 0.03	2.001 ± 0.011	2.76 ± 0.07	2.3 ± 0.3	2.1 ± 0.7



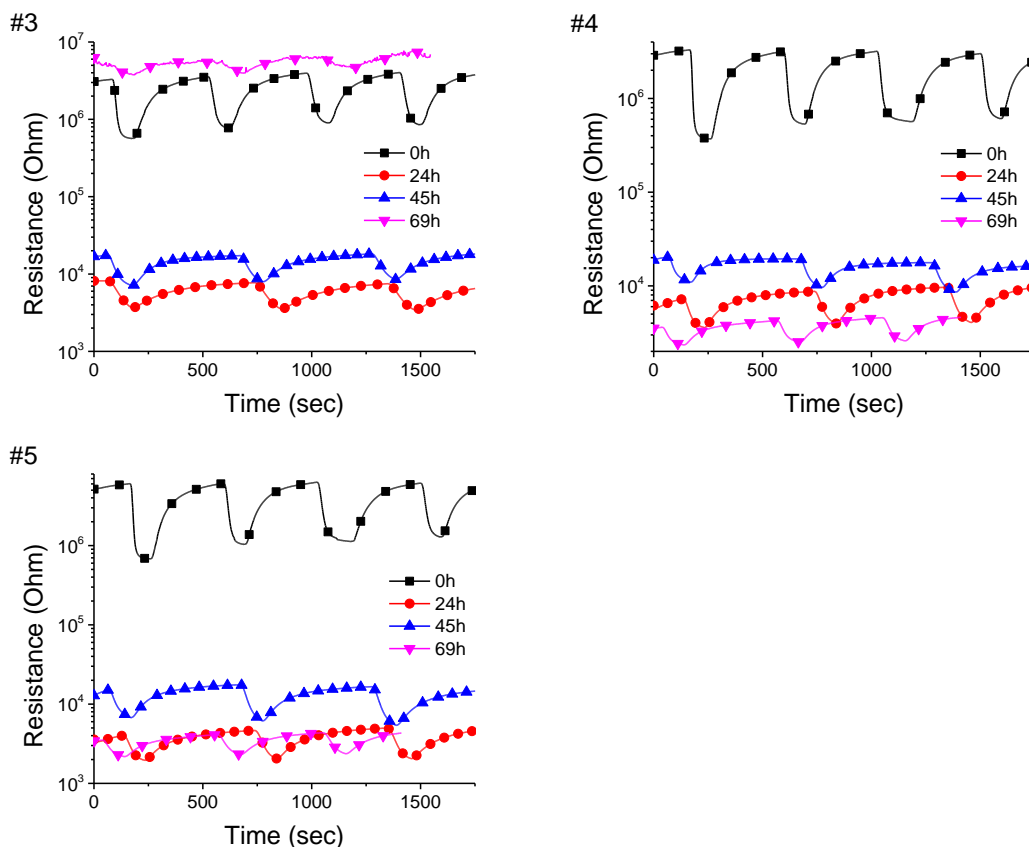


**Figure 118.** Transient response curves towards 0.5 ppm C<sub>2</sub>H<sub>2</sub> measured at 200 °C for the sensors that underwent the accelerated aging treatment at 700°C for 0, 24, 45, and 69 h.

**Table 27.** Response values for the sensors treated at 700°C for different amount of times

Aging time (h)	Response (R <sub>air</sub> /R <sub>gas</sub> )					Average
	#1	#2	#3	#4	#5	
0	3.58 ± 0.08	4.44 ± 0.15	4.57 ± 0.16	5.5 ± 0.5	5.4 ± 0.6	4.7 ± 0.8
24	1.469 ± 0.010	2.31 ± 0.06	2.19 ± 0.03	2.37 ± 0.16	2.41 ± 0.14	2.1 ± 0.4
45	1.678 ± 0.017	2.15 ± 0.04	2.14 ± 0.03	1.98 ± 0.11	2.7 ± 0.4	2.1 ± 0.4
69	1.737 ± 0.015	1.89 ± 0.06	1.37 ± 0.03	1.67 ± 0.11	1.75 ± 0.12	1.68 ± 0.19



The response values were revealed to decrease exponentially with aging time as shown in **Figure 119**. The times to failure were estimated to be 83 hours at 600 °C, and 22 hours at 700 °C.

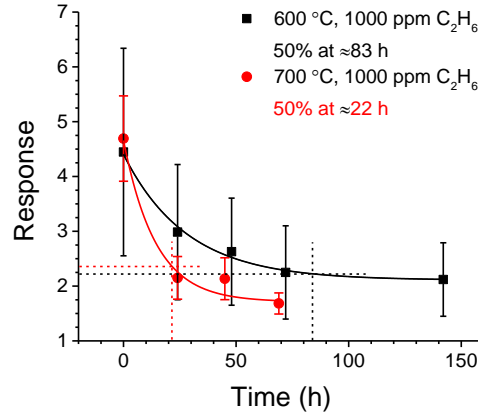


**Figure 119.** Response average as a function of accelerated aging time. The exponentially fitted curves were used to estimate the failure time.

The service life at normal operational condition is estimated based on Arrhenius model.

$$t_T = Ae^{-\frac{E_a}{RT}} \quad (52)$$

$t_T$  is the time to failure at temperature  $T$ ,  $A$  is a constant,  $E_a$  is activation energy,  $R$  is gas constant, and  $T$  is temperature in K. By rearranging and plugging in the time to failure data (eq 53-55), the activation energy is estimated to be around 40.7KJ/mol.

$$\ln t_T = \ln A - \frac{E_a}{RT} \quad (53)$$

$$\ln t_{973.15K} - \ln t_{873.15K} = \frac{E_a}{R} \times \left( \frac{1}{873.15K} - \frac{1}{973.15K} \right) \quad (54)$$

$$E_a = R \times \frac{\ln t_{973.15K} - \ln t_{873.15K}}{\left( \frac{1}{873.15K} - \frac{1}{973.15K} \right)} = 40.7 \text{ kJ/mol} \quad (55)$$

The time for the sensing material to fail at 200°C is estimated to be around 1.1 years (eq 56).

$$\ln t_{473.15K} = \ln t_{873.15K} + \frac{E_a}{R} \times \left( \frac{1}{873.15K} - \frac{1}{473.15K} \right) \approx 9537hr \approx 1.1 \text{ year} \quad (56)$$

However, in real application, the sensor will not be exposed to the dissolved gas all the time. During the 1-hour long sampling period, the sensor will be exposed to dissolved gas for only 5 min. For the rest of the hour, the sensor will regenerate in clean air. Therefore, the true service life is the estimated time to fail multiply by 12, which equals to 13.2 years.

### 7.7 Prototype Design, Construction, and Initial Tests

The sensor box was designed and fabricated by the collaborator at Clemson University. **Figure 120** shows a top-down view of the component inside the sensor box. Eight semiconductor sensors were loaded in series inside the steel chamber. Other main components include a power supply, 9 control boards, a data acquisition board, and a gas chamber with IR sensor inside for CO<sub>2</sub> detection.

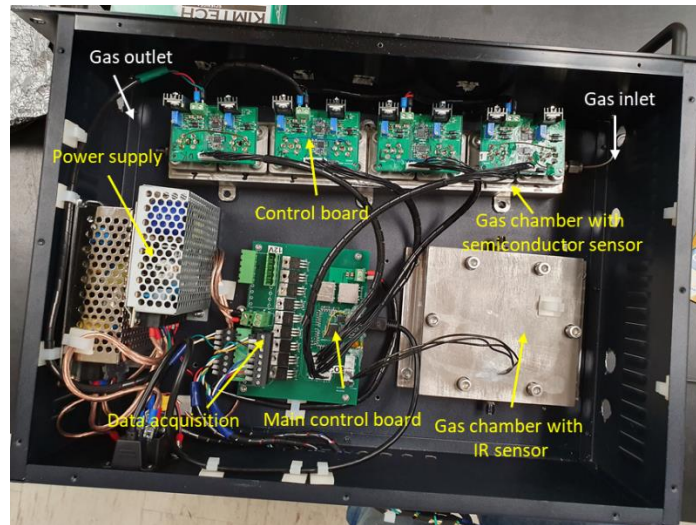


**Figure 120.** Picture of sensor box prototype.

**Figure 120** is a screenshot of the graphic user interface developed by Clemson. The testing condition is: Heating voltage: 5V (~200°C); Gas type: CO; Concentration: 0.5 ppm; Flow rate: 200 ccm.

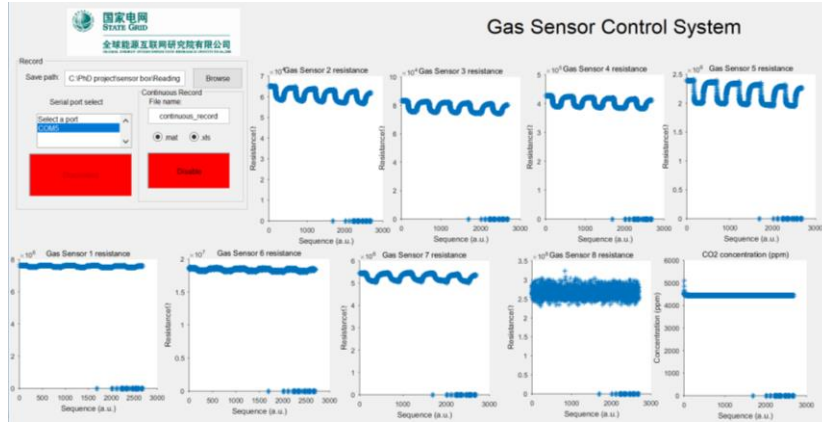


**Figure 121.** screenshot of the gas sensor control user interface developed by Clemson University.

The sensor box with complete sensor array was tested and calibrated in single gas condition, and the testing parameters and sensor responses were summarized in the tables and figures below.

**Table 28.** Semiconductor gas sensors: specifications.

Sensor No.	Composition	Heating voltage (v)
1	CuO nanosheet	3.2
2	5% Al-SnO <sub>2</sub>	7.5
3	2% Au-SnO <sub>2</sub>	5
4	ZnO nanowire	6.25
5	2% Ag-SnO <sub>2</sub>	6
6	2% Pd-SnO <sub>2</sub>	7
7	5% Cu-SnO <sub>2</sub>	6
8	1% Ni-SnO <sub>2</sub>	7

i. Calibration curves of the semiconductor gas sensors

Sensor 1: CuO nanosheet

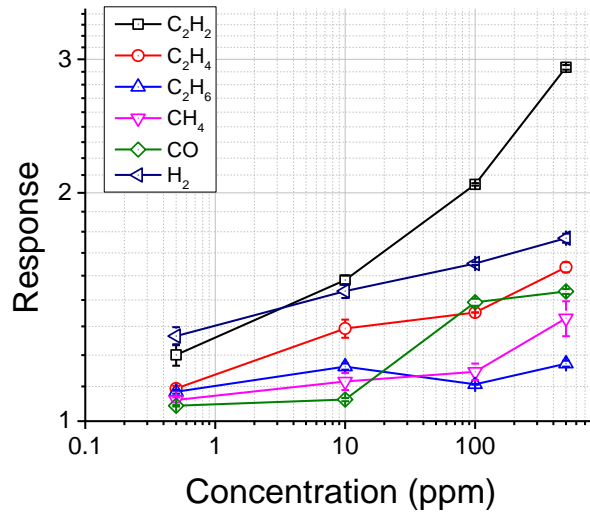


**Figure 122.** concentration vs. response curves of 6 gases.

**Table 29.** Summary of response values.

Concentration (ppm)	Response (R <sub>air</sub> /R <sub>gas</sub> )					
	H <sub>2</sub>	CO	CH <sub>4</sub>	C <sub>2</sub> H <sub>6</sub>	C <sub>2</sub> H <sub>4</sub>	C <sub>2</sub> H <sub>2</sub>
500	1.74	1.48	1.37	1.19	1.60	2.93
100	1.61	1.43	1.16	1.12	1.39	2.05
10	1.48	1.07	1.13	1.18	1.32	1.53
0.5	1.29	1.05	1.07	1.09	1.10	1.22

Sensor 2: 5%Al-SnO<sub>2</sub>

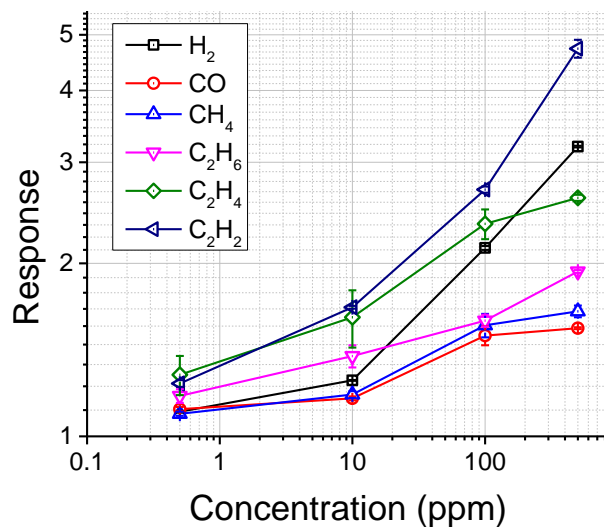


**Figure 123.** Concentration vs. response curves of 6 gases.

**Table 30.** Summary of response values.

Concentration (ppm)	Response (Rair/Rgas)					
	H <sub>2</sub>	CO	CH <sub>4</sub>	C <sub>2</sub> H <sub>6</sub>	C <sub>2</sub> H <sub>4</sub>	C <sub>2</sub> H <sub>2</sub>
0.5	1.10	1.12	1.10	1.18	1.28	1.24
10	1.25	1.16	1.18	1.38	1.61	1.68
100	2.13	1.50	1.56	1.59	2.34	2.69
500	3.19	1.54	1.65	1.94	2.60	4.73

Sensor 3: 2% Au-SnO<sub>2</sub>

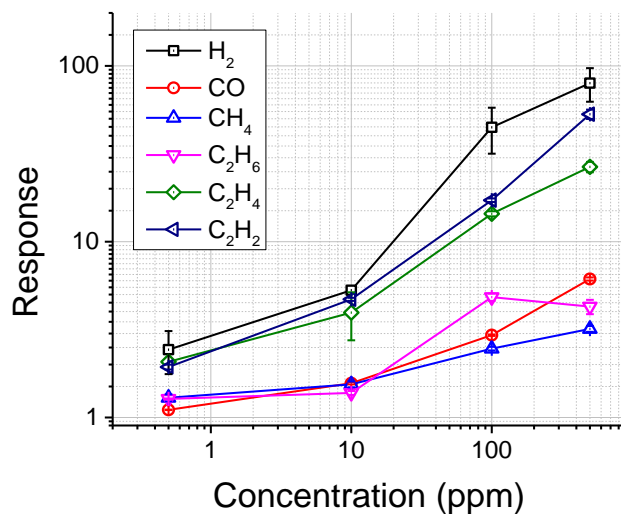


**Figure 124.** concentration vs. response curves of 6 gases.

**Table 31.** Summary of response values.

Concentration (ppm)	Response (Rair/Rgas)					
	H <sub>2</sub>	CO	CH <sub>4</sub>	C <sub>2</sub> H <sub>6</sub>	C <sub>2</sub> H <sub>4</sub>	C <sub>2</sub> H <sub>2</sub>
0.5	2.43	1.10	1.29	1.27	2.07	1.94
10	5.29	1.57	1.54	1.38	3.95	4.70
100	44.74	2.94	2.46	4.84	14.40	17.21
500	79.73	6.13	3.19	4.27	26.62	53.09

Sensor 4: ZnO nanowire

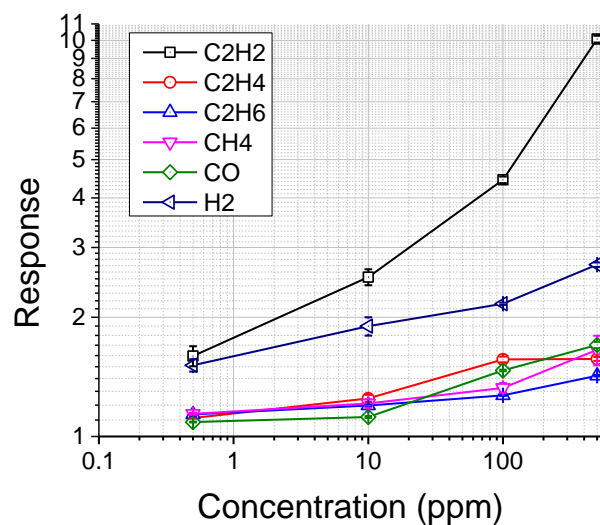


**Figure 125.** Concentration vs. response curves of 6 gases.

**Table 32.** Summary of response values.

Concentration (ppm)	Response ( $R_{air}/R_{gas}$ )					
	H <sub>2</sub>	CO	CH <sub>4</sub>	C <sub>2</sub> H <sub>6</sub>	C <sub>2</sub> H <sub>4</sub>	C <sub>2</sub> H <sub>2</sub>
500	2.71	1.70	1.65	1.42	1.57	10.07
100	2.16	1.47	1.33	1.27	1.57	4.45
10	1.90	1.12	1.21	1.20	1.25	2.53
0.5	1.51	1.09	1.14	1.14	1.11	1.60

Sensor 5: 2% Ag-SnO<sub>2</sub>

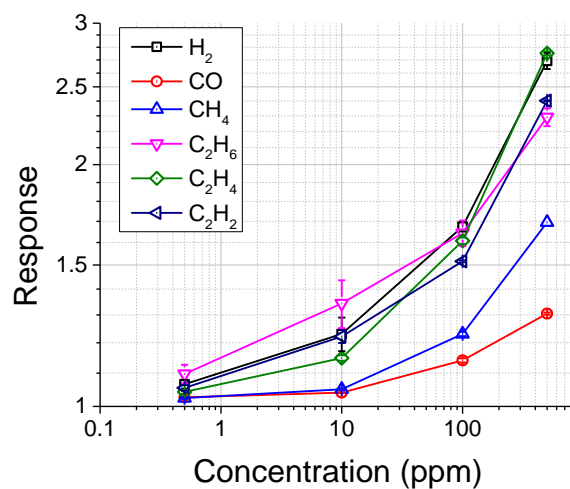


**Figure 126.** Concentration vs. response curves of 6 gases.

**Table 33.** Summary of response values.

Concentration (ppm)	Response (Rair/Rgas)					
	H <sub>2</sub>	CO	CH <sub>4</sub>	C <sub>2</sub> H <sub>6</sub>	C <sub>2</sub> H <sub>4</sub>	C <sub>2</sub> H <sub>2</sub>
0.5	1.07	1.03	1.02	1.10	1.04	1.05
10	1.23	1.04	1.05	1.34	1.15	1.22
100	1.67	1.14	1.23	1.64	1.61	1.52
500	2.69	1.31	1.70	2.29	2.75	2.40



Sensor 6: 2%Pd-SnO<sub>2</sub>

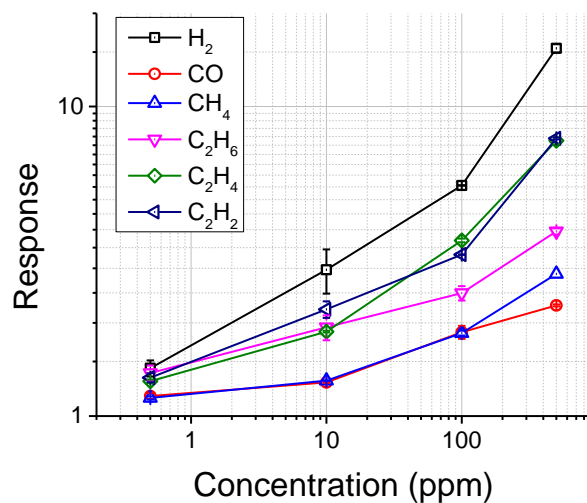


**Figure 127.** Concentration vs. response curves of 6 gases.

**Table 34.** Summary of response values.

Concentration (ppm)	Response (Rair/Rgas)					
	H <sub>2</sub>	CO	CH <sub>4</sub>	C <sub>2</sub> H <sub>6</sub>	C <sub>2</sub> H <sub>4</sub>	C <sub>2</sub> H <sub>2</sub>
0.5	1.43	1.16	1.14	1.38	1.30	1.33
10	2.97	1.28	1.30	1.94	1.87	2.21
100	5.56	1.87	1.85	2.50	3.69	3.33
500	15.41	2.28	2.88	3.95	7.75	7.89

Sensor 7: 5% Cu-SnO<sub>2</sub>

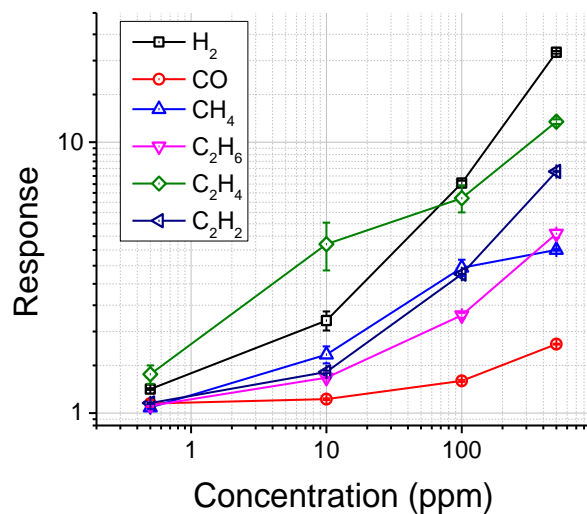


**Figure 128.** Concentration vs. response curves of 6 gases.

**Table 35.** Summary of response values.

Concentration (ppm)	Response (R <sub>air</sub> /R <sub>gas</sub> )					
	H <sub>2</sub>	CO	CH <sub>4</sub>	C <sub>2</sub> H <sub>6</sub>	C <sub>2</sub> H <sub>4</sub>	C <sub>2</sub> H <sub>2</sub>
0.5	1.23	1.09	1.05	1.06	1.39	1.09
10	2.19	1.13	1.64	1.35	4.20	1.42
100	7.06	1.32	3.44	2.30	6.21	3.26
500	21.47	1.80	4.00	4.60	11.91	7.80

Sensor 8: 1% Ni-SnO<sub>2</sub>

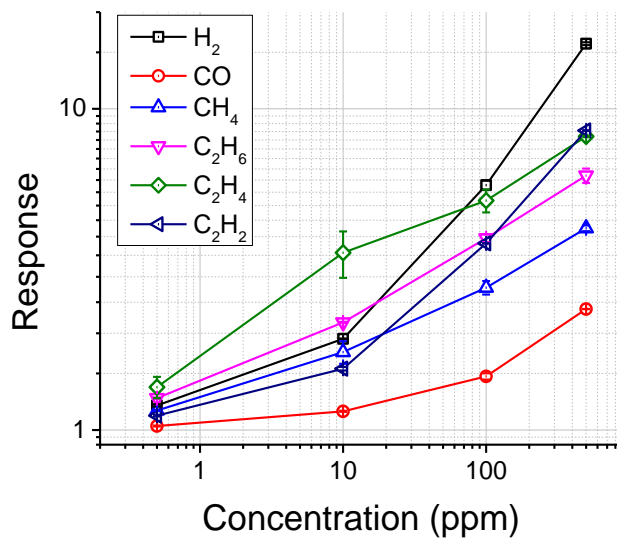


**Figure 129.** Concentration vs. response curves of 6 gases.

**Table 36.** Summary of response values.

Concentration (ppm)	Response (Rair/Rgas)					
	H <sub>2</sub>	CO	CH <sub>4</sub>	C <sub>2</sub> H <sub>6</sub>	C <sub>2</sub> H <sub>4</sub>	C <sub>2</sub> H <sub>2</sub>
0.5	1.19	1.03	1.15	1.26	1.36	1.11
10	1.92	1.14	1.75	2.16	3.56	1.55
100	5.78	1.47	2.78	3.95	5.18	3.81
500	15.95	2.38	4.25	6.20	8.21	8.56

## 8. CONCLUSIONS AND FUTURE WORK

Major conclusions derived from the entire work are formulated below. New challenges and directions for future work arisen from the findings of this thesis are given then.

### Chapter 3

In summary, we developed a simple, versatile, and highly reproducible self-assembly method for fabricating sensors composed of only a monolayer of CuO or ZnO nanosheets. The film formation mechanism is attributed to the amphiphilic nature of the as-prepared nanosheets. The quality of the monolayer film is dictated by the addition amount and the dispersion of nanosheet. Multilayer deposition using the same self-assembly technique is enabled by an annealing treatment after depositing each layer. Among the CuO-based H<sub>2</sub>S sensors, CuO-mono shows highest sensitivity, fastest response and recovery, and excellent immunity to the humidity interference. Moreover, the sensing performance (i.e. sensitivity, response and recovery rate) is found to be negatively impacted by increasing sensing film thickness for the CuO-based sensors. The negative influence from sensing film thickness is attributed to the analyte gas dilution effect and impeded gas diffusion, both of which aggravate with increasing thickness. A model considering Knudsen diffusion of gas in the inter-nanosheet spaces (~3 nm), Langmuir isotherm equation for H<sub>2</sub>S adsorption on the nanosheet surface, and first order reaction kinetic for surface reaction consuming H<sub>2</sub>S, was established, and it describes well the experimentally measured sensor response data. The same correlation between sensing performance and sensing film thickness is also observed for the ZnO nanosheet based H<sub>2</sub> sensor. Both the experimental and the simulation data

suggest that monolayer configuration is less prone to the gas-diffusion-related effects and should be adopted for enhanced sensitivity and response transient.

#### Chapter 4

In conclusion, humidity independent H<sub>2</sub>S sensing performance is achieved for the first time without applying any surface additive. The self-assembled monolayer films of CuO nanosheets show constant response to H<sub>2</sub>S (coefficient of variations < 3%) regardless of humidity variations. The monolayer sensor also displays excellent sensitivity for H<sub>2</sub>S (detection limit 3 ppb), prominent selectivity over typical interfering VOCs, i.e. toluene, ethanol and acetone, and high stability in operating conditions with varied humidity levels. The XPS study confirms the reaction between hydroxyl groups and H<sub>2</sub>S on the surface of CuO, which generates a resistive surface layer of Cu<sub>2</sub>S and S. In humid environment, the diminishing role of redox reaction between ionosorbed oxygen species and H<sub>2</sub>S in generating the increase in electrical resistance is filled in by the change in geometric factors (D<sub>C</sub> and D<sub>G</sub>). In comparison to using moisture adsorbent for alleviating humidity interference, the new strategy has an advantage of long-term usage in humid environment without needs for the regeneration of adsorbent. However, to achieve humidity independent sensing of H<sub>2</sub>S with CuO sensor, it is essential to prepare ultra-thin sensing film for the rapid diffusion of H<sub>2</sub>S in the shrinking pores due to the formation of Cu<sub>2-x</sub>S.

#### Chapter 5

In conclusion, ultrathin films of aligned ZnO nanowires with periodic v-grooves can be obtained via Langmuir Blodgett assembly. The sintering behavior of Au clusters on ZnO LB film was analyzed based on the evolution of particle size distribution. Au NPs is

observed to achieve a stable size of 11 nm on ZnO LB film, while particle sintering and growth is still observed after Au NPs grew beyond 20 nm on conventional thin film. The origin of the sintering resistance on ZnO LB film is attributed to the ridges of the v-grooves, which serves as diffusion barriers for particle migration. The sensing performance of pristine ZnO LB film is superior to conventional thin film in all key parameters, thanks to the high gas accessibility of ZnO LB film. With high dispersion of small Au NPs as surface dopants, the ZnO LB film is converted into a highly responsive conductance switch, the bulk conductivity of which is fully determined by its surface chemistry. Unprecedented sensitivity ( $37 \text{ ppm}^{-1}$ ) and detection limit (3 ppb) towards acetylene ( $\text{C}_2\text{H}_2$ ) are observed for Au-doped ZnO LB film.

## Chapter 6

In summary,  $\text{SnO}_2$  with dopant-segregation-induced core (dopant-free)/shell (dopant-rich) structure was achieved by annealing  $\text{Al}_2\text{O}_3/\text{SnO}_2$  metastable solid solution. After the thermal treatment, Al-rich shell were observed for the Al-doped  $\text{SnO}_2$  samples, due to the dopant migration driven by strain and electrostatic interaction energy.

The prominent solute drag effect in the Al-rich shell helped retarding grain growth for the samples with core-shell structure. As a result, smaller crystallite size ( $D_{\text{XRD}}$ ) and lower level of coalescence ( $D_{\text{BET}}/D_{\text{XRD}}$ ) were observed than that of pure  $\text{SnO}_2$ . Moreover, the growth inhibition effectiveness of the Al-rich shell was discovered to be proportional to the  $\text{Al}^{3+}$  concentration at the particle surface, which confirms with the classical theory of solute drag effect. The  $\text{Al}^{3+}$  concentration at the particle surface initially increase with  $\text{Al}^{3+}$  dopant concentration, until reaching a maximum value at 5 mol%, at which the  $D_{\text{XRD}}$

and  $D_{\text{BET}}/D_{\text{XRD}}$  are also the lowest. Doping more than 5 mol% leads to the nucleation of Al-rich nanoparticles at the expense of the dopant rich shell, which decreases the surface concentration of  $\text{Al}^{3+}$ , and in turn, downgrades the solute drag effect within the Al-rich shell.

Notable enhancement in  $\text{H}_2$  sensitivity Al was observed for the  $\text{SnO}_2$  samples with Al-rich shell over the pure  $\text{SnO}_2$  sample. Besides, dependence on  $\text{Al}^{3+}$  dopant concentration same as that of structural changes (crystallite size and coalescence level) was observed for  $\text{H}_2$  sensitivity, with maximum sensor response value achieved also by  $\text{SnO}_2$  sample doped with 5 mol% Al. A semiquantitative multigrain model was proposed to bridge the connection between the structural changes and the sensitivity enhancement by suggesting that with core-shell structure, smaller crystallite size and lower level of coalescence lead to more gas-sensitive double Schottky barriers and constricted conduction channel along the conduction path, which leads to higher sensitivity. Based on previous findings, forming dopant-segregation induced core-shell structure is a promising strategy to enhance thermal stability as well as gas sensitivity for nanocrystalline based metal oxide gas sensor.

## Chapter 7

Designed and built a sensor evaluation system enabling 4 sensor nodes testing across 6 decades of analyte concentrations. Developed a scalable sensor fabrication technique, and designed methods for evaluating the performance. Tailored the structure and composition of the sensing film to meet the targets on detection limits and response time. Developed strategies (e.g. semipermeable membrane, chemical modifier) to differentiate similar dissolved gases. Performed accelerated life testing and principal component

analysis to select 9 sensors for building the sensor array. Delivered the assembled sensor array to the industrial partner on time. Collaborated in the design and testing of an automated dissolved gas analysis system prototype.

#### FUTURE WORKS

1. Perform TPD and DRIFT analysis on Au@ZnO samples to verify the claim on surface reaction based on the conduction measurement
2. Develop the lithography step to pattern the monolayer film deposited by Langmuir-Blodgett assembly
3. Testing the thermal mechanical and electrical properties of the microheater
4. Develop processes to deposit monolayer film of 2D metal chalcogens, carbon nanotubes, and graphene with Langmuir-Blodgett assembly
5. Develop machine learning algorithm for sensor array study



## REFERENCES

- (1) Kanazawa, E.; Sakai, G.; Shimanoe, K.; Kanmura, Y.; Teraoka, Y.; Miura, N.; Yamazoe, N. Metal Oxide Semiconductor N<sub>2</sub>O Sensor for Medical Use. *Sensors and Actuators B: Chemical* **2001**, *77* (1), 72–77. [https://doi.org/10.1016/S0925-4005\(01\)00675-X](https://doi.org/10.1016/S0925-4005(01)00675-X).
- (2) Wang, X.; Zhao, M.; Liu, F.; Jia, J.; Li, X.; Cao, L. C<sub>2</sub>H<sub>2</sub> Gas Sensor Based on Ni-Doped ZnO Electrospun Nanofibers. *Ceramics International* **2013**, *39* (3), 2883–2887. <https://doi.org/10.1016/j.ceramint.2012.09.062>.
- (3) Blaschke, M.; Tille, T.; Robertson, P.; Mair, S.; Weimar, U.; Ulmer, H. MEMS Gas-Sensor Array for Monitoring the Perceived Car-Cabin Air Quality. *IEEE Sensors Journal* **2006**, *6* (5), 1298–1308. <https://doi.org/10.1109/JSEN.2006.881399>.
- (4) Santos, J. P.; Lozano, J.; Aleixandre, M. Electronic Noses Applications in Beer Technology. *Brewing Technology* **2017**. <https://doi.org/10.5772/intechopen.68822>.
- (5) Huyberechts, G.; Szc owka, P.; Roggen, J.; Licznarski, B. W. Simultaneous Quantification of Carbon Monoxide and Methane in Humid Air Using a Sensor Array and an Artificial Neural Network. *Sensors and Actuators B: Chemical* **1997**, *45* (2), 123–130. [https://doi.org/10.1016/S0925-4005\(97\)00283-9](https://doi.org/10.1016/S0925-4005(97)00283-9).
- (6) Xiao, G.; Chen, W.; Yu, C.; Jin, L. Study on ZnO-Based Gas Sensor for Detection of Acetylene Dissolved in Transformer Oil. In *2018 IEEE International Instrumentation and Measurement Technology Conference (I2MTC)*; 2018; pp 1–6. <https://doi.org/10.1109/I2MTC.2018.8409830>.
- (7) Hill, D.; Binions, R. Breath Analysis for Medical Diagnosis. *International Journal on Smart Sensing and Intelligent Systems* **2012**, *5* (2), 401–440. <https://doi.org/10.21307/ijssis-2017-488>.
- (8) Masson, N.; Piedrahita, R.; Hannigan, M. Approach for Quantification of Metal Oxide Type Semiconductor Gas Sensors Used for Ambient Air Quality Monitoring. *Sensors and Actuators B: Chemical* **2015**, *208*, 339–345. <https://doi.org/10.1016/j.snb.2014.11.032>.
- (9) Sharma, R. K.; Chan, P. C. H.; Tang, Z.; Yan, G.; Hsing, I. M.; Sin, J. K. O. Investigation of Stability and Reliability of Tin Oxide Thin-Film for Integrated Micro-Machined Gas Sensor Devices. *Sensors and Actuators, B: Chemical* **2001**, *81* (1), 9–16. [https://doi.org/10.1016/S0925-4005\(01\)00920-0](https://doi.org/10.1016/S0925-4005(01)00920-0).
- (10) Jeong, Y. K.; Choi, G. M. Nonstoichiometry and Electrical Conduction of CuO. *Journal of Physics and Chemistry of Solids* **1996**, *57* (1), 81–84. [https://doi.org/10.1016/0022-3697\(95\)00130-1](https://doi.org/10.1016/0022-3697(95)00130-1).

- (11) Simon, I.; Bârsan, N.; Bauer, M.; Weimar, U. Micromachined Metal Oxide Gas Sensors: Opportunities to Improve Sensor Performance. *Sensors and Actuators B: Chemical* **2001**, *73* (1), 1–26. [https://doi.org/10.1016/S0925-4005\(00\)00639-0](https://doi.org/10.1016/S0925-4005(00)00639-0).
- (12) Hausner, M.; Zacheja, J.; Binder, J. Multi-Electrode Substrate for Selectivity Enhancement in Air Monitoring. *Sensors and Actuators B: Chemical* **1997**, *43* (1), 11–17. [https://doi.org/10.1016/S0925-4005\(97\)00140-8](https://doi.org/10.1016/S0925-4005(97)00140-8).
- (13) Gas Sensors - Principles, Operation and Developments | G. Sberveglieri | Springer <https://www.springer.com/gp/book/9780792320043> (accessed Aug 12, 2020).
- (14) Sahm, T.; Gurlo, A.; Bârsan, N.; Weimar, U. Basics of Oxygen and SnO<sub>2</sub> Interaction; Work Function Change and Conductivity Measurements. *Sensors and Actuators B: Chemical* **2006**, *118* (1), 78–83. <https://doi.org/10.1016/j.snb.2006.04.004>.
- (15) Kohl, D. Surface Processes in the Detection of Reducing Gases with SnO<sub>2</sub>-Based Devices. *Sensors and Actuators* **1989**, *18* (1), 71–113. [https://doi.org/10.1016/0250-6874\(89\)87026-X](https://doi.org/10.1016/0250-6874(89)87026-X).
- (16) Oxygen in Catalysis on Transition Metal Oxides: Catalysis Reviews: Vol 19, No 1 <https://www.tandfonline.com/doi/abs/10.1080/03602457908065099> (accessed Aug 12, 2020).
- (17) Mizokawa, Y.; Nakamura, S. ESR and Electric Conductance Studies of the Fine-Powdered SnO<sub>2</sub>. *Jpn. J. Appl. Phys.* **1975**, *14* (6), 779. <https://doi.org/10.1143/JJAP.14.779>.
- (18) Kappers, L. A.; Gilliam, O. R.; Evans, S. M.; Halliburton, L. E.; Giles, N. C. EPR and Optical Study of Oxygen and Zinc Vacancies in Electron-Irradiated ZnO. *Nuclear Instruments and Methods in Physics Research Section B: Beam Interactions with Materials and Atoms* **2008**, *266* (12), 2953–2957. <https://doi.org/10.1016/j.nimb.2008.03.146>.
- (19) Barsan, N.; Weimar, U. Conduction Model of Metal Oxide Gas Sensors. *Journal of Electroceramics* **2001**, *7* (3), 143–167. <https://doi.org/10.1023/A:1014405811371>.
- (20) Pulkkinen, U.; Rantala, T. T.; Rantala, T. S.; Lantto, V. Kinetic Monte Carlo Simulation of Oxygen Exchange of SnO<sub>2</sub> Surface. *Journal of Molecular Catalysis A: Chemical* **2001**, *166* (1), 15–21. [https://doi.org/10.1016/S1381-1169\(00\)00466-0](https://doi.org/10.1016/S1381-1169(00)00466-0).
- (21) Harbeck, S.; Szatvanyi, A.; Barsan, N.; Weimar, U.; Hoffmann, V. DRIFT Studies of Thick Film Un-Doped and Pd-Doped SnO<sub>2</sub> Sensors: Temperature Changes Effect and CO Detection Mechanism in the Presence of Water Vapour. *Thin Solid Films* **2003**, *436* (1), 76–83. [https://doi.org/10.1016/S0040-6090\(03\)00512-1](https://doi.org/10.1016/S0040-6090(03)00512-1).

- (22) Pavelko, R. G.; Daly, H.; Hübner, M.; Hardacre, C.; Llobet, E. Time-Resolved DRIFTS, MS, and Resistance Study of SnO<sub>2</sub> Materials: The Role of Surface Hydroxyl Groups in Formation of Donor States. *J. Phys. Chem. C* **2013**, *117* (8), 4158–4167. <https://doi.org/10.1021/jp312532u>.
- (23) Koziej, D.; Bârsan, N.; Hoffmann, V.; Szuber, J.; Weimar, U. Complementary Phenomenological and Spectroscopic Studies of Propane Sensing with Tin Dioxide Based Sensors. *Sensors and Actuators B: Chemical* **2005**, *108* (1), 75–83. <https://doi.org/10.1016/j.snb.2004.12.076>.
- (24) Krivetskiy, V. V.; Rummyantseva, M. N.; Gaskov, A. M. Chemical Modification of Nanocrystalline Tin Dioxide for Selective Gas Sensors. *Russ. Chem. Rev.* **2013**, *82* (10), 917–941. <https://doi.org/10.1070/RC2013v082n10ABEH004366>.
- (25) Ramgir, N. S.; Ganapathi, S. K.; Kaur, M.; Datta, N.; Muthe, K. P.; Aswal, D. K.; Gupta, S. K.; Yakhmi, J. V. Sub-Ppm H<sub>2</sub>S Sensing at Room Temperature Using CuO Thin Films. *Sensors and Actuators B: Chemical* **2010**, *151* (1), 90–96. <https://doi.org/10.1016/j.snb.2010.09.043>.
- (26) Koziej, D.; Bârsan, N.; Weimar, U.; Szuber, J.; Shimanoe, K.; Yamazoe, N. Water–Oxygen Interplay on Tin Dioxide Surface: Implication on Gas Sensing. *Chemical Physics Letters* **2005**, *410* (4), 321–323. <https://doi.org/10.1016/j.cplett.2005.05.107>.
- (27) Chemical Sensor Technology, Volume 1 - 1st Edition <https://www.elsevier.com/books/chemical-sensor-technology/seiyama/978-0-444-98901-7> (accessed Aug 12, 2020).
- (28) Gurlo, A.; Riedel, R. In Situ and Operando Spectroscopy for Assessing Mechanisms of Gas Sensing. *Angewandte Chemie International Edition* **2007**, *46* (21), 3826–3848. <https://doi.org/10.1002/anie.200602597>.
- (29) Yamazoe, N.; Shimanoe, K. Roles of Shape and Size of Component Crystals in Semiconductor Gas Sensors. *Journal of The Electrochemical Society* **9**.
- (30) Huo, L.; Li, W.; Lu, L.; Cui, H.; Xi, S.; Wang, J.; Zhao, B.; Shen, Y.; Lu, Z. Preparation, Structure, and Properties of Three-Dimensional Ordered  $\alpha$ -Fe<sub>2</sub>O<sub>3</sub> Nanoparticulate Film. *Chem. Mater.* **2000**, *12* (3), 790–794. <https://doi.org/10.1021/cm990690+>.
- (31) Hua, Z.; Li, Y.; Zeng, Y.; Wu, Y. A Theoretical Investigation of the Power-Law Response of Metal Oxide Semiconductor Gas Sensors I: Schottky Barrier Control. *Sensors and Actuators B: Chemical* **2018**, *255*, 1911–1919. <https://doi.org/10.1016/j.snb.2017.08.206>.

- (32) Barsan, N.; Simion, C.; Heine, T.; Pokhrel, S.; Weimar, U. Modeling of Sensing and Transduction for P-Type Semiconducting Metal Oxide Based Gas Sensors. *J Electroceram* **2010**, *25* (1), 11–19. <https://doi.org/10.1007/s10832-009-9583-x>.
- (33) Puigcorbé, J.; Vilà, A.; Cerdà, J.; Cirera, A.; Gràcia, I.; Cané, C.; Morante, J. R. Thermo-Mechanical Analysis of Micro-Drop Coated Gas Sensors. *Sensors and Actuators A: Physical* **2002**, *97–98*, 379–385. [https://doi.org/10.1016/S0924-4247\(01\)00858-5](https://doi.org/10.1016/S0924-4247(01)00858-5).
- (34) Suematsu, K.; Harano, W.; Oyama, T.; Shin, Y.; Watanabe, K.; Shimanoe, K. Pulse-Driven Semiconductor Gas Sensors Toward Ppt Level Toluene Detection. *Anal. Chem.* **2018**, *90* (19), 11219–11223. <https://doi.org/10.1021/acs.analchem.8b03076>.
- (35) Yang, P.; Kim, F. Langmuir–Blodgett Assembly of One-Dimensional Nanostructures. *ChemPhysChem* **2002**, *3* (6), 503–506. [https://doi.org/10.1002/1439-7641\(20020617\)3:6<503::AID-CPHC503>3.0.CO;2-U](https://doi.org/10.1002/1439-7641(20020617)3:6<503::AID-CPHC503>3.0.CO;2-U).
- (36) Tao, A.; Kim, F.; Hess, C.; Goldberger, J.; He, R.; Sun, Y.; Xia, Y.; Yang, P. Langmuir–Blodgett Silver Nanowire Monolayers for Molecular Sensing Using Surface-Enhanced Raman Spectroscopy. *Nano Lett.* **2003**, *3* (9), 1229–1233. <https://doi.org/10.1021/nl0344209>.
- (37) Song, H.; Kim, F.; Connor, S.; Somorjai, G. A.; Yang, P. Pt Nanocrystals: Shape Control and Langmuir–Blodgett Monolayer Formation. *J. Phys. Chem. B* **2005**, *109* (1), 188–193. <https://doi.org/10.1021/jp0464775>.
- (38) Tao, A.; Sinsermsuksakul, P.; Yang, P. Tunable Plasmonic Lattices of Silver Nanocrystals. *Nature Nanotechnology* **2007**, *2* (7), 435–440. <https://doi.org/10.1038/nnano.2007.189>.
- (39) Cheng, W.; Ju, Y.; Payamyar, P.; Primc, D.; Rao, J.; Willa, C.; Koziej, D.; Niederberger, M. Large-Area Alignment of Tungsten Oxide Nanowires over Flat and Patterned Substrates for Room-Temperature Gas Sensing. *Angewandte Chemie International Edition* **2015**, *54* (1), 340–344. <https://doi.org/10.1002/anie.201408617>.
- (40) Korotcenkov, G.; Cho, B. K. Instability of Metal Oxide-Based Conductometric Gas Sensors and Approaches to Stability Improvement (Short Survey). *Sensors and Actuators, B: Chemical*. 2011, pp 527–538. <https://doi.org/10.1016/j.snb.2011.02.024>.
- (41) Baik, N. S.; Sakai, G.; Shimanoe, K.; Miura, N.; Yamazoe, N. Hydrothermal Treatment of Tin Oxide Sol Solution for Preparation of Thin-Film Sensor with Enhanced Thermal Stability and Gas Sensitivity. *Sensors and Actuators, B: Chemical* **2000**, *65* (1), 97–100. [https://doi.org/10.1016/S0925-4005\(99\)00403-7](https://doi.org/10.1016/S0925-4005(99)00403-7).

- (42) Liu, F.; Kirchheim, R. Nano-Scale Grain Growth Inhibited by Reducing Grain Boundary Energy through Solute Segregation. *Journal of Crystal Growth* **2004**, *264* (1–3), 385–391. <https://doi.org/10.1016/j.jcrysgr.2003.12.021>.
- (43) Leite, E. R.; Weber, I. T.; Longo, E.; Varela, J. A. A New Method to Control Particle Size and Particle Size Distribution of SnO<sub>2</sub> Nanoparticles for Gas Sensor Applications. *Advanced Materials* **2000**, *12* (13), 965–968. [https://doi.org/10.1002/1521-4095\(200006\)12:13<965::AID-ADMA965>3.0.CO;2-7](https://doi.org/10.1002/1521-4095(200006)12:13<965::AID-ADMA965>3.0.CO;2-7).
- (44) Leite, E. R.; Maciel, A. P.; Weber, I. T.; Lisboa-Filho, P. N.; Longo, E.; Paiva-Santos, C. O.; Andrade, A. V. C.; Pakoscimas, C. A.; Maniette, Y.; Schreiner, W. H. Development of Metal Oxide Nanoparticles with High Stability against Particle Growth Using a Metastable Solid Solution. *Advanced Materials* **2002**, *14* (12), 905–908. [https://doi.org/10.1002/1521-4095\(20020618\)14:12<905::AID-ADMA905>3.0.CO;2-D](https://doi.org/10.1002/1521-4095(20020618)14:12<905::AID-ADMA905>3.0.CO;2-D).
- (45) Kang, S.-J. L. 13 - Densification and Grain Growth in Ionic Compounds. In *Sintering*; 2005; pp 181–196. <http://dx.doi.org/10.1016/B978-075066385-4/50013-3>.
- (46) Madou, M. J.; Morrison, S. R. *Chemical Sensing with Solid State Devices*; Elsevier, 2012.
- (47) Miao, J.; Chen, C.; Lin, Y. S. Metal-Oxide Nanoparticles with a Dopant-Segregation-Induced Core–Shell Structure: Gas Sensing Properties. *J. Phys. Chem. C* **2018**, *122* (37), 21322–21329. <https://doi.org/10.1021/acs.jpcc.8b04391>.
- (48) Jalal, A. H.; Alam, F.; Roychoudhury, S.; Umasankar, Y.; Pala, N.; Bhansali, S. Prospects and Challenges of Volatile Organic Compound Sensors in Human Healthcare. *ACS Sens.* **2018**, *3* (7), 1246–1263. <https://doi.org/10.1021/acssensors.8b00400>.
- (49) Kumar, R.; Goel, N.; Kumar, M. UV-Activated MoS<sub>2</sub> Based Fast and Reversible NO<sub>2</sub> Sensor at Room Temperature. *ACS Sens* **2017**, *2* (11), 1744–1752. <https://doi.org/10.1021/acssensors.7b00731>.
- (50) Leonardi, S. G. Two-Dimensional Zinc Oxide Nanostructures for Gas Sensor Applications. *Chemosensors* **2017**, *5* (2), 17. <https://doi.org/10.3390/chemosensors5020017>.
- (51) Neri, G. Thin 2D: The New Dimensionality in Gas Sensing. *Chemosensors* **2017**, *5* (3), 21. <https://doi.org/10.3390/chemosensors5030021>.
- (52) Kannan, P. K.; Late, D. J.; Morgan, H.; Rout, C. S. Recent Developments in 2D Layered Inorganic Nanomaterials for Sensing. *Nanoscale* **2015**, *7* (32), 13293–13312. <https://doi.org/10.1039/C5NR03633J>.

- (53) Liu, X.; Ma, T.; Pinna, N.; Zhang, J. Two-Dimensional Nanostructured Materials for Gas Sensing. *Advanced Functional Materials* **2017**, *27* (37), 1702168. <https://doi.org/10.1002/adfm.201702168>.
- (54) Su, D.; Xie, X.; Dou, S.; Wang, G. CuO Single Crystal with Exposed {001} Facets - A Highly Efficient Material for Gas Sensing and Li-Ion Battery Applications. *Scientific Reports* **2014**, *4*, 5753. <https://doi.org/10.1038/srep05753>.
- (55) Hoa, N. D.; El-Safty, S. A. Synthesis of Mesoporous NiO Nanosheets for the Detection of Toxic NO<sub>2</sub> Gas. *Chemistry – A European Journal* **2011**, *17* (46), 12896–12901. <https://doi.org/10.1002/chem.201101122>.
- (56) Liu, J.; Guo, Z.; Meng, F.; Luo, T.; Li, M.; Liu, J. Novel Porous Single-Crystalline ZnO Nanosheets Fabricated by Annealing ZnS(En)0.5(En = Ethylenediamine) Precursor. Application in a Gas Sensor for Indoor Air Contaminant Detection. *Nanotechnology* **2009**, *20* (12), 125501. <https://doi.org/10.1088/0957-4484/20/12/125501>.
- (57) Ji, F.; Ren, X.; Zheng, X.; Liu, Y.; Pang, L.; Jiang, J.; Liu, S. (Frank). 2D-MoO<sub>3</sub> Nanosheets for Superior Gas Sensors. *Nanoscale* **2016**, *8* (16), 8696–8703. <https://doi.org/10.1039/C6NR00880A>.
- (58) Liu, X.; Sun, Y.; Yu, M.; Yin, Y.; Du, B.; Tang, W.; Jiang, T.; Yang, B.; Cao, W.; Ashfold, M. N. R. Enhanced Ethanol Sensing Properties of Ultrathin ZnO Nanosheets Decorated with CuO Nanoparticles. *Sensors and Actuators B: Chemical* **2018**, *255*, 3384–3390. <https://doi.org/10.1016/j.snb.2017.09.165>.
- (59) Mirzaei, A.; Leonardi, S. G.; Neri, G. Detection of Hazardous Volatile Organic Compounds (VOCs) by Metal Oxide Nanostructures-Based Gas Sensors: A Review. *Ceramics International* **2016**, *42* (14), 15119–15141. <https://doi.org/10.1016/j.ceramint.2016.06.145>.
- (60) Xiang, Q.; Meng, G. F.; Zhao, H. B.; Zhang, Y.; Li, H.; Ma, W. J.; Xu, J. Q. Au Nanoparticle Modified WO<sub>3</sub> Nanorods with Their Enhanced Properties for Photocatalysis and Gas Sensing. *J. Phys. Chem. C* **2010**, *114* (5), 2049–2055. <https://doi.org/10.1021/jp909742d>.
- (61) Williams, D. E.; Henshaw, G. S.; Pratt, K. F. E.; Peat, R. Reaction–Diffusion Effects and Systematic Design of Gas-Sensitive Resistors Based on Semiconducting Oxides. *J. Chem. Soc., Faraday Trans.* **1995**, *91* (23), 4299–4307. <https://doi.org/10.1039/FT9959104299>.
- (62) Sakai, G.; Matsunaga, N.; Shimanoe, K.; Yamazoe, N. Theory of Gas-Diffusion Controlled Sensitivity for Thin Film Semiconductor Gas Sensor. *Sensors and Actuators B: Chemical* **2001**, *80* (2), 125–131. [https://doi.org/10.1016/S0925-4005\(01\)00890-5](https://doi.org/10.1016/S0925-4005(01)00890-5).

- (63) Lu, H.; Ma, W.; Gao, J.; Li, J. Diffusion-Reaction Theory for Conductance Response in Metal Oxide Gas Sensing Thin Films. *Sensors and Actuators B: Chemical* **2000**, *66* (1), 228–231. [https://doi.org/10.1016/S0925-4005\(00\)00370-1](https://doi.org/10.1016/S0925-4005(00)00370-1).
- (64) Gardner, J. W. A Diffusion-Reaction Model of Electrical Conduction in Tin Oxide Gas Sensors. *Semicond. Sci. Technol.* **1989**, *4* (5), 345–350. <https://doi.org/10.1088/0268-1242/4/5/003>.
- (65) Gardner, J. W. A Non-Linear Diffusion-Reaction Model of Electrical Conduction in Semiconductor Gas Sensors. *Sensors and Actuators B: Chemical* **1990**, *1* (1), 166–170. [https://doi.org/10.1016/0925-4005\(90\)80194-5](https://doi.org/10.1016/0925-4005(90)80194-5).
- (66) Vilanova, X.; Llobet, E.; Alcubilla, R.; Sueiras, J. E.; Correig, X. Analysis of the Conductance Transient in Thick-Film Tin Oxide Gas Sensors. *Sensors and Actuators B: Chemical* **1996**, *31* (3), 175–180. [https://doi.org/10.1016/0925-4005\(96\)80063-3](https://doi.org/10.1016/0925-4005(96)80063-3).
- (67) Matsunaga, N.; Sakai, G.; Shimanoe, K.; Yamazoe, N. Diffusion Equation-Based Study of Thin Film Semiconductor Gas Sensor-Response Transient. *Sensors and Actuators B: Chemical* **2002**, *83* (1), 216–221. [https://doi.org/10.1016/S0925-4005\(01\)01043-7](https://doi.org/10.1016/S0925-4005(01)01043-7).
- (68) Matsunaga, N.; Sakai, G.; Shimanoe, K.; Yamazoe, N. Formulation of Gas Diffusion Dynamics for Thin Film Semiconductor Gas Sensor Based on Simple Reaction–Diffusion Equation. *Sensors and Actuators B: Chemical* **2003**, *96* (1), 226–233. [https://doi.org/10.1016/S0925-4005\(03\)00529-X](https://doi.org/10.1016/S0925-4005(03)00529-X).
- (69) Yu, H.; Yang, T.; Zhao, R.; Xiao, B.; Li, Z.; Zhang, M. Fast Formaldehyde Gas Sensing Response Properties of Ultrathin SnO<sub>2</sub> Nanosheets. *RSC Advances* **2015**, *5* (126), 104574–104581. <https://doi.org/10.1039/C5RA22755K>.
- (70) Akatsuka, K.; Haga, M.; Ebina, Y.; Osada, M.; Fukuda, K.; Sasaki, T. Construction of Highly Ordered Lamellar Nanostructures through Langmuir–Blodgett Deposition of Molecularly Thin Titania Nanosheets Tens of Micrometers Wide and Their Excellent Dielectric Properties. *ACS Nano* **2009**, *3* (5), 1097–1106. <https://doi.org/10.1021/nn900104u>.
- (71) Tanaka, T.; Fukuda, K.; Ebina, Y.; Takada, K.; Sasaki, T. Highly Organized Self-Assembled Monolayer and Multilayer Films of Titania Nanosheets. *Advanced Materials* **2004**, *16* (11), 872–875. <https://doi.org/10.1002/adma.200306470>.
- (72) Yang, F.; Guo, J.; Liu, M.; Yu, S.; Yan, N.; Li, J.; Guo, Z. Design and Understanding of a High-Performance Gas Sensing Material Based on Copper Oxide Nanowires Exfoliated from a Copper Mesh Substrate. *J. Mater. Chem. A* **2015**, *3* (41), 20477–20481. <https://doi.org/10.1039/C5TA06806A>.

- (73) Volanti, D. P.; Felix, A. A.; Orlandi, M. O.; Whitfield, G.; Yang, D.-J.; Longo, E.; Tuller, H. L.; Varela, J. A. The Role of Hierarchical Morphologies in the Superior Gas Sensing Performance of CuO-Based Chemiresistors. *Advanced Functional Materials* **2013**, *23* (14), 1759–1766. <https://doi.org/10.1002/adfm.201202332>.
- (74) Chen, J.; Wang, K.; Hartman, L.; Zhou, W. H<sub>2</sub>S Detection by Vertically Aligned CuO Nanowire Array Sensors. *J. Phys. Chem. C* **2008**, *112* (41), 16017–16021. <https://doi.org/10.1021/jp805919t>.
- (75) Chang, Y.; Zeng, H. C. Controlled Synthesis and Self-Assembly of Single-Crystalline CuO Nanorods and Nanoribbons. *Crystal Growth & Design* **2004**, *4* (2), 397–402. <https://doi.org/10.1021/cg034127m>.
- (76) Han, X.-G.; He, H.-Z.; Kuang, Q.; Zhou, X.; Zhang, X.-H.; Xu, T.; Xie, Z.-X.; Zheng, L.-S. Controlling Morphologies and Tuning the Related Properties of Nano/Microstructured ZnO Crystallites. *J. Phys. Chem. C* **2009**, *113* (2), 584–589. <https://doi.org/10.1021/jp808233e>.
- (77) Mirzaei, A.; Janghorban, K.; Hashemi, B.; Bonyani, M.; Leonardi, S. G.; Neri, G. Highly Stable and Selective Ethanol Sensor Based on  $\alpha$ -Fe<sub>2</sub>O<sub>3</sub> Nanoparticles Prepared by Pechini Sol–Gel Method. *Ceramics International* **2016**, *42* (5), 6136–6144. <https://doi.org/10.1016/j.ceramint.2015.12.176>.
- (78) Moulder, J. F. *Handbook of X-Ray Photoelectron Spectroscopy: A Reference Book of Standard Spectra for Identification and Interpretation of XPS Data*; Physical Electronics Division, Perkin-Elmer Corporation, 1992.
- (79) Adamson, A. W.; Gast, A. P. *Physical Chemistry of Surfaces*, 6 th.; Wiley: New York, 1997.
- (80) Hu, J.; Li, D.; Lu, J. G.; Wu, R. Effects on Electronic Properties of Molecule Adsorption on CuO Surfaces and Nanowires. *J. Phys. Chem. C* **2010**, *114* (40), 17120–17126. <https://doi.org/10.1021/jp1039089>.
- (81) Mishra, A. K.; Roldan, A.; de Leeuw, N. H. CuO Surfaces and CO<sub>2</sub> Activation: A Dispersion-Corrected DFT+U Study. *J. Phys. Chem. C* **2016**, *120* (4), 2198–2214. <https://doi.org/10.1021/acs.jpcc.5b10431>.
- (82) Bowden, N.; Choi, I. S.; Grzybowski, B. A.; Whitesides, G. M. Mesoscale Self-Assembly of Hexagonal Plates Using Lateral Capillary Forces: Synthesis Using the “Capillary Bond.” *J. Am. Chem. Soc.* **1999**, *121* (23), 5373–5391. <https://doi.org/10.1021/ja983882z>.
- (83) Kralchevsky, P. A.; Nagayama, K. Capillary Interactions between Particles Bound to Interfaces, Liquid Films and Biomembranes. *Advances in Colloid and Interface Science* **2000**, *85* (2), 145–192. [https://doi.org/10.1016/S0001-8686\(99\)00016-0](https://doi.org/10.1016/S0001-8686(99)00016-0).



- (84) Wang, Y.; Lü, Y.; Zhan, W.; Xie, Z.; Kuang, Q.; Zheng, L. Synthesis of Porous Cu<sub>2</sub>O/CuO Cages Using Cu-Based Metal–Organic Frameworks as Templates and Their Gas-Sensing Properties. *J. Mater. Chem. A* **2015**, *3* (24), 12796–12803. <https://doi.org/10.1039/C5TA01108F>.
- (85) Sing, K. S. W. Reporting Physisorption Data for Gas/Solid Systems with Special Reference to the Determination of Surface Area and Porosity (Recommendations 1984). *Pure and Applied Chemistry* **1985**, *57* (4), 603–619. <https://doi.org/10.1351/pac198557040603>.
- (86) Hübner, M.; Simion, C. E.; Tomescu-Stănoiu, A.; Pokhrel, S.; Bârsan, N.; Weimar, U. Influence of Humidity on CO Sensing with P-Type CuO Thick Film Gas Sensors. *Sensors and Actuators B: Chemical* **2011**, *153* (2), 347–353. <https://doi.org/10.1016/j.snb.2010.10.046>.
- (87) Zhang, F.; Zhu, A.; Luo, Y.; Tian, Y.; Yang, J.; Qin, Y. CuO Nanosheets for Sensitive and Selective Determination of H<sub>2</sub>S with High Recovery Ability. *J. Phys. Chem. C* **2010**, *114* (45), 19214–19219. <https://doi.org/10.1021/jp106098z>.
- (88) Steinhauer, S.; Brunet, E.; Maier, T.; Mutinati, G. C.; Köck, A. Suspended CuO Nanowires for Ppb Level H<sub>2</sub>S Sensing in Dry and Humid Atmosphere. *Sensors and Actuators B: Chemical* **2013**, *186*, 550–556. <https://doi.org/10.1016/j.snb.2013.06.044>.
- (89) Kim, H.; Jin, C.; Park, S.; Kim, S.; Lee, C. H<sub>2</sub>S Gas Sensing Properties of Bare and Pd-Functionalized CuO Nanorods. *Sensors and Actuators B: Chemical* **2012**, *161* (1), 594–599. <https://doi.org/10.1016/j.snb.2011.11.006>.
- (90) Ayesh, A. I.; Abu-Hani, A. F. S.; Mahmoud, S. T.; Haik, Y. Selective H<sub>2</sub>S Sensor Based on CuO Nanoparticles Embedded in Organic Membranes. *Sensors and Actuators B: Chemical* **2016**, *231*, 593–600. <https://doi.org/10.1016/j.snb.2016.03.078>.
- (91) Li, Z.; Wang, N.; Lin, Z.; Wang, J.; Liu, W.; Sun, K.; Fu, Y. Q.; Wang, Z. Room-Temperature High-Performance H<sub>2</sub>S Sensor Based on Porous CuO Nanosheets Prepared by Hydrothermal Method. *ACS Appl. Mater. Interfaces* **2016**, *8* (32), 20962–20968. <https://doi.org/10.1021/acsami.6b02893>.
- (92) Li, Z.; Wang, J.; Wang, N.; Yan, S.; Liu, W.; Fu, Y. Q.; Wang, Z. Hydrothermal Synthesis of Hierarchically Flower-like CuO Nanostructures with Porous Nanosheets for Excellent H<sub>2</sub>S Sensing. *Journal of Alloys and Compounds* **2017**, *725*, 1136–1143. <https://doi.org/10.1016/j.jallcom.2017.07.218>.
- (93) Tricoli, A.; Nasiri, N.; De, S. Wearable and Miniaturized Sensor Technologies for Personalized and Preventive Medicine. *Advanced Functional Materials* **2017**, *27* (15), 1605271. <https://doi.org/10.1002/adfm.201605271>.

- (94) Elmi, I.; Zampolli, S.; Cozzani, E.; Mancarella, F.; Cardinali, G. C. Development of Ultra-Low-Power Consumption MOX Sensors with Ppb-Level VOC Detection Capabilities for Emerging Applications. *Sensors and Actuators B: Chemical* **2008**, *135* (1), 342–351. <https://doi.org/10.1016/j.snb.2008.09.002>.
- (95) Hagedorn, K.; Li, W.; Liang, Q.; Dilger, S.; Noebels, M.; Wagner, M. R.; Reparaz, J. S.; Dollinger, A.; Günne, J. S. auf der; Dekorsy, T.; Schmidt-Mende, L.; Polarz, S. Catalytically Doped Semiconductors for Chemical Gas Sensing: Aerogel-Like Aluminum-Containing Zinc Oxide Materials Prepared in the Gas Phase. *Advanced Functional Materials* **2016**, *26* (20), 3424–3437. <https://doi.org/10.1002/adfm.201505355>.
- (96) Tai, H.; Duan, Z.; He, Z.; Li, X.; Xu, J.; Liu, B.; Jiang, Y. Enhanced Ammonia Response of Ti<sub>3</sub>C<sub>2</sub>T<sub>x</sub> Nanosheets Supported by TiO<sub>2</sub> Nanoparticles at Room Temperature. *Sensors and Actuators B: Chemical* **2019**, *298*, 126874. <https://doi.org/10.1016/j.snb.2019.126874>.
- (97) Zhang, Y.; Zhang, J.; Jiang, Y.; Duan, Z.; Liu, B.; Zhao, Q.; Wang, S.; Yuan, Z.; Tai, H. Ultrasensitive Flexible NH<sub>3</sub> Gas Sensor Based on Polyaniline/SrGe<sub>4</sub>O<sub>9</sub> Nanocomposite with Ppt-Level Detection Ability at Room Temperature. *Sensors and Actuators B: Chemical* **2020**, *319*, 128293. <https://doi.org/10.1016/j.snb.2020.128293>.
- (98) Behera, B.; Chandra, S. An Innovative Gas Sensor Incorporating ZnO–CuO Nanoflakes in Planar MEMS Technology. *Sensors and Actuators B: Chemical* **2016**, *229*, 414–424. <https://doi.org/10.1016/j.snb.2016.01.079>.
- (99) Castagna, M. E.; Modica, R.; Cascino, S.; Moschetti, M.; Cerantonio, V.; Messina, A.; Santangelo, A. A High Stability and Uniformity W Micro Hot Plate. *Sensors and Actuators A: Physical* **2018**, *279*, 617–623. <https://doi.org/10.1016/j.sna.2018.06.046>.
- (100) Bhati, V. S.; Ranwa, S.; Fanetti, M.; Valant, M.; Kumar, M. Efficient Hydrogen Sensor Based on Ni-Doped ZnO Nanostructures by RF Sputtering. *Sensors and Actuators B: Chemical* **2018**, *255*, 588–597. <https://doi.org/10.1016/j.snb.2017.08.106>.
- (101) Park, S.-H.; Ryu, J.-Y.; Choi, H.-H.; Kwon, T.-H. Zinc Oxide Thin Film Doped with Al<sub>2</sub>O<sub>3</sub>, TiO<sub>2</sub> and V<sub>2</sub>O<sub>5</sub> as Sensitive Sensor for Trimethylamine Gas. *Sensors and Actuators B: Chemical* **1998**, *46* (2), 75–79. [https://doi.org/10.1016/S0925-4005\(97\)00324-9](https://doi.org/10.1016/S0925-4005(97)00324-9).
- (102) Lee, S. W.; Tsai, P. P.; Chen, H. Comparison Study of SnO<sub>2</sub> Thin- and Thick-Film Gas Sensors. *Sensors and Actuators B: Chemical* **2000**, *67* (1), 122–127. [https://doi.org/10.1016/S0925-4005\(00\)00390-7](https://doi.org/10.1016/S0925-4005(00)00390-7).

- (103) Zhao, J.; Wu, S.; Liu, J.; Liu, H.; Gong, S.; Zhou, D. Tin Oxide Thin Films Prepared by Aerosol-Assisted Chemical Vapor Deposition and the Characteristics on Gas Detection. *Sensors and Actuators B: Chemical* **2010**, *145* (2), 788–793. <https://doi.org/10.1016/j.snb.2010.01.039>.
- (104) Du, X.; George, S. M. Thickness Dependence of Sensor Response for CO Gas Sensing by Tin Oxide Films Grown Using Atomic Layer Deposition. *Sensors and Actuators B: Chemical* **2008**, *135* (1), 152–160. <https://doi.org/10.1016/j.snb.2008.08.015>.
- (105) Rosental, A.; Tarre, A.; Gerst, A.; Sundqvist, J.; Hårsta, A.; Aidla, A.; Aarik, J.; Sammelselg, V.; Uustare, T. Gas Sensing Properties of Epitaxial SnO<sub>2</sub> Thin Films Prepared by Atomic Layer Deposition. *Sensors and Actuators B: Chemical* **2003**, *93* (1), 552–555. [https://doi.org/10.1016/S0925-4005\(03\)00236-3](https://doi.org/10.1016/S0925-4005(03)00236-3).
- (106) Wenas, W. W.; Riyadi, S. Carrier Transport in High-Efficiency ZnO/SiO<sub>2</sub>/Si Solar Cells. *Solar Energy Materials and Solar Cells* **2006**, *90* (18), 3261–3267. <https://doi.org/10.1016/j.solmat.2006.06.026>.
- (107) Polarz, S.; Roy, A.; Lehmann, M.; Driess, M.; Kruis, F. E.; Hoffmann, A.; Zimmer, P. Structure–Property–Function Relationships in Nanoscale Oxide Sensors: A Case Study Based on Zinc Oxide. *Advanced Functional Materials* **2007**, *17* (8), 1385–1391. <https://doi.org/10.1002/adfm.200700139>.
- (108) Parkinson, G. S.; Novotny, Z.; Argentero, G.; Schmid, M.; Pavelec, J.; Kosak, R.; Blaha, P.; Diebold, U. Carbon Monoxide-Induced Adatom Sintering in a Pd–Fe<sub>3</sub>O<sub>4</sub> Model Catalyst. *Nature Materials* **2013**, *12* (8), 724–728. <https://doi.org/10.1038/nmat3667>.
- (109) Simonsen, S. B.; Chorkendorff, I.; Dahl, S.; Skoglundh, M.; Sehested, J.; Helveg, S. Ostwald Ripening in a Pt/SiO<sub>2</sub> Model Catalyst Studied by in Situ TEM. *Journal of Catalysis* **2011**, *281* (1), 147–155. <https://doi.org/10.1016/j.jcat.2011.04.011>.
- (110) Feng, J.; Gao, C.; Yin, Y. Stabilization of Noble Metal Nanostructures for Catalysis and Sensing. *Nanoscale* **2018**, *10* (44), 20492–20504. <https://doi.org/10.1039/C8NR06757K>.
- (111) Hansen, T. W.; DeLaRiva, A. T.; Challa, S. R.; Datye, A. K. Sintering of Catalytic Nanoparticles: Particle Migration or Ostwald Ripening? *Acc. Chem. Res.* **2013**, *46* (8), 1720–1730. <https://doi.org/10.1021/ar3002427>.
- (112) Korotcenkov, G.; Brinzari, V.; Gulina, L. B.; Cho, B. K. The Influence of Gold Nanoparticles on the Conductivity Response of SnO<sub>2</sub>-Based Thin Film Gas Sensors. *Applied Surface Science* **2015**, *353*, 793–803. <https://doi.org/10.1016/j.apsusc.2015.06.192>.

- (113) T. Campbell, C.; V. Sellers, J. R. Anchored Metal Nanoparticles: Effects of Support and Size on Their Energy, Sintering Resistance and Reactivity. *Faraday Discussions* **2013**, *162* (0), 9–30. <https://doi.org/10.1039/C3FD00094J>.
- (114) Ma, J.; Ren, Y.; Zhou, X.; Liu, L.; Zhu, Y.; Cheng, X.; Xu, P.; Li, X.; Deng, Y.; Zhao, D. Pt Nanoparticles Sensitized Ordered Mesoporous WO<sub>3</sub> Semiconductor: Gas Sensing Performance and Mechanism Study. *Advanced Functional Materials* **2018**, *28* (6), 1705268. <https://doi.org/10.1002/adfm.201705268>.
- (115) Duriyasart, F.; Irizawa, A.; Hayashi, K.; Ohtani, M.; Kobiro, K. Sintering-Resistant Metal Catalysts Supported on Concave-Convex Surface of TiO<sub>2</sub> Nanoparticle Assemblies. *ChemCatChem* **2018**, *10* (16), 3392–3396. <https://doi.org/10.1002/cctc.201800624>.
- (116) Liu, J.; Ji, Q.; Imai, T.; Ariga, K.; Abe, H. Sintering-Resistant Nanoparticles in Wide-Mouthed Compartments for Sustained Catalytic Performance. *Scientific Reports* **2017**, *7* (1), 41773. <https://doi.org/10.1038/srep41773>.
- (117) Goodman, E. D.; Schwalbe, J. A.; Cargnello, M. Mechanistic Understanding and the Rational Design of Sinter-Resistant Heterogeneous Catalysts. *ACS Catal.* **2017**, *7* (10), 7156–7173. <https://doi.org/10.1021/acscatal.7b01975>.
- (118) Chung, T.; Lee, Y.; Ahn, M.-S.; Lee, W.; Bae, S.-I.; Hwang, C. S. H.; Jeong, K.-H. Nanoislands as Plasmonic Materials. *Nanoscale* **2019**, *11* (18), 8651–8664. <https://doi.org/10.1039/C8NR10539A>.
- (119) Altomare, M.; Truong Nguyen, N.; Schmuki, P. Templated Dewetting: Designing Entirely Self-Organized Platforms for Photocatalysis. *Chemical Science* **2016**, *7* (12), 6865–6886. <https://doi.org/10.1039/C6SC02555B>.
- (120) Choi, Y. M.; Cho, S.-Y.; Jang, D.; Koh, H.-J.; Choi, J.; Kim, C.-H.; Jung, H.-T. Ultrasensitive Detection of VOCs Using a High-Resolution CuO/Cu<sub>2</sub>O/Ag Nanopattern Sensor. *Advanced Functional Materials* **2019**, *29* (9), 1808319. <https://doi.org/10.1002/adfm.201808319>.
- (121) Anchored metal nanoparticles: Effects of support and size on their energy, sintering resistance and reactivity - Faraday Discussions (RSC Publishing) <https://pubs.rsc.org/en/content/articlelanding/2013/fd/c3fd00094j/unauth#!divAbstract> (accessed May 17, 2020).
- (122) Parker, S. C.; Campbell, C. T. Reactivity and Sintering Kinetics of Au/TiO<sub>2</sub>(110) Model Catalysts: Particle Size Effects. *Top Catal* **2007**, *44* (1–2), 3–13. <https://doi.org/10.1007/s11244-007-0274-z>.
- (123) Miao, J.; Chen, C.; Meng, L.; Lin, Y. S. Self-Assembled Monolayer of Metal Oxide Nanosheet and Structure and Gas-Sensing Property Relationship. *ACS Sens.* **2019**, *4* (5), 1279–1290. <https://doi.org/10.1021/acssensors.9b00162>.

- (124) Hansen, T. W.; DeLaRiva, A. T.; Challa, S. R.; Datye, A. K. Sintering of Catalytic Nanoparticles: Particle Migration or Ostwald Ripening? *Acc. Chem. Res.* **2013**, *46* (8), 1720–1730. <https://doi.org/10.1021/ar3002427>.
- (125) Li, L.; Plessow, P. N.; Rieger, M.; Sauer, S.; Sánchez-Carrera, R. S.; Schaefer, A.; Abild-Pedersen, F. Modeling the Migration of Platinum Nanoparticles on Surfaces Using a Kinetic Monte Carlo Approach. *J. Phys. Chem. C* **2017**, *121* (8), 4261–4269. <https://doi.org/10.1021/acs.jpcc.6b11549>.
- (126) Liu, J.; Qiao, B.; Song, Y.; Tang, H.; Huang, Y.; Liu, J. Highly Active and Sintering-Resistant Heteroepitaxy of Au Nanoparticles on ZnO Nanowires for CO Oxidation. *Journal of Energy Chemistry* **2016**, *25* (3), 361–370. <https://doi.org/10.1016/j.jechem.2016.03.010>.
- (127) Kaneti, Y. V.; Zhang, Z.; Yue, J.; Zakaria, Q. M. D.; Chen, C.; Jiang, X.; Yu, A. Crystal Plane-Dependent Gas-Sensing Properties of Zinc Oxide Nanostructures: Experimental and Theoretical Studies. *Phys. Chem. Chem. Phys.* **2014**, *16* (23), 11471–11480. <https://doi.org/10.1039/C4CP01279H>.
- (128) Hu, S.; Li, W.-X. Metal-Support Interaction Controlled Migration and Coalescence of Supported Particles. *Sci. China Technol. Sci.* **2019**, *62* (5), 762–772. <https://doi.org/10.1007/s11431-018-9407-3>.
- (129) Kolmakov, A.; Klenov, D. O.; Lilach, Y.; Stemmer, S.; Moskovits, M. Enhanced Gas Sensing by Individual SnO<sub>2</sub> Nanowires and Nanobelts Functionalized with Pd Catalyst Particles. *Nano Lett.* **2005**, *5* (4), 667–673. <https://doi.org/10.1021/nl050082v>.
- (130) Jia, J.; Haraki, K.; Kondo, J. N.; Domen, K.; Tamaru, K. Selective Hydrogenation of Acetylene over Au/Al<sub>2</sub>O<sub>3</sub> Catalyst. *J. Phys. Chem. B* **2000**, *104* (47), 11153–11156. <https://doi.org/10.1021/jp001213d>.
- (131) Hua, Z.; Qiu, Z.; Li, Y.; Zeng, Y.; Wu, Y.; Tian, X.; Wang, M.; Li, E. A Theoretical Investigation of the Power-Law Response of Metal Oxide Semiconductor Gas Sensors II: Size and Shape Effects. *Sensors and Actuators B: Chemical* **2018**, *255*, 3541–3549. <https://doi.org/10.1016/j.snb.2017.09.189>.
- (132) Yamazoe, N.; Shimano, K. Theory of Power Laws for Semiconductor Gas Sensors. *Sensors and Actuators, B: Chemical* **2008**, *128* (2), 566–573. <https://doi.org/10.1016/j.snb.2007.07.036>.
- (133) Hübner, M.; Koziej, D.; Grunwaldt, J.-D.; Weimar, U.; Barsan, N. Au Clusters Related Spill-over Sensitization Mechanism in SnO<sub>2</sub>-Based Gas Sensors Identified by Operando HERFD-XAS, Work Function Changes, DC Resistance and Catalytic Conversion Studies. *Physical Chemistry Chemical Physics* **2012**, *14* (38), 13249–13254. <https://doi.org/10.1039/C2CP41349C>.

- (134) Azizi, Y.; Petit, C.; Pitchon, V. Role of Support in the Oxidation of Acetylene over Gold Catalysts. *Journal of Catalysis* **2010**, *269* (1), 26–32. <https://doi.org/10.1016/j.jcat.2009.10.011>.
- (135) Propylene Oxidation Mechanisms and Intermediates Using in Situ Soft X-ray Fluorescence Methods on the Pt(111) Surface | Journal of the American Chemical Society <https://pubs-acsc-org.ezproxy1.lib.asu.edu/doi/full/10.1021/ja992865m#> (accessed Aug 30, 2020).
- (136) Mechanism of acetylene oxidation on the Pt(111) surface using in situ fluorescence yield near-edge spectroscopy - ScienceDirect [https://www-sciencedirect-com.ezproxy1.lib.asu.edu/science/article/pii/S0021951704005573?casa\\_token=0KAW4I\\_S97kAAAAA:DuY1xmEceKAmI\\_1jphmV5r1w-mvgM11Sn5VlcMOWnQ3sNPtm3PMImLfvXJ-L6thirBIJ1gq\\_Tc4](https://www-sciencedirect-com.ezproxy1.lib.asu.edu/science/article/pii/S0021951704005573?casa_token=0KAW4I_S97kAAAAA:DuY1xmEceKAmI_1jphmV5r1w-mvgM11Sn5VlcMOWnQ3sNPtm3PMImLfvXJ-L6thirBIJ1gq_Tc4) (accessed Aug 30, 2020).
- (137) Segura, Y.; López, N.; Pérez-Ramírez, J. Origin of the Superior Hydrogenation Selectivity of Gold Nanoparticles in Alkyne + Alkene Mixtures: Triple- versus Double-Bond Activation. *Journal of Catalysis* **2007**, *247* (2), 383–386. <https://doi.org/10.1016/j.jcat.2007.02.019>.
- (138) Azizi, Y.; Petit, C.; Pitchon, V. Formation of Polymer-Grade Ethylene by Selective Hydrogenation of Acetylene over Au/CeO<sub>2</sub> Catalyst. *Journal of Catalysis* **2008**, *256* (2), 338–344. <https://doi.org/10.1016/j.jcat.2008.04.003>.
- (139) Li, C.; Lin, Y.; Li, F.; Zhu, L.; Meng, F.; Sun, D.; Zhou, J.; Ruan, S. Synthesis and Highly Enhanced Acetylene Sensing Properties of Au Nanoparticle-Decorated Hexagonal ZnO Nanorings. *RSC Advances* **2015**, *5* (106), 87132–87138. <https://doi.org/10.1039/C5RA16552K>.
- (140) Kondalkar, V. V.; Duy, L. T.; Seo, H.; Lee, K. Nanohybrids of Pt-Functionalized Al<sub>2</sub>O<sub>3</sub>/ZnO Core–Shell Nanorods for High-Performance MEMS-Based Acetylene Gas Sensor. *ACS Appl. Mater. Interfaces* **2019**, *11* (29), 25891–25900. <https://doi.org/10.1021/acsami.9b06338>.
- (141) Qiang, Y. Comparative Study on the Detection Characteristics of C<sub>2</sub>H<sub>2</sub> in Various ZnO Nanosensors. *IOP Conf. Ser.: Mater. Sci. Eng.* **2019**, *490*, 022018. <https://doi.org/10.1088/1757-899X/490/2/022018>.
- (142) Qiao, P.-Y.; Zhang, L.-X.; Zhu, M.-Y.; Yin, Y.-Y.; Zhao, Z.-W.; Sun, H.-N.; Dong, J.-Y.; Bie, L.-J. Acetylene Sensing Enhancement of Mesoporous ZnO Nanosheets with Morphology and Defect Induced Structural Sensitization. *Sensors and Actuators B: Chemical* **2017**, *250*, 189–197. <https://doi.org/10.1016/j.snb.2017.04.158>.
- (143) Shen, Z.; Zhang, X.; Ma, X.; Chen, Y.; Liu, M.; Chen, C.; Ruan, S. Synthesis of Hierarchical 3D Porous ZnO Microspheres Decorated by Ultra-Small Au

- Nanoparticles and Its Highly Enhanced Acetylene Gas Sensing Ability. *Journal of Alloys and Compounds* **2018**, *731*, 1029–1036. <https://doi.org/10.1016/j.jallcom.2017.10.156>.
- (144) Uddin, A. S. M. I.; Chung, G. Acetylene Gas Sensing Properties of Silver Nanoparticles Decorated ZnO Morphologies with Reduced Graphene Oxide Hybrids. In *2015 IEEE SENSORS*; 2015; pp 1–4. <https://doi.org/10.1109/ICSENS.2015.7370204>.
- (145) Uddin, A. S. M. I.; Chung, G.-S. Synthesis of Highly Dispersed ZnO Nanoparticles on Graphene Surface and Their Acetylene Sensing Properties. *Sensors and Actuators B: Chemical* **2014**, *205*, 338–344. <https://doi.org/10.1016/j.snb.2014.09.005>.
- (146) Uddin, A. S. M. I.; Chung, G.-S. Fabrication and Characterization of C<sub>2</sub>H<sub>2</sub> Gas Sensor Based on Ag-Loaded Vertical ZnO Nanowires Array. *Procedia Engineering* **2015**, *120*, 582–585. <https://doi.org/10.1016/j.proeng.2015.08.730>.
- (147) Wang, B.; Jin, H. T.; Zheng, Z. Q.; Zhou, Y. H.; Gao, C. Low-Temperature and Highly Sensitive C<sub>2</sub>H<sub>2</sub> Sensor Based on Au Decorated ZnO/In<sub>2</sub>O<sub>3</sub> Belt-Tooth Shape Nano-Heterostructures. *Sensors and Actuators B: Chemical* **2017**, *244*, 344–356. <https://doi.org/10.1016/j.snb.2016.12.044>.
- (148) Zhang, H.; Chen, W.; Song, Z.; Jiang, Z.; Li, X.; Zhang, R. Gas Sensors Based on Flower-like ZnO Structures: Detection of Acetylene Gas Dissolved in Transformer Oil. In *2018 IEEE International Conference on High Voltage Engineering and Application (ICHVE)*; 2018; pp 1–4. <https://doi.org/10.1109/ICHVE.2018.8642082>.
- (149) Peng, S.; Chen, W.; Jin, L.; Xu, L.; Teng, L.; Zhou, Q. Pt-Doped SnO<sub>2</sub> Nanoflower Gas Sensor Detection Characteristic for Hydrocarbon Gases Dissolved in Transformer Oil. In *2016 IEEE International Conference on High Voltage Engineering and Application (ICHVE)*; 2016; pp 1–4. <https://doi.org/10.1109/ICHVE.2016.7800893>.
- (150) Tasaki, T.; Takase, S.; Shimizu, Y. Fabrication of Sm-Based Perovskite-Type Oxide Thin-Films and Gas Sensing Properties to Acetylene. *JST* **2012**, *02* (02), 75–81. <https://doi.org/10.4236/jst.2012.22011>.
- (151) Jin, L.; Chen, W.; Zhang, H.; Xiao, G.; Yu, C.; Zhou, Q. Characterization of Reduced Graphene Oxide (RGO)-Loaded SnO<sub>2</sub> Nanocomposite and Applications in C<sub>2</sub>H<sub>2</sub> Gas Detection. *Applied Sciences* **2017**, *7* (1), 19. <https://doi.org/10.3390/app7010019>.
- (152) Zhou, Q.; Cao, M.; Li, W.; Tang, C.; Zhu, S. Research on Acetylene Sensing Properties and Mechanism of SnO<sub>2</sub> Based Chemical Gas Sensor Decorated with

SnO<sub>2</sub> <https://www.hindawi.com/journals/jnt/2015/714072/abs/> (accessed Jan 11, 2020). <https://doi.org/10.1155/2015/714072>.

- (153) Bârsan, N.; Rebolz, J.; Weimar, U. Conduction Mechanism Switch for SnO<sub>2</sub> Based Sensors during Operation in Application Relevant Conditions; Implications for Modeling of Sensing. *Sensors and Actuators B: Chemical* **2015**, *207*, 455–459. <https://doi.org/10.1016/j.snb.2014.10.016>.
- (154) Saboor, F. H.; Ueda, T.; Kamada, K.; Hyodo, T.; Mortazavi, Y.; Khodadadi, A. A.; Shimizu, Y. Enhanced NO<sub>2</sub> Gas Sensing Performance of Bare and Pd-Loaded SnO<sub>2</sub> Thick Film Sensors under UV-Light Irradiation at Room Temperature. *Sensors and Actuators, B: Chemical* **2016**, *223* (2), 429–439. <https://doi.org/10.1016/j.snb.2015.09.075>.
- (155) Moon, C. S.; Kim, H. R.; Auchterlonie, G.; Drennan, J.; Lee, J. H. Highly Sensitive and Fast Responding CO Sensor Using SnO<sub>2</sub> nanosheets. *Sensors and Actuators, B: Chemical* **2008**, *131* (2), 556–564. <https://doi.org/10.1016/j.snb.2007.12.040>.
- (156) Rothschild, A.; Komem, Y. The Effect of Grain Size on the Sensitivity of Nanocrystalline Metal-Oxide Gas Sensors. *Journal of Applied Physics* **2004**, *95* (11 I), 6374–6380. <https://doi.org/10.1063/1.1728314>.
- (157) Franke, M. E.; Koplín, T. J.; Simon, U. Metal and Metal Oxide Nanoparticles in Chemiresistors: Does the Nanoscale Matter? *Small*. 2006, pp 36–50. <https://doi.org/10.1002/smll.200500261>.
- (158) Wang, X.; Yee, S. S.; Carey, W. P. Transition between Neck-Controlled and Grain-Boundary-Controlled Sensitivity of Metal-Oxide Gas Sensors. *Sensors and Actuators: B. Chemical* **1995**, *25* (1–3), 454–457. [https://doi.org/10.1016/0925-4005\(94\)01395-0](https://doi.org/10.1016/0925-4005(94)01395-0).
- (159) Wu, J.; Huang, Q.; Zeng, D.; Zhang, S.; Yang, L.; Xia, D.; Xiong, Z.; Xie, C. Al-Doping Induced Formation of Oxygen-Vacancy for Enhancing Gas-Sensing Properties of SnO<sub>2</sub>NTs by Electrospinning. *Sensors and Actuators, B: Chemical* **2014**, *198*, 62–69. <https://doi.org/10.1016/j.snb.2014.03.012>.
- (160) Hübner, M.; Bârsan, N.; Weimar, U. Influences of Al, Pd and Pt Additives on the Conduction Mechanism as Well as the Surface and Bulk Properties of SnO<sub>2</sub> Based Polycrystalline Thick Film Gas Sensors. *Sensors and Actuators B: Chemical* **2012**, *171–172*, 172–180. <https://doi.org/10.1016/j.snb.2012.02.080>.
- (161) Ohya, Yutaka & Horinouchi, Kazuhiro & Ban, Takayuki & Takahashi, Yasutaka & Murayama, N. Gas Sensing Properties of Al<sub>2</sub>O<sub>3</sub>/SnO<sub>2</sub> Multilayered Films Modified with Pt. *Journal of the Ceramic Society of Japan* **2002**, *110*, 950–953.
- (162) Aragón, F. H.; Coaquira, J. A. H.; Villegas-Lelovsky, L.; Da Silva, S. W.; Cesar, D. F.; Nagamine, L. C. C. M.; Cohen, R.; Menéndez-Proupin, E.; Morais, P. C.



- Evolution of the Doping Regimes in the Al-Doped SnO<sub>2</sub>nanoparticles Prepared by a Polymer Precursor Method. *Journal of Physics Condensed Matter* **2015**, 27 (9). <https://doi.org/10.1088/0953-8984/27/9/095301>.
- (163) Hill, R. J. IUCr Commission on Powder Diffraction Rietveld Refinement Round Robin. I. Analysis of Standard X-Ray and Neutron Data for PbSO<sub>4</sub>. *Journal of Applied Crystallography* **1992**, 25, 589–610.
- (164) Hill, R. J.; Cranswick, L. M. D. IUCr Commission on Powder Diffraction Rietveld Refinement Round Robin. II. Analysis of Monoclinic ZrO<sub>2</sub>. *Journal of Applied Crystallography* **1994**, 27, 802–844.
- (165) Doebelin, N.; Kleeberg, R. Profex: A Graphical User Interface for the Rietveld Refinement Program BGMN. *Journal of Applied Crystallography* **2015**, 48, 1573–1580. <https://doi.org/10.1107/S1600576715014685>.
- (166) Lücke, K.; Detert, K. A Quantitative Theory of Grain-Boundary Motion and Recrystallization in Metals in the Presence of Impurities. *Acta Metallurgica* **1957**, 5 (11), 628–637. [https://doi.org/10.1016/0001-6160\(57\)90109-8](https://doi.org/10.1016/0001-6160(57)90109-8).
- (167) Rabkin, E. On the Grain Size Dependent Solute and Particle Drag. *Scripta Materialia* **2000**, 42 (12), 1199–1206. [https://doi.org/10.1016/S1359-6462\(00\)00359-6](https://doi.org/10.1016/S1359-6462(00)00359-6).
- (168) Szczuko, D.; Werner, J.; Oswald, S.; Behr, G.; Wetzig, K. XPS Investigations of Surface Segregation of Doping Elements in SnO<sub>2</sub>. *Applied Surface Science* **2001**. [https://doi.org/10.1016/S0169-4332\(01\)00298-7](https://doi.org/10.1016/S0169-4332(01)00298-7).
- (169) Leite, E. R., Cerri, J. A., Longo, E., Varela, J. A., & Paskocima, C. A. Sintering of Ultrafine Undoped SnO<sub>2</sub> Powder. *Journal of the European Ceramic Society* **2001**, 21 (5), 669–675.
- (170) Yuan, L.; Guo, Z. P.; Konstantinov, K.; Liu, H. K.; Dou, S. X. Nano-Structured Spherical Porous SnO<sub>2</sub> Anodes for Lithium-Ion Batteries. *Journal of Power Sources* **2006**. <https://doi.org/10.1016/j.jpowsour.2006.04.048>.
- (171) Wang, M.; Vandermaar, A. J.; Srivastava, K. D. Review of Condition Assessment of Power Transformers in Service. *IEEE Electrical Insulation Magazine* **2002**. <https://doi.org/10.1109/MEI.2002.1161455>.
- (172) Muhamad, N. a.; Phung, B. T.; Blackburn, T. R.; Coporation, H.; Duval, M.; Committee, T.; Uasl, U.; Universitesi, S.; Xplore, I.; Committee, T.; Power, I.; Society, E. *IEEE Std C57.104<sup>TM</sup>-2008 (Revision of IEEE Std C57.104-1991), IEEE Guide for the Interpretation of Gases Generated in Oil-Immersed Transformers*; 2002. <https://doi.org/10.1109/MEI.2002.1014963>.

- (173) Bakar, N.; Abu-Siada, A.; Islam, S. A Review of Dissolved Gas Analysis Measurement and Interpretation Techniques. *IEEE Electrical Insulation Magazine*. 2014. <https://doi.org/10.1109/MEI.2014.6804740>.

APPENDIX A

LIST OF PUBLICATIONS

The chapters in this dissertation are modified versions of papers published or to be submitted for publication:

Chapter 3:

**Miao, J.;** Meng, L.; Chen, C.; Lin, Y. S. Self-assembled Monolayer of Metal Oxide Nanosheet and Structure and Gas Sensing Property Relationship. *ACS Sens.* 2019, 4 (5), 1279-1290.

Chapter 4:

**Miao, J.;** Chen, C.; Lin, Y. S. Humidity Independent Hydrogen Sulfide Sensing Performance Achieved with Monolayer Film of CuO Nanosheets. *Sens. Act. B.* 2020, 127785.

Chapter 5:

**Miao, J.;** Lin, Y. S. Ultrathin nanostructured Au-ZnO Langmuir-Blodgett films for few-ppb level acetylene detection. *ACS Appl. Nano Mater.* (Accepted)

Chapter 6:

**Miao, J.;** Chen, C.; Lin, Y. S. Metal-Oxide Nanoparticles with a Dopant-segregation-induced Core-shell Structure: Gas Sensing Properties. *J. Phys. Chem. C* 2018, 122 (37), 21322–21329.